UCLouvain
Institute for Information
and Communication Technologies,
Electronics and Applied Mathematics

UCLouvain
Institute of NeuroScience

Interweaving Structure and Function in Human Brain Networks

Benjamin Chiêm

Thesis submitted in partial fulfillment of the requirements for the degree of
Docteur en sciences de l'ingénieur

Dissertation committee:

Prof. Philippe Lefèvre	Chairman – UCLouvain
Prof. Jean-Charles Delvenne	Supervisor – UCLouvain
Prof. Frédéric Crevecoeur	Supervisor – UCLouvain
Prof. Julien Hendrickx	UCLouvain
Prof. Daniele Marinazzo	Universiteit Gent, Belgium
Prof. Joaquín Goñi	Purdue University, USA

Abstract

The human brain is a complex organ. Recent progress in neuroimaging has enabled the mapping of large-scale brain regions and their connections. In parallel, advances in the study of complex networks and systems have impacted diverse research areas. The field of *Network Neuroscience* leverages these developments to model the brain as a network where nodes and edges are estimated from neuroimaging data. Structural networks summarize the anatomical links between delimited brain regions, and functional networks represent the statistical links between the physiological activity of the same regions. Structural and functional connectivity form distinct and complementary components of the complex system that is the brain.

In this thesis, we first use machine learning to illustrate the complementarity of structural and functional connectivity in the detection of schizophrenia in brain networks. Secondly, we propose that observed functional connectivity can be explained by a controllable linear dynamics spreading on the structural network. We derive a model in which different sets of brain regions controlling the dynamics produce coactivation patterns corresponding to different functional states. This model provides a principled way to identify potential control centers in the brain. The identification of control regions is then applied in two case studies where we show that they significantly differ *i)* between schizophrenic patients and healthy controls and *ii)* during meditation with respect to resting-state.

Next, we focus on the individual-level variability of functional connectivity. We build on previous work that applied data-driven methods to extract the individual *fingerprint* of functional networks. We show that applying degree-normalization to functional networks modulates the influence of strongly connected nodes and systematically improves several fingerprinting metrics.

Eventually, we explore an information-theoretic measure called *transfer entropy* in order to detect directed functional interactions between brain regions. We show on a bivariate synthetic example that transfer entropy is able to capture time-varying and delayed interactions in non-stationary signals. In empirical data, we illustrate the challenge of interpreting the results provided by the estimation of transfer entropy.

Acknowledgements

Il s'en passe des choses en quatre années de thèse.
Essais, erreurs, montagnes russes émotionelles, défis, échecs, réussites, syndrome de l'imposteur, voyages, rencontres...
Pour me soutenir dans cette aventure, j'ai eu la chance d'être entouré de personnes formidables. À tous et à toutes, je vous crie un grand **MERCI** !

Je remercie sincèrement mes promoteurs Pr. Jean-Charles Delvenne et Pr. Frédéric Crevecoeur pour leur accompagnement, leurs conseils, leurs encouragements et leur patience durant ces années. J'ai appris beaucoup grâce à vous, et cet enseignement continuera de m'être précieux à l'avenir.

Je remercie également les membres du jury et de mon comité d'accompagnement, les Professeurs P. Lefèvre, D. Marinazzo, J. Goñi, J. Hendrickx et M. Saerens pour vos conseils et votre implication dans l'évaluation de mon travail.

Je suis reconnaissant envers le fonds pour la Formation à la Recherche dans l'Industrie et dans l'Agriculture pour m'avoir octroyé la bourse qui a financé mes recherches.

Avec un sujet de thèse à l'intersection de plusieurs disciplines, j'ai eu la chance de faire partie de différentes équipes de recherche. Merci aux membres de la team 'networks', Leonardo, Alexandre, Martin, Alexey, Leto, Mauro, Mridul pour nos échanges et collaborations. Louer un château pour y faire un *sciencathon*, what else? Merci aussi aux membres de la team 'neuro', Antoine, Laurent, Félicien, Anne, Florence, Ghady, James, Benoît, Nicolas, Lise, David, Irene pour les lundis midi en *Journal Club* et tous les échanges que nous avons pu avoir.

I am truly grateful for the opportunity offered by Prof. Joaquín Goñi to join the team of the CONNplexity Lab in Purdue University. From my meeting with Enrico and you during the first edition of Brainhack Networks to my research stay in Lafayette, you have been a great source of inspiration. I also thank all the team members, Enrico, Uttara, Kausar, Federico, Duy, Mintao, Meenu, Diana, Michael, Brad for our collaborations, for your warm welcome, for the interesting discussions that we have had, and for the great time we spent together during conferences.

Thank you also to the colleagues and friends that I met during these meetings, Josh, Giulia, Caio, Ana, Juan, with whom I had inspiring exchanges.

Merci à l'ensemble de mes collègues de l'Euler pour ces années et particulièrement à celles et ceux qui m'ont aidé dans diverses tâches administratives et techniques, Marie, Pascale, Etienne, François, Astrid, Nathalie, Marie-Hélène.

L'application de mes recherches à l'étude de la méditation a été rendue possible grâce à Dr. Laurence Dricot et Dr. Ron Kupers. Je vous remercie vivement pour cette opportunité qui a enrichi mon travail, ainsi que pour vos suggestions lors de la relecture de mes manuscrits.

Une thèse, ce n'est pas que de la recherche ; c'est aussi un ensemble d'activités scientifiques passionantes. Merci aux membres de l'IEEE Student Branch et de l'Association des Chercheurs et Chercheuses de l'Institut ICTEAM pour les journées de team-building et autres séminaires organisés avec vous. Vive les cookies !

Qui dit thèse, dit co-thésard·e·s... Céline, Sébastien, Antoine, Vincent, Nicolas, Guillaume, Charles, Jean, Api, Horace : sans vous, l'expérience du doctorat aurait été bien moins fun !

Un merci spécial également à l'équipe encadrant le concours et les coachings 'Ma thèse en 180 secondes', Sophie L. et Fanny W., ainsi qu'à tou·te·s les participant·e·s. Cette expérience a été une véritable bouffée d'oxygène entre la rédaction de ma thèse et le confinement interminable lié à la crise du Covid-19.

Pour décompresser et me changer les idées, j'ai pu compter sur des ami·e·s extraordinaires qui se reconnaîtront. Entre verres au Dude, dégustations de whisky, restos, emménagements, mariages, Skypéros, séances d'ordre, événements improbables et tranches de rire mémorables, vous avez été les meilleures personnes qu'on puisse espérer avoir à ses côtés. Merci !

Enfin j'aimerais remercier l'ensemble de ma famille, Papa, Maman, Parrain, JC, Nathalie, Brent, Aurore, Tristan, Miko, Siloé, Mathéo, Bastien, Jocelyne, ainsi que ma future belle-famille et bien sûr Gipsy et Pilou, pour leurs encouragements et leur soutien tout au long de cette aventure. Et je n'oublie pas de te remercier d'être toujours à mes côtés, toi Sarah, ma fiancée, mon amour, mon essentielle.

Data were provided in part by the Human Connectome Project, WU-Minn Consortium (Principal Investigators: David Van Essen and Kamil Ugurbil; 1U54MH091657) funded by the 16 NIH Institutes and Centers that support the NIH Blueprint for Neuroscience Research; and by the McDonnell Center for Systems Neuroscience at Washington University.

Just when you think you know something,
you have to look at it in another way.
Even though it may seem silly
or wrong, you must try.

– John Keating (Robin Williams), in "Dead Poets Society"

Sometimes the best way to solve your
own problems is to help someone else.

– Uncle Iroh, in "Avatar: The Legend of Korra"

Pour toi, Maman.

x

Contents

Acronyms and Notations **1**

1 Introduction **3**

2 Preliminaries **13**
2.1 Networks 13
2.2 Building brain networks 16
2.2.1 Elements of neuroanatomy 16
2.2.2 Magnetic Resonance Imaging 18
2.2.3 Parcellation 19
2.2.4 Structural networks 21
2.2.5 Functional networks 23
2.2.6 Datasets summary 25
2.3 Machine learning 25
2.3.1 Supervised classification 28
2.3.2 Feature selection 28
2.3.3 Validation 29
2.4 Network controllability 29
2.5 Brain fingerprinting 31

3 Supervised Classification of Brain Networks **35**
3.1 Introduction 36
3.2 Materials and Methods 38
3.2.1 Dataset 38
3.2.2 Brain networks reconstruction 38
3.2.3 Embedded feature selection 39
3.2.4 Statistical evaluation 40
3.2.5 Connectivity features and stability assessment 42
3.3 Results 43
3.3.1 Classification and stability performance 43
3.3.2 Brain regions affected in schizophrenia 48

3.4 Discussion . . . 49
3.4.1 Machine learning and biomarker identification . . . 49
3.4.2 Complementary effects of structure and function . . . 52
3.4.3 Limitations . . . 53
3.4.4 Conclusion . . . 53

4 Structure-Informed Functional Connectivity 55
4.1 Introduction . . . 56
4.2 Materials and Methods . . . 57
4.2.1 Dataset . . . 57
4.2.2 Brain networks reconstruction . . . 58
4.2.3 Structure-informed functional connectivity . . . 60
4.2.4 Normalized Laplacian diffusion . . . 61
4.2.5 Correlation score . . . 62
4.2.6 Genetic algorithms . . . 62
4.2.7 Consensus input set . . . 63
4.2.8 Jaccard index . . . 63
4.2.9 Baselines . . . 63
4.2.10 Modal controllability . . . 64
4.2.11 2D visualization of input sets with t-SNE . . . 64
4.3 Results . . . 65
4.3.1 Linking the connectome to multiple functional states . . . 65
4.3.2 Analysis of input ROIs across functional subsystems . . . 68
4.3.3 Analysis of input ROIs across states . . . 70
4.3.4 Topological properties of input ROIs . . . 72
4.3.5 Robustness of consensus input sets . . . 74
4.4 Discussion . . . 76
4.4.1 Combining brain communication models and linear controllability . . . 76
4.4.2 Well-defined sets of control regions drive state-specific functional connectivity . . . 78
4.4.3 Distinguishing resting-state from task conditions . . . 79
4.4.4 Limitations . . . 81
4.4.5 Conclusion . . . 81

5 Control Regions in Schizophrenia and Meditation 83
5.1 Introduction . . . 84
5.2 Materials and Methods . . . 85
5.2.1 Datasets . . . 85
5.2.2 Structure-informed functional connectivity and control regions 87

5.2.3 Classification and feature selection 87
5.3 Results 89
5.3.1 Schizophrenia 89
5.3.2 Meditation 93
5.4 Discussion 96
5.4.1 Control regions as fundamental features to describe brain states 96
5.4.2 Investigating the neural mechanisms of meditation 98
5.4.3 Limitations 99
5.4.4 Conclusion 99

6 Functional Connectivity Fingerprinting 101
6.1 Introduction 102
6.2 Materials and Methods 104
6.2.1 Dataset 104
6.2.2 Preprocessing 104
6.2.3 Degree-normalization of a functional connectome 105
6.2.4 Functional connectome fingerprinting 106
6.2.5 Quantifying the level of identifiability 108
6.2.6 Control experiment : Surrogate degree-normalization . . . 109
6.2.7 Statistical comparison between modalities 109
6.3 Results 109
6.4 Discussion 116
6.4.1 Improved fingerprinting in a lower-dimensional space . . . 118
6.4.2 Surrogate degree-normalization improves differential identifiability, but not identification rate or matching rate 118
6.4.3 Matching rate as a correction of identification rate 119
6.4.4 Pros and cons of different fingerprinting metrics 119
6.4.5 Limitations 120
6.4.6 Conclusion 121

7 Exploring Brain Interactions with Transfer Entropy 123
7.1 Introduction 124
7.2 Materials and Methods 126
7.2.1 Dataset 126
7.2.2 Transfer entropy 127
7.2.3 Numerical estimation 128
7.2.4 Dealing with non-stationarity 130
7.3 Results 132
7.3.1 Validation using synthetic data 132

7.3.2 Estimating interaction delays in empirical MEG data . . . 134
7.4 Discussion . . . 136
7.4.1 The challenge of exploring interactions in the brain . . . 136
7.4.2 Model-free, but not parameterless . . . 138
7.4.3 Limitations . . . 139
7.4.4 Conclusion . . . 139

8 Conclusion **141**

Bibliography **145**

A Supplementary Material of Chapter 4 **163**

B Supplementary Material of Chapter 5 **185**

C Supplementary Material of Chapter 6 **187**

D MRI acquisition parameters **195**

List of Figures

1.1 Cerebellar neurons. 3
1.2 Seven bridges of Königsberg. 5
1.3 Structure-function relationship. 7

2.1 Examples of networks. 14
2.2 Anatomical organization of the human nervous system. 17
2.3 Magnetic Resonance Imaging. 18
2.4 Examples of brain parcellations. 20
2.5 Building a structural brain network. 22
2.6 Building a functional brain network. 23
2.7 Supervised classification. 27
2.8 Network controllability. 30
2.9 Functional connectivity fingerprinting. 32

3.1 Support Vector Machine. 40
3.2 Nested cross-validation. 41
3.3 Accuracy and stability of structural features. 44
3.4 Accuracy and stability of functional features. 45
3.5 Accuracy and stability of multimodal features. 46
3.6 Repartition of selected multimodal features. 48
3.7 Brain regions affected in schizophrenia - Structural mode. 50
3.8 Brain regions affected in schizophrenia - Functional mode. 51

4.1 Structure-informed functional connectivity. 66
4.2 Relating structure-informed and empirical functional connectivity: Group-level analysis and individual-level variability. 67
4.3 Analysis across functional subsystems (group-level). 69
4.4 Analysis across functional states. 71
4.5 Cortical surface view of state-specific input ROIs. 73
4.6 Robustness analysis. 75

5.1 Using control regions as features in a classification problem. . . . 88
5.2 Schizophrenia : Accuracy and stability. 90
5.3 Schizophrenia : Discriminative regions. 91
5.4 Meditation : Accuracy and stability. 94
5.5 Meditation : Discriminative regions. 95

6.1 Degree-normalization of a Functional Connectome (FC). 107
6.2 Impact of degree-normalization on differential identifiability. 111
6.3 Impact of degree-normalization on I_{self} and I_{others}. 112
6.4 Impact of degree-normalization on identifiability matrices. 113
6.5 Degree-normalization corrects the profile of outlier FCs. 114
6.6 Impact of degree-normalization on identification rate. 115
6.7 Impact of degree-normalization on matching rate. 117

7.1 Estimating transfer entropy in non-stationary signals. 129
7.2 Estimating transfer entropy: synthetic example. 133
7.3 Estimating cortico-muscular conduction delays. 135

List of Tables

2.1 Summary of the datasets. 26

3.1 Dimension of feature vectors. 42
3.2 Number of selected features. 47

4.1 Topological properties of input ROIs. 74

Acronyms and Notations

This is a non-exhaustive list of acronyms and mathematical notations used throughout the chapters. Their meaning is provided along with their first occurrence in the text.

Acronyms

BOLD	Blood-Oxygenation-Level Dependent
CIS	Consensus Input Set
CV	Cross-Validation
dMRI	Diffusion-weighted Magnetic Resonance Imaging
EC	Effective Connectivity / Effective Connectome
EMG	ElectroMyoGraphy
FC	Functional Connectivity / Functional Connectome
fMRI	Functional Magnetic Resonance Imaging
HCP	Human Connectome Project
KSG	Kraskov-Stögbauer-Grassberger
MEG	MagnetoEncephaloGraphy
MRI	Magnetic Resonance Imaging
PCA	Principal Component Analysis
RFE	Recursive Feature Elimination
ROI	Region of Interest
SC	Structural Connectivity / Structural Connectome
SVM	Support Vector Machine
TE	Transfer Entropy
t-SNE	t-Distributed Stochastic Neighbor Embedding

Mathematical notations

N	Number of nodes
m	Number of input nodes (or control regions)
$\mathbf{S}$	Adjacency matrix of a structural network
$\mathbf{F}$	Adjacency matrix of a functional network
$\lvert\mathbf{F}\rvert$	Adjacency matrix of a functional network in absolute value
$\mathcal{F}$	Adjacency matrix of a degree-normalized functional network
$\mathbf{F}_{emp}$	Empirical functional connectivity
$\mathbf{F}_{SI}$	Structure-informed functional connectivity
$\mathbf{A}$	Transition matrix
$\mathbf{E}$	Identifiability matrix
$\mathbf{B}$	Input matrix
$\mathbf{D}$	Degree matrix
r	Pearson's correlation coefficient
ρ	Spearman's correlation coefficient
J	Jaccard index
KI	Kuncheva Index
$\mathbf{\Sigma}$	State-covariance matrix / Controllability Gramian
$\tilde{\mathbf{\Sigma}}$	State-correlation matrix / Normalized controllability Gramian
I_{diff}	Differential identifiability
ID_{rate}	Identification rate
M_{rate}	Matching rate

1 Introduction

Around 85,000,000,000 neurons.
More than 100,000,000,000,000 connections.
An intricate organization that evolves over multiple scales of time and space.

The human brain is a complex organ that forms the command center of the central nervous system. It is the result of millions of years of evolution and consumes up to 20% of the total energy required by the body everyday [Attwell and Laughlin, 2001]. It receives, processes and transfers various types of information in order to inform decisions and control actions. Yet, many questions about its functioning remain unanswered and neuroscience research has become a central topic even for governments [Insel et al., 2013].

Modern neuroscience is based on the notion introduced by Ramón y Cajal (Nobel laureate in 1906) that individual cells – the neurons (Figure 1.1) – are the fundamental units of the nervous system [Glickstein, 2006]. Since the emergence of the *neuron doctrine*, neuroscientists understood the importance of mapping brain cells and their connections in order to investigate how they support the processes allowing us to move, to think and to interact with our environment. Considerable

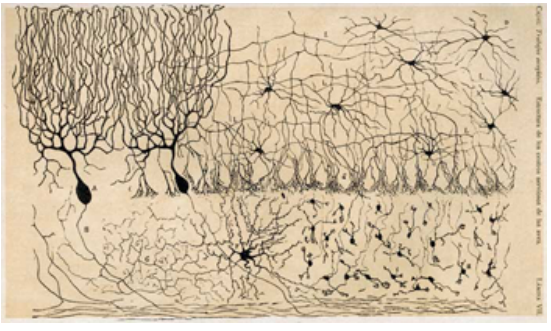

Figure 1.1: **Cerebellar neurons.** Hand drawings of neurons and their connections in the cerebellum, by Ramón y Cajal.

progress has been made in an effort to build a comprehensive map of a brain. A noteworthy example is that of the nematode worm *Caenorhabditis Elegans* (abbreviated *C. Elegans*) for which White and colleagues provided for the first time a list of about 302 neurons, 5000 synapses and 2000 neuromuscular connections [White et al., 1986]. In 2005, Sporns et al. introduced the concept of **connectome** to designate such a description of all pairwise anatomical connections (or edges) between neural elements (or nodes) of the brain [Sporns et al., 2005]. In other words, the connectome is the wiring diagram, or **network**, of the brain.

The level of detail obtained in the *C. Elegans* connectome is unfortunately still intractable for the human brain. Nevertheless, recent years have witnessed important advances in the field of neuroimaging such as the development of Magnetic Resonance Imaging (MRI). These technological evolutions opened opportunities to explore the healthy brain as well as neurological disorders such as schizophrenia and Alzheimer's disease. Importantly, the idea that key information in the understanding of the brain lies in the way different neural regions interact with each other became central. Researchers therefore used these novel imaging methods to map large-scale brain connections spanning the entire brain [Hagmann et al., 2008]. These connections represent bundles of neural fibers between large brain regions, providing a coarse-grained but meaningful description of the networks of the brain [Bullmore and Sporns, 2009]. Motivated by the need of mathematical methods to describe and quantify the organizational properties of brain networks, the field of **network neuroscience** emerged at the crossing between neuroscience and network science [Bassett and Sporns, 2017].

Network science is a research field that founds its origin in graph theory. In 1736, the Swiss mathematician Leonhard Euler formulated the famous problem of the Seven Bridges of Königsberg (Figure 1.2). The question was to determine whether it was possible to walk around the town of Königsberg (now Kaliningrad, Russia) using a path that crosses each bridge exactly once, and to come back to the starting point. The mathematical abstraction used by Euler to prove that such a path doesn't exist ignored geographical details of the town but rather focused on the *topology* of landmasses and their connections (the bridges). Such a mathematical description of discrete elements (the vertices or nodes) and their links (the edges) is called a graph. Important developments in the topological description and the statistical analysis of graphs followed Euler's work. The use of graph theory to describe the organization of complex physical systems became popular, especially with the ever increasing amount of data collected from various sources in our digital world [Newman, 2018]. The field of network science emerged with the

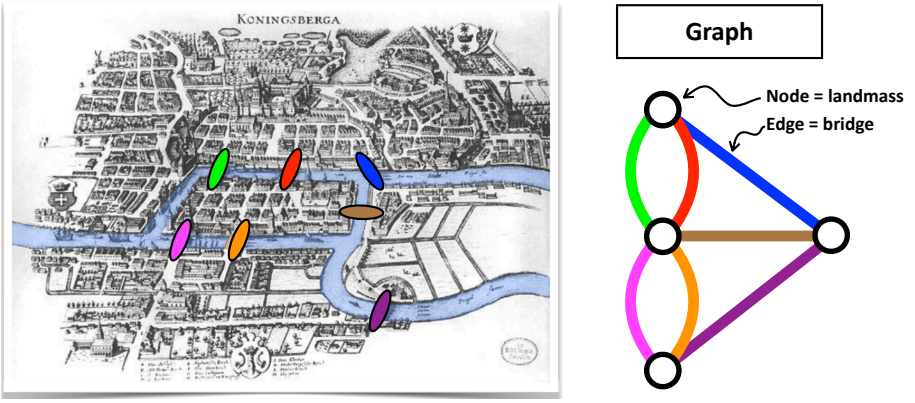

Figure 1.2: **Seven bridges of Königsberg.** The problem consists in determining whether it is possible to walk around the town using a path that crosses each bridge once and only once, and leading back to the starting point. The abstraction in the form of a graph is given on the right. The colors give the correspondence between bridges on the map and edges in the graph. Euler showed that such a path did not exist.

aim to provide a physical interpretation to graph-theoretical results proper to each type of system. The seminal work of Watts and Strogatz found that many real-world networks neither have a completely random topology nor a perfectly regular one, but rather lie between these two extremes [Watts and Strogatz, 1998]. As an illustration, they studied the neural organization of *C. Elegans*. They modeled it as a network where neuronal elements are nodes and synaptic connections are edges, and they showed that the *C. Elegans* connectome features what they named the 'small-world property', which characterizes a dense local clustering of edges with a short average path length between any two nodes. This finding was reassessed on macroscale human brain networks [Bassett and Bullmore, 2006, Bassett and Bullmore, 2017] and researchers suggested that this topological property gives the brain a moderate wiring cost while supporting a high communication efficiency, two qualities that are beneficial from a biological standpoint. This example showed the potential of applying network science to study the brain and motivated researchers to further explore the organization of brain networks.

A number of measures have been used to describe not only networks of brain anatomy – **structural connectivity** – but also networks of functional interactions between brain regions – **functional connectivity** [Bullmore and Sporns, 2009, Rubinov and Sporns, 2010]. The degree of a node in a network is a basic measure of how strongly it is connected to its neighbors. The investigation of the degree of

the nodes (i.e. brain regions) in structural and functional brain networks revealed the existence of hubs i.e., brain regions that are strongly connected to many others [van den Heuvel and Sporns, 2013]. Hubs are brain regions that are 'central' in the network and that facilitate an efficient neural communication. Their centrality however entails that connectivity alterations in hub regions might be linked to brain dysfunction. Studies also showed that hubs in the brain tend to be more densely connected among themselves than with nodes of lower degree, forming a 'rich-club' [van den Heuvel and Sporns, 2011]. This set of brain regions constitutes a backbone for the integration of neural signals [van den Heuvel et al., 2012]. In addition to these measures of integration, it has been shown that the brain has a modular organization [Meunier et al., 2010, Sporns and Betzel, 2016]. A module is a group of regions that are more strongly connected to each other than with regions outside the group. Modules participate in the locally specialized processing of information in the brain. Studies of brain organization have provided insightful descriptions of the biological trade-off between cost and efficiency [Bullmore and Sporns, 2012]. However, many challenges in network neuroscience are still active research questions. For instance, understanding how neural activity arises from the nontrivial organization of brain anatomy is a fundamental goal of neuroscience, which can be addressed with modeling approaches applied to brain networks.

The connectome of *C. Elegans*, as detailed as it is, does not provide information about the physiological processes unfolding on it. The same remark is valid for coarse-grained networks of the human brain anatomy. In contrast, functional imaging provides localized recordings of brain activity supporting task execution and rest. As already mentioned, the organization of functional interactions in the brain has also been investigated with network measures [Bullmore and Sporns, 2009]. These two types of networks – structural and functional – are distinct yet complementary and connected representations of the complex system that is the brain (Figure 1.3). After the topological analysis of structural and functional brain networks, a further step consists in modeling their relationship. A first observation made by Hagmann et al. is that structural and functional brain connectivity at rest are correlated [Hagmann et al., 2008]. This indicates that stronger anatomical connections between two brain regions favor their functional interaction. However the matching is not systematic and does not account for the variability of functional connectivity with respect to the undergoing task. Mathematical models of brain activity at different scales [Breakspear, 2017] have been applied to anatomical networks in order to improve the mapping between structure and resting-state function [Honey et al., 2009]. More recently, researchers suggested to consider the brain as a communication network and to investigate various communication dynamics in

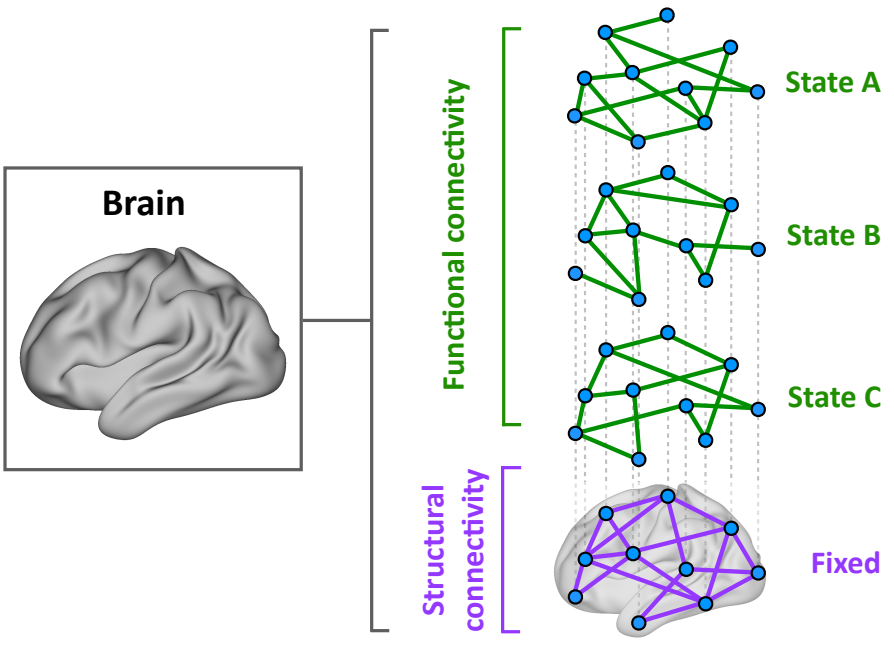

Figure 1.3: **Structure-function relationship.** A structural brain network summarizes the anatomical connections between brain regions, while a functional brain network summarizes the statistical interdependence between the activity of the same brain regions. Structural and functional connectivity provide distinct and complementary representations of the complex system that is the brain. The fixed, nontrivial organization of brain anatomy produces functional interactions patterns that vary with the ongoing task demand. Understanding the relationship between structure and function in the brain is a fundamental challenge of neuroscience.

order to reproduce observed functional interaction patterns [Avena-Koenigsberger et al., 2018]. Simultaneously, researchers studied the ability of structural brain networks to integrate external control signals in order to affect neural activity, with the aim to characterize the variety of functional states and their transitions [Gu et al., 2015, Gu et al., 2017]. In addition to improving our knowledge of healthy brain functioning, modeling the relationship between structural and functional networks is an important research topic for the understanding and treatment of brain injuries and disorders [Suárez et al., 2020].

In this thesis, we study specific questions on the properties of structural and functional brain networks and their relationship. We apply approaches from network science, machine learning, systems theory and information theory to several empirical neuroimaging datasets. The contributions presented in this work are expected to support future investigations on the processes underlying healthy brain functioning as well as neuropathologies.

Outline of the thesis and contributions

In the remaining of this introduction, we provide a brief description of the content of each chapter under the form of a 5-sentence summary. We also mention the publications that were written in the context of this thesis. The 5-sentence summaries are reproduced at the beginning of each chapter.

Chapter 3 : Supervised Classification of Brain Networks

- **We knew that** brain networks formed a meaningful representation of neural structure and function.
- **Therefore, we wondered if** we could detect disease-related features in these networks.
- **In this chapter, we** develop a machine learning approach in order to identify stable biomarkers of schizophrenia in structural and functional networks.
- **Our results show that** a mix of structural and functional connectivity features leads to a trade-off between prediction accuracy and biomarkers stability in schizophrenia.
- **This suggests that** structure and function are distinct and complementary components to consider in the study of brain networks.

The content of this chapter is adapted from the following publications :

1. **Chiêm, B.**, Crevecoeur, F., & Delvenne, J. C. (2018, May). Supervised classification of structural brain networks reveals gender differences. In *2018 19th IEEE Mediterranean Electrotechnical Conference (MELECON)* (pp. 269-274). IEEE.

2. Gutiérrez-Gómez, L., Vohryzek, J., **Chiêm, B.**, Baumann, P. S., Conus, P., Do Cuenod, K., Patric Hagmann & Delvenne, J. C. (2020). Stable biomarker identification for predicting schizophrenia in the human connectome. *NeuroImage: Clinical*, 27, 102316.

The conference paper (1) was selected for publication after peer-review in the context of the *IEEE R8 Student Paper Contest*. The journal paper (2) is the result of a collaboration with multiple authors. Participants recruitment and data acquisition was done at the Lausanne University Hospital by P.S. Baumann, P. Conu and K. Do Cuenod. Both P. Hagmann and J.C. Delvenne supervised the work.

Chapter 4 : Structure-Informed Functional Connectivity

- **We suggested that** structure and function are distinct and complementary components to consider in the study of brain networks.
- **Therefore, we wondered if** we could model the relationship between structure and function in human brain networks and across several tasks.
- **In this chapter, we** leverage systems theory in order to model functional connectivity as the covariance matrix of a linear dynamics spreading on the anatomical brain network, and we provide a principled approach for identifying the control regions driving the dynamics.
- **Our results show that** well-defined, sparse and robust sets of control regions, partially overlapping across several tasks and resting-state, produce functional connectivity patterns comparable to empirical ones.
- **This suggests that** controllability is a fundamental feature allowing brain anatomy to support different functional states thanks to state-specific control regions.

The content of this chapter is adapted from the following publication:

> 3. **Chiêm, B.**, Crevecoeur, F., & Delvenne, J.C. (2021). Structure-informed Functional Connectivity Driven by Identifiable and State-Specific Control Regions. Network Neuroscience, *in press*.

Chapter 5 : Control Regions in Schizophrenia and Meditation

- **We suggested that** controllability is a fundamental feature allowing brain anatomy to support different functional states thanks to state-specific control regions.
- **Therefore, we wondered if** control regions in the brain could form a signature that allows us to characterize disease-related or deep mental states.
- **In this chapter, we** apply the structure-informed functional connectivity model in order to identify control regions in *i)* schizophrenia and *ii)* meditation.
- **Our results show that** both schizophrenia and meditation are described by control regions that allow their discrimination from baseline conditions.
- **This suggests that** control regions identified by our model form informative features that enable the differentiation of brain states.

The *meditation* dataset investigated in this chapter was provided by Dr. Laurence Dricot (UCLouvain) and Dr. Ron Kupers (UCLouvain) who also participated in the analysis of the results. A manuscript about this chapter is in preparation.

Chapter 6 : Functional Connectivity Fingerprinting

- **We knew that** functional connectivity contains an individual-specific fingerprint.
- **Therefore, we wondered if** we could improve existing data-driven methods for extracting these fingerprints by leveraging the degree distribution of functional networks.
- **In this chapter, we** apply degree-normalization to functional networks before extracting fingerprints and we evaluate the resulting identifiability with three metrics.
- **Our results show that** degree-normalization improves the three metrics and that extracted fingerprints are embedded in a low-dimensional space.
- **This suggests that** functional fingerprints can be efficiently extracted in order to emphasize individual-specific brain features linked to behavior or disorders.

The content of this chapter is adapted from the following publication:

4. **Chiêm, B.**, Abbas, K., Amico, E., Duong-Tran D.A., Crevecoeur, F., & Goñi, J. (2021). Improving Functional Connectome Fingerprinting with Degree-Normalization. Brain Connectivity, *in press*.

Chapter 7 : Exploring Brain Interactions with Transfer Entropy

- **We knew that** the exchange of information in the brain is directed and evolves with time during the execution of a task.
- **Therefore, we wondered if** we could build a network of directed and time-resolved brain interactions without assumption on the dynamical model governing the information transfer.
- **In this chapter, we** apply an information theoretic measure known as Transfer Entropy (TE) both on a synthetic example and on brain signals recorded during a motor task.
- **Our results show that** TE successfully detects non-linear, time-varying and delayed interactions in the synthetic example but identifies multiple significant interaction delays between the motor cortex and the muscles of the hand, which hinders the interpretation of subsequent results.
- **This suggests that** TE is a promising approach that requires further developments in order to provide impactful insights into brain mechanisms.

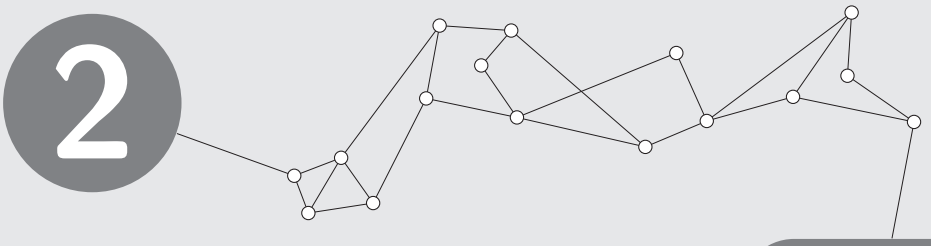

2 Preliminaries

The topics addressed in this thesis lie at the intersection of several research fields including network science, neuroimaging, systems theory, data science and machine learning. In this chapter, we cover background material related to these fields and introduce terms and notations that are used in the following chapters.

The initial idea of modeling neural connections as a network, called *connectome* [Sporns et al., 2005] or simply *brain network*, was promoted by the important progress made in neuroimaging in last years. This line of research gave rise to a specific and dedicated area applying network science to the study of the brain, known as *network neuroscience* [Bassett and Sporns, 2017]. For a thorough introduction to network science and its applications in general, we refer the reader to Mark Newman's reference book [Newman, 2018]. For an introduction to brain networks analysis, we suggest two reference books [Sporns, 2010, Fornito et al., 2016] as well as two review papers [Bullmore and Sporns, 2009, Bassett and Sporns, 2017].

2.1 Networks

A network is a model of the interactions among discrete elements of a physical system. Various types of networks are studied in the literature such as social networks [Newman and Park, 2003], protein-protein interaction networks [Vidal et al., 2011] or transportation networks [Guimera et al., 2005]. The purpose of network modeling and analysis is to account for the relationships among all elements of the system in one model instead of studying the behavior of particular instances or connections in isolation. The mathematical tool used for the analysis of networks is graph theory. In this thesis, we will use the word *network* to refer to both the mathematical object and its physical realization, although *graph* is sometimes used in the literature to distinguish the first from the latter.

A network is an ordered pair $(\mathcal{V}, \mathcal{E})$ formed by a set of nodes $\mathcal{V}$ of cardinality

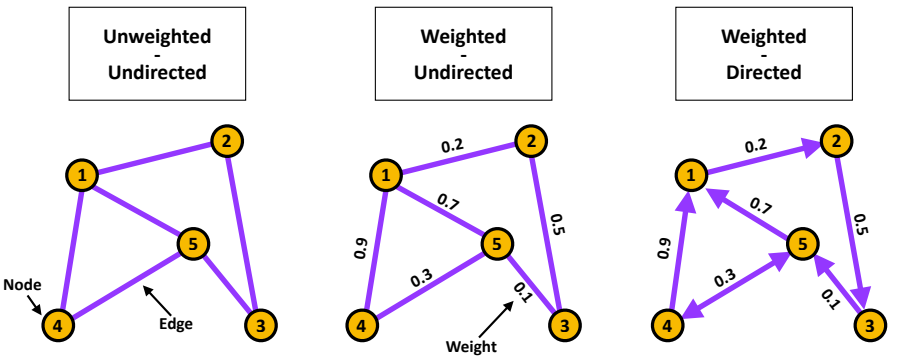

Nodes	1	2	3	4	5
1	0	1	0	1	1
2	1	0	1	0	0
3	0	1	0	0	1
4	1	0	0	0	1
5	1	0	1	1	0

Nodes	1	2	3	4	5
1	0	0.2	0	0.9	0.7
2	0.2	0	0.5	0	0
3	0	0.5	0	0	0.1
4	0.9	0	0	0	0.3
5	0.7	0	0.1	0.3	0

Nodes	1	2	3	4	5
1	0	0.2	0	0	0
2	0	0	0.5	0	0
3	0	0	0	0	0.1
4	0.9	0	0	0	0.3
5	0.7	0	0	0.3	0

Figure 2.1: **Examples of networks.** Examples of weighted/unweighted and directed/undirected networks with the corresponding adjacency matrix. Nodes are shown in orange and edges in purple. In weighted networks, weights are overlayed on the edges. In the third network, edges are directed and the adjacency matrix is not symmetric.

$|\mathcal{V}| = N$ that are connected by a set of edges $\mathcal{E} \subseteq \mathcal{V} \times \mathcal{V}$. Examples of networks are shown in Figure 2.1. The adjacency matrix of a network is the $N \times N$ matrix $\mathbf{A}$ indicating the presence of an edge between two nodes $i \in \mathcal{V}$ and $j \in \mathcal{V}$:

$$\mathbf{A}_{ij} = \begin{cases} 1 & \text{if } (i,j) \in \mathcal{E} \\ 0 & \text{otherwise} \end{cases} \tag{2.1}$$

If the edges represent a reciprocal relationship between the nodes i.e., $(i,j) \in \mathcal{E}$ and $(j,i) \in \mathcal{E}$, the network is *undirected* and the corresponding adjacency matrix is symmetric : $\mathbf{A}_{ij} = \mathbf{A}_{ji}$. When the edges are associated with a weight w_{ij} representing the strength of the relationship between nodes i and j, the network is *weighted*. The weighted adjacency matrix is written

$$\mathbf{A}_{ij} = \begin{cases} w_{ij} & \text{if } (i,j) \in \mathcal{E} \\ 0 & \text{otherwise} \end{cases} \tag{2.2}$$

A weighted undirected network verifies $w_{ij} = w_{ji}$. In this thesis, we will always consider networks with positive weights $w_{ij} \in \mathbb{R}^+$. In chapters where distinct networks are considered, specific notations are introduced in order to distinguish their respective adjacency matrix (e.g. $\mathbf{S}$ for a structural network and $\mathbf{F}$ for a functional network).

A number of coefficients can be used to describe the topology of a network (see [Rubinov and Sporns, 2010] for an overview of common coefficients and their interpretation in the context of brain networks). Among them, the degree of a node is a fundamental measure that summarizes how connected is that node to its neighbors. In undirected networks, the degree d_i of node i is computed as

$$d_i = \sum_{j=1}^{N} \mathbf{A}_{ij} \tag{2.3}$$

The degree matrix $\mathbf{D}$ is the $N \times N$ diagonal matrix defined as

$$\mathbf{D}_{ij} = \begin{cases} d_i & \text{if } i = j \\ 0 & \text{otherwise} \end{cases} \tag{2.4}$$

The definition of the degree of a node generalizes to weighted networks by considering the weighted adjacency matrix in Equation 2.3. The weighted degree of a node is also called the *strength*.

2.2 Building brain networks

The human brain shows a network structure at different spatial scales, from neurons to regions and systems. The important progress made in neuroimaging in last years enabled the large-scale mapping of neural connections. However, a complete map of all neurons and connections is still beyond reach with the notable exception of the *Caenorhabditis Elegans* nematode worm [White et al., 1986]. In this thesis, we restrict our analysis to the human brain at the macroscale i.e., using a parcellation that covers the entire brain in order to define the nodes of the network.

We first provide elements of neuroanatomy and introduce technical terms used to describe brain structure in following chapters. Then we present the parcellation procedure used to define the nodes of a brain network and we introduce brain parcellations that are used in this thesis. After that we summarize the steps to build brain networks from empirical data. This procedure widely varies across studies ; we cover the main concepts necessary for the understanding of the reader. Finally, we provide a summary table of the datasets used in this work along with their parameters.

2.2.1 Elements of neuroanatomy

The human nervous system is divided into several subcomponents (see Figure 2.2A). The Central Nervous System (CNS) is connected to the limbs and organs of the body through the peripheral nervous system. The CNS comprises the brain that is located in the head, and the spinal cord that lies along the vertebral column.

The **brain** is composed of two main volumes called hemispheres (left and right). It also comprises the diencephalon (thalamus and related structures) and the cerebellum, and it is connected to the spinal cord through the brain stem. The external part of the hemispheres is made of **gray matter**, which mostly consists of neuronal body cells and glia cells (Figure 2.2B). The internal part of the hemispheres is made of **white matter**, which is composed of bundles of axonal fibers (also called *tracts*) that link gray matter areas. The corpus callosum is a wide bundle of white matter fibers that connects both hemispheres. At the center of the hemispheres, close to the corpus callosum, lie several nuclei collectively referred to as subcortical structures. The peripheral gray matter of the hemispheres forms the cerebral **cortex**. The cortex has a folded surface where gyri designate ridges and sulci designate grooves. The cortex is subdivided into four bilateral lobes: frontal, temporal, parietal and occipital (Figure 2.2C).

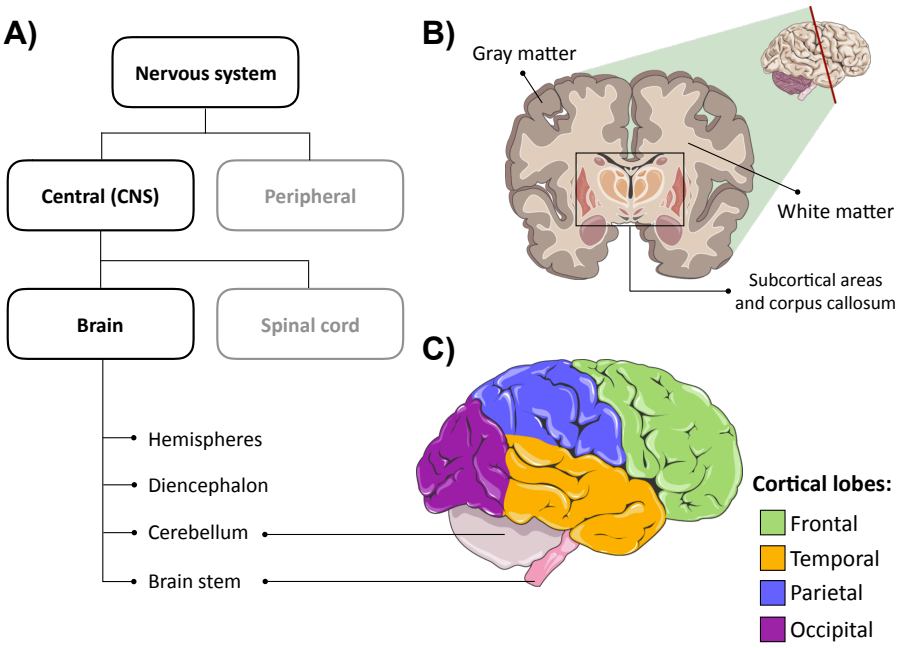

Figure 2.2: **Anatomical organization of the human nervous system. A)** Subdivisions of the human nervous system. The brain is part of the Central Nervous System (CNS). **B)** Coronal view of the hemispheres. The external part of the hemispheres is made of gray matter (dark gray) and the internal part is made of white matter (light gray). **C)** Lateral view of an hemisphere. Colors indicate the four cortical lobes : frontal (green), temporal (orange), parietal (blue) and occipital (purple).
(Source: brain images are freely available from the website `https://smart.servier.com/` under a Creative Commons 3.0 licence.)

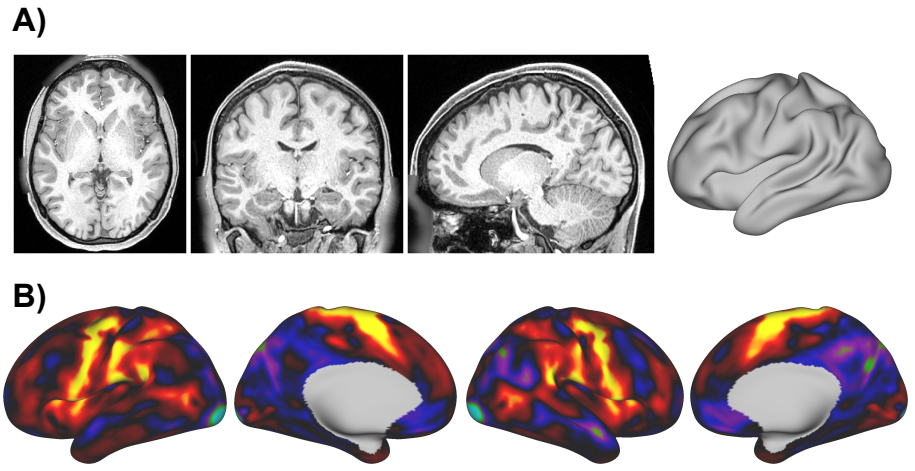

Figure 2.3: **Magnetic Resonance Imaging. A)** Examples of anatomical MRI images. From left to right: axial slice, coronal slice, parasagittal slice and 3D reconstruction of the left cortical hemisphere (inflated view). **B)** Examples of functional MRI results during the execution of a motor task (average activation over time). From left to right: left lateral, left medial, right lateral and right medial views of the 3D cortical reconstruction. The voxels showing high activation (yellow) correspond to motor areas.

2.2.2 Magnetic Resonance Imaging

Magnetic Resonance Imaging (MRI) is a medical imaging modality leveraging the magnetic properties of hydrogen atoms found in biological tissues. In this regard, it is distinct from computational tomography (CT) that uses X-rays and from positron emission tomography (PET) that uses ionizing radiations. With a strong and permanent magnetic field, the MRI scanner aligns the nuclear spins of hydrogen atoms, leading to the magnetization of tissues. Magnetic field gradients oriented along perpendicular axes are used to locally alter the magnetic field in a thin slice of the tissue. Then, a radio-frequency impulse excites the atoms that in turn emit a relaxation signal. This signal is recorded and contains information about the tissue type and its precise spatial location, which enables the reconstruction of an image (Figure 2.3A). This process is repeated for multiple slices in order to reconstruct the volume under study.

The timing and duration of the gradients activation, impulse and relaxation forms an MRI acquisition sequence. There exist many MRI sequences that allow us to obtain different contrasts, for example between gray matter, white matter and

cerebrospinal fluid in the brain. Advanced MRI sequences enable the recording of particular properties of the tissues. For instance, diffusion-weighted MRI sequences inform us on the preferential diffusion direction of water molecules, which enables the reconstruction of white matter pathways (see 'Structural networks' below). Using fast multi-slices sequences also allows the recording of the Blood-Oxygenation-Level Dependent (BOLD) signal over time, which provides an estimate of the activity in gray matter (functional MRI, see Figure 2.3B and 'Functional networks' below).

The ability of MRI to inform researchers on many aspects of brain structure and function with a high spatial resolution made it popular among scientists studying brain networks [Van Essen et al., 2012]. In this thesis, we use MRI data acquired in different sites, with different types of scanner and with various acquisitions sequences. Acquisition and processing details are provided with the description of the dataset in each chapter.

2.2.3 Parcellation

In order to build a brain network, one must first define the nodes. To this end, the standard approach consists in associating a node to a gray matter area, or parcel. In this thesis, we will use the expressions 'node', 'area', 'region' and 'Region of Interest' (ROI) interchangeably to refer to the nodes of a brain network. The seminal work of Kerbinian Brodmann in 1909 [Brodmann, 1909] defined 52 areas based on the cytoarchitectural organization of cortical neurons. In order to enable the in-vivo comparison of brain networks across individuals, automatic parcellation methods based on non-invasive neuroimaging data became popular [Desikan et al., 2006, Destrieux et al., 2010, Cammoun et al., 2012, Fan et al., 2016, Glasser et al., 2016]. These methods seek to identify non-overlapping regions that are reproducible in the brain of multiple individuals, either based on anatomical similarities (such as gyri and sulci folding, see [Desikan et al., 2006]), on functional properties [Yeo et al., 2011] or on a combination of modalities [Glasser et al., 2016]. Other approaches to brain parcellation including voxel-wise and random parcellations exist in the literature [Stanley et al., 2013] but are not considered in this thesis.

Figure 2.4 shows four examples of parcellations (or atlas) that are used in the following chapters. We observe that the number of parcels varies from 84 to 374. The fact that these atlases are based on different modalities and assumptions hinders the direct comparison of regions across parcellations. The heterogeneity of brain atlases across studies is a current limitation of brain network studies [Zalesky

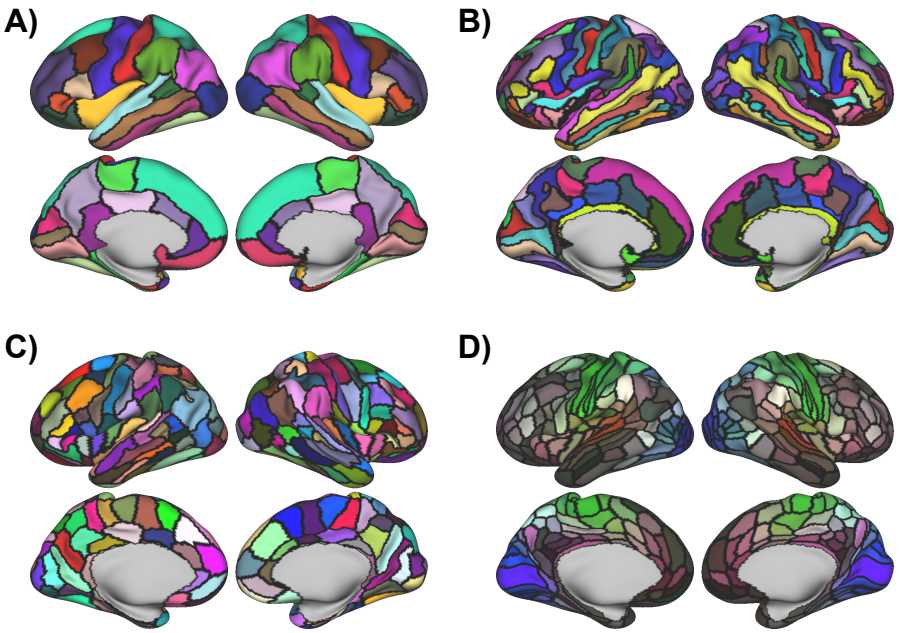

Figure 2.4: **Examples of brain parcellations. A)** Desikan-Killiany parcellation [Desikan et al., 2006], 84 regions. **B)** Destrieux parcellation [Destrieux et al., 2010], 164 regions. **C)** Brainnetome parcellation [Fan et al., 2016], 246 regions. **D)** Glasser parcellation [Glasser et al., 2016], 374 regions. All panels show an inflated view of the cortex reconstructed from MRI data.

et al., 2010, Stanley et al., 2013, Messé, 2020], and the results presented in this thesis should be interpreted in relation to the parcellation employed.

Once the nodes of a brain network are determined, one must define the edges and their weight (and possibly their direction) between each pair of nodes. Edges can be derived from several imaging modalities and represent different aspects of brain connectivity. In the following, we present the two most common types of brain networks i.e., structural (or anatomical) and functional networks. By abuse of language we will use the terms 'brain network' and 'connectome' interchangeably to designate a network of brain connectivity of either type, although 'connectome' has been first introduced by Sporns and colleagues [Sporns et al., 2005] to refer to a structural description of the brain.

2.2.4 Structural networks

The most common imaging modality used to estimate anatomical connectivity in-vivo, non-invasively and at the macroscale is diffusion-weighted Magnetic Resonance Imaging (dMRI). The signals recorded during a dMRI acquisition inform on the preferential direction of diffusion of water molecules inside the brain. In gray matter, water molecules are mostly unconstrained and the diffusion is isotropic. In contrast in white matter, neural fibers such as axons constrain water to diffuse along the fibers orientation ; the diffusion is anisotropic. During a dMRI scan, several images are acquired in different directions in order to estimate the fiber orientation distribution in each white matter voxel (Figure 2.5).

With the diffusion information, tractography algorithms seek to propagate streamlines across voxels following the preferential diffusion orientation. While deterministic tractography stricly follows the principal diffusion orientation, probabilistic tractography determines the likelihood that a streamline propagates in a certain direction according to the fiber orientation distribution. In order to estimate the whole-brain anatomical connectivity, we reconstruct a large number of streamlines starting and ending in gray matter areas spanning the brain surface. The set of reconstructed streamlines is called a tractogram. There exist many processing pipelines, tractography algorithms and further options in order to model the brain anatomical connectivity, and active research aims at improving existing methods [Oldham et al., 2020].

Eventually, pairs of nodes linked by at least one reconstructed streamline are connected by an edge in the structural network, and the associated weight repre-

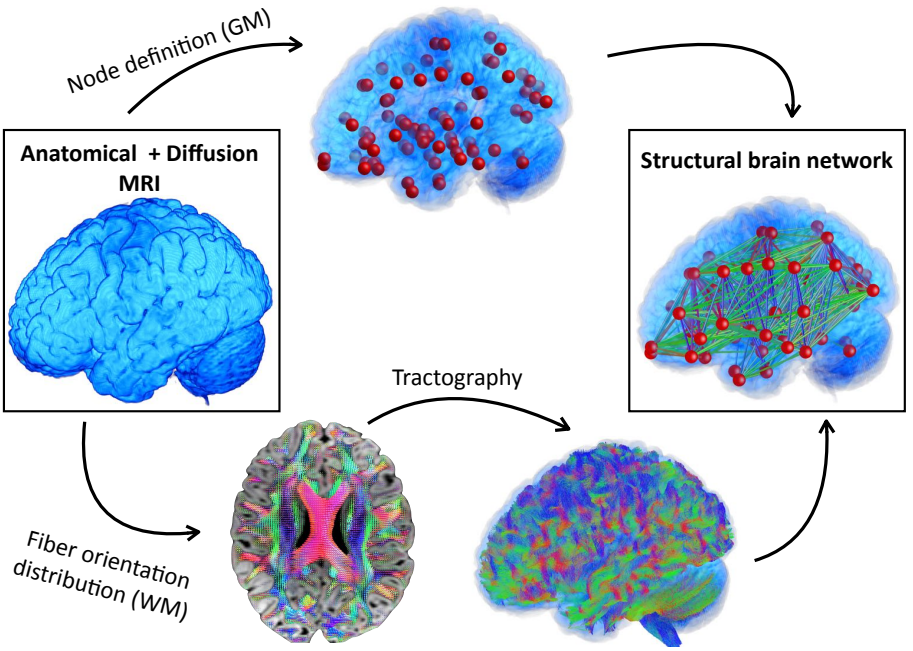

Figure 2.5: **Building a structural brain network.** Nodes are defined as gray matter (GM) areas identified in the anatomical MRI data. Using the diffusion MRI data, we first estimate the fiber orientation distribution in each voxel, which reflects the preferential diffusion direction of water molecules in white matter (WM) fibers. With that information, the tractography algorithm reconstructs a large number of streamlines representing white matter pathways. Finally, the structural brain network (or *connectome*) summarizes the contribution of reconstructed streamlines to the anatomical connectivity between the nodes previously defined.

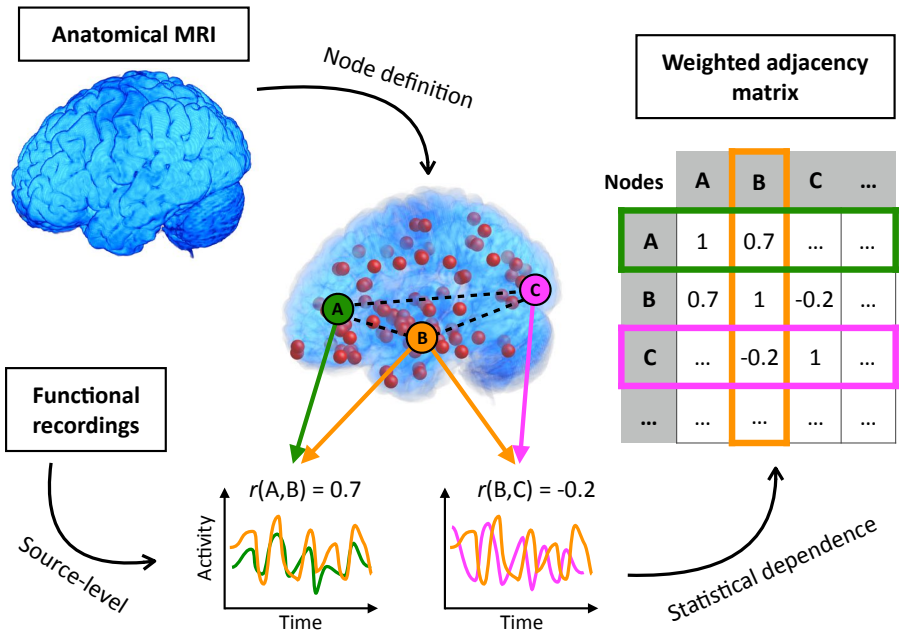

Figure 2.6: **Building a functional brain network.** Nodes are defined as gray matter areas identified in the anatomical MRI data. Functional imaging (fMRI, EEG, MEG) records brain activity in the neural sources formed by the nodes. Functional Connectivity (FC) measures the statistical interdependence between the time series of neural activity to weight the edges of the functional brain network. The most common FC measure is Pearson's correlation coefficient, denoted r. The matrix of pairwise FC values forms the weighted adjacency matrix of the functional brain network. In the case of Pearson's correlation coefficient, this matrix is symmetric (undirected network) and possibly contains negative entries.

sents the number of streamlines connecting the nodes (Figure 2.5). An alternative is to normalize the weight by the volume of the gray matter areas represented by the nodes in order to mitigate the bias towards large areas receiving many streamlines. Other weighting possibilities exist, and which is the most accurate in representing anatomical connectivity in the brain remains an open question [Oldham et al., 2020].

2.2.5 Functional networks

Functional neuroimaging estimates brain activity either at rest or during the execution of a task. Among non-invasive imaging modalities, functional MRI (fMRI), ElectroEncephaloGraphy (EEG) and MagnetoEncephaloGraphy (MEG) are the most

commonly used for estimating functional connectivity. Functional MRI records the Blood-Oxygenation-Level Dependent (BOLD) signal that reflects the local variations of hemoglobin oxygenation due to neural activity. It is therefore an indirect measure of the electrical activity of the neurons. EEG and MEG are electrophysiological methods that respectively measure electrical or magnetic activity with sensors located at the surface of the brain. On the one hand, both EEG and MEG have better temporal resolution than fMRI (millisecond vs. second). On the other hand, EEG and MEG have a lower spatial resolution (centimeter vs. millimeter) and face the problem of signal mixing. Because sensors are located at the surface of the brain, the signal produced by a neural source is recorded by multiple sensors and conversely, a sensor records a mix of signals from several sources. Source reconstruction methods such as beamforming offer approximate solutions but involve modeling assumptions and parameters, and require a separate anatomical MRI acquisition. Moreover, reconstructing sources located far from the sensors such as subcortical structures remains challenging. In sum fMRI, EEG and MEG have pros and cons, and the choice of a modality is driven by the context of the study. In this thesis we use mostly fMRI data except in Chapter 7 where we leverage the high temporal resolution of MEG to estimate cortico-muscular delays.

Functional Connectivity (FC) measures the statistical interdependence between the time series of neural activity derived from functional imaging (Figure 2.6). A standard statistical measure is Pearson's correlation coefficient $r \in [-1, 1]$ that quantifies the linear relationship between two time series. Other measures have been used in FC studies such as partial correlation [Marrelec et al., 2006], coherence [Sun et al., 2004] and mutual information [Hlinka et al., 2011]. The choice of an FC measure is driven by the context of the study, by the underlying assumptions and by the nature of the data. While some authors argue in favor of one measure compared to others, there is no consensus on which one to use as they provide complementary insights into functional brain connections [Korhonen et al., 2021]. The subsequent results must therefore be interpreted with respect to the chosen statistical measure. The default FC measure used in this thesis is Pearson's correlation coefficient.

The matrix of pairwise FC values between neural time series can be interpreted as the adjacency matrix of a functional brain network (Figure 2.6). This network associates brain regions that have a *statistically dependent* activity, and its topology changes with the condition under study (task or rest). Because the association between brain regions is statistical and not physical, the interpretation of an FC matrix as a network is not straightforward. For instance when FC is measured as

a correlation coefficient, negative values might appear. These values can either be preserved, thresholded or taken in absolute value, and the subsequent analysis must account for this methodological choice. Moreover, network metrics quantifying a physical property (e.g. the shortest path between two nodes [Rubinov and Sporns, 2010]) must be interpreted with caution in functional networks as edges represent statistical rather than physical connections. In this context, we consider the network modeling approach as a mathematical *tool* – as opposed to a physical communication network – for analyzing the organization of brain functional interactions, which are the result of neural processes constrained by the anatomical – hence physical – network of brain anatomy.

In addition to *undirected* FC, functional recordings are also used for estimating *directed* FC i.e., directed functional interactions in the brain. When directed FC is estimated using a generative model, we refer to it as *effective* connectivity [Friston, 2011] although this appellation is commonly used for 'model-free' estimation methods too [Vicente et al., 2011]. The estimation of directed FC is challenging and is expected to provide important insight into the neural mechanisms supporting cognition and behavior. Chapter 7 investigates one method to estimate directed FC in non-stationary MEG data.

2.2.6 Datasets summary

We provide in Table 2.1 a summary of the datasets used in this thesis and their main properties. Further details are provided in each chapter. All datasets also contain an anatomical MRI acquisition for each individual that is not mentioned in the Table. Note that several brain parcellations, imaging modalities and functional conditions are leveraged throughout the chapters.

2.3 Machine learning

Machine learning is a field of artificial intelligence that studies and designs numerical algorithms able to *learn* from data [James et al., 2013]. It lies at the intersection of several research fields including computer science, applied mathematics and statistics. The information learnt by machine learning algorithms is used to make predictions about unseen data samples or to inform decisions. One distinguishes three main subfields in machine learning: unsupervised learning, supervised learning and reinforcement learning (Figure 2.7A).

Unsupervised learning is used for exploratory data analysis. It learns patterns

Table 2.1: **Summary of the datasets.** Denomination and properties of the datasets used in the thesis. All datasets also contain an anatomical MRI acquisition for each individual. LAU: Lausanne [Cammoun et al., 2012]. DES: Destrieux [Destrieux et al., 2010]. BN: Brainnetome [Fan et al., 2016]. MMP: Glasser multimodal [Glasser et al., 2016]. DK: Desikan-Killiany [Desikan et al., 2006]. (*) The analysis in Chapter 7 is limited to two variables and does not leverage the $N = 84$ nodes.

Dataset	Imaging modality	Parcellation	Individuals	Conditions	Chapter(s)
Schizophrenia	dMRI fMRI	LAU $N \in \{83,129,234\}$	27 patients 27 controls	Resting-state	3 and 5
HCP 100	dMRI fMRI	DES $N = 164$	100 healthy participants	Resting-state and 7 tasks	4
Meditation	dMRI fMRI	BN $N = 246$	50 meditators	Resting-state and meditation	5
HCP 409	fMRI	MMP $N = 374$	409 healthy participants	Resting-state and 7 tasks	6
HCP MEG	MEG	DK $N = 84$ (*)	18 healthy participants	Motor task (right hand)	7

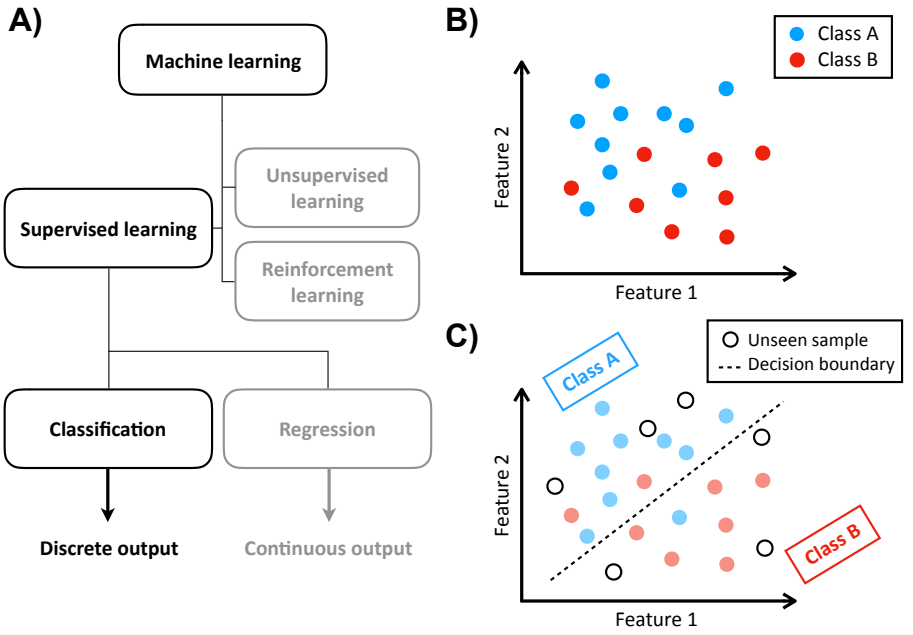

Figure 2.7: **Supervised classification. A)** Machine learning is divided into several fields among which supervised classification aims at predicting a discrete output (or class) from labelled data. **B)** Data points lie in a feature space and are associated to a class. In this thesis data points represent individuals, features are derived from brain connectivity data and classes are used to differentiate either patients from controls (Chapters 3 and 5) or two functional states (Chapter 5). **C)** The classification algorithm learns a decision boundary from labelled data during the training phase. Then, the class of unseen samples is predicted according to this boundary during the test phase.

and structure from data without *a priori* knowledge. Unsupervised learning tasks include clustering and dimensionality reduction. Reinforcement learning algorithms leverage past experience and current knowledge in order to select actions that optimize a cumulative reward along time. It is rooted into the formalism of Markov decision processes. Supervised learning methods learn an input-output mapping. Given data points associated with an output variable, supervised algorithms approximate the function linking the points to their output in order to predict the output of new samples. Among supervised learning tasks, regression aims at predicting a continuous output variable while classification aims at predicting a discrete output variable, or class (Figure 2.7A).

2.3.1 Supervised classification

In this thesis we apply a supervised classification method known as *Support Vector Machine* (SVM, see Chapter 3) in order to predict the class (or group) of individuals on the basis of their brain connectivity data. From the brain networks of each individual, we extract a vector of variables called *features*. In the space spanned by these features, individuals are data points belonging to a class (Figure 2.7B). The classification algorithm learns a decision boundary that separates classes in the feature space (training phase) in order to predict the class of new samples (test phase). Figure 2.7C shows the particular case of a linear decision boundary used to separate two non-linearly separable classes. Note that the feature space is represented in two dimensions for visualization, although it is of much higher dimension in general.

2.3.2 Feature selection

Using very high-dimensional feature vectors to describe data points can result in unexpected and poor behaviors of the machine learning algorithm, a phenomenon named the *curse of dimensionality* [James et al., 2013]. It is therefore important to select relevant features beforehand via feature selection methods. Alongside standard univariate approaches based on correlation or mutual information, some classification algorithms are designed such that a feature selection is embedded in the training phase. For instance when the decision boundary is linear in the original feature space (Figure 2.7C), the coefficients of the hyperplane inform us on the importance of each feature in the classification outcome. This information allows us to select a subset of relevant features in a multivariate fashion. This observation is leveraged in the Recursive Feature Elimination (RFE) method that is used in combination with a linear SVM classifier in Chapters 3 and 5.

2.3.3 Validation

In order to validate the performance of a classification model, one must use different samples for the training phase and the test phase (out-of-sample testing). The goal is to measure the ability of the trained model to generalize to new data. A popular approach for the statistical validation of a classification model is the k-fold cross-validation [James et al., 2013].

The method consists in randomly dividing the complete dataset into k groups of equal size. In turn, each group is used as an independent set of unseen samples (test set) while the remaining $k-1$ groups are used to train the classification model (training set). At the end, the k measures of performance obtained on the test sets are averaged in order to provide an estimate of the general performance of the model. Standard choices for k are $k = 5$ or $k = 10$. A k-fold cross-validation can also be performed internally on the training set in order to fix parameters of the classification model. This procedure is called *nested* k-fold cross-validation and is detailed in Chapter 3.

2.4 Network controllability

A network is a mathematical representation of the elements of a physical system and their connections. Each element (or node) is associated with a state that evolves over time according to the dynamics governing the system. In addition, control nodes integrate external signals in order to alter the overall state of the system (Figure 2.8A). *Controllability* refers to the ability of a system to be driven from any initial state to any final state by appropriate control signals (Figure 2.8B).

In a network of N nodes, we note $\mathbf{x} \in \mathbb{R}^N$ the vector of the states of the nodes. The class of discrete-time Linear Time Invariant (LTI) systems is described by the equation

$$\mathbf{x}(k+1) = \mathbf{A}\mathbf{x}(k) + \mathbf{B}\mathbf{u}(k) \tag{2.5}$$

where k is a discrete time index, $\mathbf{A}$ is the $N \times N$ matrix representing the transition dynamics among the states of the systems, $\mathbf{B}$ is the $N \times m$ input matrix indicating the identity of the m control nodes and $\mathbf{u}(k)$ contains the control signals at time k. A fundamental result on the controllability of an LTI system states that if the

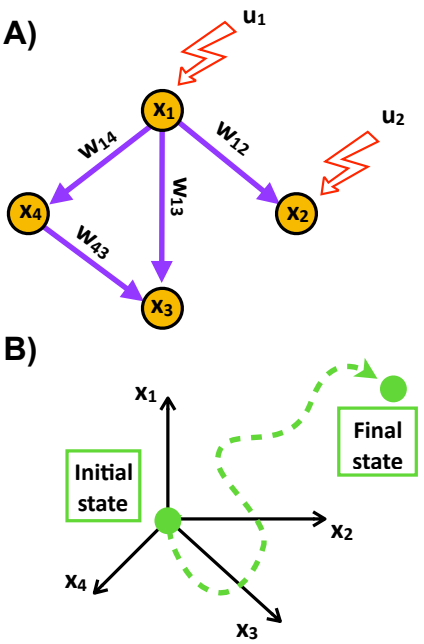

C)

$$\mathbf{x}(k+1) = \mathbf{A}\mathbf{x}(k) + \mathbf{B}\mathbf{u}(k)$$

$$\mathbf{A} = \begin{bmatrix} 0 & 0 & 0 & 0 \\ w_{12} & 0 & 0 & 0 \\ w_{13} & 0 & 0 & w_{43} \\ w_{14} & 0 & 0 & 0 \end{bmatrix}$$

$$\mathbf{B} = \begin{bmatrix} 1 & 0 \\ 0 & 1 \\ 0 & 0 \\ 0 & 0 \end{bmatrix}$$

$$\mathbf{C} = \begin{bmatrix} \mathbf{B} & \mathbf{AB} & \mathbf{A}^2\mathbf{B} & \mathbf{A}^3\mathbf{B} \end{bmatrix}$$

$$\text{rank}(\mathbf{C}) = N$$

Figure 2.8: **Network controllability.** **A)** Example of a weighted directed network with state variables $\mathbf{x} = [x_1, x_2, x_3, x_4]^T$ and control signals $\mathbf{u}(k) = [u_1(k), u_2(k)]^T$. **B)** Illustration of the concept of controllability. In the state-space of the system, controllability refers to the ability to reach any final state from any initial state. **C)** The standard rank criterion indicates that the network in **A)** is controllable, without information on the control energy required. (This figure is adapted from [Liu et al., 2011])

controllability matrix

$$\mathbf{C} = \begin{bmatrix} \mathbf{B} & \mathbf{AB} & \mathbf{A}^2\mathbf{B} & \cdots & \mathbf{A}^{N-1}\mathbf{B} \end{bmatrix} \tag{2.6}$$

has full rank, then the system is controllable [Liu et al., 2011]. An example of a controllable system is shown in Figure 2.8. This criterion does not inform us on the energy that is required in order to control the system. For instance, a networked system might be theoretically controllable while featuring states that would require a prohibitive amount of control energy in order to be reached, which precludes controllability in practice.

In order to derive quantitative measures of the controllability of a system, we consider the controllability Gramian $\mathbf{\Sigma}$ defined as

$$\mathbf{\Sigma} = \sum_{i=0}^{\infty} \mathbf{A}^i \mathbf{B}\mathbf{B}^T (\mathbf{A}^T)^i \tag{2.7}$$

This $N \times N$ matrix is also the solution of the following discrete Lyapunov (or Stein) equation :

$$\mathbf{\Sigma} - \mathbf{A}\mathbf{\Sigma}\mathbf{A}^T = \mathbf{B}\mathbf{B}^T \tag{2.8}$$

Several results in the literature show that the spectrum of $\mathbf{\Sigma}$ is linked to energy of control signals required to reach the states of the system [Pasqualetti et al., 2014]. Studies applied these results to brain networks [Gu et al., 2015] and suggested that the human connectome is theoretically controllable through any single node, although this would require an unrealistic amount of control energy.

2.5 Brain fingerprinting

Functional connectivity describes the statistical interdependence between the activity of brain regions, during task execution or at rest. Recently, it has been shown that Functional Connectivity matrices or equivalently *Functional Connectomes* (both denoted FCs) contain a fingerprint that is proper to each individual [Finn et al., 2015]. This entails that in a dataset composed of two FCs per individual, it is possible to retrieve the pairs of matched FCs by measuring their similarity. This observation underlined the importance of individual-level analyses in the study of brain connectivity and its relation to individual behavior. Moreover, it motivated researchers to develop methods for extracting fingerprints from FCs in order to accentuate individual properties of brain functional connectivity.

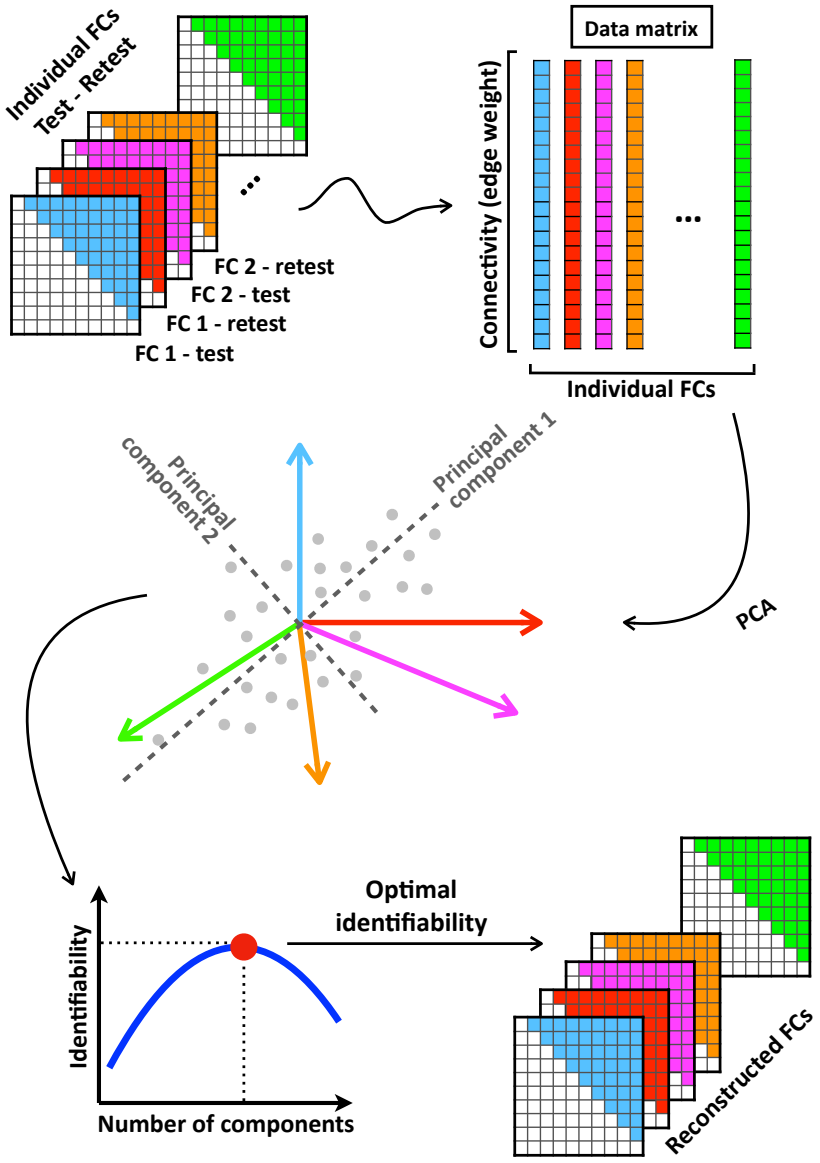

Figure 2.9: **Functional connectivity fingerprinting.** The framework is based on the work of Amico and Goñi [Amico and Goñi, 2018]. First, Functional Connectivity matrices (FCs) are vectorized in order to form the data matrix. Second, we apply Principal Component Analysis (PCA) to the data matrix in order to identify the orthogonal axes capturing most of the variance of the data. Third, we reconstruct FCs with an increasing number of components and compute a fingerprinting metric that quantifies the identifiability of reconstructed FCs. This allows us to identify the optimal number of components generating maximally identifiable FCs.

The framework developed by Amico and Goñi for FC fingerprinting [Amico and Goñi, 2018] is based on group-level data decomposition. It is illustrated in Figure 2.9. Starting from a dataset containing two FCs per individual (test and retest) and assuming that matrices are symmetric, we vectorize the upper triangular part of each FC in order to form the data matrix. This matrix represents the coordinates of data points that correspond to edge weights (or connectivity strength) in the space spanned by individual FCs. Principal Component Analysis (PCA) is a data decomposition method that identifies the orthogonal axes (called principal components) capturing most of the variance of the data points in this space [James et al., 2013]. By selecting a number of principal components, we can project data points on these new axes and reconstruct the data matrix. This procedure is used for data denoising or dimensionality reduction for instance. Here, Amico and Goñi proposed to compute a fingerprinting metric of the dataset as a function of the number of principal components used for FCs reconstruction. They showed that there exists an optimal number of components and that this procedure allows us to optimize the identifiability of FCs.

3

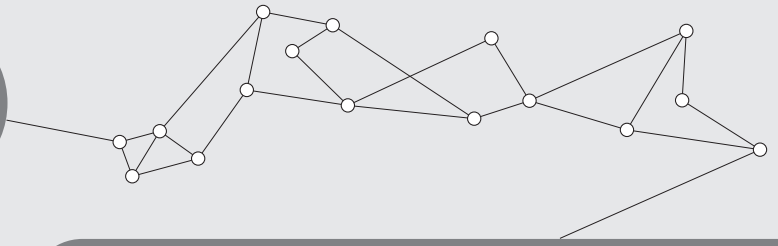

Supervised Classification of Brain Networks

This chapter in 5 sentences

- **We knew that** brain networks formed a meaningful representation of neural structure and function.
- **Therefore, we wondered if** we could detect disease-related features in these networks.
- **In this chapter, we** develop a machine learning approach in order to identify stable biomarkers of schizophrenia in structural and functional networks.
- **Our results show that** a mix of structural and functional connectivity features leads to a trade-off between prediction accuracy and biomarkers stability in schizophrenia.
- **This suggests that** structure and function are distinct and complementary components to consider in the study of brain networks.

The content of this chapter is adapted from the following publications :

1. **Chiêm, B.**, Crevecoeur, F., & Delvenne, J. C. (2018, May). Supervised classification of structural brain networks reveals gender differences. In *2018 19th IEEE Mediterranean Electrotechnical Conference (MELECON)* (pp. 269-274). IEEE.
2. Gutiérrez-Gómez, L., Vohryzek, J., **Chiêm, B.**, Baumann, P. S., Conus, P., Do Cuenod, K., Patric Hagmann & Delvenne, J. C. (2020). Stable biomarker identification for predicting schizophrenia in the human connectome. *NeuroImage: Clinical*, 27, 102316.

3.1 Introduction

The development of neuroimaging techniques such as Magnetic Resonance Imaging (MRI) enabled the mapping of both anatomical and functional connections in the human brain [Sporns et al., 2005, Hagmann et al., 2008, Bullmore and Sporns, 2009]. The study of brain networks provided important insights into the brain organizational principles in healthy individuals [Bassett and Bullmore, 2006, Rubinov and Sporns, 2010, van den Heuvel and Sporns, 2011, Stam and Van Straaten, 2012, Sporns and Betzel, 2016]. In turn, researchers suggested that certain brain disorders can be characterized in terms of brain connectivity alterations [Supekar et al., 2008, Ponten et al., 2009, Bassett and Bullmore, 2009, Seeley et al., 2009, Gilson et al., 2020]. Among these neuropathologies, schizophrenia is a severe psychiatric condition characterized by hallucinations and delusions, as well as impairments in memory, attention, executive and other high-order cognitive functions [Van Os et al., 2010]. Several studies showed reproducible connectivity alterations in schizophrenic patients and marked a shift in support of the conceptualization of schizophrenia as a dysconnectivity syndrome [Bullmore and Sporns, 2009, Lynall et al., 2010, Griffa et al., 2013, Griffa et al., 2015]. In this context, deriving novel biomarkers of schizophrenia is essential for both diagnosis and treatment [Bassett et al., 2008, Kim et al., 2010].

From the connectivity standpoint, anatomical studies showed decreased white matter integrity in frontal, temporal and parietal regions in schizophrenic patients, while functional studies showed changes in activation of frontal and parietal areas [van den Heuvel and Fornito, 2014]. The analysis of the structure-function relationship in schizophrenia also revealed aberrant behaviors in fronto-striatal, fronto-thalamic and fronto-temporal couplings [Cocchi et al., 2014]. Topological studies found alterations that are characterized by a lower global efficiency and a limited capacity of functional integration [Griffa et al., 2013]. Further research using diffusion spectrum imaging reported brain areas mainly responsible for the loss of global integration and segregation properties with prefrontal, pericentral, superior, left temporal-occipital and thalamic areas as well as striatum [Griffa et al., 2013, Griffa et al., 2015, Griffa et al., 2019]. However, these anomalies were identified using conventional univariate techniques performing a separate statistical test at each edge of the brain network under scrutiny, which requires stringent corrections for multiple comparisons. In contrast, multivariate methods offer a powerful alternative, provided that specialized approaches are used when the number of parameters dominates the number of observations [Bühlmann and Van De Geer, 2011].

Here, we address the problem of identifiying biomarkers related to schizophrenia using a machine learning framework. We apply a multivariate classification method known as Support Vector Machine (SVM) [Boser et al., 1992, Cortes and Vapnik, 1995] on brain connectivity data, either structural or functional, or a combination of both. The SVM classifier presents an embedded multivariate feature selection method called Recursive Feature Elimination (RFE), which allows us to identify the set of features most informative for the discrimination between patients and controls. The combination of the SVM classifier with RFE (SVM-RFE) has been introduced to perform gene selection for cancer diagnosis on microarray data [Guyon et al., 2002]. It has also been used for the mapping and classification of fMRI voxelwise spatial patterns [De Martino et al., 2008] and functional connectivity data [Pallarés et al., 2018]. More recently, it has been used on human brain networks to identify differences in structural connectivity related to gender [Chiêm et al., 2018]. A key challenge in feature selection lies in the fact that selected features may widely vary from one subsample of the dataset to another, or between different datasets. In the perspective of future experimental or clinical applications, identified biomarkers must be robust to data variations. This underlines the need to assess the stability of the feature selection process when investigating biomarkers in a machine learning framework [Kuncheva, 2007].

In this chapter, we propose an approach that not only identifies biomarkers of schizophrenia in brain connectivity data, but also evaluates their stability across independent tests on different data samples. Our results show that a mix of structural and functional features leads to the best trade-off between prediction accuracy and feature selection stability. From the identified connectivity biomarkers, we derive the Regions of Interest (ROIs) most affected by the disease and find an overlap with ROIs reported in previous structural studies. In sum, we provide a systematic method for detecting stable biomarkers of brain connectivity, and we underline that structure and function are distinct and complementary components to consider in the study of brain networks in health and disease. Our findings are expected to encourage future research applying machine learning to characterize neurological disorders on the basis of multimodal brain connectivity data, although the clinical utility of the proposed method remains to be assessed and compared to existing clinical biomarkers.

3.2 Materials and Methods

3.2.1 Dataset

The cohort consists of two groups: 27 schizophrenic patients (41.9 $\pm$ 9.6 years old) in one group and 27 healthy controls (35 $\pm$ 6.8 years old) in the other group. Patients were recruited from the Service of General Psychiatry at the Lausanne University Hospital, and they met DSM-IV criteria for schizophrenic and schizoaffective disorders [DSM-IV-TR., 2000]. Out of the 27 patients, 24 were under medication with chlorpromazine equivalent dose (CPZ) (average medication 431 $\pm$ 288 mg) [Andreasen et al., 2010]. Healthy controls were recruited through advertisement and assessed with the Diagnostic Interview for Genetic Studies [Preisig et al., 1999]. Among controls, individuals with major mood, psychotic or substance-use disorders, and having a first-degree relative with a psychotic disorder were excluded. A history of neurological disease was an exclusion criterion for all participants. Written informed consent from all participants was obtained following the institutional guidelines approved by the Ethics Committee of Clinical Research of the Faculty of Biology and Medicine, University of Lausanne, Switzerland.

3.2.2 Brain networks reconstruction

Anatomical, diffusion-weighted and resting-state functional MRI scans were acquired for each participant. The acquisition protocol is detailed in Appendix D.

Structural and diffusion MRI data were used to estimate the weighted and undirected structural connectivity matrices in the Connectome Mapping Toolkit [Daducci et al., 2012, Cammoun et al., 2012, Griffa et al., 2015]. White matter, gray matter and cerebrospinal fluid segmentation was performed on the structural data. The resulting image was linearly registered to the diffusion-weighted images. The first three scales of the Lausanne multi-scale atlas were used to parcellate the gray matter. The first scale consisted of 68 cortical brain regions and 15 subcortical regions, with scale two and three subdividing the first scale into 114 and 219 cortical regions [Cammoun et al., 2012]. The number of nodes therefore verifies $N \in \{83, 129, 234\}$. Deterministic tractography with 32 diffusion directions per voxels was used to reconstruct white matter streamlines from the diffusion-weighted data [Wedeen et al., 2005]. The normalized connection density quantifies

the structural connectivity between brain regions and is defined as

$$s_{ij} = \frac{2}{S_i S_j} \sum_{f \in E_f} \frac{1}{\ell(f)} \tag{3.1}$$

where s_{ij} is the weight of a connection between brain regions i and j, S_i and S_j are the surface areas of regions i and j, $f \in E_f$ represents a streamline f in the set of streamlines E and $\ell(f)$ is a length of a given streamline f [Hagmann et al., 2008, Griffa et al., 2015]. The normalization by brain region surfaces accounts for their varying size and the streamline length normalization accounts for a bias towards longer connections imposed by the tractography algorithm.

Functional connectivity matrices were computed from fMRI BOLD time series. The first four time points of each time series were excluded, yielding a total of 276 time points [Jenkinson et al., 2002]. Rigid-body registration was applied to individual timeslices for motion-correction. The signal was then linearly detrended and corrected for physiological confounds and motion artifacts by regressing white matter, cerebrospinal fluid, and six motion (translations and rotations) signals. Lastly, the signal was spatially smoothed and bandpass-filtered between 0.01-0.1 Hz with Hamming windowed sinc FIR filter. Linear registration was performed between the average fMRI and anatomical images to obtain the regional time series [Jenkinson et al., 2002]. The absolute value of Pearson's correlation coefficient was computed between regional time series in order to obtain functional connectivity matrices. All of the above was performed in the participants native space with Connectome Mapper Toolkit and personalized Python and Matlab scripts [Daducci et al., 2012, Griffa et al., 2017].

3.2.3 Embedded feature selection

We consider a set of n feature vectors of dimension p representing data points $\mathbf{x}_i \in \mathbb{R}^p$, $i = 1, \ldots, n$, and a vector $\mathbf{y} \in \{-1, 1\}^n$ indicating the class of each point. The Support Vector Machine (SVM) classifier seeks the hyperplane maximizing the margin between classes in the space spanned by the feature vectors. The mathematical formulation is

$$\begin{aligned} \min_{\mathbf{w},b} \quad & ||\mathbf{w}||_2^2 + C \sum_{i=1}^{n} \zeta_i \\ \text{subject to} \quad & y_i(\mathbf{w}^T \mathbf{x}_i + b) \geq 1 - \zeta_i, \quad \forall i \in \{1, 2, ..., n\} \\ & \zeta_i \geq 0, \qquad\qquad\qquad\quad \forall i \in \{1, 2, ..., n\} \end{aligned} \tag{3.2}$$

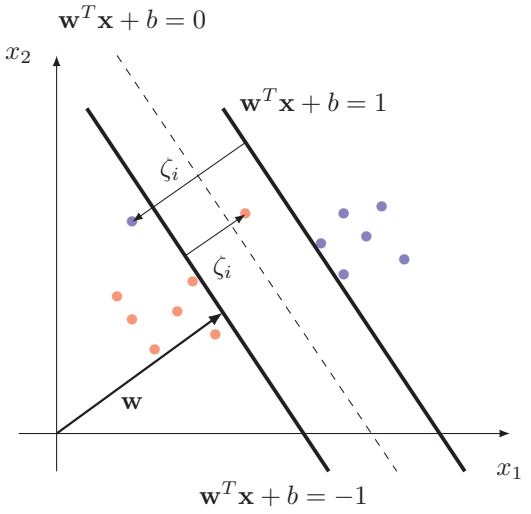

Figure 3.1: **Support Vector Machine.** Illustration of the margin width maximization principle leveraged by the SVM. Data points are described by two features : $\mathbf{x} = [x_1, x_2]$. The color of data points indicates their class. The dashed line represents the decision hyperplane. Solide lines show the margin width between classes.

where $\mathbf{w} \in \mathbb{R}^p$ is a vector normal to the hyperplane, ζ_i are slack variables controlling the overlapping between classes cased by noisy examples and the parameter C trades-off the margin width and the misclassifications. An illustration of the margin width maximization principle is shown in Figure 3.1.

After optimization, the coefficients in $\mathbf{w}$ indicate the contribution of each feature to the orientation of the decision hyperplane. Recursive Feature Elimination (RFE) leverages these coefficients as a ranking criterion in order to iteratively discard non-informative features [Guyon et al., 2002]. This procedure involves two parameters: the step size i.e., the fraction of features to discard at each iteration, and the final number of features desired. These parameters determine the total number of trained SVMs and thus govern the global computational cost of the feature selection. We used Python 2.7 with the SVM-RFE implementation of the Scikit-learn module [Pedregosa et al., 2011].

3.2.4 Statistical evaluation

Our evaluation methodology is based on the work of Abeel and colleagues [Abeel et al., 2010]. We perform a nested 5-fold cross-validation (CV) as shown in Figure

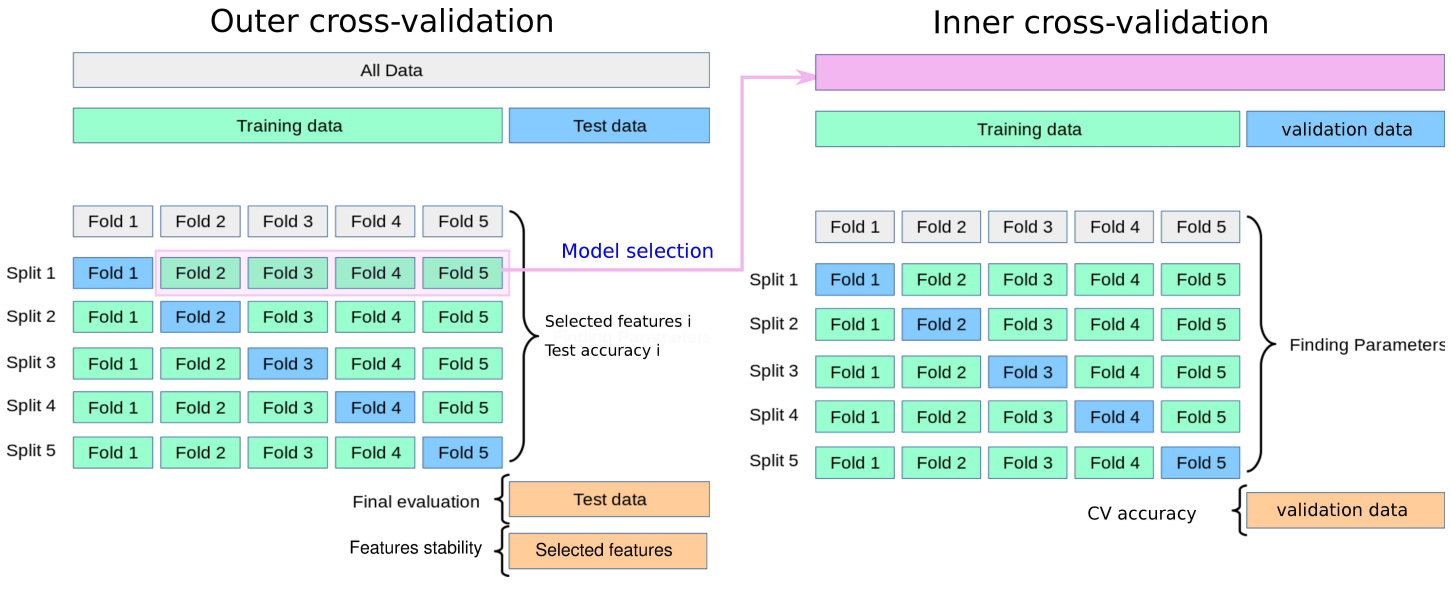

Figure 3.2: **Nested cross-validation.** We perform a nested 5-fold cross-validation. We split the complete dataset into 5 folds. In turn, each fold is retained as the test set (left, blue) while the remaining four are used for the inner cross-validation (pink). This data is used for model training and parameter selection using again a 5-fold cross-validation. The optimal model is used to evaluate the classification accuracy and the feature selection stability on the test data. This is repeated for each outer fold. The complete process is repeated 20 times interwinded with random shufflings of the dataset.

Table 3.1: **Dimension of feature vectors.** We consider 3 brain parcellations ($N \in \{83, 129, 234\}$) and 3 feature modalities : structural connectivity (SC), functional connectivity (FC) and multimodal (MM) i.e., the concatenation of structural and functional feature vectors.

Parcellation resolution: N	83	129	234
Dimension of structural or functional feature vector: $\frac{N(N-1)}{2}$	3403	8256	27261
Dimension of multimodal feature vector: $N(N-1)$	6806	16512	54522

3.2. The inner CV is used for model training and parameter selection on 80% of the original data, whereas the outer CV is used to provide an estimate of the classifier performance on unseen instances in the remaining 20% of the data. We generate 100 subsamples of the original dataset, shuffling the outer 5-fold CV scheme 20 times. The model achieving the best performance on the validation set is selected together with the features retained by the RFE. This model is used to predict the class of unseen instances in the test data and assess the accuracy of the classifier. The prediction accuracy is defined as the fraction of correct predictions on the test data. The global accuracy reported in our results is the mean accuracy across subsamples.

3.2.5 Connectivity features and stability assessment

In order to encode a symmetric brain connectivity matrix in a feature vector, we vectorize the upper triangular part of the matrix. For a matrix of dimension N, the resulting feature vector has dimension $\frac{N(N-1)}{2}$. The combination of structural and functional features is obtained as the concatenation of the respective feature vectors and is denoted as a *multimodal* feature vector. For the brain parcellations that we consider ($N \in \{83, 129, 234\}$), the dimension of the structural, functional or multimodal feature vectors are shown in Table 3.1.

Considering feature vectors of dimension p, applying RFE on two subsamples of the data produces two sets of selected features $\mathcal{S}_1$ and $\mathcal{S}_2$ with fixed cardinality $s = |\mathcal{S}_1| = |\mathcal{S}_2|$ and overlap $r = |\mathcal{S}_1 \cap \mathcal{S}_2|$. The stability index KI introduced by Kuncheva et al. [Kuncheva, 2007] quantifies the overlap of two sets having the same cardinality and corrects for the probability that elements are found in both sets by chance. The expected size of the overlap, assuming a hypergeometric distribution for the random drawing of elements in both sets, is $\mathbb{E}\{r\} = \frac{s^2}{p}$.

The stability index KI is defined as

$$KI(\mathcal{S}_1, \mathcal{S}_2) = \frac{\text{Observed } r - \text{Expected } r}{\text{Maximum } r - \text{Expected } r} \tag{3.3}$$

$$= \frac{r - \frac{s^2}{p}}{s - \frac{s^2}{p}} \tag{3.4}$$

$$= \frac{rp - s^2}{s(p - s)} \tag{3.5}$$

The global stability index $\overline{KI}$ for k subsamples is the average over pairwise stability indices:

$$\overline{KI} = \frac{2}{k(k-1)} \sum_{i=1}^{k-1} \sum_{j=i+1}^{k} KI(\mathcal{S}_i, \mathcal{S}_j) \tag{3.6}$$

The stability index is in the range $\overline{KI} \in [-1, 1]$ where $\overline{KI} = 1$ indicates a perfectly stable overlap among sets of selected features, and increases monotonically with the overlap r.

In our experiments, we fix the number s of features selected by RFE as a percentage of the total number of features for each brain parcellation. Because multimodal feature vectors are twice longer than structural or functional ones, we adapt the percentage of selected features accordingly. Table 3.2 summarizes the number of selected features for each parcellation, with respect to the RFE parameter. In order to assess the role of the feature selection procedure, we also compute the classification accuracy and the Kuncheva index for a randomly selected set of features with the same cardinality as the one selected by RFE.

3.3 Results

3.3.1 Classification and stability performance

First, we investigate the effect of different brain connectivity features and parcellations in the discrimination between schizophrenic patients and healthy controls. For each case, we control the RFE step size and the percentage of selected features (see Methods), assessing their impact on the classification accuracy and the stability of the selected features. Figures 3.3, 3.4 and 3.5 show the average classification accuracy and the stability of structural, functional and multimodal features respectively. We observe that the RFE step size has a limited influence on the

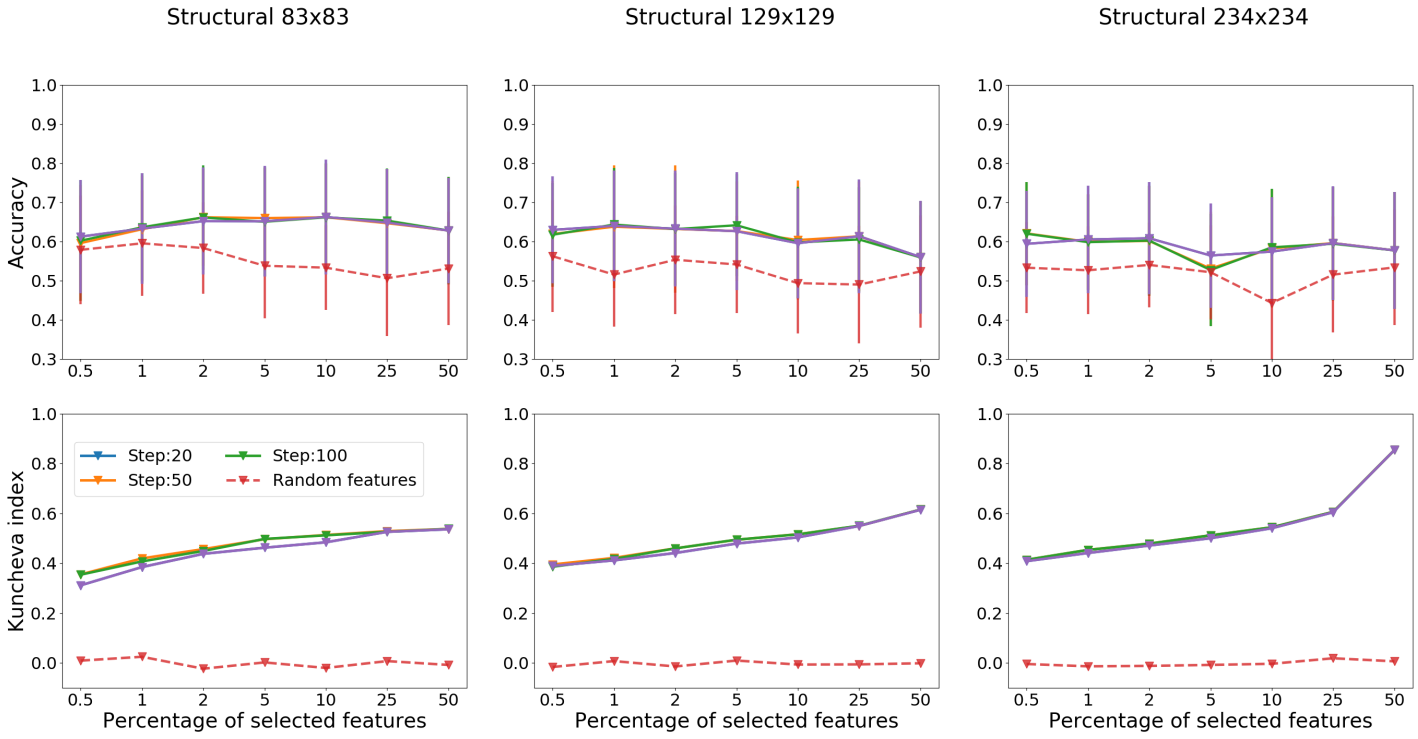

Figure 3.3: **Accuracy and stability of structural features.** The top row reports the mean accuracy over 100 test sets (see Methods) with respect to the percentage of selected features. Error bars indicate the standard deviation across test sets. The 'Random features' curve (dashed, red) presents the result for randomly selected sets of features. The bottom row shows the Kuncheva index ($\overline{KI}$), which quantifies the stability of the feature selection. The experiment is repeated for three brain parcellations of 83, 129 and 234 regions respectively.

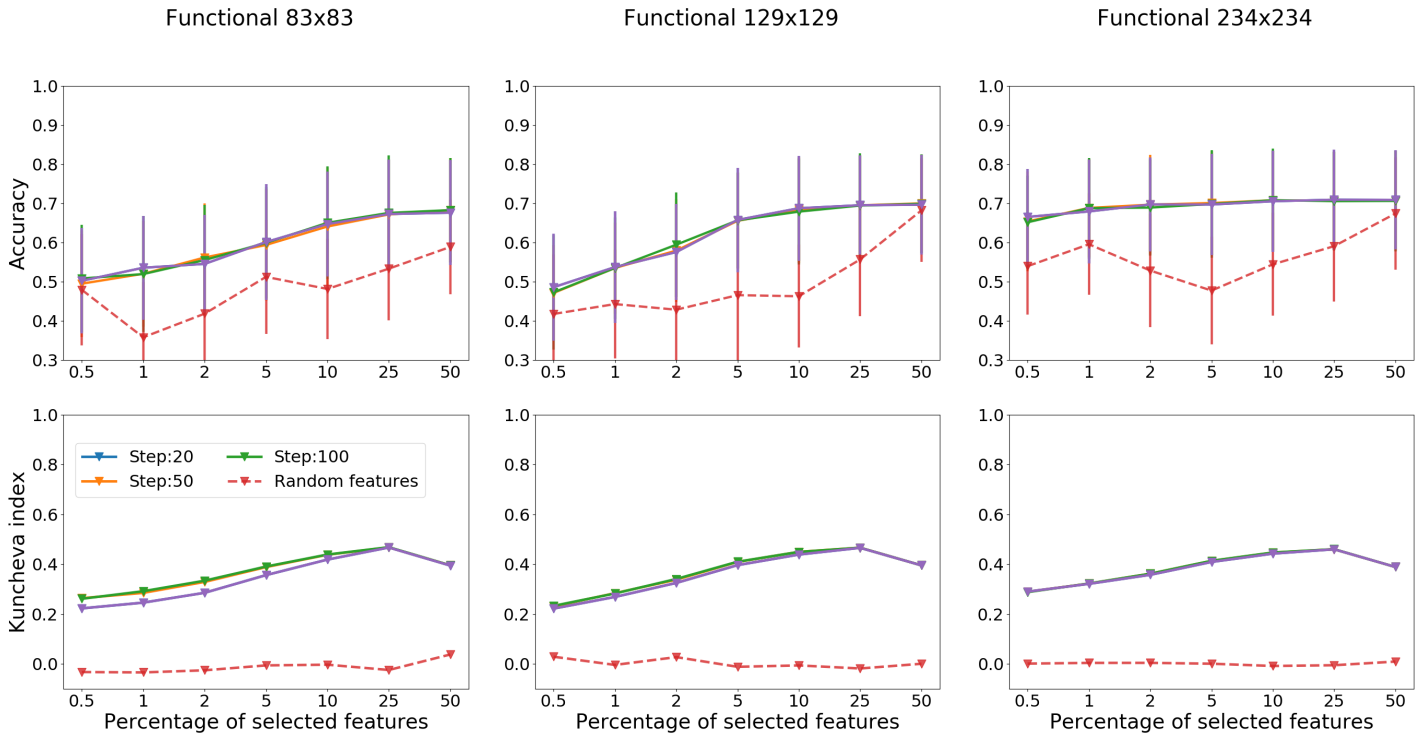

Figure 3.4: **Accuracy and stability of functional features.** The top row reports the mean accuracy over 100 test sets (see Methods) with respect to the percentage of selected features. Error bars indicate the standard deviation across test sets. The 'Random features' curve (dashed, red) presents the result for randomly selected sets of features. The bottom row shows the Kuncheva index ($\overline{KI}$), which quantifies the stability of the feature selection. The experiment is repeated for three brain parcellations of 83, 129 and 234 regions respectively.

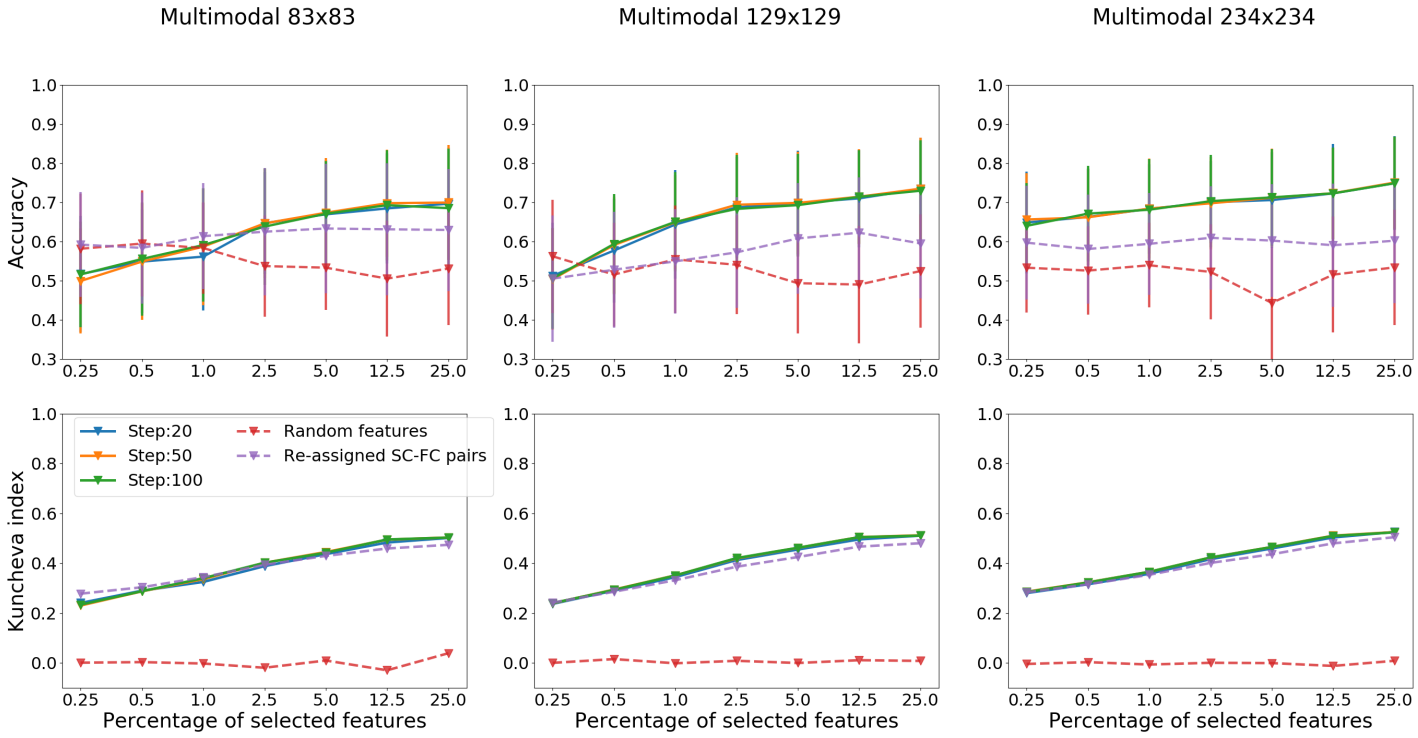

Figure 3.5: **Accuracy and stability of multimodal features.** The top row reports the mean accuracy over 100 test sets (see Methods) with respect to the percentage of selected features. Error bars indicate the standard deviation across test sets. The 'Random features' curve (dashed, red) presents the result for randomly selected sets of features. The 'Re-assigned SC-FC pairs' curve (dashed, purple) is obtained by randomly assigning the the structural features of each individual to the functional features of a different individual of the same group. The bottom row shows the Kuncheva index ($\overline{KI}$), which quantifies the stability of the feature selection. The experiment is repeated for three brain parcellations of 83, 129 and 234 regions respectively.

Table 3.2: **Number of selected features.** We fix the number of features to be selected by RFE as a percentage of the total number of feature for each resolution (see Table 3.1). The percentage is adapted in the multimodal case combining structural and functional features in order to balance the twice larger number of features.

Number of selected features		Parcellation resolution		
Percentage of structural or functional features	Percentage of multimodal features	83	129	234
0.5 %	0.25 %	17	41	136
1 %	0.5 %	34	82	272
2 %	1 %	68	165	545
5 %	2.5 %	170	412	1363
10 %	5 %	340	825	2726
25 %	12.5 %	850	2064	6815
50 %	25 %	1701	4128	13630

results.

In Figure 3.3, we observe that structural features produce accuracy scores that are essentially constant across parcellations and percentages of selected features. Moreover these scores are close to that achieved with randomly selected features especially for the 234 $\times$ 234 parcellation. The Kuncheva index lies in the range $\overline{KI} \in [0.4, 0.6]$ with the exception of the 234 $\times$ 234 parcellation with 50% of selected features where $\overline{KI} > 0.8$. Note that in this specific case the prediction accuracy is almost equal to the chance level. Because the feature selection and the accuracy assessment are performed on different folds of the datasets (respectively the training set and the test set), the variability of the accuracy score across different tests is not necessarily reduced when the feature selection stability increases. In Figure 3.4, we observe that functional features generate accuracy scores that increase with the percentage of selected features and reach 0.69 in the 234 $\times$ 234 parcellation with 50% of selected features. Again, this score is close to the score obtained with a random set of features. The Kuncheva index is in the range $\overline{KI} \in [0.2, 0.5]$. In Figure 3.5, we observe that multimodal features achieve the best accuracy score (0.73) in the 234 $\times$ 234 parcellation with 50% of selected features and that this score is above the chance level. The Kuncheva index at this point reaches $\overline{KI} > 0.5$. In order to evaluate the complementarity of structural and functional features at the level of each individual, we provide in Figure 3.5 an additional baseline where we randomly re-assign the structural features of each individual to the functional features of a different individual of the same group,

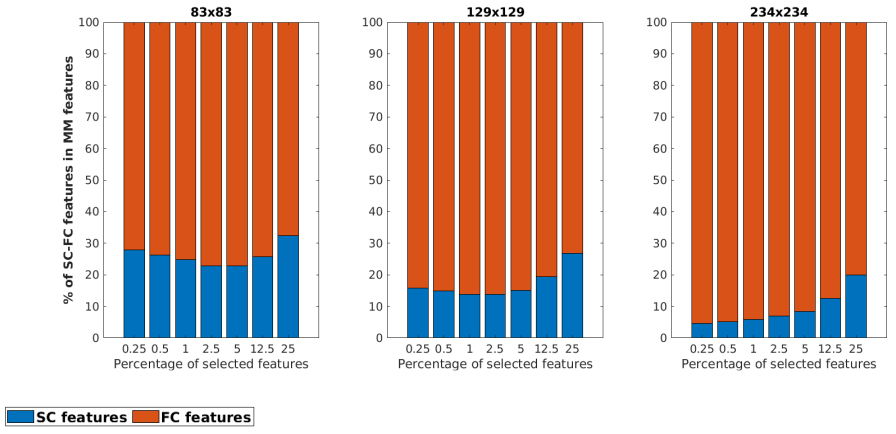

Figure 3.6: **Repartition of selected multimodal features.** Share of structural (SC, blue) and functional (FC, red) features selected in the multimodal case, across parcellations.

before applying the classification model. We observe that this approach generates a higher prediction accuracy than that obtained with a random set of features. Preserving the individual correspondence of structure-function pairs in multimodal data provides significantly higher accuracies than the additional baseline when at least 12.5% of the features are selected in the 83 $\times$ 83 resolution, and when at least 0.5% of the features are selected in the 129 $\times$ 129 and 234 $\times$ 234 resolutions (unpaired t-tests, α=0.005). Because the features are selected by the RFE and not randomly in this baseline, the Kuncheva index in comparable to that obtained with the preserved structure-function pairs. Figure 3.6 quantifies the respective involvement of structural and functional features selected in the multimodal case with preserved structure-function pairs. We observe that a non-zero proportion of both structural and functional features are selected, with a dominance of functional features over structural ones.

3.3.2 Brain regions affected in schizophrenia

Because multimodal features provide the best classification accuracy and a good feature selection stability (Figure 3.5), we focus on the multimodal case and turn to the problem of relating the selected features (or edges) to the brain regions (or nodes) most involved in the contrast between schizophrenic patients and healthy controls. We consider the share of structural and functional edges of the multimodal case separately. We define the *degree of relevance* d_i of a brain region i, in

both structural and functional cases, as

$$d_i = \sum_{j=1}^{N} f_{ij} \tag{3.7}$$

where f_{ij} is the frequency at which the edge (i, j) was selected across the 100 subsamples. In other words, d_i is the degree of node i in a network with edges weighted by their selection frequency. Figures 3.7 and 3.8 show the degree of relevance of brain regions in the 83 $\times$ 83 parcellation, according to structural and functional features respectively. In Figure 3.7, we highlight in blue the set of regions identified by Griffa and colleagues [Griffa et al., 2015] in structural data using the same parcellation. We observe an overlap of these regions with those having the highest degree of relevance.

3.4 Discussion

In this chapter, we investigated a machine learning approach to identify biomarkers of schizophrenia in brain networks. Our results showed that a combination of structural and functional features provides a trade-off between prediction accuracy and feature selection stability. The selected features allowed us to detect brain regions involved in the discrimination between schizophrenic patients and healthy controls. Theses regions form a set that overlaps with previously identified regions linked to the disease. Overall, we illustrated that biomarkers derived from network models of multimodal neuroimaging data are useful for researchers studying schizophrenia. Further validation is however required in order to leverage this approach along with existing biomarkers in future clinical applications.

3.4.1 Machine learning and biomarker identification

Translating the problem of biomarker identification into a machine learning framework is beneficial in several regards. The use of a feature selection procedure embedded in the classifier allowed us to detect features of interest in an automated, multivariate and data-driven fashion. The fact that we identified not only regions that were previously linked to the disease but also additional regions (Figure 3.7) suggests that supervised classification and feature selection together are able to detect relevant brain areas that have been underlooked in previous work. The accuracy obtained with multimodal data (Figure 3.5), though above the chance level, is moderate due to the biological nature of the data, to the limited sample size and to the fact that we restricted our analysis to a linear classifier. Future

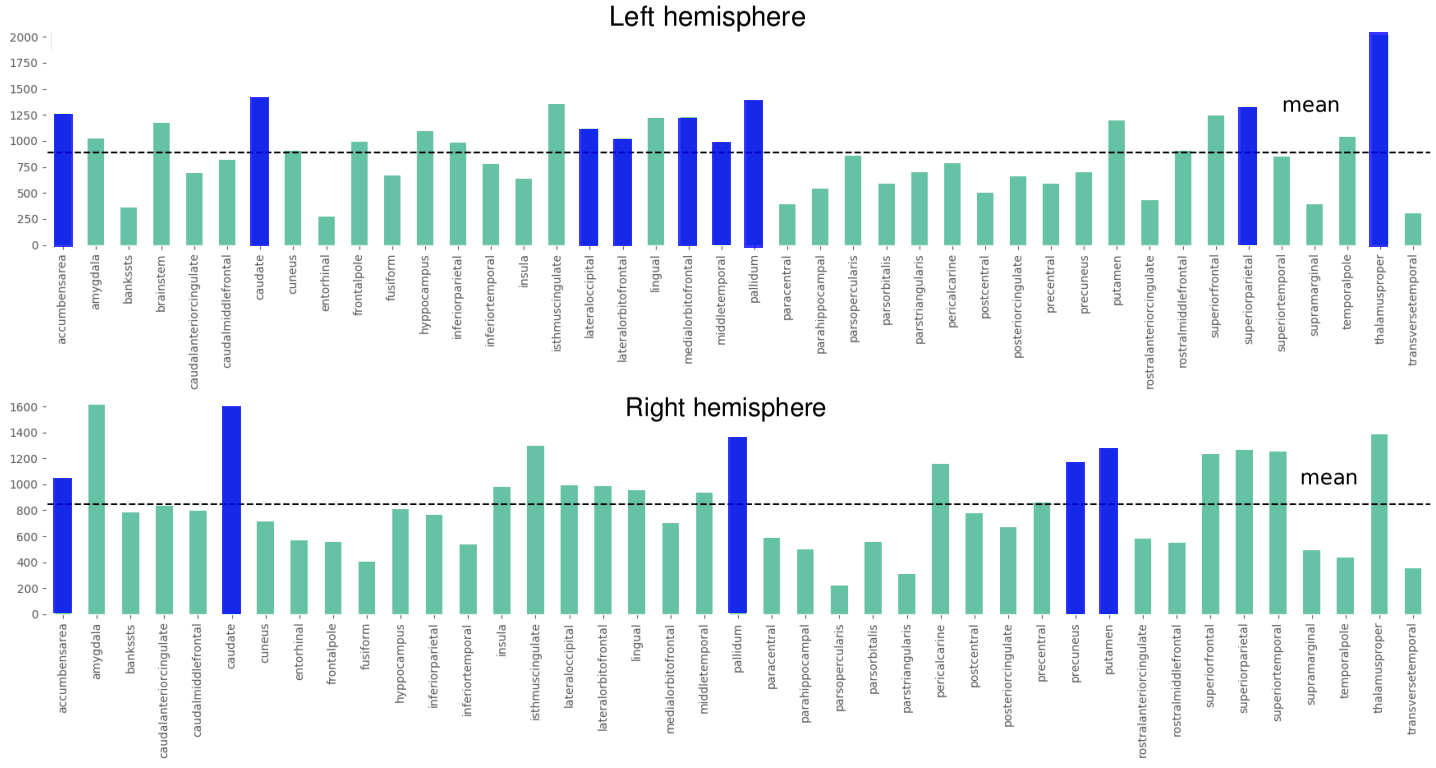

Figure 3.7: **Brain regions affected in schizophrenia - Structural mode.** From the feature selection procedure applied to multimodal connectivity values, we compute the degree of relevance of brain regions with respect to the share of *structural* connections. We show the degree of relevance of each ROI of the 83 $\times$ 83 parcellation. The dashed line indicates the average degree of relevance. Blue bars indicate the above-average ROIs overlapping with the affected regions identified by Griffa et al. [Griffa et al., 2015].

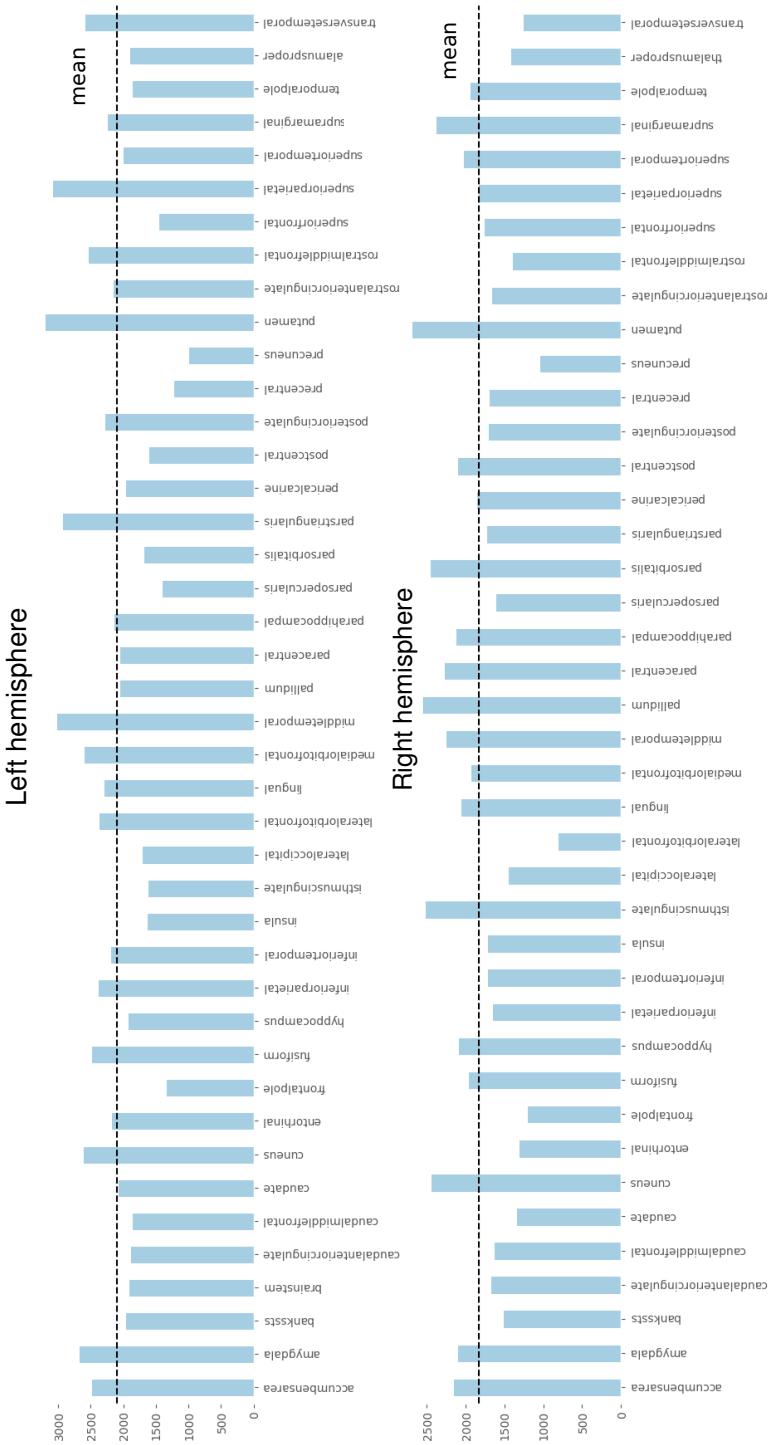

Figure 3.8: **Brain regions affected in schizophrenia - Functional mode.** From the feature selection procedure applied to multimodal connectivity values, we compute the degree of relevance of brain regions with respect to the share of *functional* connections. We show the degree of relevance of each ROI of the 83 $\times$ 83 parcellation. The dashed line indicates the average degree of relevance. The *affected core* of Griffa and colleagues [Griffa et al., 2015] was identified in structural data, which is why we do not highlight the overlap here.

work should investigate the performance of other classifiers with embedded feature selection such as regularized logistic regression or random forests. Note that the recursive feature elimination used in this chapter assumes linearly separable classes. The linearity of the classifier enables the interpretation of selected features in the original feature space. On the other hand, extensions to non-linear classifier, for instance using kernel methods, are expected to produce better classification accuracies but would require a separate feature selection procedure at the possible expense of a loss of interpretability.

Because feature selection relies on the data under consideration, evaluating the robustness of retrieved features to variations in the data is required in order to generalize the findings to external datasets. On the one hand, the values of the Kuncheva index obtained in our analysis indicate that identified features are consistent across subsamples ($\overline{KI} > 0$), as confirmed by the overlap found with previous work (Figures 3.3, 3.4, 3.5 and 3.7). On the other hand, these values do not reveal a perfect stability. This suggests that selected features are still sensitive to data variations, an effect that might be emphasized by the small number of instances included in the dataset considered here (54 participants). Further work assessing feature stability on larger samples is required to validate the relevance of identified biomarkers.

The framework developed in this chapter is not restricted to the study of schizophrenia. Future studies on datasets related to other pathologies such as Alzheimer's disease might benefit from our approach to detect disease-specific biomarkers. This framework should be extended in order to account for different stages of the disease, either by considering multi-class classification or continuous regression from early to late stages of the disease. These investigations could in turn enable a shift from diagnosis to prognosis. Moreover, future work should assess additional performance metrics along with the classification accuracy, in order to account for the repartition of misclassifications into the false positive or false negative category and to provide a more exhaustive view of the classification performance.

3.4.2 Complementary effects of structure and function

Our results showed that mixing structural and functional connectivity features allows us to achieve a trade-off between significant classification accuracy and feature selection stability (Figure 3.5), with a majority of functional features (Figure 3.6). While obtaining a better or equal classification accuracy was expected when

increasing the number of features, we illustrated here that the classifier systematically selects a mix of structural and functional features. On the one hand, most studies on the detection of disease-related biomarkers consider either one of these modalities, or both but in separate experiments. On the other hand, researchers have shown that structural and functional connectivity are related yet distinct. Our observations suggest that structural and functional connections provide complementary pieces of information that are valuable for the characterization of schizophrenia in brain networks.

The nature of the link between structure and function in the human brain remains elusive [Suárez et al., 2020]. Active research has proposed modeling approaches in order to explain the structure-function relationship based on the idea that the anatomical network forms a 'backbone' for the transfer of information among brain regions that is ultimately reflected in functional connectivity [Goñi et al., 2014, Abdelnour et al., 2014, Avena-Koenigsberger et al., 2018, Seguin et al., 2018]. While we proposed in this chapter to mix structural and functional connections in a feature vector ignoring their relationship, we suggest that models of the structure-function relationship can be leveraged in order to derive features that characterize this relationship and that summarize the complementary information necessary for the discrimination between patients and controls. This possibility is explored in the next two chapters of this thesis.

3.4.3 Limitations

The small sample size (54 participants) is responsible for the large variance of the prediction accuracy across test subsamples (Figures 3.3, 3.4 and 3.5). Further investigation on larger datasets is required in order to confirm the relevance of the biomarkers derived in this study. In addition, fMRI data was only acquired at rest (resting-state fMRI). In a similar way as structural and functional connectivity (at rest) were found complementary, integrating task-fMRI data or behavioral scores to the proposed approach could provide supplementary insights into the characterization of the disease. Finally, we note that most patients were under medication at time of data acquisition (see Methods), which could affect their classification outcome.

3.4.4 Conclusion

We proposed a machine learning framework in order to classify brain networks based on their connectivity values. We illustrated the performance of our approach on brain networks of schizophrenic patients and healthy controls and we suggested

brain regions affected by the disease. Our results underlined the complementary roles that structure and function play in the characterization of schizophrenia. We suggested several areas of improvement including the refinement of the classification problem in order to detect different stages of the disease, and the derivation of features specific to the structure-function relationship in brain networks.

4

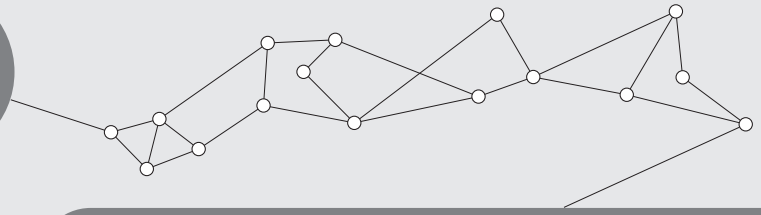

Structure-Informed Functional Connectivity

This chapter in 5 sentences

- **We suggested that** structure and function are distinct and complementary components to consider in the study of brain networks.
- **Therefore, we wondered if** we could model the relationship between structure and function in human brain networks and across several tasks.
- **In this chapter, we** leverage systems theory in order to model functional connectivity as the covariance matrix of a linear dynamics spreading on the anatomical brain network, and we provide a principled approach for identifying the control regions driving the dynamics.
- **Our results show that** well-defined, sparse and robust sets of control regions, partially overlapping across several tasks and resting-state, produce functional connectivity patterns comparable to empirical ones.
- **This suggests that** controllability is a fundamental feature allowing brain anatomy to support different functional states thanks to state-specific control regions.

The content of this chapter is adapted from the following publication:

- **Chiêm, B.**, Crevecoeur, F., & Delvenne, J.C. (2021). Structure-informed Functional Connectivity Driven by Identifiable and State-Specific Control Regions. Network Neuroscience, 5(2), 591-613.

4.1 Introduction

Recently, approaches combining Magnetic Resonance Imaging (MRI) and network science emerged in order to characterize links among neural Regions of Interest (ROIs) [Bassett and Sporns, 2017]. Most studies focus either on structural connections or on functional interactions, which capture two distinct aspects of brain connectivity. On the one hand, diffusion MRI (dMRI) with tractography [Mori and Zhang, 2006] enables the mapping of white matter pathways and describes the anatomical links between ROIs. This structural description of the human brain forms a network called the *connectome* [Sporns et al., 2005, Hagmann et al., 2008]. On the other hand, the Blood-Oxygenation-Level Dependent (BOLD) signal in functional MRI (fMRI) provides an estimate of brain activity in gray matter areas [Ogawa et al., 1990]. The matrix of pairwise Pearson's correlation coefficients between regional BOLD time series is a common tool to quantify *functional connectivity* (FC) among ROIs [Bassett and Sporns, 2017]. Unlike the connectome that is a fixed network of anatomical links, functional connectivity varies over short timescales and across resting-state and task conditions (see Figure 1.3 and [Cole et al., 2014]).

An important challenge in neuroscience is to characterize the relationship between the connectome and functional connectivity [Honey et al., 2010, Batista-García-Ramó and Fernández-Verdecia, 2018, Suárez et al., 2020]. Several approaches have been proposed in the literature in order to elucidate this relationship in macroscale brain networks and understand the importance of the anatomical organization in promoting particular patterns of activity. Along with methods based on graph signal processing and spectral decompositions [Preti and Van De Ville, 2019, Tewarie et al., 2020], it has been proposed that describing the link between structural and functional connectivity requires a model of information flow between ROIs [Avena-Koenigsberger et al., 2018]. For instance, models based on random walks and diffusion on the connectome have been able to partly reproduce resting-state FC [Abdelnour et al., 2014, Goñi et al., 2014, Mišić et al., 2015]. Viewing the brain as a dynamical system allows us to study the controllability of this system i.e., its ability to account for context-dependent control signals in order to affect the overall state of the brain [Gu et al., 2015, Medaglia, 2019]. The framework of network controllability requires to define input nodes i.e., control regions capable of integrating external signals in order to modify the state of the network [Liu et al., 2011]. Earlier work in macroscale brain networks showed that any isolated brain region was theoretically sufficient to get controllability of the connectome [Gu et al., 2015, Tu et al., 2018, Pasqualetti et al., 2019]. One shortcoming is that al-

though controllable in theory, some configurations are practically unfeasible as they would require excessive control energy. Moreover, several pieces of evidence from the fields of motor and cognitive control suggest that *sets* of regions are responsible for the control of brain activity [Dosenbach et al., 2007, Power and Petersen, 2013, Cole et al., 2014, Omrani et al., 2016, Eisenreich et al., 2017]. Despite these advances in brain communication modeling and connectome controllability, an integrated explanation for the emergence of multiple FC patterns from the static structure of the connectome is still lacking.

In this chapter, we develop a principled approach for identifying potential control centers in the brain by modeling state-specific FC as the correlation matrix of a controllable dynamics unfolding on the connectome. We leverage the observation that the Gramian matrix used in controllability studies [Pasqualetti et al., 2014, Gu et al., 2015] corresponds to the covariance matrix of the activities in the different nodes of a network, assuming a linear transition dynamics among them. This observation brings us to introduce the concept of structure-informed FC i.e., the pairwise functional correlation matrix derived from the structure of the connectome. Since this matrix depends on the choice of input nodes, we show that it is possible to identify the set of control regions maximizing the mapping between structure-informed and empirical FC in different states. Using dMRI and fMRI data (resting-state and 7 tasks) from the Human Connectome Project [Van Essen et al., 2013], we find that sparse input sets produce FC matrices that are comparable to empirical ones. Moreover, we show that the identified sets are well defined, stable, and state-specific. We discuss their properties and the fact that the method is able to capture the singularity of resting-state compared to the other task-related conditions. Along with the numerical assessment of control regions identified with our model, we suggest that they may have an important physiological role in driving neural activity towards a desired state. In addition to the experiments of this chapter, we provide in Chapter 5 two case studies illustrating the relevance of the identified control regions for characterizing brain states. Overall, our approach relies on a model linking structure and function in brain networks in order to identify possible subsets of brain regions underlying task-specific control.

4.2 Materials and Methods

4.2.1 Dataset

We retrieved the preprocessed '100 unrelated subjects' dataset of the Human Connectome Project (HCP) database (`https://db.humanconnectome.org/`), HCP

1200 release [Van Essen et al., 2013]. All individuals (54 females, 46 males, 22-36 y.o.) gave written informed consent to the HCP consortium. Scanning protocols were approved by the local Institutional Review Board at Washington University in Saint Louis. Acquisition parameters are detailed in previous HCP reports [Van Essen et al., 2012, Van Essen et al., 2013, Glasser et al., 2013]. Preprocessing consisted of HCP minimal preprocessing pipelines [Glasser et al., 2013]. We applied further processing steps in agreement with previously published studies using HCP data [Amico et al., 2019, Tipnis et al., 2018, Rosenthal et al., 2018].

4.2.2 Brain networks reconstruction

We used the cortical parcellation introduced by Destrieux and colleagues [Destrieux et al., 2010] and composed of 148 non-overlapping Regions of Interest (ROIs). Subcortical structures (thalamus, caudate nucleus, putamen, pallidum, hippocampus, amygdala, accumbens nucleus) and cerebellum were extracted using the FMRIB Software Library [Jenkinson et al., 2012] and added to the parcellation for completeness, bringing the number of ROIs to $N = 164$.

The processing of diffusion data was conducted for each individual using state-of-the-art methods implemented in the MRtrix3 toolbox [Tournier et al., 2019]. In summary, a tissue-segmented image was generated (MRtrix command `5ttgen`) in order to perform Anatomically-Constrained Tractography [Smith et al., 2012]. Then, multi-shell, multi-tissue response functions were computed (MRtrix command `dwi2response msmt_5tt`) in order to inform the Constrained Spherical Deconvolution (MRtrix command `dwi2fod msmt_csd`) [Jeurissen et al., 2014]. Probabilistic tractography (MRtrix command `tckgen`) was performed using a second-order integration over fiber orientation distributions (iFOD2 method, [Tournier et al., 2010]) to allow for a more precise fiber tracking through crossing regions. This produced an initial tractogram composed of 10 millions streamlines. The tractogram was corrected (SIFT2 approach, MRtrix command `tcksift2`) by assigning a weight to each streamline such that the weighted contribution of all streamlines to the spherical deconvolution diffusion model matches as well as possible the fiber orientation distribution lobe integrals of the diffusion data [Smith et al., 2015]. This posthoc operation produced a more biologically meaningful representation of white matter tracts. Eventually, we built the adjacency matrix $\mathbf{S}$ of the connectome by computing the fiber density between each pair of previously defined ROIs (MRtrix command `tck2connectome` with option `-scale_invnodevol`). The group-average adjacency matrix is obtained as the entrywise average of the $K = 100$ individual-level adjacency matrices. Both group-average and individual matrices

were kept unthresholded. Tractograms composed of 1 million or 100,000 streamlines were shown to produce a group-level matrix that is highly correlated ($r > 0.99$) with that used in the main analysis (see Appendix A.2.12).

We included fMRI data acquired during resting-state and seven tasks. The emotional processing task (EMOTION) consisted in recognizing which of the two faces (resp. shapes) presented at the bottom of a screen matched the one presented at the top of the screen. Faces were aimed to represent either anger or fear. In the gambling task (GAMBLING), participants played a card guessing game in order to win or loose money. The acquisition comprised neutral blocks, blocks with mostly reward trials and blocks with mostly loss trials. The language processing task (LANGUAGE) alternated story blocks and math blocks. In story blocks, participants had to answer a 2-choice question after the hearing of a brief story. In math blocks, participants had to choose the right answer out of two after hearing an arithmetic operation. In the motor task (MOTOR), participants had to move either their fingers (left or right), their toes (left or right) or their tongue following visual cues on a screen. In the relational processing task (RELATIONAL), participants are presented with pairs of objects on a screen. Each object is one shape filled with one texture. Participants were asked to determine what dimension (shape or texture) differs between the objects. The social cognition task (SOCIAL) consisted in video clips presenting objects (squares, circles, triangles) either interacting in some way or moving randomly. Participants were asked to decide whether objects had an interaction or not, or not sure. In the working-memory task (WM), participants were presented with pictures to be memorized (0-back and 2-back trials). Separate blocks presented pictures of places, tools, faces and body parts. Full details about the fMRI tasks protocols along with the references from which they are derived are available in the HCP 1200 reference manual.

The preprocessing of fMRI data included distortion correction, subject motion correction, intensity normalization and registration to standard MNI space [Glasser et al., 2013]. Resting-state Blood-Oxygenation-Level Dependent (BOLD) time series were filtered in forward and reverse directions (1st-order Butterworth, bandpass = [0.001,0.08] Hz, see [Power et al., 2014]). We did not regress out the global signal in the main analysis ; the impact of global signal regression is discussed in Appendix A.1.3. For both resting-state and task fMRI, the voxel time series were then z-scored and averaged in each ROI using the Connectome Workbench toolbox [Marcus et al., 2011] and excluding outlier time points outside 3 standard deviations from the mean (Workbench command `-cifti-parcellate`). Empirical functional connectivity (FC) matrices $\mathbf{F}_{emp}$ were obtained by computing Pearson's

correlation coefficient between each pair of resulting time series. For each task, FC matrices of both fMRI phase encoding directions (left-to-right and right-to-left) were averaged in order to reduce the effect of artifactual noise. For resting-state, the four resulting matrices (2 scans, 2 phase encoding directions) were averaged for the same reason. The group-average FC matrix (for each task and resting-state) is obtained as the entrywise average of the $K = 100$ individual-level FC matrices. Both group-average and individual matrices were kept unthresholded.

4.2.3 Structure-informed functional connectivity

In order to investigate how the connectome shapes Functional Connectivity (FC), we study the covariance matrix of a linear dynamics defined on the connectome. In a network of N nodes, let $\mathbf{x}(k)$ be the N-dimensional state-vector containing the activity level of each node at time k. The trajectory of $\mathbf{x}$ is governed by the following equation:

$$\mathbf{x}(k+1) = \mathbf{A}\mathbf{x}(k) + \mathbf{B}\mathbf{u}(k) \tag{4.1}$$

The $N \times N$ system matrix $\mathbf{A}$ describes the interactions among the nodes of the network, the columns of the $N \times m$ input matrix $\mathbf{B}$ are canonical vectors identifying the m input nodes and $\mathbf{u}(k)$ is an m-dimensional vector providing the value of external input signals at time k.

We excite the system with white noise signals $\mathbf{u}$, and we assume that $\mathbf{x}$ is centered, $\mathbf{A}$ is stable (see section 4.2.4), the input signals are not correlated with the initial state of the system (i.e. $\mathbb{E}\{\mathbf{x}(0)\mathbf{u}^T(k)\} = \mathbf{0}$, $\forall k$) and input signals in $\mathbf{u}$ have unit variance. The steady-state covariance matrix $\mathbf{\Sigma} = \mathrm{Cov}(\mathbf{x})$ of System 4.1 is

$$\begin{aligned}
\mathbf{\Sigma}(k+1) &= \mathbb{E}\left\{\mathbf{x}(k+1)\mathbf{x}^T(k+1)\right\} \\
&= \mathbb{E}\left\{\left(\mathbf{A}\mathbf{x}(k) + \mathbf{B}\mathbf{u}(k)\right)\left(\mathbf{A}\mathbf{x}(k) + \mathbf{B}\mathbf{u}(k)\right)^T\right\} \\
&= \mathbf{A}\mathbb{E}\left\{\mathbf{x}(k)\mathbf{x}^T(k)\right\}\mathbf{A}^T + \mathbf{A}\mathbb{E}\left\{\mathbf{x}(k)\mathbf{u}^T(k)\right\}\mathbf{B}^T \\
&\quad + \mathbf{B}\mathbb{E}\left\{\mathbf{u}(k)\mathbf{x}^T(k)\right\}\mathbf{A}^T + \mathbf{B}\mathbb{E}\left\{\mathbf{u}(k)\mathbf{u}^T(k)\right\}\mathbf{B}^T \\
&= \mathbf{A}\mathbf{\Sigma}(k)\mathbf{A}^T + \mathbf{B}\mathbf{B}^T \qquad \text{using the assumptions on } \mathbf{u}(k) \\
\Rightarrow \mathbf{\Sigma} &= \mathbf{A}\mathbf{\Sigma}\mathbf{A}^T + \mathbf{B}\mathbf{B}^T \qquad \text{in steady-state}
\end{aligned}$$

Notice that excitation signals with non-unit variance would result in a scaling of matrix $\mathbf{B}$, which would not affect further results.

The solution $\mathbf{\Sigma}$ is known as the controllability Gramian (see Section 2.4). Here, in contrast to previous studies where $\mathbf{\Sigma}$ is used to derive quantitative control properties of individual nodes in the network [Pasqualetti et al., 2014, Gu et al., 2015, Karrer et al., 2020], we interpret the Gramian as the state-covariance matrix obtained by stochastic excitation of the system through a set of control nodes. This allows us to relate it to the concept of functional connectivity. Denoting $\mathbf{P}$ as the diagonal matrix containing only the diagonal entries of $\mathbf{\Sigma}$ (i.e. the states variances), we apply a symmetric normalization to the steady-state covariance matrix to obtain a pairwise correlation matrix that we use as a model of functional connectivity:

$$\tilde{\mathbf{\Sigma}} = \mathbf{P}^{-1/2}\mathbf{\Sigma}\mathbf{P}^{-1/2} \tag{4.2}$$

$$\mathbf{F}_{SI} = \tilde{\mathbf{\Sigma}} \tag{4.3}$$

The *Structure-informed* FC, $\mathbf{F}_{SI}$, is the FC matrix associated with the structural network, its dynamics and its control regions. This model of functional brain interactions assumes a correlation-based definition of functional connectivity [Korhonen et al., 2021] and ignores the internal processing of neural signals performed individually by brain regions.

Using the mathematical expression of structure-informed FC, we turn to the problem of identifying the set of control regions defined by $\mathbf{B}$, that maximizes the similarity between $\mathbf{F}_{SI}$ and an empirical FC matrix $\mathbf{F}_{emp}$ obtained from external recordings of the system. For that, we formulate the optimization problem

$$\begin{aligned} \mathbf{B}^* &= \arg\max_{\mathbf{B}} sim\left(\mathbf{F}_{SI}, \mathbf{F}_{emp}\right) \\ \text{such that} \quad & m \leq U \end{aligned} \tag{4.4}$$

where $\mathbf{F}_{SI}$ is a function of $\mathbf{B}$, m is the number of columns of $\mathbf{B}$ i.e., the cardinality of the input set, and U is an upper bound to be fixed in order to control the number of input nodes.

4.2.4 Normalized Laplacian diffusion

We consider a diffusion process unfolding on the connectome, as proposed by Abdelnour and colleagues in order to model the communication dynamics among brain regions [Abdelnour et al., 2014]. The state transition matrix $\mathbf{A}$ has the

following form:

$$\mathbf{A} = e^{-\beta\mathcal{L}} \tag{4.5}$$

Here, with $\mathbf{D}$ being the diagonal matrix of the weighted degree of the nodes in the connectome, the matrix $\mathcal{L} = \mathbf{D}^{-1/2}(\mathbf{D} - \mathbf{S})\mathbf{D}^{-1/2}$ is the normalized Laplacian of the connectome. The parameter $\beta = \bar{\beta}\Delta T$ accounts for the diffusion time constant $\bar{\beta}$ and the sampling time ΔT of the process. We chose to hold this parameter out of the optimization and to set $\bar{\beta} = 1$ and $\Delta T = \text{TR}$, where TR$= 0.72s$ is the repetition time of the fMRI data [Van Essen et al., 2013]. This choice is arbitrary and the optimal β is state-dependent (see Appendix A.2.14), although choosing $\beta \in [0.1, 4.0]$ has a weak impact on the results (see Appendix A.2.15). Note that other dynamics can be investigated and that any hyperparameter coming with the chosen transition matrix can be included in the optimization, at the expense of a possibly prohibitive computational cost.

In order to ensure that System 4.1 unforced dynamics is intrinsically stable so that the activities decay to zero in the absence of control signals (see [Gu et al., 2015], [Kim et al., 2018] and the detailed discussion in [Karrer et al., 2020]), the entries of matrix $\mathbf{A}$ were further divided by $1 + \lambda_{\text{max}}(\mathbf{A})$, where $\lambda_{\text{max}}(\mathbf{A})$ is the largest eigenvalue of $\mathbf{A}$. In our case, the smallest eigenvalue of $\mathcal{L}$ is always 0 since the Laplacian of an unsigned graph is positive semi-definite, and always possesses a zero eigenvalue [Mohar et al., 1991]. Therefore, $\lambda_{\text{max}}(e^{-\beta\mathcal{L}})$ is always equal to 1.

4.2.5 Correlation score

The similarity between $\mathbf{F}_{SI}$ and $\mathbf{F}_{emp}$ (Problem 4.4) is computed as the entry-wise Pearson's correlation coefficient r, following previous work [Abdelnour et al., 2014, Goñi et al., 2014, Mišić et al., 2015, Finn et al., 2015, Tipnis et al., 2018]. Denoting $\overset{\triangle}{\mathbf{F}}_{SI}$ (resp. $\overset{\triangle}{\mathbf{F}}_{emp}$) as the vectorized version of the upper triangular part of $\mathbf{F}_{SI}$ (resp. $\mathbf{F}_{emp}$), we define r as

$$r = corr(\overset{\triangle}{\mathbf{F}}_{SI}, \overset{\triangle}{\mathbf{F}}_{emp}) \tag{4.6}$$

4.2.6 Genetic algorithms

Given the combinatorial nature of the optimization Problem 4.4, we must resort to heuristic methods in order to approach optimal solutions, without guarantee of optimality. A convenient choice is the family of genetic algorithms [Wolsey and

Nemhauser, 1999]. The steps involved in the genetic algorithm that we used are *i*) generating a random population of admissible input sets, *ii*) selecting the best input sets in the population, *iii*) breeding a new generation of solutions by crossovers between selected input sets, *iv*) applying random modifications in the new population to avoid getting trapped in a local optimum and *v*) repeating the process until no more improvement is achieved after a given number of iterations. We use the Matlab implementation of genetic algorithms, from the Global Optimization Toolbox, with default options and parameters.

4.2.7 Consensus input set

In order to mitigate the lack of optimality guarantee of genetic algorithms, we compute multiple solutions using random initializations. We define the consensus input set as the set of ROIs selected at least n times. Inspecting the histogram of ROIs selections allows us to set the threshold value n. In our analysis, the distribution of ROIs selections is bimodal (see Appendix A.2.3 for a typical example). Therefore choosing different thresholds n between both modes of the histogram has a limited impact on the results (see Appendix A.2.4). Note that the notion of *consensus input set* used in this chapter is not related to and should not be confused with the concept of *consensus dynamics* between agents in a network [Blondel et al., 2005].

4.2.8 Jaccard index

The Jaccard index J between two sets $\mathcal{S}_1$ and $\mathcal{S}_2$ measures the overlap between these sets and is computed as

$$J(\mathcal{S}_1, \mathcal{S}_2) = \frac{|\mathcal{S}_1 \cap \mathcal{S}_2|}{|\mathcal{S}_1 \cup \mathcal{S}_2|} \tag{4.7}$$

where $J = 0$ indicates no overlap and $J = 1$ indicates a complete overlap. A derivation of the expected value of the Jaccard index of two sets of fixed cardinality is provided in Appendix A.1.5.

4.2.9 Baselines

In order to assess how well our approach maps structure to function, we provide three baseline values.

- **Baseline 1** is the Pearson's correlation coefficient between the vectorized upper-triangular of the adjacency matrix of the connectome $\mathbf{S}$ and the empirical FC matrix $\mathbf{F}_{emp}$, without any transformation.

- To obtain **Baseline 2**, we randomly re-label the ROIs of the connectome matrix $\mathbf{S}$ while keeping $\mathbf{F}_{emp}$ unchanged, and then apply our method. This null-model breaks the ROI-to-ROI correspondence between structure and function and preserves all network properties of the connectome. In particular, it preserves the distribution of weighted degrees and allows us to test whether the selection of control ROIs is exclusively driven by their degree. In the results, we report the maximum correlation score obtained over 30 random re-labellings.

- **Baseline 3** aims to assess the usefulness of solving the optimization Problem 4.4 to identify optimal input sets. We compute the correlation score between $\mathbf{F}_{emp}$ and $\mathbf{F}_{SI}$ obtained with an input set drawn uniformly at random, with cardinality m matching that of optimized input sets. In the results, we report the maximum correlation score obtained over 30 random input sets.

4.2.10 Modal controllability

Given a system defined on a network of N nodes, modal controllability is a nodal property that quantifies the ability of a single node to steer the system towards states requiring substantial input energy [Pasqualetti et al., 2014, Gu et al., 2015, Karrer et al., 2020]. We compute the modal controllability ϕ_i of node i from the eigenvalues λ and the eigenvectors $\mathbf{v}$ of the adjacency matrix $\mathbf{S}$ of the connectome:

$$\phi_i = \sum_{j=1}^{n} \left(1 - \lambda_j^2(\mathbf{S})\right) v_{ij}^2$$

We use the Matlab implementation provided by the authors of [Gu et al., 2015] in order to compute modal controllability.

4.2.11 2D visualization of input sets with t-SNE

In a network of N nodes, we represent an input set as an N-dimensional binary vector indicating which node is selected (1) or not (0). In order to visualise how multiple input sets relate to each other, we apply dimensionality reduction to embed the N-dimensional vectors in two dimensions. In particular, the t-distributed Stochastic Neighbor Embedding [Maaten and Hinton, 2008] aims at finding a low-dimensional representation of high-dimensional vectors while preserving their local structure, such that similar vectors are represented by close points in 2D and vice-versa, with high probability. In this chapter, we use the Jaccard index to measure the similarity between vectors and we use the Matlab implementation of t-SNE.

4.3 Results

We apply our model of structure-informed FC (Equation 4.3) to empirical MRI data of 100 unrelated individuals. In order to identify the control regions (or input nodes ; see Figure 4.1) driving FC on the connectome, we solve Problem 4.4. For each individual, we extract a connectome and FC matrices for resting-state and seven tasks (Figure 4.1B ; see Methods for a description of the tasks). Although the properties of resting-state FC are known to be fundamentally different from that of task FC [Deco et al., 2011], we choose to treat resting-state in the same way as task conditions in order to test whether our approach is able to distinguish it. For simplicity, we refer to both resting-state and task conditions as *states* in the remainder of this chapter.

We provide an illustration of the method based on data simulated from a synthetic example in Figure 4.1C. First, we simulate 2000 time steps of a diffusion process driven by white noise on a graph composed of $N = 10$ nodes ($m = 3$ input nodes), with edge weights uniformly distributed between 0 and 1. Using these time series, we compute the associated FC matrix $\mathbf{F}_{emp}$. Then, we solve Problem 4.4 for U varying from 1 to N. We observe that the method retrieves the correct input set and produces an FC matrix that is similar to the empirical one.

4.3.1 Linking the connectome to multiple functional states

For the group-level analysis, we compute an average connectome and an average FC matrix $\mathbf{F}_{emp}$ for each state (see Methods). In order to study the evolution of our results with respect to the number of input ROIs, we solve Problem 4.4 with U increasing from 1 to N. For each upper bound U, we define the consensus input set as the set of ROIs selected at least 25 times over 30 optimization runs (see Methods). Figure 4.2A shows the correlation score r between $\mathbf{F}_{emp}$ and $\mathbf{F}_{SI}$ using the consensus input set. The curves increase with U, up to small drops due to the heuristic nature of the optimization (see Methods), until they reach a plateau at values ranging from $r = 0.54$ for resting-state to $r = 0.7$ for the motor task. We can compare these values with three baselines (see Methods for details about the baselines definition). The first one is the correlation score between $\mathbf{F}_{emp}$ and the adjacency matrix of the connectome. The second is the plateau correlation obtained by applying our approach to a randomly re-labelled connectome. The third baseline is the maximum correlation score between $\mathbf{F}_{SI}$ and $\mathbf{F}_{emp}$ obtained with random input sets having the same average cardinality as the identified sets. In Figure 4.2A, we draw for each baseline the highest value

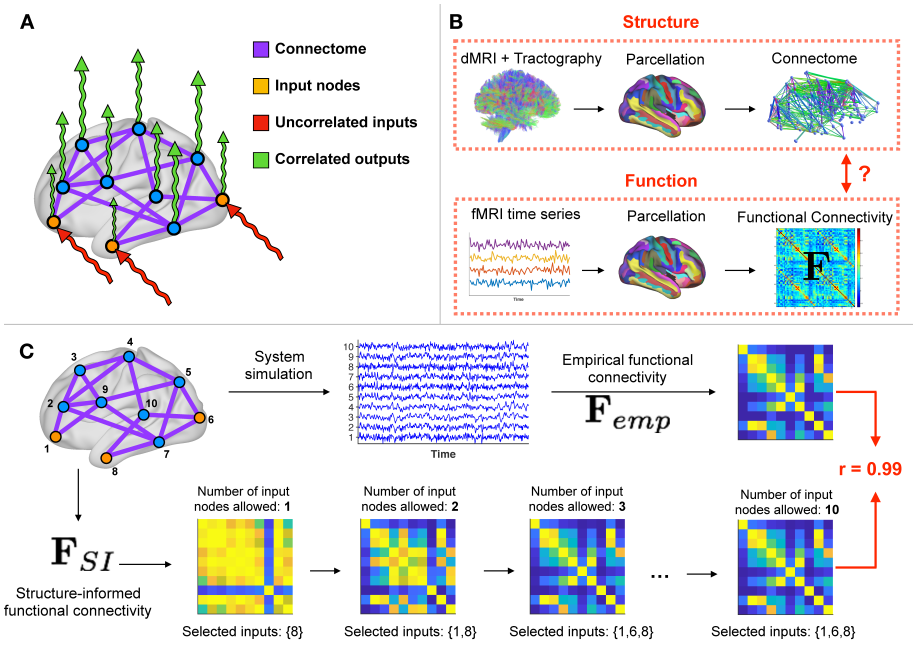

Figure 4.1: **Structure-informed functional connectivity.** **A)** In order to investigate how the connectome shapes functional connectivity, we define a diffusion dynamics on the connectome (purple) and excite it with uncorrelated signals (white noise, red). Depending on the set of input nodes (orange) driving the dynamics, the output signals (green) present correlations patterns that are similar to empirical data. **B)** Data processing workflow. Top row: We extract the connectome using diffusion imaging (dMRI) and tractography. Nodes correspond to Regions of Interest (ROIs) from a predefined automatic parcellation. Bottom row: At each ROI, we also retrieve the fMRI BOLD time series and compute the functional connectivity matrix $\mathbf{F}_{emp}$ between these signals. This step is repeated for 7 tasks and resting-state. **C)** Example on simulated data. We start from a network of $N = 10$ nodes, with uniformly distributed random weights on the edges. Top row: In our synthetic example, we choose a set of $m = 3$ input nodes, simulate the noise diffusion process and compute the 'empirical' functional connectivity matrix $\mathbf{F}_{emp}$. Bottom row: Our model applied to the network identifies the correct set of input nodes and generates a structure-informed functional connectivity matrix $\mathbf{F}_{SI}$ comparable to the empirical one.

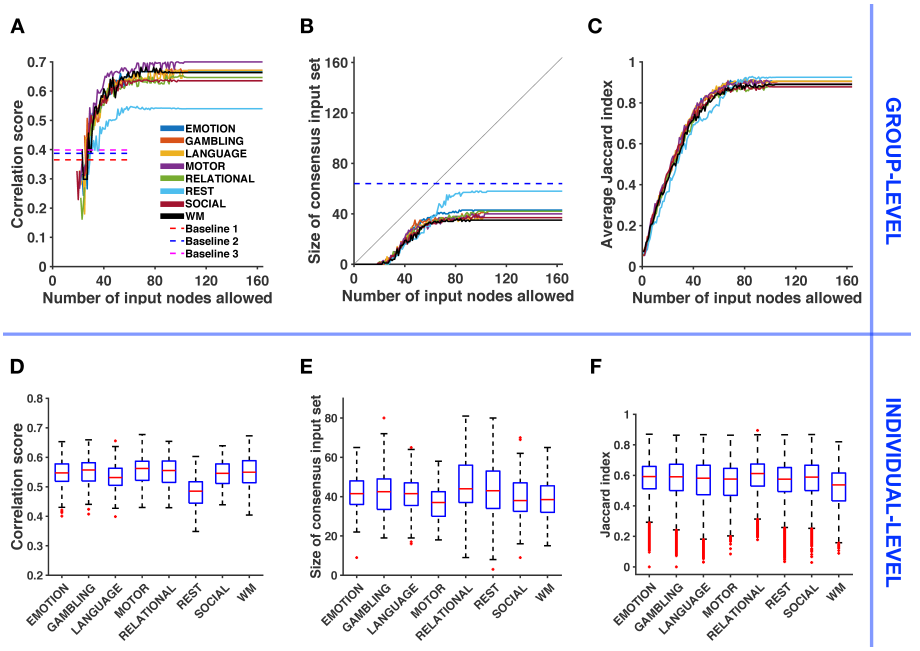

Figure 4.2: **Relating structure-informed and empirical functional connectivity: Group-level analysis and individual-level variability. A)** Correlation score between structure-informed and empirical functional connectivity with respect to the number of input nodes allowed U (group-level). $\mathbf{F}_{SI}$ is obtained using the consensus input set. Dashed lines represent baselines corresponding to the similarity between $\mathbf{F}_{emp}$ and (1) the adjacency matrix of the connectome, (2) $\mathbf{F}_{SI}$ based on a re-labelled connectome and (3) $\mathbf{F}_{SI}$ obtained with a random input set (see Methods). **B)** Size of the consensus input set with respect to the number of input nodes allowed U (group-level). The gray line denotes the identity function $y = x$. The dashed blue line corresponds to the minimum number of input nodes selected for Baseline 2, over all states and all randomizations. **C)** Average Jaccard index between the 30 input sets identified by the optimization algorithm with respect to the number of input nodes allowed U (group-level). **D)** Variability across individuals of the correlation score between structure-informed and empirical correlation matrices, with $U = N$. **E)** Variability of the size of the corresponding consensus input set. **F)** Jaccard index between all pairs ($\frac{100\times99}{2} = 4950$) of consensus input sets (25 selections over 30 runs) across individuals.

across states and see that our approach produces a better matching for all states. Figure 4.2B shows that the consensus input set is empty for all states until we allow the selection of at least 19 input nodes. Then its size stabilizes between $m = 35$ for the working-memory task (WM) and $m = 58$ for resting-state. These values are lower than the number of input nodes selected when applying our approach to a randomly re-labelled connectome (Baseline 2, $m = 64$, minimum across states and randomizations). To evaluate the consistency of identified input sets across optimization runs, we report in Figure 4.2C the evolution of the average Jaccard index $\bar{J}$ (see Methods), computed over all pairs of the 30 optimized input sets. We observe that the method selects consistent input sets ($\bar{J} \geq 0.85$) when $U \geq 70$.

We also perform an individual-level analysis in the following way. As the plateaus observed in Figures 4.2A and 4.2B are also observed for a random sample of 20 individuals (see Appendices A.2.5 and A.2.6), we apply the method to each individual and set $U = N$ in order to reduce the computational cost of the optimization. We obtain one consensus input set and one correlation score for each individual and for each state. In Figure 4.2D, we notice that the correlation scores are lower than at the group-level, for all states. A repeated measures ANOVA determines that the mean correlation score differs significantly between states ($F(7, 693) = 27.928$, $p < 10^{-25}$, Greenhouse-Geisser corrected). The variance in each condition does not significantly differ (Levene's test, $p > 0.5$), and a post-hoc analysis after visual inspection confirms that the mean correlation score in resting-state is significantly different than in any task condition (Tukey's HSD, $p < 0.005$). The post-hoc analysis also reveals that the mean correlation score significantly differs between the language task and the motor task (Tukey's HSD, $p < 0.005$). Figure 4.2E shows the variability of the size of the consensus input set in the population. The relational processing task and the resting-state display a higher variability in the number of input ROIs selected than other states. In Figure 4.2F, we evaluate the variability of the consensus input set *in the population* by computing the Jaccard index J of all pairs of the 100 consensus input sets (one for each individual). We observe a moderate overlap of the consensus input set across individuals (median $J \approx 0.6$, expected value of J for randomly chosen sets with cardinality $m = 40$: $\mathbb{E}\{J\} \approx 0.14$, see Appendix A.1.5 for the derivation). A Friedman test finds that Jaccard indices come from different distributions across tasks ($p < 10^{-244}$).

4.3.2 Analysis of input ROIs across functional subsystems

At the group-level, we turn our attention to the ROIs composing the input sets that we identified. In Figures 4.3A (motor task) and 4.3B (resting-state), we follow

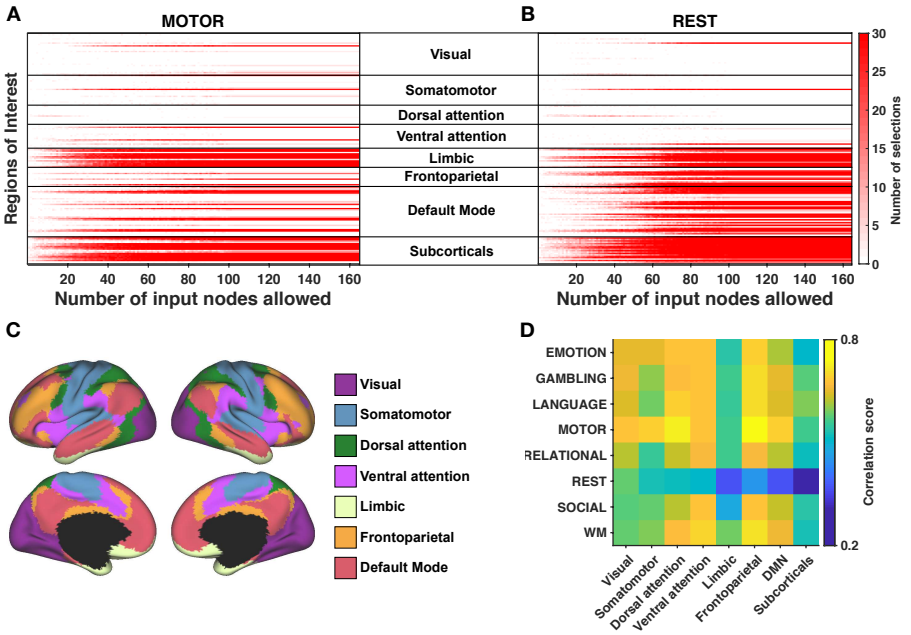

Figure 4.3: **Analysis across functional subsystems (group-level). A, B**) Evolution of the number of selections (from 0-white, to 30-red) of each ROI with respect to the number of input nodes allowed U for the motor task and resting-state. ROIs are arranged according to the functional subsystems described by Yeo and colleagues [Thomas Yeo et al., 2011]. The cerebellum is included in the 'subcorticals' subsystem for visualization and corresponds to the last two lines (left and right hemispheres). Corresponding figures for the other tasks are available in Appendix A.2.7. **C)** Cortical localization of Yeo's subsystems. **D)** Correlation between structure-informed and empirical functional connectivity with $U = N$, splitted into Yeo's subsystems.

the evolution of the number of selections of each ROI when the maximum cardinality U of the input set increases. We point out that when U is incremented, we perform the new optimization runs while ignoring previously computed solutions in order to assess the consistency of successively computed solutions. A first observation is that the selection of input ROIs is stable i.e., once a region is selected it is typically selected again for higher values of U, as indicated by the horizontal red lines. Moreover, dark red pixels for a given ROI indicate that it is consistently selected across 30 independent optimization runs for a fixed U. We make a second observation by grouping ROIs according to the functional subsystems defined by Yeo et al. [Thomas Yeo et al., 2011] and presented in Figure 4.3C (we include the cerebellum in the 'subcortical' subsystem for visualization). Regions belonging to limbic and subcortical subsystems are selected together, up to some exceptions. These observations are also valid for the other tasks (corresponding figures are available in Appendix A.2.7).

Recent studies investigated how the connectome shapes functional connectivity at the level of subsystems and showed that the coupling between structure and function is stronger for some subsystems than others [Mišić et al., 2016, Tipnis et al., 2018, Osmanlıoğlu et al., 2019, Vázquez-Rodríguez et al., 2019, Baum et al., 2020]. In Figure 4.3D, we use the consensus input sets identified at the group-level and compute the correlation score between the entries of $\mathbf{F}_{SI}$ and $\mathbf{F}_{emp}$ associated with the subsystems of Figure 4.3C (see the discussion in Appendix A.1.4). The results indicate that the association is the greatest in the frontoparietal lobe during the motor task ($r = 0.74$). Moreover, the limbic and subcortical subsystems show low correlation scores for all states, while we observe for the resting-state a gradient going from high correlation in primary sensory systems (visual, somatomotor) to low correlation in systems associated with higher-order cognition (limbic, default mode, subcorticals).

4.3.3 Analysis of input ROIs across states

Next, we compare the composition of the identified input sets across states, at the group-level. Since we observed in Figure 4.2A that the correlation score reaches a plateau when U increases, we set $U = N$ for this analysis. Moreover, we increase the number of optimization runs to 100 to evaluate more precisely the selection of each ROI. Thus, we obtain 100 input sets for each condition.

Figure 4.4A depicts the number of selections of each ROI across states. Blue lines indicate ROIs that have been selected at least 90 times for all states. These

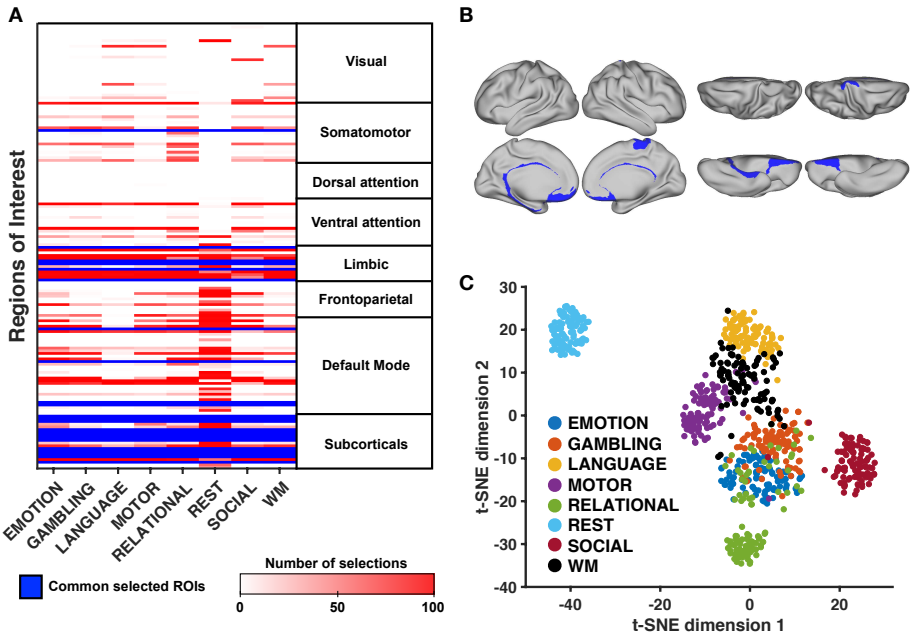

Figure 4.4: **Analysis across functional states. A)** Table summarizing the most frequently selected ROIs for each task. ROIs that are consistently selected at least 90 times over 100 runs for all functional states are highlighted in blue. ROIs are grouped according to Yeo's functional subsystems. The cerebellum is included in the 'subcorticals' subsystem for visualization and corresponds to the last two lines (left and right hemispheres) **B)** Cortical view of ROIs consistently selected across all tasks and resting-state. **C)** Two-dimensional projection of all input sets (100 runs, 8 states). We use the t-distributed Stochastic Neighbor Embedding algorithm (t-SNE, see Methods) in order to visualize the Jaccard similarity among all input sets. Each data point represents one such input set, and their proximity is proportional to their similarity.

ROIs mostly correspond to subcorticals (accumbens nucleus, amygdala, hippocampus, pallidum, thalamus and subcallosal gyrus) and limbic regions (medial orbital sulcus, gyrus rectus and left suborbital sulcus). Regions of the default mode network (pericallosal sulcus, right suborbital sulcus and left posterior-ventral part of the cingulate gyrus) and of the somatomotor system (right paracentral lobule) complete the set of ROIs consistently selected across states. A cortical view of these regions is shown in Figure 4.4B. We observe that most of these regions are located in the midline. Appendix A.3.2 provides the detailed numerical results by ROI.

In order to visualize the divergence of input sets across states, we use a dimensionality reduction method to project in two dimensions the N-dimensional binary vectors indicating which ROIs belong to each input set (t-SNE, see Methods). In Figure 4.4C, each data point represents one identified input set (100 runs, 8 states), and the proximity with each other is indicative of their overlap (Jaccard similarity). We distinguish clusters of points corresponding to different states. In particular, the cluster corresponding to resting-state is isolated. Among task conditions, there is a partial overlap of the clusters, with the input sets related to the social cognition task being more isolated from the others. A comparative cortical view of input ROIs for each state is provided in Figure 4.5.

4.3.4 Topological properties of input ROIs

In order to gain further insight into the topological properties of input ROIs in the connectome, we analyze the statistical association of the number of selections of each ROI with two nodal metrics : the weighted degree and modal controllability. The weighted degree of a node describes the strength of the connections with its neighbors, while modal controllability describes the ability of a node to drive the network towards hard-to-reach states requiring much control energy (see Methods and references: [Pasqualetti et al., 2014, Gu et al., 2015] for further details about modal controllability). For all tasks and resting-state, we report in Table 4.1 the correlation between these nodal metrics and the number of selections of ROIs. On the one hand, we find an inverse relationship between weighted degree and number of selections (lowest association: Spearman's $\rho = -0.3963$ in resting-state, $p < 10^{-7}$ for all states), which suggests that low-degree ROIs are selected more often. On the other hand, we find a direct relationship between modal controllability and number of selections (lowest association: Spearman's $\rho = 0.4769$ in resting-state, $p < 10^{-10}$ for all states), indicating that ROIs having a high modal controllability are selected more frequently. While both associations are significant,

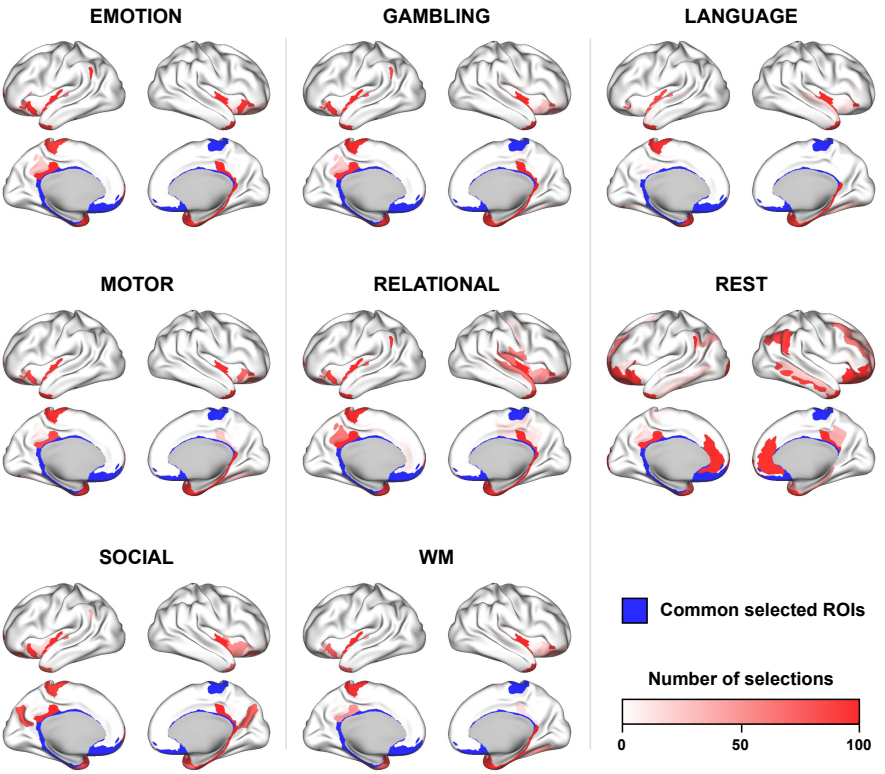

Figure 4.5: **Cortical surface view of state-specific input ROIs.** Over 100 runs of the optimization algorithm with $U = N$, we depict for each state the number of times each ROI is selected. Regions that were consistently selected across all states (≥ 90 selections) are shown in blue. Detailed numerical results by ROI are available in Appendix A.3.2.

Table 4.1: **Topological properties of input ROIs.** Spearman's rank correlation between the number of selections of each ROI (out of 100 independent optimization runs, with $U = N$, group-level) and two nodal coefficients: the strength (weighted degree) and the modal controllability [Pasqualetti et al., 2014]. EMO: emotional processing, GAM: gambling, LAN: language processing, MOT: motor task, REL: relational processing, REST: resting-state, SOC: social cognition, WM: working-memory.

Spearman's ρ	EMO	GAM	LAN	MOT	REL	REST	SOC	WM
Weighted degree	-0.5190	-0.4873	-0.4937	-0.4621	-0.4866	-0.3963	-0.4415	-0.5014
Modal Control	0.6149	0.5767	0.5672	0.5517	0.5803	0.4769	0.5305	0.5801

they are not absolute and they do not prevent the selection of high-degree ROIs such as subcortical structures (see Appendix A.2.1).

We also compare the modal controllability and weighted degree of cortical regions consistently selected across states (in blue, Figures 4.4B and 4.5) with that of other regions. We find that the modal controllability is higher (Wilcoxon rank-sum test, $p < 0.001$) and the weighted degree is lower (Wilcoxon rank-sum test, $p < 0.01$) in these regions.

4.3.5 Robustness of consensus input sets

Finally, we study the robustness of the link between structure-informed ($\mathbf{F}_{SI}$) and empirical ($\mathbf{F}_{emp}$) functional connectivity when the consensus input set is attacked. An attack refers to the removal of a ROI from the initial input set, not from the connectome. We start from the correlations between $\mathbf{F}_{SI}$ and $\mathbf{F}_{emp}$ obtained at the group-level with $U = N$ (Figure 4.2A). We progressively remove nodes from the consensus input set until it becomes empty. After each removal, we compute the correlation score obtained with the attacked input set. Since we previously observed that low-degree (resp. high modal controllability) ROIs are more likely to be part of the input set, the removal ordering is fixed by increasing order of weighted degree (resp. by decreasing order of modal controllability). In addition, we report the results related to 50 random removal sequences.

In Figure 4.6, we show the results for the motor task and the resting-state. We observe that the correlation score between $\mathbf{F}_{SI}$ and $\mathbf{F}_{emp}$ decreases slowly with the number of nodes removed from the consensus input set, no matter the removal ordering. For the motor task (resp. for resting-state), up to 75% (resp. 40%) of the nodes can be removed from the consensus input set before we reach correlation

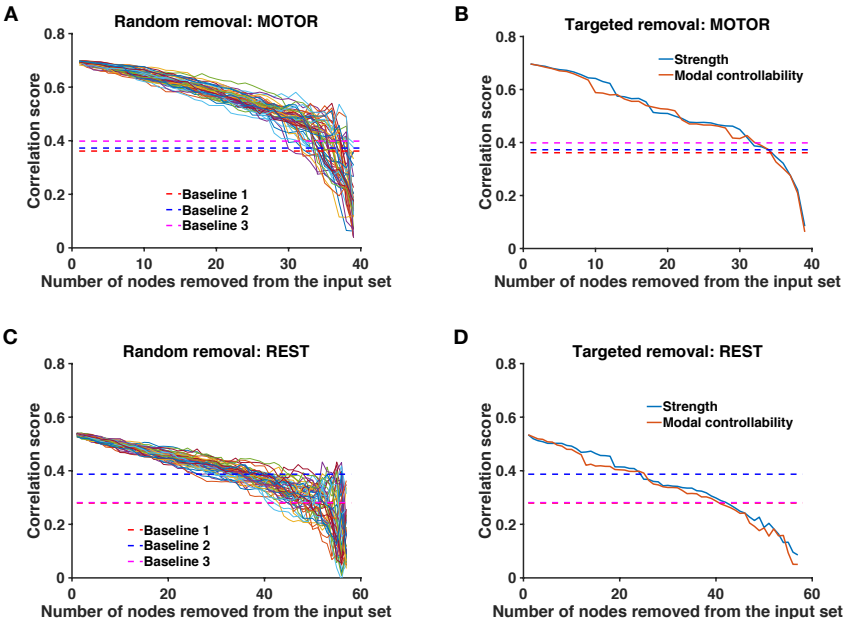

Figure 4.6: **Robustness analysis. A, C)** Evolution of the correlation between structure-informed $\mathbf{F}_{SI}$ and empirical functional connectivity $\mathbf{F}_{emp}$ as a function of the number of ROIs removed from the consensus input set. Dashed lines represent the three baselines (see Methods) i.e., the correlation between $\mathbf{F}_{emp}$ and (i) the adjacency matrix of the connectome, (ii) $\mathbf{F}_{SI}$ based on a re-labelled connectome and (iii) $\mathbf{F}_{SI}$ obtained with a random input set. We consider 50 random removal orderings. **B, D)** Same analysis, with removal ordering fixed by increasing weighted degree and decreasing modal controllability.

scores comparable to the three baselines previously defined (see Methods). Similar observations are valid for the other tasks (see Appendices A.2.9 and A.2.10).

4.4 Discussion

In this chapter, we studied the structure-function relationship in brain networks [Honey et al., 2010, Batista-García-Ramó and Fernández-Verdecia, 2018, Suárez et al., 2020] across different task conditions as well as in resting-state. We showed that functional connectivity (FC) i.e., the coactivations among brain regions, can be explained by the correlations between the activities of these regions resulting from a linear dynamics spreading through the structure of the brain. This model, termed *structure-informed* FC, happens to be mathematically linked to the Gramian matrix used in controllability studies [Pasqualetti et al., 2014, Gu et al., 2015, Karrer et al., 2020]. This provides a novel interpretation of FC in which we can leverage control theory to explain state-specific FC configurations arising from a fixed anatomical architecture. We thus proposed that different groups of regions controlling a diffusion dynamics through the wiring diagram of the brain are responsible for FC matrices corresponding to different states. We introduced a principled approach to test this hypothesis and found that sparse and stable groups of control regions, which partially overlap across states, generate FC matrices that are statistically comparable to empirical ones.

4.4.1 Combining brain communication models and linear controllability

Several models of brain communication dynamics have been proposed in order to map structure and function during resting-state and in the absence of external input signals [Goñi et al., 2014, Seguin et al., 2018, Avena-Koenigsberger et al., 2018, Avena-Koenigsberger et al., 2019]. In parallel, other linear models considered the idea that brain activity can be modulated by external signals and first assumed that all brain regions are input nodes [Galán, 2008, Honey et al., 2009]. Subsequent studies on the controllability of brain networks [Medaglia, 2019] relaxed this assumption and assessed the role of individual input nodes [Gu et al., 2015, Karrer et al., 2020]. Later, the study of brain state transitions pointed out to the theoretical and empirical motivations of considering a set of control regions [Gu et al., 2017]. However, the question of how to identify the control set associated with a given brain state from empirical data remains challenging (see Appendix A.1.1 for a comparison with previous work). Here, we addressed this challenge and proposed a principled method to identify state-specific sets of control regions from empirical

data. We considered a symmetric Laplacian diffusion dynamics following previous work [Abdelnour et al., 2014], though the framework can be applied to other communication dynamics. For instance, we also tested our approach with (i) the random-walk Laplacian instead of the symmetric normalized version or (ii) with the adjacency matrix of the connectome as the transition matrix. We obtained similar results with significant overlap of the computed inputs sets (see Appendix A.3.1 for a comparison). Alternative dynamics including decentralized (i.e. directed) brain communication models [Goñi et al., 2014, Seguin et al., 2018] could provide complementary insights into the structure-function relationship in the human brain.

As in former connectomic studies [Abdelnour et al., 2014, Pasqualetti et al., 2014, Gu et al., 2015, Karrer et al., 2020], our approach relies on linear time-invariant modeling (Equation 4.1). Despite the known non-linearities of neural dynamics [Breakspear, 2017], first-order approximations have been proved useful in capturing various aspects of brain functioning at different spatio-temporal scales [Galán, 2008, Schaub et al., 2015, Yan et al., 2017]. In addition, time-invariance implies that the structure of the system does not evolve over time. Although the white matter architecture evolves over long timescales [Sexton et al., 2014, Tang et al., 2017], significant changes in the topology of the connectome are not expected over the duration of an MRI scan. Assuming linearity and time-invariance allowed us to derive an analytical expression of structure-informed FC (Equation 4.3). Since the heuristic optimization computes this matrix a large number of times in order to find a near-optimal input set, relying on an efficiently solved analytical expression of structure-informed FC rather than simulating the system at each iteration is computationally beneficial, although the computational cost remains a limitation of our framework. In sum, we argue that linear and time-invariant modeling of functional connectivity constitutes a reasonable and computationally tractable approach. Future studies are required to assess how much these assumptions can or should be relaxed in light of more realistic models compatible with the biology.

We considered in this chapter a coarse-grained parcellation spanning the entire brain [Destrieux et al., 2010]. We suggest that the proposed method is also suitable at the level of subregions. For example, future research could investigate control centers in the cerebellum, using a refined and dedicated parcellation of cerebellar nuclei [Diedrichsen et al., 2011]. At the microscale, studies of the controllability of the *C. Elegans* connectome have shown the potential of linear models at the neuronal level [Yan et al., 2017, Towlson and Barabási, 2020]. It has also been reported that the strength of the structure-function relationship in brain networks

is parcellation-dependent [Messé, 2020]. The application of our approach with a coarser whole-brain parcellation (Desikan-Killiany atlas, 84 ROIs, see Appendix A.2.11) produced lower correlation scores but did not invalidate our conclusions. We encourage future research assessing the relevance of the proposed model across parcellations spanning multiple spatial scales.

4.4.2 Well-defined sets of control regions drive state-specific functional connectivity

In our analyses, we identified sparse groups of regions that are thought to support the control of state-specific brain activity. The fact that our method finds such *sparse* input sets (Figure 4.2B) i.e., that empirical FC can be explained more simply from the true connectome structure than from a randomly re-labelled network, suggests the fitness of our model in line with Occam's razor principle. Our model also captured differences between states in terms of their respective input sets (Figure 4.4C), supporting the idea that different states are triggered by partially overlapping yet distinct sets of control regions. Because our approach involves a heuristic optimization algorithm, we assessed the consistency of the identification procedure (Figure 4.3A-B) and the robustness of the identified input sets (Figure 4.6). The slow decrease of the correlation score observed when the optimal input set is eroded, no matter the removal ordering, indicates a redundant and collective effect of the control regions. Moreover, we found that ROIs having low degree and high modal controllability, which are topological properties associated with the brain structure independently of any activation measure, have a higher probability to be part of an input set (Table 4.1). Still, we showed that the selection of control regions was not exclusively driven by those nodal properties of the connectome, since subcortical areas are high-degree nodes consistently selected across states (Figure 4.4A and Appendix A.2.1) and input sets are specific to each functional state (Figure 4.4C). Together, these results suggest that the identified input ROIs play a central role in driving FC across the white matter wiring.

Importantly, this role does not imply that identified ROIs systematically match the active areas traditionally detected in fMRI analyses. For example, the primary motor cortex (M1) is not part of the input set of the motor task (Figure 4.5), although it displays strong activation in the functional data. This activation results from the fact that M1 forms a hub in the motor task, receiving projections from multiple regions, including the somatosensory and parietal cortices as well as premotor areas, and sending output commands to the periphery. This 'centrality' however does not entail that M1 is part of the set of drivers that put the brain

in a state that is suitable for motor control. In this regard, our findings are supported by recent experimental evidence in mice showing that thalamic inputs are essential to drive the motor cortex during movement execution [Sauerbrei et al., 2020]. A similar example is that of Wernicke's area, which was not part of the input set of the language processing task (Figure 4.5) but whose activation is often associated with language understanding. More generally, the fact that drivers are preferentially (but not exclusively) ROIs with low degree and high modal controllability is consistent with the idea that reaching demanding states requires the control of decentralized and distributed areas, which in turn influence the whole system including hubs, such as M1 or Wernicke's area [Liu et al., 2011, Gu et al., 2015, Omrani et al., 2016, Eisenreich et al., 2017, Amico et al., 2019].

In order to gain a better insight into the role of the ROIs that we identified, we turn our attention to the drivers common to all states. The presence of subcortical structures (including basal ganglia, amygdala, hippocampus and thalamus) in the input set of all states is consistent with their strong contribution to whole-brain communication [Bell and Shine, 2016], motor control [Shadmehr and Krakauer, 2008], language processing [Ketteler et al., 2008], reward-related processing [Delgado et al., 2000] and cognition in general [Koziol and Budding, 2009]. Anatomical and physiological evidence established the existence of cortico-subcortical loops supporting functionally segregated systems [Alexander et al., 1986]. Within these loops, which include the anterior cingulate and dorsolateral prefrontal cortices that have been designated as cognitive control centers [Dosenbach et al., 2007, Cole et al., 2013, Power and Petersen, 2013], subcortical structures are thought to modulate the process of action selection, given afferent cortical signals [Koziol and Budding, 2009]. Regarding the other identified regions, we can speculate that their pericallosal situation and their proximity to subcortical regions supports interhemispheric communication and the integration of cortico-subcortical loops [van der Knaap and van der Ham, 2011, Koziol and Budding, 2009]. We provided in our analyses a numerical assessment of their consistency in the context of our model. Their functional relevance remains to be further validated in neurophysiological studies involving tailored experimental protocols, and the present study can guide future research investigating brain regions that underlie task-specific control.

4.4.3 Distinguishing resting-state from task conditions

In this study, we applied our approach to both resting-state and task-based FC without *a priori* distinction, although their properties are different [Deco et al., 2011] and resting-state was the only condition that did not require any active in-

volvement of the individuals. Our method captured the singularity of resting-state in several regards : the matching between structure-informed and empirical FC is lower (Figure 4.2A-D) and requires more input regions (Figure 4.2B-E). Moreover, the input set related to resting-state is distinct from that of task conditions (Figure 4.4C) and includes more regions belonging to the frontoparietal subsystem and to the default mode network (Figure 4.4A).

The larger variability of resting-state connectivity across individuals compared to task-based FC, as individuals are left to wander freely, can influence the significance of the group-level resting-state FC (see Methodological considerations). This could explain the lower correlation score obtained at the group-level (Figure 4.2A). However, we also observed lower correlation scores at the individual-level (Figure 4.2D) and the overlap of consensus input sets across individuals in resting-state is in the same range as other tasks (Figure 4.2F). This suggests that there exists a common set of control ROIs driving resting-state that is detected by our model. Further analyses of these regions at the individual-level are required to validate their physiological role.

The gradient of structure-function coupling observed for the resting-state in Figure 4.3D, from high correlation in primary sensory areas to low correlation in regions associated with more abstract functions, is consistent with recent studies [Preti and Van De Ville, 2019, Vázquez-Rodríguez et al., 2019, Liégeois et al., 2020]. It has been suggested that the stronger correspondence between structure and function in visuomotor networks can support the fast reaction to peripheral inputs [Preti and Van De Ville, 2019], while the structure-function decoupling in transmodal regions can promote their involvement in higher-order cognitive functions [Vázquez-Rodríguez et al., 2019]. During active tasks, the overall structure-function coupling is stronger than in resting-state indicating that the brain anatomy can support a variety of functional configurations that adjust to the ongoing task-demand. Note that we computed the correlation score for subsystems including connections linking different subsystems. Excluding these connections modifies the results reported in Figure 4.3D and the associated interpretation (see Appendix A.1.4).

Accumulating evidence from fMRI studies speculate that resting-state FC forms a 'standard' architecture in which segregated functional subsystems are represented, and which supports the transfer of information related to the implementation of tasks [Greicius et al., 2003, van den Heuvel and Pol, 2010, Thomas Yeo et al., 2011, Deco et al., 2011, Cole et al., 2014, Ito et al., 2017]. This could explain why,

from a controllability viewpoint, our results distinguish rest (the passive, default state) from task conditions (the active, target states). Following the hypothesis that resting-state connectivity supports task implementation, an extension of this study consists in applying our framework to the graph structure defined by resting-state FC instead of the connectome, in order to investigate which brain regions drive the rest-to-task transitions.

4.4.4 Limitations

Our study relies on several methodological choices. In the construction of the connectome matrix, we defined the weight of a structural connection between two regions as the streamline density between these regions i.e., the number of reconstructed streamlines normalized by the size of the ROIs they are linking [Hagmann et al., 2008]. This normalization is used in order to mitigate the bias due to the variable size of ROIs (see Appendix A.1.2). Alternative weightings exist for structural connections, and which one is the most appropriate remains an open question [Oldham et al., 2020]. In the construction of the functional connectivity matrices, we preserved the full length of BOLD time series for each fMRI condition (see Appendix C.2.3). In particular, resting-state has the longest scanning duration, which could partly explain its singular behavior in the results. Future work should investigate the impact of varying fMRI scanning duration. In order to derive the group-level FC matrices, we computed the entry-wise average of individual-level matrices. Other approaches include computing the pairwise correlations of the concatenation of individual-level BOLD time series [Liégeois et al., 2020] or computing the barycenter of individual-level matrices, using the fact that they belong to the manifold of positive semi-definite matrices [Venkatesh et al., 2020]. Finally, our approach assumes that FC is defined as the linear correlation between activity time series. More complex measures of FC, such as partial correlations [Liégeois et al., 2020] or mutual information [Hlinka et al., 2011], could provide complementary insights into the structure-function relationship but would require adjustments in the derivation of structure-informed FC.

4.4.5 Conclusion

This chapter presented a system-theoretic framework for identifying potential state-specific control regions through a model linking structure and function in human brain networks. In this regard, it linked concepts of brain communication dynamics and connectome controllability. We expect that future research, for instance in clinical populations, will further validate the proposed approach by studying the impact of neurological deficits and lesions on the identified control regions.

This work could in turn guide physiological studies investigating the role of particular regions in controlling brain processes. In the next chapter, we apply the structure-informed functional connectivity model in two case studies leveraging control regions in schizophrenia and meditation respectively.

5

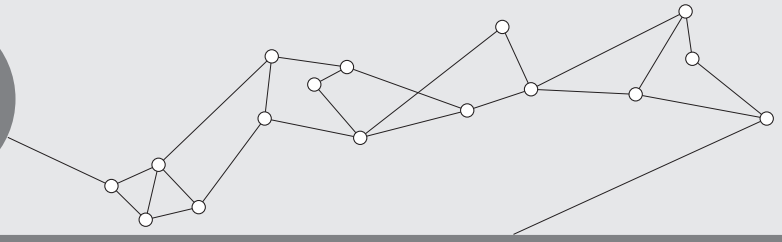

Control Regions in Schizophrenia and Meditation

This chapter in 5 sentences

- **We suggested that** controllability is a fundamental feature allowing brain anatomy to support different functional states thanks to state-specific control regions.
- **Therefore, we wondered if** control regions in the brain could form a signature that allows us to characterize disease-related or deep mental states.
- **In this chapter, we** apply the structure-informed functional connectivity model in order to identify control regions in *i)* schizophrenia and *ii)* meditation.
- **Our results show that** both schizophrenia and meditation are described by control regions that allow their discrimination from baseline conditions.
- **This suggests that** control regions identified by our model form informative features that enable the differentiation of brain states.

The *meditation* dataset investigated in this chapter was provided by Dr. Laurence Dricot (UCLouvain) and Dr. Ron Kupers (UCLouvain) who also participated in the analysis of the results. A manuscript about this chapter is in preparation.

5.1 Introduction

In the previous chapter, we introduced a principled model linking structure and function in human brain networks. The *structure-informed functional connectivity* assumes that a controllable communication dynamics unfolding on the connectome generates Functional Connectivity (FC) patterns comparable to those observed empirically. This model allowed us to identify candidate sets of control regions driving state-specific FC. We numerically assessed the role of these regions and suggested that this model can inform future work studying the mechanisms underlying either brain disorders or particular mental states. In this chapter, we illustrate this application on two case studies investigating control regions *i)* in schizophrenia and *ii)* during meditation.

Schizophrenia is a psychiatric condition characterized by chronic psychosis episodes [Van Os et al., 2010]. In Chapter 3, we used a supervised classification method with feature selection in order to detect brain connections that were most discriminative between patients and healthy controls. The results illustrated that mixing structural and functional connections in the features used for classification was beneficial to the prediction accuracy. Moreover, when computing the *degree of relevance* of brain regions based on the selection rate of their connections, we obtained a set of relevant regions that partially coincides with previously reported regions affected in schizophrenia. Here, we address the same classification problem as in Chapter 3 and we use the control regions identified by structure-informed FC as input features. Our hypothesis is that control regions at rest are different between schizophrenic patients and healthy controls. Because we use the same connectivity data and the same evaluation protocol as in Chapter 3 with features derived from the model introduced in Chapter 4, the analysis presented here allows us to evaluate the relevance of identified control regions in characterizing schizophrenia, and to suggest new hypotheses about the mechanisms driving the syndrome.

In a second application, we investigate control regions supporting meditation in expert practitioners. Meditation refers to a family of complex mental training practices aiming at improving psychological well-being [Tang et al., 2015]. The regular practice of meditation is associated with various health benefits such as stress reduction, improved emotional intelligence or reduced cardiovascular risks [Balaji et al., 2012, Galante et al., 2014, Grossman et al., 2004, Sedlmeier et al., 2012]. Along with the first studies reporting evidence of meditation-induced morphometric differences in gray matter [Lazar et al., 2005, Luders et al., 2009, Hölzel et al.,

2011a, Fox et al., 2014, Pernet et al., 2021], researchers sought to understand the mechanisms supporting meditation [Bærentsen et al., 2010, Hölzel et al., 2011b, Zeidan et al., 2011, Tang et al., 2012, Alexander et al., 2020]. In this regard, we propose here to identify control regions in the connectome of meditators practicing a meditation technique focused on the heart, known as *heartfulness* meditation. We use the control regions identified during resting-state and during meditation as features in order to classify both states. This allows us to derive a set of potential brain regions involved in the control of sustained meditation.

This chapter illustrates two applications of the structure-informed FC model. The results suggest that control regions form informative features that differentiate brain states. For each application, we propose a candidate set of discriminative regions that can guide future studies. Overall, this chapter provides additional numerical evidence of the significance of the control regions identified in our model.

5.2 Materials and Methods

5.2.1 Datasets

Schizophrenia

We use the same dataset as in Chapter 3. Participants are divided into two groups of 27 schizophrenic patients on the one hand and 27 healthy controls on the other hand. The brain parcellation follows the Lausanne multi-scale atlas [Cammoun et al., 2012]. We use the $N = 234$ parcellation in the main analysis and report results for coarser resolutions ($N = 83$ an $N = 129$) in Appendices B.1.1 and B.1.2.

Meditation

The cohort consists of 50 heartfulness meditation practitioners (42.9 $\pm$ 5.6 years old, 26 women). The entire study protocol was submitted to and approved by the Biomedical Ethics Commission of the Université Catholique de Louvain (Belgium). None of the participants had a history of neurological or vascular disease, head injury or alcohol abuse, nor did they display cognitive complaints. Participants could also not have a contraindication for magnetic resonance imaging (MRI). All participants gave a written informed consent.

Brain networks reconstruction (Meditation) Anatomical, diffusion-weighted and functional MRI (resting-state and meditation) scans were acquired for each

participant. The acquisition protocol is detailed in Appendix D.

We processed structural and diffusion-weighted MRI data with QSIprep 0.11.6 [Cieslak et al., 2020], which implements standardized processing pipelines based on Nipype 1.5.1 [Gorgolewski et al., 2011]. The analysis is done for each participant separately. The T1-weighted (T1w) image was corrected for intensity non-uniformity [Tustison et al., 2010] and used as T1w-reference throughout the workflow. The T1w-reference was then skull-stripped and spatially normalized to MNI template [Fonov et al., 2009] through nonlinear registration [Avants et al., 2008]. Brain tissue segmentation of cerebrospinal fluid, white matter and gray matter was performed on the brain-extracted T1w using the FSL Automatic Segmentation Tool (FAST) [Smith et al., 2004, Zhang et al., 2001]. Diffusion-weighted images underwent denoising, distortion correction, head motion correction and registration to the T1w-reference with FSL [Smith et al., 2004]. Probabilistic tractography was performed with MRtrix3 [Tournier et al., 2019]. A single-shell-optimized multi-tissue [Dhollander and Connelly, 2016, Dhollander et al., 2016] constrained spherical deconvolution [Tournier et al., 2004, Tournier et al., 2008] algorithm was used to estimate the Fiber Orientation Distribution (FOD). A second-order integration over the FOD [Tournier et al., 2010] was used to generate a tractogram composed of 10 millions streamlines. A posthoc correction of the tractogram was applied [Smith et al., 2015] in order to obtain a more biologically meaningful representation of white matter tracts. Eventually, we built the adjacency matrix of the structural network by computing the fiber density between each pair of the $N = 246$ Regions of Interest (ROIs) defined by the Brainnetome atlas [Fan et al., 2016]. All matrices were kept unthresholded.

Preprocessing of the fMRI data included linear trend removal to exclude scanner-related signal drift, temporal high-pass filter to remove frequencies lower than 0.005 Hz and correction for head movements. Data was corrected for slice-timing differences, co-registered to the T1w-reference and normalized in the MNI space. Additional preprocessing steps were added to remove non-neural artifacts from the BOLD signals. Regression analyses were performed to remove artifacts due to residual motion (the six movement regressors were obtained via rigid body correction of head motion as implemented in BrainVoyager [Goebel, 2012]) and changes in ventricles. The final data was smoothed in the spatial domain (Gaussian filter: Full Width at Half Maximum = 5mm). We used BrainVoyager and a customized Matlab code to calculate pairwise correlations between the average time-course signals, extracted from the 246 ROIs defined by the Brainnetome atlas [Fan et al., 2016]. All matrices were kept signed and unthresholded.

5.2.2 Structure-informed functional connectivity and control regions

We apply the structure-informed functional connectivity model introduced in Chapter 4 to the preprocessed data. In summary, we define a linear diffusion dynamics driven by control regions on the connectome (i.e., the structural network). The state-correlation matrix of this system forms the structure-informed functional connectivity matrix $\mathbf{F}_{SI}$. We solve an optimization problem in order to identify the set of control regions maximizing the similarity between $\mathbf{F}_{SI}$ and the empirical functional connectivity matrix $\mathbf{F}_{emp}$.

Similarly to the previous chapter, we set the diffusion constant of the dynamics β to the repetition time (TR) of the fMRI acquisition: $\beta = \text{TR}$ (see Equation 4.5). We use a genetic algorithm in order to identify the control regions maximizing the correlation score between $\mathbf{F}_{SI}$ and $\mathbf{F}_{emp}$. We allow the algorithm to select any number of control regions ($U = N$, see Equation 4.4). To mitigate the lack of optimality guarantee of the genetic algorithm, we perform 30 independent optimizations with random initialization. The set of control regions consistently selected over the 30 runs defines the Consensus Input Set (CIS). To determine whether a region belongs to the CIS, we fix a threshold over 30 runs and include regions whose number of selections is above the threshold. Because this parameter is arbitrary, we perform the analysis for thresholds ranging from 21 to 30 selections over runs.

5.2.3 Classification and feature selection

We treat the datasets in separate experiments. From the *Schizophrenia* dataset, we obtain 54 connectomes (27 patients, 27 controls) each associated to one resting-state functional connectivity matrix. This produces 54 CIS and we classify two groups of individuals (patients and controls). From the *Meditation* dataset, we obtain 50 connectomes, each associated with 2 functional matrices (resting-state and meditation). This produces 100 CIS and we classify two conditions (resting-state and meditation).

In order to compare the results with those obtained in Chapter 3 with the *Schizophrenia* dataset, we apply the same supervised classification procedure to N-dimensional *binary* feature vectors indicating identified control regions instead of $\frac{N(N-1)}{2}$-dimensional vectors of real connectivity values. Thus, the binary features

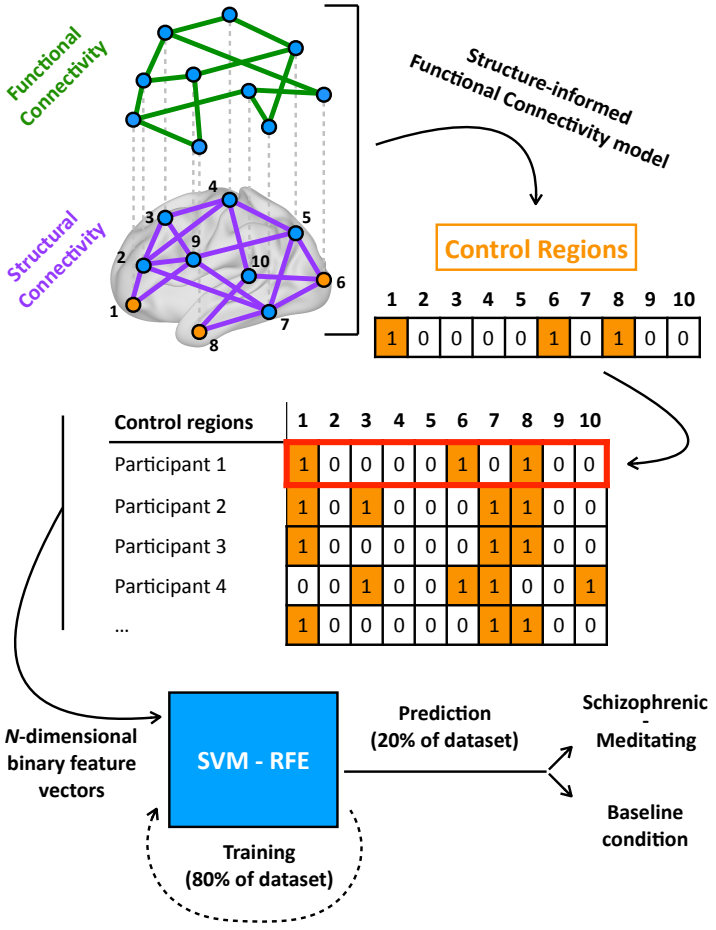

Figure 5.1: **Using control regions as features in a classification problem.** In order to assess the relevance of the control regions identified with the structure-informed functional connectivity model (see Chapter 4), we use them as features in a supervised classification problem. Each participant (or condition) is characterized by a binary vector indicating the control regions maximizing the mapping between her/his connectome (structural connectivity) and functional connectivity. These vectors form a binary data matrix that is passed to a Support Vector Machine (SVM) that uses Recursive Feature Elimination (RFE) for features selection. We use the same evaluation protocol as in Chapter 3, with a training phase on 80% of the dataset and predictions on the remaining 20%. We consider two separate problems: *i)* classifying schizophrenic patients from healthy controls as in Chapter 3 (two groups of participants), and *ii)* classifying the meditative state from the resting-state (one group of participants, two conditions).

that we use only indicate the identity of control regions, not their BOLD activation or any other quantitative measure. We use a nested 5-fold cross-validation to train a Support Vector Machine (SVM) on 80% of the dataset. During the training phase, the Recursive Feature Elimination (RFE) selects the most discriminative regions between the two classes investigated. We predict the class of the samples in the remaining 20% of the dataset. We obtain the prediction accuracy i.e., the proportion of correct predictions, on each fold and we repeat the procedure 20 times. We report the mean accuracy computed over the $5 \times 20 = 100$ test sets. Along with the prediction accuracy, we report the Kuncheva index $\overline{KI}$ [Kuncheva, 2007] that quantifies the feature selection stability (see Chapter 3). In short, $\overline{KI} \in [-1, 1]$ indicates how consistent the selected features are across training phases, with $\overline{KI} = 1$ indicating that features selected for the classification are always the same. Figure 5.1 summarizes the experimental protocol.

5.3 Results

We evaluate the role of the control regions identified by optimization of the structure-informed functional connectivity (see Chapter 4). We test whether they vary *i)* between schizophrenic patients and healthy controls, and *ii)* between resting-state and meditation. We address this problem in a supervised classification framework and use the same evaluation protocol as in Chapter 3.

5.3.1 Schizophrenia

First, we focus on the classification of schizophrenic patients from healthy controls. We consider the $N = 234$ network resolution. Results for coarser resolutions $N = 83$ and $N = 129$ are shown in Appendices B.1.1 and B.1.2 and lead to similar observations. The classes are balanced (27 patients, 27 controls). Along with the classification accuracy on unseen samples, we report the stability of the feature selection as quantified by the Kuncheva index $\overline{KI}$ [Kuncheva, 2007]. This analysis is analogous to that of Chapter 3 with the difference that input features are not connectivity values but binary variables indicating the membership of each region to the Consensus Input Set (CIS) of the individuals. In order to evaluate the sensitivity of the classification results to the definition of the CIS, we consider CIS thresholds ranging from 21 to 30 over 30 optimization runs (see Methods).

Figure 5.2 presents the classification accuracy and the feature selection stability as a function of the number of features (i.e., Regions of Interest, ROIs) selected by the Recursive Feature Elimination (RFE) . The accuracy curves increase from values

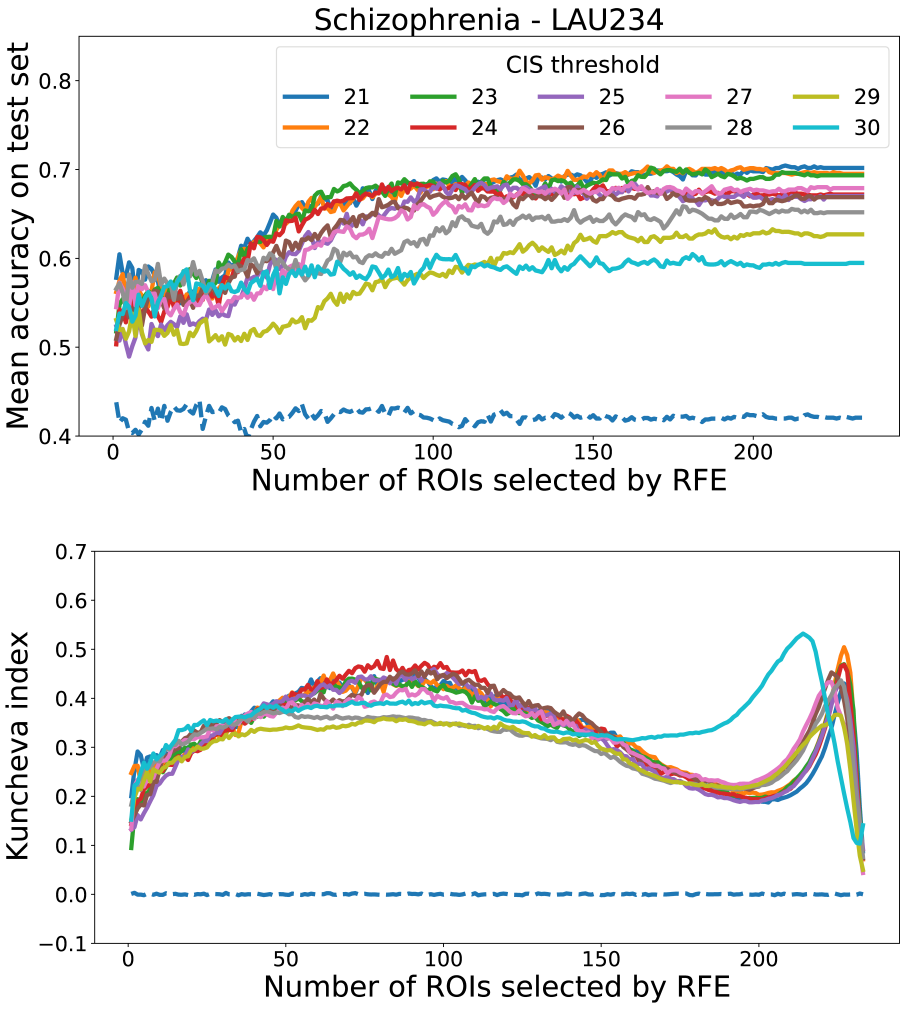

Figure 5.2: **Schizophrenia : Accuracy and stability.** Top: Mean accuracy over 100 test sets (5-fold cross-validation, repeated 20 times) as a function of the number of ROIs (i.e., features) selected by the Recursive Feature Elimination (RFE). Bottom: stability of the set of features selected by RFE, quantified by the Kuncheva index (see Methods), as a function of the number of ROIs selected. In both panels, solid lines correspond to the results obtained with different thresholds defining the Consensus Input Set (CIS, see Methods). The dashed line shows the results obtained with random binary feature vectors.

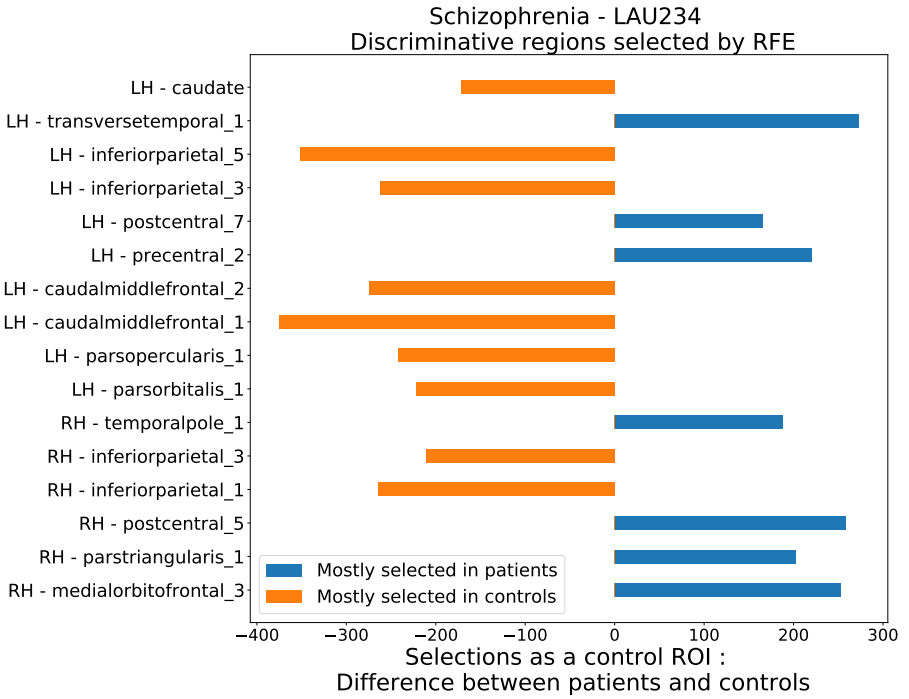

Figure 5.3: **Schizophrenia : Discriminative regions.** The regions listed on the left were selected by RFE in more than 80% of the tests performed and correspond to the most informative ROIs for differentiating both classes. The nomenclature follows the Lausanne multi-scale atlas [Cammoun et al., 2012], which is a finer version of the Desikan-Killiany parcellation [Desikan et al., 2006]. The bar plot indicates in which class these ROIs were selected in majority as control ROIs (maximum difference : 810).

in $[0.49, 0.6]$ until they reach plateau values in $[0.6, 0.71]$ when more than 100 ROIs are selected for the classification. These scores are obtained with N-dimensional binary feature vectors. In comparison, we reached an average accuracy of 0.73 in Chapter 3 with the same parcellation and $(N^2 - N)$-dimensional feature vectors of multimodal connectivity values. We also observe that the threshold defining the CIS influences the maximum accuracy reached by the classifier. In Figure 5.2, lower thresholds produce better scores but we cannot generalize this observation as shown in the results about meditation (see below) and in Appendices B.1.1 and B.1.2. As a control experiment, the classification accuracy obtained with random binary feature vectors varies in $[0.4, 0.45]$. We notice that considering the *inverse* decision of a classifier trained on random binary features would lead to an accuracy close to 0.6. The stability of the feature selection shows a bell-shaped curve between 1 and 200 ROIs selected with a local maximum $\overline{KI} \in [0.35, 0.5]$ varying with the CIS threshold, followed by a peak $\overline{KI} \in [0.38, 0.51]$ between 200 and 234 ROIs selected. These values are comparable to the ones obtained in Chapter 3 with the same parcellation and multimodal connectivity features. By definition, random binary feature vectors are unstable and correspond to $\overline{KI} \sim 0$.

We turn to the characterization of the most discriminative ROIs between schizophrenic patients and healthy controls. We performed the feature selection on 100 training sets, for CIS thresholds ranging from 21 to 30 and for a number of ROIs to select ranging from 1 to $N = 234$. Therefore, each region was possibly selected by RFE $100 \times 10 \times 234$ times in total. Figure 5.3 lists the regions selected more frequently than 80% of the total number of possible selections. This percentage is chosen arbitrarily to extract the most relevant regions. Among the most discriminative regions, we find that the left caudate nucleus and the left inferior parietal cortex overlap with the regions having the highest degree of relevance in Chapter 3. Moreover, the left caudate nucleus, bilateral postcentral, left precentral, left caudal-middle-frontal, left parsopercularis, left parsorbitalis, right parstriangularis and right medial-orbitofrontal regions overlap with the *affected core* identified by Griffa and colleagues [Griffa et al., 2015]. In the optimization of structure-informed FC, we performed 30 optimization runs for each of the 27 patients and 27 controls. In Figure 5.3, the bars indicate for each ROI the difference in the number of selections as control ROI between patients and control, over a theoretical maximum of $30 \times 27 = 810$, which corresponds to a control ROI always selected in one class and never in the other. We observe that the most discriminative regions are divided into control ROIs mostly selected in patients or controls.

5.3.2 Meditation

Motivated by the results obtained in the *Schizophrenia* dataset, we proceed with the classification of meditation with respect to resting-state in order to investigate the control regions driving the meditative state in expert practitioners. The brain parcellation includes $N = 246$ regions [Fan et al., 2016]. We classify two states in the same group of 50 participants. The classes are therefore balanced : 50 'meditation' samples and 50 'resting-state' samples. As in the previous section, we report the stability of the feature selection. We test the same range of thresholds defining the CIS.

Figure 5.4 presents the classification accuracy and the feature selection stability as a function of the number of features (i.e., ROIs) selected by RFE. The accuracy curves rapidly reach a local maximum in the range $[0.62, 0.66]$ when less than 50 ROIs are selected as features for the classification. The CIS threshold has a moderate impact on the accuracy scores. As a control experiment, the classification accuracy obtained with random binary feature vectors varies in $[0.51, 0.57]$. The stability of the feature selection rapidly reaches a maximum value $\overline{KI} \in [0.45, 0.61]$ when about 40 ROIs are selected by RFE and then decreases linearly with the number of ROIs selected. Again, random binary feature vectors are unstable and correspond to $\overline{KI} \sim 0$.

We turn to the characterization of the most discriminative ROIs between meditation and resting-state. We performed the feature selection on 100 training sets, for CIS thresholds ranging from 21 to 30 and for a number of ROIs to select ranging from 1 to $N = 246$. Therefore, each region was possibly selected by RFE $100 \times 10 \times 246$ times in total. Figure 5.5 lists the regions selected more frequently than 80% of the total number of possible selections. In the optimization of structure-informed FC, we performed 30 optimization runs for each of the 50 participants, in resting-state and meditation. In Figure 5.5, the bars indicate for each ROI the difference in the number of selections as control ROI between patients and control, over a theoretical maximum of $30 \times 50 = 1500$. We observe that the most discriminative regions are divided into control ROIs mostly selected in meditation or resting-state. Structures mostly found as control regions in meditation (Figure 5.5, blue) include bilateral thalamic and temporal insular areas, as well as portions of the primary motor cortex (Brodmann area 4).

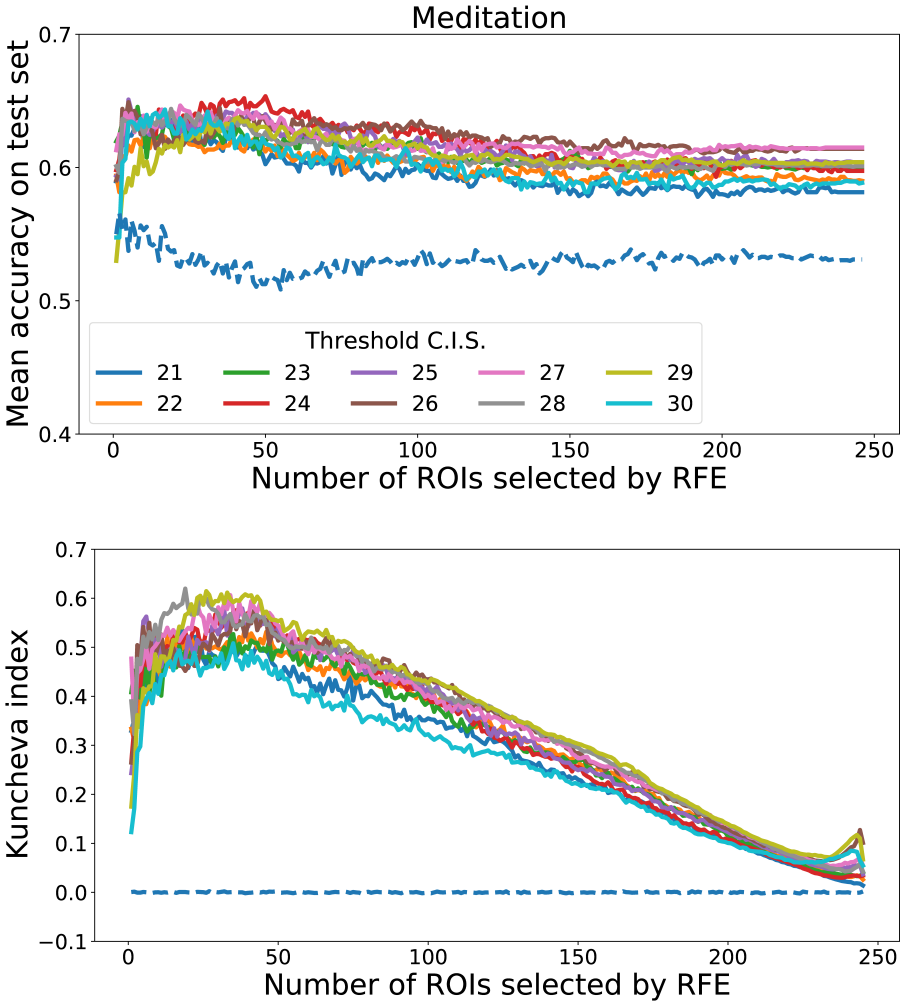

Figure 5.4: **Meditation : Accuracy and stability.** Top: Mean accuracy over 100 test sets (5-fold cross-validation, repeated 20 times) as a function of the number of ROIs (i.e., features) selected by the Recursive Feature Elimination (RFE). Bottom: stability of the set of features selected by RFE, quantified by the Kuncheva index (see Methods), as a function of the number of ROIs selected. In both panels, solid lines correspond to the results obtained with different thresholds defining the Consensus Input Set (CIS, see Methods). The dashed line shows the results obtained with random binary feature vectors.

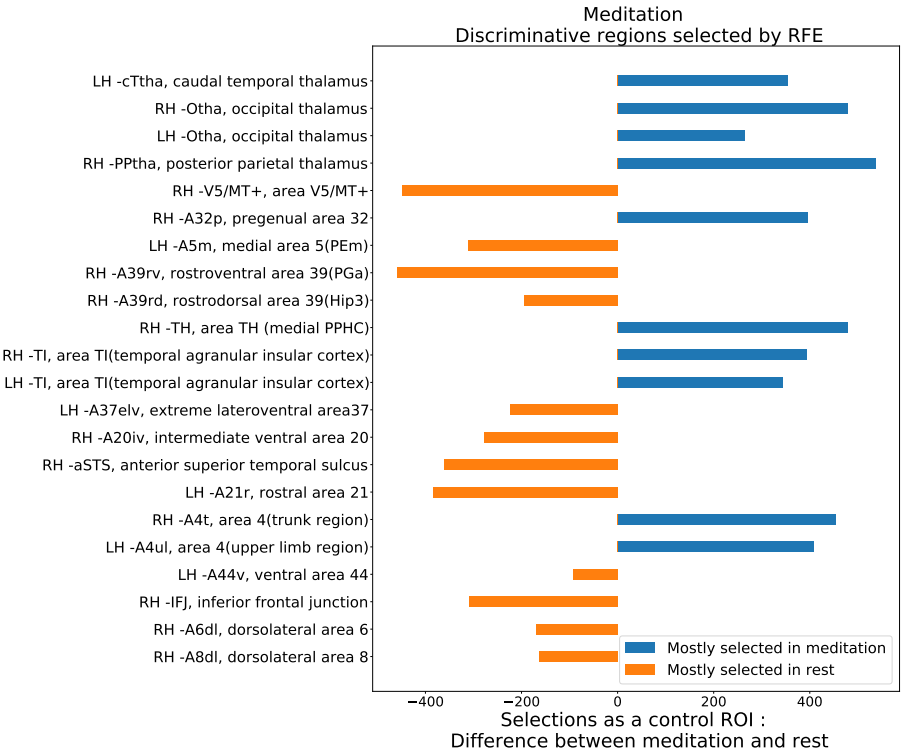

Figure 5.5: **Meditation : Discriminative regions.** The regions listed on the left were selected by RFE in more than 80% of the tests performed and correspond to the most informative ROIs for differentiating both classes. The nomenclature follows the Brainnetome atlas [Fan et al., 2016] and area numbers refer to Brodmann areas. The bar plot indicates in which class these ROIs were selected in majority as control ROIs (maximum difference : 1500).

5.4 Discussion

We assessed the relevance of control regions identified by means of the structure-informed FC model introduced in the previous chapter. We used control regions as features in a machine learning framework in order to classify *i)* schizophrenic patients from healthy controls and *ii)* meditation from resting-state. The results suggest that the identified control regions form a meaningful description of brain states in which the presence or absence of a control region enables the classification of the state, without considering their activation level.

5.4.1 Control regions as fundamental features to describe brain states

The brain is a controllable system [Dosenbach et al., 2007, Medaglia, 2019, Gu et al., 2015]. Based on this observation, we introduced in the previous chapter a model linking structure and state-specific function in brain networks. This model relies on the identification of control regions that describe how the connectome is able to support a particular functional state. In this chapter, we observed that these control regions can be used as features for differentiating schizophrenic patients from healthy controls (Figure 5.2) and meditators in resting-state or during sustained meditation (Figure 5.4). This result confirms the observation made in Chapter 4 that distinct brain states are characterized by distinct control regions (Figure 4.4C). Moreover, it strengthens our hypothesis that structure-informed FC can guide future physiological studies by providing a candidate set of brain regions involved in the neural mechanism under investigation.

In the *Schizophrenia* dataset, the classification accuracy obtained with N-dimensional binary vectors encoding control regions (Figure 5.2) is comparable to the scores obtained in Chapter 3 with $(N^2 - N)$-dimensional vectors of multimodal connectivity values (Figure 3.5). This suggests that control regions enclose important information that helps differentiating patients and controls. We note that the moderate accuracy of 71% does not entail that control regions alone constitute a biomarker of clinical utility. However, we suggest that they can be part of a larger list of biomarkers and that they come with an intelligible interpretation in the context of our model. The observation that a classifier trained on random binary features provides an accuracy that deviates from the 50% chance level (Figure 5.2) is a consequence of the limited size of the dataset, as reported in previous classification experiments [Combrisson and Jerbi, 2015]. The same argument applies to the accuracy of random binary features in meditation (Figure 5.4). We

can expect that better performance will be achieved on larger datasets. In Figure 5.2 we also observed that selecting around 100 over 234 ROIs (or features) for the classification provides a trade-off between prediction accuracy and feature selection stability. This result is consistent with the finding of sparse input sets in the previous chapter, and indicates that few control regions differ between patients and controls. The decrease of the feature selection stability (measured by the Kuncheva index) when more than 100 ROIs are selected suggests that additional ROIs are not informative and are selected interchangeably with others, lowering the overall consistency of the selected features. We note that the decrease in stability is not followed by a decrease in accuracy, suggesting that the classifier ignores these uninformative features. The peak in stability when more than 200 ROIs are selected possibly reflects a priority among uninformative ROIs where a small group of regions are selected after the others, which generates a local agreement in the selection of ~ 220 regions. Overall, the classification results in Figure 5.2 indicate the importance of control regions in differentiating patients and controls. Future work should assess whether including quantitative information about these regions (e.g. their average BOLD activation) instead of restricting ourselves to binary feature vectors would further improve the classification performance.

The most discriminative control regions in schizophrenia (see Figure 5.3) partially overlap with affected regions found in Chapter 3 as well as in the work of Griffa and colleagues [Griffa et al., 2015]. Yet, we should not expect this overlap to be complete because the regions identified here are thought to play a different role compared to previous studies. Similarly to the discussion made in the previous chapter that *control region* is not a synonym of *active region*, we suggest that discriminative control regions are not equivalent to the regions most affected in schizophrenia. Instead, they bring mechanistic information about the effects of the disease under the assumptions of structure-informed FC. Although the physiological role of these regions remains to be validated, we illustrated here the ability of our framework to formulate new hypotheses about the mechanisms underlying a brain condition.

The finding that discriminative control regions in Figure 5.3 are divided into control regions found either in patients or in controls indicates that the two groups are characterized by different control systems rather than by a lower or higher involvement of a unique control system. In other words, the discriminative regions listed in Figure 5.3 were not exclusively selected as control region in one group. This suggests that the connectivity alterations observed in schizophrenia [Lynall et al., 2010, Griffa et al., 2013, Griffa et al., 2015] do not result from the non-

engagement of control regions. Because patients were diagnosed at an advanced stage of the disorder, we can speculate that changes in the resting-state control regions occurred gradually. Longitudinal studies are required to further monitor the variations of control regions with the progression of the symptoms.

5.4.2 Investigating the neural mechanisms of meditation

Meditation has been described as a separate cognitive state of consciousness [Cahn and Polich, 2006, Tang et al., 2015]. The beneficial effects of meditation on health have been demonstrated in several studies [Baer, 2003, Ospina et al., 2007, Balaji et al., 2012, Galante et al., 2014, Sedlmeier et al., 2012] and active research investigates the neural processes supporting meditation [Bærentsen et al., 2010, Tang et al., 2012, Alexander et al., 2020]. In order to inform future work on this topic, we applied the structure-informed FC model and proposed a set of brain areas possibly involved in the control of sustained meditation.

The classification of meditation versus resting-state based on their respective control regions produced significant but moderate accuracy scores (Figure 5.4), which indicates that both states share several common control regions. The feature selection stability reached a peak around 30 selected ROIs and then decreased linearly. These results suggest that the difference between meditation and resting-state lies in the selection of a limited number of control regions.

Importantly, these regions might reflect only one of the two mechanisms supporting the meditative state [Travis and Wallace, 1999, Bærentsen et al., 2010]. Because participants entered the meditative state before the start of the fMRI acquisition (see Methods), the control regions listed in Figure 5.5 should be in charge of *maintaining* meditation but not necessarily of *entering* the meditative state. Future work should investigate the regions triggering the transition from resting-state to meditation using fMRI acquisitions during this transition, which can last several minutes depending on the participants.

Last, in a way similar to schizophrenic patients being diagnosed at an advanced stage of the disorder, meditators recruited in this study were expert practitioners. Note that changes in gray matter density related to meditation were reported as early as after 8 weeks of practice in novice individuals [Hölzel et al., 2011a]. Longitudinal studies could therefore monitor the variations of control regions with meditation practice over limited time periods.

5.4.3 Limitations

In addition to the methodological considerations related to the structure-informed FC model (see Chapter 4), the applications presented here have limitations. First in the *Schizophrenia* dataset, 24 patients out of 27 were under medication at the time of the MRI acquisitions (see Methods). It is not clear what impact this treatment can have on our analysis and the results should be interpreted by taking this element into consideration. Second, the *Meditation* dataset was exclusively composed of individuals practicing a specific type of meditation known as heartfulness meditation. Various meditation styles exist and we encourage future studies to investigate their similarities and differences in terms of control processes. Last, in order to compare our analysis with that of Chapter 3 we used the same machine learning pipeline. Further work should test alternative classification and feature selection methods.

5.4.4 Conclusion

In this chapter we showed that control regions identified by the structure-informed functional connectivity model formed informative features that enable the classification of *i)* schizophrenic patients from healthy controls and *ii)* meditation from resting-state. This work provides further numerical evidence of the relevance of our model mapping structure and state-specific function in brain networks, although physiological validation remains necessary. We encourage future research investigating the role of control regions in order to describe other brain disorders or other cognitive states.

6

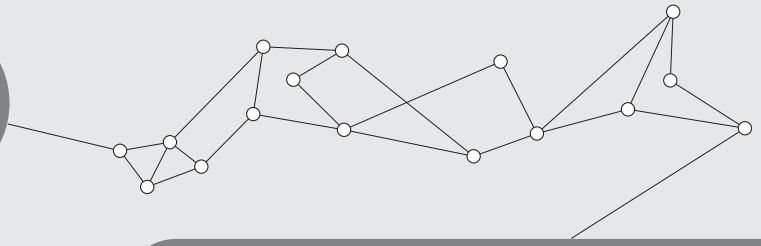

Functional Connectivity Fingerprinting

This chapter in 5 sentences

- **We knew that** functional connectivity contains an individual-specific fingerprint.
- **Therefore, we wondered if** we could improve existing data-driven methods for extracting these fingerprints by leveraging the degree distribution of functional networks.
- **In this chapter, we** apply degree-normalization to functional networks before extracting fingerprints and we evaluate the resulting identifiability with three metrics.
- **Our results show that** degree-normalization improves the three metrics and that extracted fingerprints are embedded in a low-dimensional space.
- **This suggests that** functional fingerprints can be efficiently extracted in order to emphasize individual-specific brain features linked to behavior or disorders.

The content of this chapter is adapted from the following publication:

- **Chiêm, B.**, Abbas, K., Amico, E., Duong-Tran D.A., Crevecoeur, F., & Goñi, J. (2021). Improving Functional Connectome Fingerprinting with Degree-Normalization. Brain Connectivity, *in press*.

6.1 Introduction

The study of brain functional connectivity aims to understand how distributed neural Regions of Interest (ROIs) interact with each other during resting-state and task conditions [Bullmore and Sporns, 2009, Fornito et al., 2016]. Thanks to advances in functional Magnetic Resonance Imaging (fMRI), the measurement of Blood-Oxygenation-Level Dependent (BOLD) signals provides an estimate of brain activity across conditions [Ogawa et al., 1990]. In this context, a widespread approach to quantify functional connectivity is to compute pairwise Pearson's correlation coefficients between BOLD time series measured at each ROI (see Figure 2.6). The resulting symmetric correlation matrix is referred to as a Functional Connectome (FC) and can be understood as the adjacency matrix of a network where nodes are ROIs and edges represent functional interactions between those ROIs [Bullmore and Sporns, 2009, Fornito et al., 2016].

The network analysis of brain connectivity is able to capture important features of cortical organization, such as integration and segregation [Bullmore and Sporns, 2009, Shine et al., 2016, Shine et al., 2018, Shine et al., 2019], as well as modularity [Sporns and Betzel, 2016, Betzel et al., 2016, Betzel et al., 2019, Puxeddu et al., 2020]. Furthermore, FCs have been used in the study of several brain disorders [Fornito et al., 2015] such as schizophrenia [Micheloyannis et al., 2006, Lynall et al., 2010, Gutiérrez-Gómez et al., 2020] and Alzheimer's disease [Supekar et al., 2008, Svaldi et al., 2019]. Several studies demonstrated the existence of a fingerprint embedded in individual-level neuroimaging data, allowing participant identification in test-retest settings. Various types of descriptors have been investigated in order to uncover brain fingerprints, ranging from anatomical features [Valizadeh et al., 2018] and morphometric measures [Wachinger et al., 2015] to white matter fiber trajectories [Kumar et al., 2017] and multimodal embeddings [Kumar et al., 2018]. In parallel to these non-connectomic studies, a growing interest in the brain fingerprint specific to functional networks has emerged with the motivation that functional connectivity describes in a simple form the intrinsic brain organization across several tasks [Finn et al., 2015, Gratton et al., 2018, Mars et al., 2018, Satterthwaite et al., 2018, Pallarés et al., 2018, Liu et al., 2018, Iturria-Medina et al., 2018, Seitzman et al., 2019, Menon and Krishnamurthy, 2019]. This fingerprint can be extracted through data driven procedures [Amico and Goñi, 2018, Byrge and Kennedy, 2019] as well as reproduced across sites [Bari et al., 2019]. These findings have important implications in the perspective of individual-level functional connectivity analysis. For instance, personalized medicine in the study of brain disorders can benefit from FCs revealing robust individual traits [Iturria-Medina

et al., 2018, Svaldi et al., 2019]. Moreover, participant identifiability across test-retest fMRI sessions has recently been proposed as an indicator of scan reliability for both researchers and clinicians, provided that appropriate and possibly complementary fingerprinting metrics are investigated [Milham et al., 2020]. In sum, uncovering meaningful brain fingerprints enables a shift from population-level research to individual-based scientific investigation and clinical examination.

As recently shown [Rajapandian et al., 2020], fingerprints are also reflected in different network properties of FCs. To characterize the topology of functional networks, several networks statistics have been introduced [Rubinov and Sporns, 2010]. One of the most fundamental measures for binary networks is the degree of a node i.e., the number of nodes it is connected to. In weighted networks, the weighted degree (or strength) of a node is the sum of the weights of its neighboring edges. The weighted degree sequence denotes the vector gathering the weighted degree of all nodes in the network.

Here we show the benefits of applying a mathematical operation, known as degree-normalization, to FCs prior to extracting functional connectivity fingerprints. Degree-normalization uses the information encoded in the weighted degree sequence in order to reduce the weight of edges lying between strongly connected nodes (hubs) comparatively to others, thereby balancing their excessive influence in the network. This operation has been applied in previous studies on weighted communicability measures of networks [Crofts and Higham, 2009, Estrada et al., 2012, Rajapandian et al., 2020] as well as in the study of random walks on networks through the use of the normalized Laplacian [Lambiotte et al., 2014]. We adopt the differential identifiability framework recently developed by Amico and Goñi for FC fingerprinting [Amico and Goñi, 2018] based on a Principal Component Analysis (PCA) decomposition-reconstruction procedure. Because computing the absolute value of FCs is an intermediate step required prior to applying degree-normalization, we compare the results of this framework applied on *i*) the original (signed) FCs, *ii*) the FCs taken in absolute value and *iii*) the degree-normalized FCs. In order to assess the quality of the fingerprint extraction, we consider two previously introduced metrics, namely differential identifiability [Amico and Goñi, 2018] and identification rate [Finn et al., 2015], and we introduce a variant of the latter called matching rate. Our results show that degree-normalization improves the fingerprinting scores for all metrics and that reconstructing the corresponding optimally identifiable FCs requires fewer principal components compared to original FCs. We also highlight the difference in the interpretation of the identification rate and the matching rate and argue that the latter provides a more robust depiction

of the individual fingerprint in FCs.

6.2 Materials and Methods

6.2.1 Dataset

We included 409 unrelated individuals from the Human Connectome Project (HCP) 1200-participants release [Van Essen et al., 2013]. This subset of unrelated individuals was chosen from the overall dataset to ensure that no two participants have a shared parent. The criterion to exclude siblings (whether they share one or both parents) was crucial to avoid confounding effects in our analyses due to family-structure. Data from resting-state (REST) and seven functional Magnetic Resonance Imaging (fMRI) tasks were used: emotional processing, gambling, language, motor, relational processing, social cognition and working-memory (see section 4.2.2 for a description of the tasks). In this chapter, we will collectively refer to the resting-state and all the tasks as conditions.

For each condition, subjects underwent two sessions corresponding to two different phase-encoding directions (left-to-right and right-to-left). The resting-state fMRI scans were acquired on two different days with a total of four sessions. In this study, we used the two sessions from the first day. The HCP scanning protocol was approved by the Institutional Review Board at Washington University in St. Louis. Full details on the HCP dataset have been published previously [Van Essen et al., 2012, Glasser et al., 2013, Smith et al., 2013].

The brain atlas used in this chapter is the multimodal parcellation MMP1.0 proposed by Glasser et al. [Glasser et al., 2016] and comprising 180 cortical regions by hemisphere. For completeness, we added 14 subcortical regions (covering the bilateral striatum, thalamus, hippocampus and amygdala) provided by the HCP release, for a total of $N = 374$ Regions of Interest (ROIs).

6.2.2 Preprocessing

We used the minimally preprocessed data provided by the HCP [Glasser et al., 2013]. This pipeline includes artifacts removal, motion correction, and registration to standard template. Full details on this pipeline can be found in earlier publications [Glasser et al., 2013, Smith et al., 2013]. In addition, we applied the following processing steps to the extracted BOLD signals. For resting-state fMRI data: *i*) we regressed out the global gray-matter signal from the voxel time

courses [Power et al., 2014], *ii*) we applied a bandpass first-order Butterworth filter in the forward and reverse directions (0.001Hz to 0.08Hz ; Python function `filtfilt` from the Scipy package v1.2.1), and *iii*) the voxel time courses were z-scored and then averaged per brain region, excluding any outlier time points that were outside of 3 standard deviations from the mean (Workbench software, command `-cifti-parcellate`). For task fMRI data, we applied the same steps, with a larger frequency range for the band-pass filter (0.001Hz to 0.25Hz) since the relationship between different tasks and optimal frequency ranges is still unclear [Cole et al., 2014].

6.2.3 Degree-normalization of a functional connectome

We compute a functional connectivity matrix $\mathbf{F}$ as the $N \times N$ matrix of pairwise Pearson's correlation coefficients between the N regional BOLD time series:

$$\mathbf{F} = [\mathbf{F}_{ij}] \tag{6.1}$$

where $\mathbf{F}_{ij} \in [-1, 1]$ and $\mathbf{F}_{ij} = \mathbf{F}_{ji}$. Without loss of generality, we ignore self-loops in the functional network by setting $\mathbf{F}_{ii} = 0$. This matrix, which we denote as the *Baseline FC*, can be directly treated as the adjacency matrix of a weighted, undirected and signed network, as done in previous fingerprinting studies [Finn et al., 2015, Amico and Goñi, 2018]. In this chapter, we also consider the unsigned version in order to avoid the occurrence of complex numbers due to the degree-normalization (see below). This is done by taking the entry-wise absolute value of correlation coefficients in $\mathbf{F}$. We denote this as the *Absolute FC*, $|\mathbf{F}|$, with entries verifying $|\mathbf{F}|_{ij} \in [0, 1]$.

The degree d_i of node i of an unsigned network is defined as the sum of the weights of its neighboring edges :

$$d_i = \sum_{j=1}^{N} |\mathbf{F}|_{ij} \tag{6.2}$$

The degree matrix $\mathbf{D}$ is the $N \times N$ matrix containing the degree sequence on its diagonal, and zeros elsewhere:

$$\mathbf{D}_{ii} = d_i \tag{6.3}$$

$$\mathbf{D}_{ij} = 0, \forall i \neq j \tag{6.4}$$

The degree-normalization of $|\mathbf{F}|$ is mathematically defined as follows:

$$\mathcal{F} = \mathbf{D}^{-1/2}|\mathbf{F}|\mathbf{D}^{-1/2} \tag{6.5}$$

The resulting matrix $\mathcal{F}$ is symmetric and corresponds to the adjacency matrix of the *Normalized FC* [Crofts and Higham, 2009, Estrada et al., 2012] where any excessive influence of nodes has been modulated by their corresponding weighted degree. Figure 6.1 summarizes the degree-normalization procedure. It is worth noting that degree-normalization on signed networks would potentially involve negative node degrees (Equation 6.2), which would in turn generate complex entries in the normalized FCs (Equation 6.5). Ignoring complex values or separating the node degrees into positive and negative components before applying degree-normalization did not provide better results than those presented in this chapter (results not shown). For this reason, we restrict our analysis to the degree-normalization of unsigned FCs i.e., FCs taken in absolute value.

6.2.4 Functional connectome fingerprinting

We analyse each fMRI condition separately. In order to quantify the variability of our results in the population, we use sampling without replacement. We generate 100 random subsamples out of the 409 individuals in the database to obtain 100 datasets containing $K = 327$ (80% of 409) different individuals. For each condition, the dataset is composed of $2K = 654$ FCs i.e., two FCs per individual corresponding to the two fMRI phase-encoding directions. Thus, we have for each individual a test FC and a retest FC. In order to extract functional connectivity fingerprints from this dataset, we adopt the differential identifiability framework based on group-level Principal Component Analysis (PCA) [Amico and Goñi, 2018]. In summary, the procedure consists in vectorizing the upper-triangular part (excluding diagonal values) of all FCs in the dataset, and then gathering these vectors in a data matrix of $\frac{N(N-1)}{2}$ rows associated to FC entries, and $2K$ columns associated to test-retest scans of each individual (see Figure 2.9). Following the PCA decomposition of this matrix, FCs are reconstructed using an incrementally increasing number of components, selected in decreasing order of explained variance.

For each number of components, we compute the identifiability matrix $\mathbf{E} \in [-1, 1]^{K\times K}$. The element $\mathbf{E}_{ij}$ is the entry-wise Pearson's correlation coefficient between the test FC of individual i and the retest FC of individual j. Therefore, the diagonal elements $\mathbf{E}_{ii}$ represent the individuals' self-similarity between test and retest, while off-diagonal elements represent between-individuals similarities. Importantly, this means that $\mathbf{E}$ is not symmetric. Intuitively, the higher the

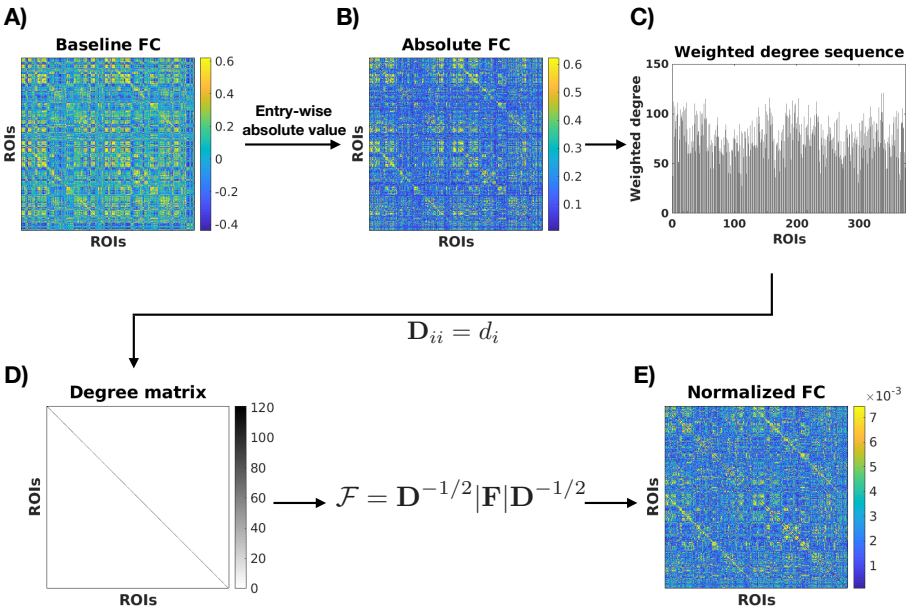

Figure 6.1: **Degree-normalization of a Functional Connectome (FC). A)** A functional connectome is computed as a matrix of pairwise Pearson's correlation coefficients between regional BOLD time series. Hence all values in the *Baseline FC* are within the range $[-1, 1]$. **B)** The next step consists of taking the absolute value of all entries, which produces the *Absolute FC*, denoted by $|\mathbf{F}|$. **C)** From that unsigned FC, we can extract the weighted degree sequence. **D)** The degree matrix is a square matrix containing the weighted degree sequence on its diagonal and zeros elsewhere. **E)** Finally, we apply degree-normalization (Equation 6.5) to obtain the *Normalized FC*.

contrast between diagonal and off-diagonal elements, the better are the extracted fingerprints.

6.2.5 Quantifying the level of identifiability

We consider three metrics to estimate the amount of fingerprint in each subsample: the differential identifiability (I_{diff}), the identification rate (ID_{rate}) and the matching rate (M_{rate}). Let $I_{self} = \langle \mathbf{E}_{ii} \rangle$ denote the average of the diagonal elements of the identifiability matrix and let $I_{others} = \langle \mathbf{E}_{ij} \rangle$, $i \neq j$ be the average of the off-diagonal elements. The differential identifiability score [Amico and Goñi, 2018] is then defined as

$$I_{diff} = 100 \cdot (I_{self} - I_{others}) \tag{6.6}$$

Each time a diagonal element $\mathbf{E}_{ii}$ is the highest of its row, we state that individual i's retest FC has been correctly identified on the basis of her/his test FC. The identification rate [Finn et al., 2015] is then

$$ID_{rate} = \frac{\text{Number of correctly identified individuals}}{\text{Total number of individuals}} \tag{6.7}$$

As we can also compute this metric column-wise (i.e. test FC identified from retest FC), we report the average of row-wise and column-wise ID_{rate}. Note that as per Finn et al. [Finn et al., 2015], ID_{rate} is a procedure with replacement, such that the algorithm is not forced to identify a unique subject on each iteration within a condition.

It might happen that the test FC of an individual i is most similar not only to its own retest FC, but also to that of other individuals. In the extreme case of an FC being highly similar to many others, this will negatively impact the identification rate since many individuals will not be correctly identified. To remedy this, we propose a variant of identification rate, called matching rate (M_{rate}), where every time an FC from test session is matched with a retest FC (or vice versa) using the highest value of correlation along a row (or column) of an identifiability matrix, the matched test-retest pair is removed before the next comparison is made. In other words, M_{rate} is equivalent to ID_{rate} but without replacement. This way, all FCs are matched only once, no matter if they are similar to many others or not.

6.2.6 Control experiment : Surrogate degree-normalization

In this chapter, we evaluate the impact of normalizing each FC by its own degree sequence. As a control experiment, we also report the results of normalizing each FC by the degree sequence of a surrogate individual chosen uniformly at random, a process denoted as *surrogate degree-normalization*. Mathematically, this comes down to performing the fingerprinting analysis with the following normalized FCs for individual u with surrogate v:

$$\mathcal{F}_{u,\text{surr}} = \mathbf{D}_v^{-1/2} |\mathbf{F}|_u \mathbf{D}_v^{-1/2} \tag{6.8}$$

Here, $|\mathbf{F}|_u$ is the absolute FC of individual u, $\mathbf{D}_v$ is the degree matrix of individual v and $\mathcal{F}_{u,\text{surr}}$ is the surrogate-normalized FC of individual u. Surrogate individuals were assigned uniformly at random, with the constraint that an individual cannot be associated with her/his own degree sequence. This permutation was preserved for both test and retest FCs, as well as across fMRI conditions. The ordering of brain regions in the surrogate degree sequence was preserved. In this chapter, normalizing an FC by its own degree sequence is sometimes referred to as *self degree-normalization* to avoid any ambiguity with surrogate degree-normalization.

6.2.7 Statistical comparison between modalities

In order to assess the difference of fingerprinting scores obtained with baseline, absolute, surrogate-normalized and self-normalized FCs (denoted together as modalities), we compute for each fingerprinting metric (I_{diff}, ID_{rate} and M_{rate}) and each modality the optimal score for the 100 subsamples of the dataset. Then, we perform paired t-tests in order to compare these optimal scores between modalities (significance level: $\alpha = 0.005$). We perform the analogous analysis in order to compare the number of principal components corresponding to the optimal fingerprinting scores.

6.3 Results

We apply the differential identifiability framework [Amico and Goñi, 2018] to baseline, absolute and normalized FCs. We compute three metrics : differential identifiability score (I_{diff}), identification rate (ID_{rate}) and the newly introduced matching rate (M_{rate}). The analysis is done for each fMRI condition separately, and performed independently on the 100 randomly drawn subsamples.

Degree-normalization modulates the influence of high- and low-degree regions of functional connectomes. In order to provide insight into the brain regions most affected by degree-normalization, Appendices C.2.1 and C.2.2 show information about the brain regions with the highest and lowest average weighted degrees, for each fMRI condition. In addition, cortical visualizations of the mean and standard deviation of regional weighted degree across individuals are shown in Appendices C.1.2 and C.1.3.

Figure 6.2 presents the results related to differential identifiability (I_{diff}). We observe that the evolution of I_{diff} with respect to the number of principal components used for FCs reconstruction is concave, with sharper curves in the case of normalized FCs, for all fMRI conditions. Figure 6.2D compares the optimal value of differential identifiability reached for baseline, absolute, surrogate-normalized and self-normalized FCs. We see that absolute and surrogate-normalized FCs achieve better scores than baselines FCs, for all conditions except the emotional processing task. Self-normalized FCs provide the best I_{diff} scores for all fMRI conditions, with an average gain of 9.6% between baseline and self-normalized FCs (minimum gain: 7.9% for emotion ; maximum gain: 10.73% for working memory). When comparing the effect of self-normalization with respect to surrogate-normalization for each fMRI condition, Figure 6.2D shows that the former systematically led to significantly higher I_{diff} values than the latter ($p < 0.005$). We notice however that in resting-state, surrogate degree-normalization leads to I_{diff} values that are close to that of self degree-normalization. Figure 6.2E shows the number of principal components corresponding to the optimal I_{diff} values of Figure 6.2D. We observe that absolute and surrogate-normalized FCs require fewer components than baseline FCs, for all conditions except the language processing task and the working memory task for which baseline FCs and absolute FCs require a similar number of components. Self-normalized FCs require the lowest number of components for most conditions, with the exceptions of the gambling task, the relational processing task and resting-state for which the surrogate and self degree-normalization require a comparable number of components.

Figure 6.3 reports the behavior of I_{self} and I_{others}. As shown in Figure 6.2, when looking at I_{diff}, self-normalization systematically performs better than surrogate-normalization (null model) for all fMRI conditions. Hence for this analysis, we focus on baseline, absolute and self-normalized FCs. Overall, both I_{self} and I_{others} decrease with the number of principal components kept for FCs reconstruction. However, we observe for normalized FCs that I_{others} decreases faster than I_{self} in the first 200 components. This observation is valid for all fMRI conditions.

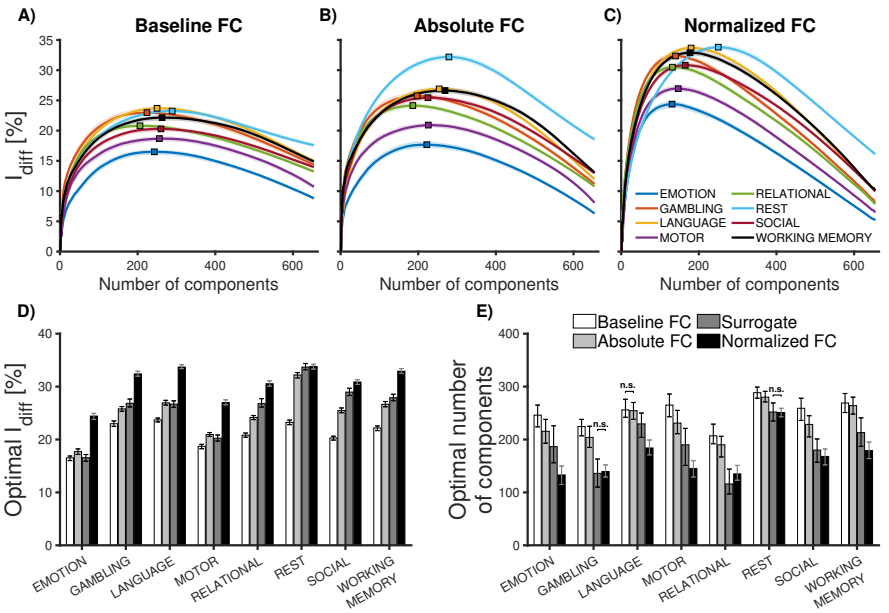

Figure 6.2: **Impact of degree-normalization on differential identifiability.** Panels **A)**, **B)** and **C)** present the evolution of I_{diff} with respect to the number of principal components used for FCs reconstruction, for baseline, absolute and normalized FCs respectively. Solid lines represent the median value across 100 random subsamples (without replacement) of the database and shaded areas correspond to the inter-percentile range (2.5 and 97.5 percentiles). Note that the inter-percentile range is sometimes small enough that the shaded area is hidden by the solid line. Square symbols highlight the optimum I_{diff} of the median curves.**D)** Comparison of optimal I_{diff} values for baseline, absolute, surrogate-normalized and self-normalized FCs. Error bars show the inter-percentile range (2.5 and 97.5 percentiles) across 100 random subsamples of the database. **E)** Number of principal components corresponding to the optimal I_{diff} values of panel D). Pairs of bars highlighted by 'n.s.' indicate paired t-tests that are not significant at the level $p < 0.005$.

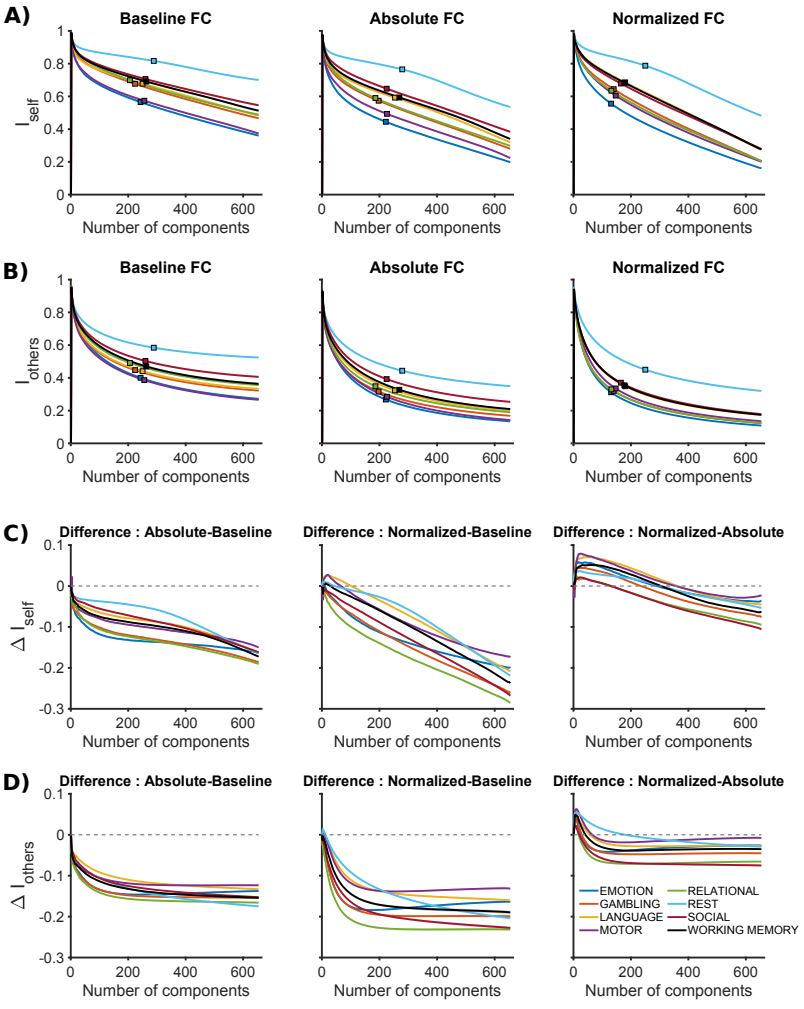

Figure 6.3: **Impact of degree-normalization on I_{self} and I_{others}. A)** Evolution of I_{self} with the number of principal components added in descending order of explained variance for Baseline (left), Absolute (middle) and Normalized FC (right). Panel **B)** shows the analogous figures for I_{others} . Optimal number of components for maximizing I_{diff} are shown as square symbols in all cases. **C)** Evolution of ΔI_{self}, which is the pointwise I_{self} difference between Baseline, Absolute or Normalized FC along principal components. Panel **D)** shows the analogous analysis for ΔI_{others} . In all plots of the figure, solid lines represent the median value across 100 random subsamples (without replacement) of the database and shaded areas correspond to the inter-percentile range (2.5 and 97.5 percentiles). Note that the inter-percentile range is sometimes small enough that the shaded area is hidden by the solid line.

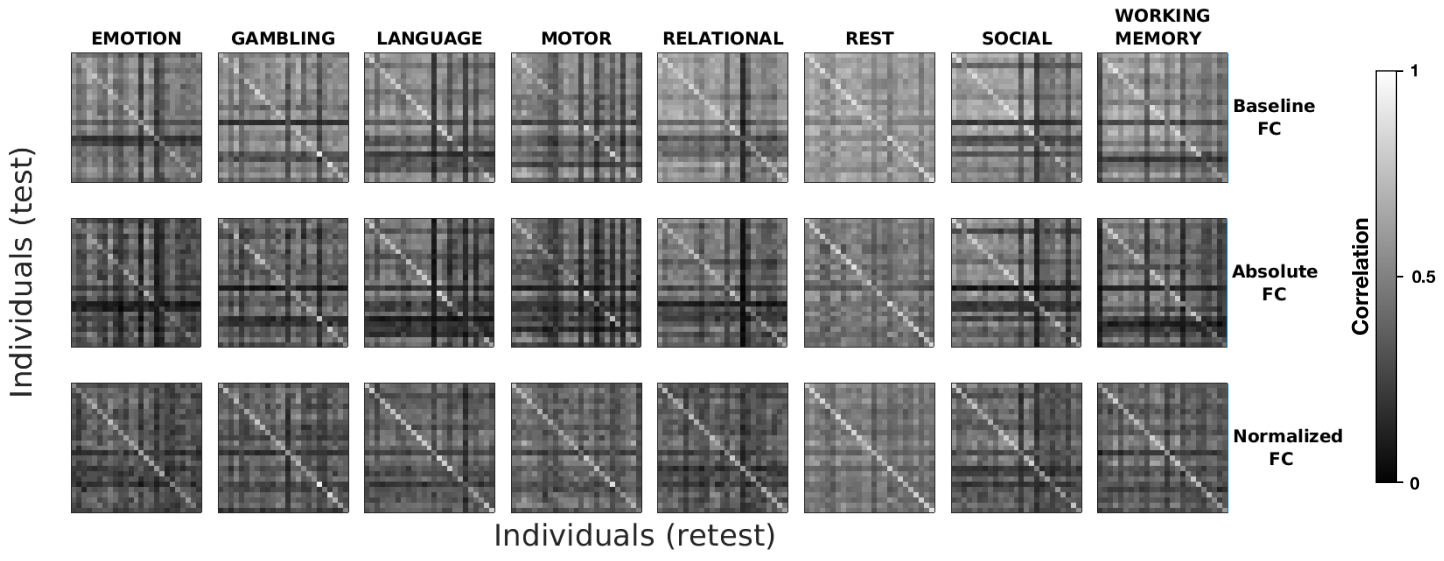

Figure 6.4: **Impact of degree-normalization on identifiability matrices.** Top row: Identifiability matrices obtained with the baselines FCs at the optimal I_{diff} value, for all fMRI conditions. For visualization purposes, only 25 randomly selected individuals of one subsample of the database are displayed. Middle and bottom rows show the same analysis for absolute and self-normalized FCs respectively.

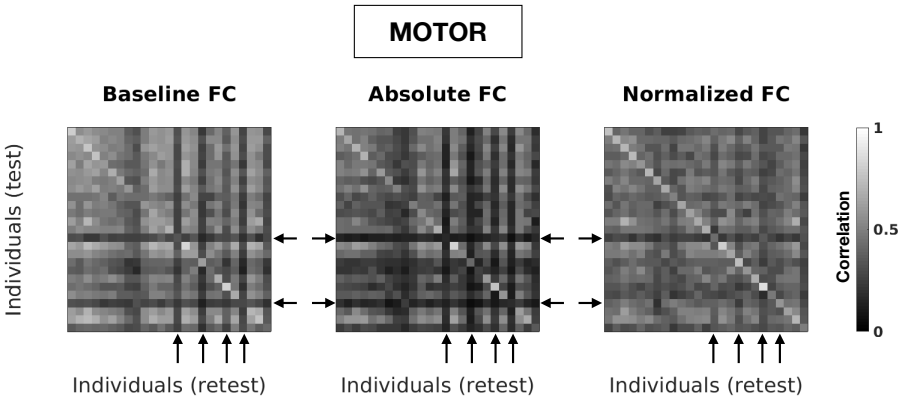

Figure 6.5: **Degree-normalization corrects the profile of outlier FCs.** Zoom on the panels of Figure 6.4 related to the motor task. Arrows highlight typical examples of FCs that are very different to any other FC in the cohort. Note that this effect is alleviated after degree-normalization.

In Figure 6.4, we display identifiability matrices obtained with baseline, absolute and normalized FCs, at the optimal I_{diff} reconstruction point. We observe that diagonal elements stand out in all cases, indicating that individuals' self-similarity is correctly captured. Moreover, we see that degree-normalization smooths the distribution of off-diagonal elements while maintaining a good contrast with diagonal elements. Figure 6.5 highlights, for the motor task as an example, how degree-normalization is able to correct the identifiability profile of some individuals.

Figure 6.6 presents the results related to the identification rate (ID_{rate}). The ID_{rate} curves are concave with a sudden rise in the last 50 components, for all fMRI conditions. This phenomenon is particularly pronounced for normalized FCs and highlights a shortcoming of the identification rate metric. As shown in Appendix C.1.1, the identification rate is driven down by a few FCs being highly similar to others when around 600 principal components out of 654 are used for reconstruction. The last components then correct this bias. Figure 6.6D compares the optimal identification rates reached for baseline, absolute, surrogate-normalized and self-normalized FCs. We see that baseline and absolute FCs provide comparable results, while surrogate-normalization lowers the identification with respect to baseline FCs, for all conditions. Self-normalized FCs provide the best identification rates for all conditions, with an average gain of 16% with respect to baseline FCs (minimum gain: 6% for resting-state ; maximum gain: 30% for the motor task). Figure 6.6E shows the number of principal components corresponding to

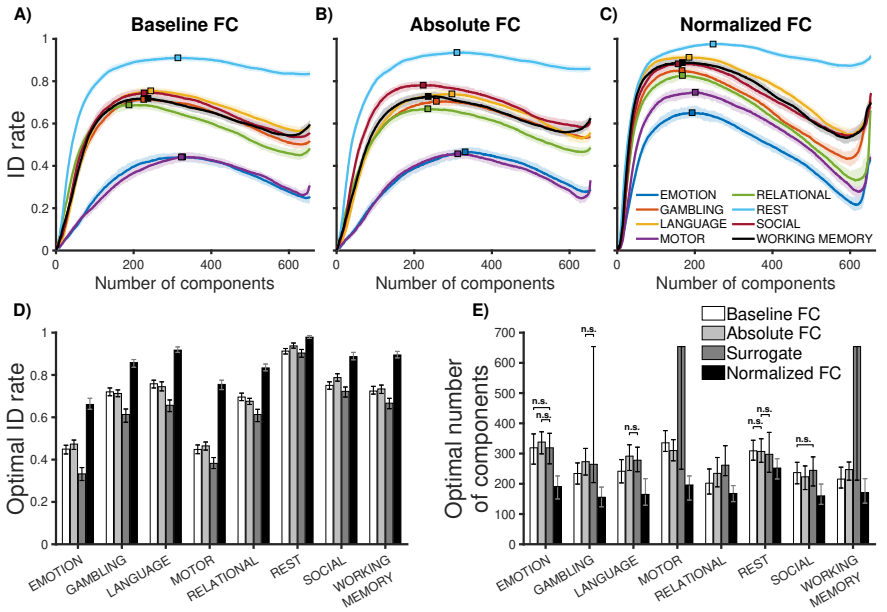

Figure 6.6: **Impact of degree-normalization on identification rate.** Panels **A)**, **B)** and **C)** present the evolution of ID_{rate} with respect to the number of principal components used for FCs reconstruction, for baseline, absolute and normalized FCs respectively. Solid lines represent the median value across 100 random subsamples (without replacement) of the database and shaded areas correspond to the inter-percentile range (2.5 and 97.5 percentiles). The inter-percentile range is sometimes small enough that the shaded area is hidden by the solid line. Square symbols highlight the optimum ID_{rate} of median curves. **D)** Comparison of optimal identification rates for baseline, absolute, surrogate-normalized and normalized FCs. Error bars show the inter-percentile range (2.5 and 97.5 percentiles) across 100 random subsamples of the database. **E)** Number of principal components corresponding to the optimal identification rates of panel D). Pairs of bars highlighted by 'n.s.' indicate paired t-tests that are not significant at the level $p < 0.005$.

the optimal identification rates of Figure 6.6D. We see that self-normalized FCs require the lowest number of components, for all fMRI conditions. We observe large error bars ($2.5 - 97.5$ inter-percentile range across 100 random subsamples) in the case of surrogate-normalized FCs for the gambling task, the motor task and the working memory task. This comes from the fact that in the realization of sampling without replacement, the highest ID_{rate} is sometimes reached using all the components and sometimes with around 200 components, leading to a bimodal distribution of the optimal number of components. Ultimately, this produces large error bars. This phenomenon occurs regularly with surrogate degree-normalization.

Figure 6.7 presents the results related to the matching rate (M_{rate}). The M_{rate} curves increase quickly until they reach a plateau value, except for the emotional processing and the motor tasks with baseline and absolute FCs. Importantly, the sudden rise in the last few components observed with identification rate does not occur with matching rate. Figure 6.7D compares the optimal matching rates reached for baseline, absolute, surrogate-normalized and self-normalized FCs. The observations made for the identification rate are still valid for the matching rate. Self-normalized FCs provide the best matching rates for all conditions, with an average gain of 14% with respect to baseline FCs (minimum gain: 5% for resting-state ; maximum gain: 22% for the motor task). Figure 6.7E shows the number of principal components corresponding to the values shown in Figure 6.7D. We see that normalized FCs require the lowest number of components, for all fMRI conditions. The large error bars (2.5-97.5 inter-percentile range across 100 random subsamples) for all conditions and all FCs are the result of the noisy plateau behavior of M_{rate} curves. Indeed, depending on the subsample, the optimal matching rate can be achieved in a large range of number of components although its actual value remains stable.

6.4 Discussion

Extracting fingerprints from Functional Connectomes (FCs) is an important challenge for future individual-level studies of functional connectivity. This can be achieved through the decomposition of functional connectivity data into principal components in order to remove noisy components that deteriorate fingerprinting scores. Here, we showed that the degree-normalization of FCs improves the fingerprinting process, according to three different metrics: differential identifiability, identification rate and matching rate. Moreover, the results indicate that the fingerprint of degree-normalized FCs is embedded in a lower-dimensional space compared to baseline FCs.

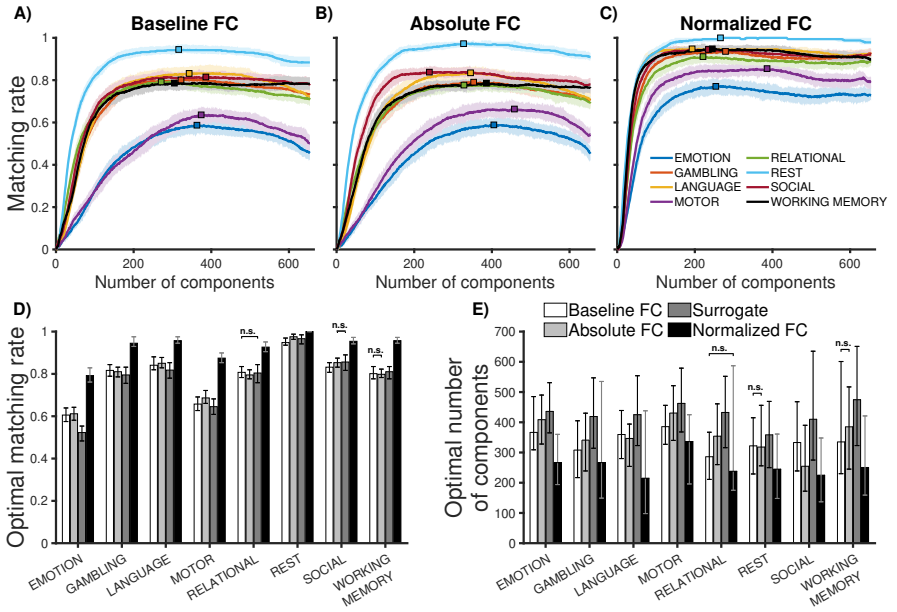

Figure 6.7: **Impact of degree-normalization on matching rate.** Panels **A)**, **B)** and **C)** present the evolution of M_{rate} with respect to the number of PCA components used for FCs reconstruction, for baseline, absolute and normalized FCs respectively. Solid lines represent the median value across 100 random subsamples of the database and shaded areas correspond to the inter-percentile range (2.5 and 97.5 percentiles). Square symbols highlight the optimum M_{rate} of median curves. **D)** Comparison of optimal matching rates for baseline, absolute, surrogate-normalized and normalized FCs. Error bars show the inter-percentile range (2.5 and 97.5 percentiles) across 100 random subsamples of the database. **E)** Number of PCA components corresponding to the optimal matching rates of panel D). Pairs of bars highlighted by 'n.s.' indicate paired t-tests that are not significant at the level $p < 0.005$.

6.4.1 Improved fingerprinting in a lower-dimensional space

Throughout our results, we observed that normalizing FCs improves the three fingerprinting scores considered in this chapter (Figures 6.2D, 6.6D and 6.7D), for all fMRI conditions. Importantly, this improvement was not driven by the participants' head motion (see Appendix C.1.4). Instead, such normalization provides a modulation (or a balance) of the influence of different brain regions that enhance subject-level fingerprints. This is achieved by accounting for the weighted degree sequence in the functional connectomes. The brain regions most affected by the degree-normalization, listed in Appendices C.2.1 and C.2.2, are the most strongly or weakly connected in each fMRI condition. The former are cortical hubs predominantly belonging to the visual and default mode networks while the latter are mostly subcortical regions, consistently with previous reports [Buckner et al., 2009, Tomasi and Volkow, 2011, Schaefer et al., 2014]. Moreover, the improved fingerprinting scores are achieved with fewer principal components than in the baseline and absolute cases (Figures 6.2E, 6.6E and 6.7E). This suggests that the degree-normalization reduces the individuals' fingerprints to a limited number of principal components (in descending order of explained variance). In addition, when looking at the cumulative percentage of explained variance of the principal components extracted from the dataset (Appendix C.1.5), we observe a reduced dominance effect. In other words, the individual contribution of components to the explained variance is more homogeneous. Together, these results indicate that the variance preserved by the components of normalized FCs, although lower, is highly specific to the contrast between individuals. From this perspective, degree-normalization could be beneficial for future FC fingerprinting research.

6.4.2 Surrogate degree-normalization improves differential identifiability, but not identification rate or matching rate

Figure 6.2 shows that differential identifiability is improved after degree-normalization for several conditions, no matter if the correspondence between FCs and their respective degree sequence is preserved (self-normalization) or not (surrogate-normalization). Normalizing FCs has a global effect of lowering the influence of hubs in the network [Crofts and Higham, 2009, Estrada et al., 2012, Rajapandian et al., 2020], which in turn allows better fingerprints to be extracted. This suggests that individual-specific components of functional connectivity might lie (in part) in sparsely connected areas whose contribution to the whole network is brought out by degree-normalization. The fact that surrogate degree-normalization sometimes improves differential identifiability compared to baseline indicates that the weighted degree sequence of FCs is similar across individuals. In Appendix C.1.6, we show

the results of the differential identifiability framework applied on degree sequences instead of functional connectivity matrices. We see that the weighted degree sequence alone imparts a moderate fingerprinting power no matter the number of components kept for the reconstruction, which was previously reported [Rajapandian et al., 2020]. However, matching FCs with their own degree sequence for degree-normalization appears to be beneficial to all metrics and all fMRI conditions, while surrogate-normalization has a null or negative effect on the identification rate and the matching rate, compared to baseline (Figures 6.2D, 6.6D and 6.7D). This indicates that the normalization of FCs by their respective weighted degree sequence helps uncovering fingerprints and suggests a synergistic effect that goes beyond the fingerprints of original FCs and degree sequences separately.

6.4.3 Matching rate as a correction of identification rate

In this chapter, we observed that the identification rate metric, which has been used in several previous studies [Finn et al., 2015, Amico and Goñi, 2018], is sometimes driven down by a few individuals being highly similar to many others (Figure 6.6C and Appendix C.1.1). This entails that the identification rate of an entire dataset can be compromised by a few or even one subject or single session of an otherwise high-quality fingerprinting dataset. Post-hoc investigations on those particular FCs significantly dropping ID_{rate} values showed that no obvious quality issues were present on the correlation matrices or their corresponding histograms (see Appendix C.1.7 for two examples). In order to take into account the reality that each individual in our setting appears only once in each of the test and retest datasets, we introduced the matching rate metric. We noticed that the matching rate results are characterized by a plateau value (Figures 6.7A, 6.7B and 6.7C) rather than a concave behavior with a well-defined maximum, as obtained with differential identifiability and identification rate (Figures 6.2A, B, C and 6.6A, B, C). This suggests that, from the perspective of the matching rate metric, the PCA decomposition does not uncover functional connectivity fingerprints, but rather detects the dimensionality to which the data can be compressed while preserving an optimal fingerprinting power.

6.4.4 Pros and cons of different fingerprinting metrics

As discussed in the previous section, while surrogate degree-normalization increases I_{diff}, its effects on ID_{rate} and M_{rate} are either neutral or negative, when compared to Baseline FCs. This highlights the limitations of I_{diff} as a metric, where we see that even though surrogate degree-normalization has improved the overall contrast between self- and between-subject similarity (increased I_{diff}), its effects on the

self-similarity are mostly negative (null or decreased ID_{rate} and M_{rate}). On the other hand, we have discussed in section 6.4.3 the limitations of ID_{rate} as a metric, where it can be severely affected by one or a few subjects/sessions of FCs that have high similarity with the rest of the population, hiding the underlying fingerprint of the dataset. This problem can be alleviated using M_{rate} instead of ID_{rate}. At the same time, we observed (Figure 6.7) that M_{rate} does not provide enough variation with number of principal components to find an optimal point of reconstruction in the differential identifiability framework. These observations highlight that we should use more than one (preferably all three) metrics to estimate the level of fingerprint in a dataset to avoid any unforeseen pitfalls. In other words, these three metrics represent a different facet of the fingerprint in a sample of FCs.

6.4.5 Limitations

The work presented in this chapter has several limitations. First, we chose to keep for each condition the total number of fMRI volumes available in the database. Previous work reported that larger numbers of frames can positively impact fingerprinting metrics [Amico and Goñi, 2018, Abbas et al., 2020b]. Here, as different scanning durations were used for each condition (see Appendix C.2.3), our results should be interpreted in light of this limitation. Future work should investigate whether degree-normalization is beneficial to fingerprinting studies using short scanning durations. Additionally, the effect of degree-normalization during functional reconfiguration could be assessed in scanning sessions that combine resting periods and tasks [Amico et al., 2020].

Second, we conducted our experiments on a single dataset and used a particular brain parcellation. In order to evaluate the variability of our results with respect to variations in the dataset, we used sampling without replacement. Future work should reassess the impact of degree-normalization on external datasets, possibly obtained with different preprocessing pipelines [Parkes et al., 2018]. We are confident that the results presented here are generalizable to other datasets and parcellations, since the other fingerprinting frameworks have been shown to be reproducible across fMRI conditions [Finn et al., 2015], robust across brain atlases [Amico and Goñi, 2018, Abbas et al., 2020a], and across scanning sites [Bari et al., 2019]. Future work should include the assessment of this framework for studying brain injuries and neurological disorders.

Third, we identified an optimal set of principal components specific to each subsample, restricting the possibility of extracting the fingerprint of an unseen individual outside this sample with the same components. Further investigation is required in order to assess the possibility to derive a 'universal' set of principal

components [Sripada et al., 2019] on which one could project a new FC in order to directly obtain its fingerprint. Initial efforts in this direction have been done by applying a leave-one-out strategy in multi-site test-retest scenarios [Bari et al., 2019]. A thorough investigation on this important topic would possibly require a significantly larger cohort and involve multi-site, multi-scanner fMRI acquisitions. On a related note, future work should evaluate how optimized fingerprinting metrics scale with a very large number of individuals and should address possible privacy concerns.

Lastly, in the construction of the identifiability matrix, we considered the statistical similarity between reconstructed FCs, operationalized by the entry-wise Pearson's correlation coefficient. In contrast, recent studies recommended considering the geometric similarity of FCs, leveraging the observation that signed FCs lie on the manifold of positive semi-definite matrices and are therefore associated with a geodesic distance [Venkatesh et al., 2020, Abbas et al., 2020b]. However, we note that taking functional connectivity in absolute value, as required by the degree-normalization, breaks the positive semi-definiteness of FCs and therefore proscribes the geometric approach. Besides, the degree-normalization procedure is parameterless whereas the geometric approach involves a dataset-dependent regularization parameter [Abbas et al., 2020b]. Overall, we suggest that future work should consider statistical or geometric similarity depending on the context and application of the study.

6.4.6 Conclusion

Fingerprints extraction from Functional Connectomes (FCs) is an important step towards refined individual-level studies of brain connectivity, with potential applications in personalized medicine. In this chapter, we showed that the degree-normalization of FCs is a simple, parameterless mathematical operation producing significant improvements of the fingerprinting quality, according to three different metrics, in resting-state and several task conditions. Furthermore, we argued that the fingerprint of FCs can be compressed in a low dimensional space, especially thanks to degree-normalization. We also showed the potential benefits and pitfalls of three different fingerprinting metrics, where each of them uncovers different aspects of the fingerprint present in a sample of FCs. Overall, our results suggest that applying degree-normalization to FCs can be beneficial for future research focused on individual differences in brain networks.

7

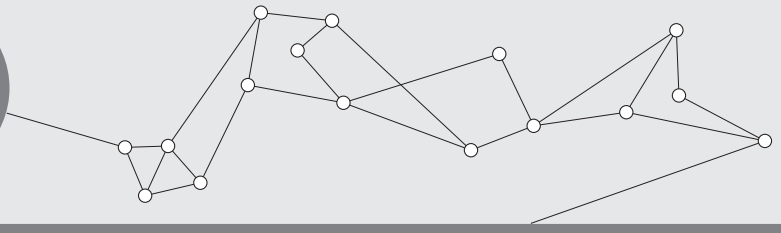

Exploring Brain Interactions with Transfer Entropy

This chapter in 5 sentences

- **We knew that** the exchange of information in the brain is directed and evolves with time during the execution of a task.
- **Therefore, we wondered if** we could build a network of directed and time-resolved brain interactions without assumption on the dynamical model governing the information transfer.
- **In this chapter, we** apply an information theoretic measure known as Transfer Entropy (TE) both on a synthetic example and on brain signals recorded during a motor task.
- **Our results show that** TE successfully detects non-linear, time-varying and delayed interactions in the synthetic example but identifies multiple significant interaction delays between the motor cortex and the muscles of the hand, which hinders the interpretation of subsequent results.
- **This suggests that** TE is a promising approach that requires further developments in order to provide impactful insights into brain mechanisms.

7.1 Introduction

The study of functional connectivity has provided important insights into the brain organization underpinning both task execution and rest. Active research continues to benefit from the richness of increasingly available neuroimaging datasets in order to extend classical approaches. For example, a focus on *dynamic Functional Connectivity* (dFC) has emerged with the purpose of exploiting the time dimension of functional data [Hutchison et al., 2013, Lurie et al., 2020]. In dFC, functional connectivity is estimated in successive time windows in order to study the time-resolved evolution of functional interactions. Another example is that of *directed* functional connectivity that seeks to determine the direction of functional interactions [Friston, 2011]. The concept of *Effective Connectivity* (EC) describes the direction of functional connections estimated via generative models. Because 'model-free' alternatives are also commonly referred to as instances of EC [Vicente et al., 2011], we will use 'EC' to refer to directed functional connectivity in general in this chapter. The effective connectome is a directed network indicating the influence of some regions onto others. The idea of directed interactions in the brain can find an origin in microscopic neuroanatomy, where axonal projections are known to be directional. In this regard, EC is expected to provide important insights into the neural mechanisms supporting brain activity. Both dFC and EC present opportunities for future research and could significantly enrich our understanding of the brain. However, they face important challenges especially when one moves from theory to practice. In this chapter, we discuss a particular approach used to estimate EC known as *Transfer Entropy* (TE). We show on a synthetic example that the numerical estimation of TE can be adapted in order to provide time-resolved estimates of directed interactions. After that, we apply the method on empirical signals recorded during a motor task in order to estimate the cortico-muscular conduction delay, and we discuss the difficulty of interpreting the results.

The most common methods for estimating EC include model-based approaches such as Granger Causality and Dynamic Causal Models. Model-based methods make assumptions on the structure and properties of the interactions. Granger causality [Granger, 1969, Seth et al., 2015] tests the statistical hypothesis that, given two random processes `X` and `Y`, knowing past realizations of `X` is useful to predict future values of `Y`. It relies on linear vector autoregressive models in order to fit the stochastic time series associated with `X` and `Y` and evaluate the reduction of the error term on `Y` when using information from `X`. When the random processes are composed of Gaussian variables, it has been shown that Granger causality and transfer entropy are equivalent [Barnett et al., 2009]. Moreover, nonlinear exten-

sions of Granger causality have been proposed [Hiemstra and Jones, 1994, Marinazzo et al., 2008]. Dynamic Causal Models assume a bilinear transition model in order to compare the Bayesian evidence of different interaction patterns between the elements of the system [Stephan et al., 2010]. These models require *a priori* knowledge on the inputs to the system and on the potential interactions to investigate. They have been applied in a wide variety of domains, with various data modalities [Friston et al., 2014, Kiebel et al., 2008]. In an exploratory setting however, the assumptions inherent to model-based approaches such as Granger causality and Dynamic Causal Models may not be verified. In that case, model-free methods such as transfer entropy form a useful alternative.

Transfer entropy is a directed measure of information transfer based on information theory [Shannon, 1948, Schreiber, 2000]. In contrast to Granger causality and Dynamic Causal Models, transfer entropy is 'model-free' and relies on conditional probabilities to measure the reduction of uncertainty on the future of a target process, knowing the past of a source process. The model-free aspect of transfer entropy motivated researchers to investigate its application to physiological signals, especially in neuroscience where strong non-linearities are common [Vicente et al., 2011, Wibral et al., 2014b]. A central challenge in the application of transfer entropy to empirical signals is its numerical estimation [Vicente and Wibral, 2014]. Indeed, not relying on modeling assumptions must be counterbalanced by a large amount of good-quality data in order to estimate the probability densities underlying the processes under investigation. Efficient estimators have been proposed [Kraskov et al., 2004, Vicente and Wibral, 2014] and extended in order to estimate information transfer delays on the one hand [Wibral et al., 2013], and to cope with non-stationary signals on the other hand [Wollstadt et al., 2014, Gómez-Herrero et al., 2015]. However, estimating interaction delays among non-stationary signals such as neurophysiological time series remains challenging.

Here, we estimate TE on empirical MagnetoEncephaloGraphy (MEG) signals during the execution of a right hand movement. We implement an estimator that leverages the repeated-trials structure of the data in order to derive a time-resolved estimate of TE suited for such non-stationary signals. First, we show on a synthetic example that TE is able to capture non-linear, non-stationary and delayed interactions in noisy data. Next, we turn to the problem of estimating the cortico-muscular conduction delay between the primary motor cortex and the contralateral hand muscles, during the execution of a visually-triggered movement. The analysis provides several significant interaction delays ranging from 19.7ms to more than 90ms. We discuss the difficulty of interpreting the results produced by the esti-

mation of TE and the challenge of extending the method for the reconstruction of large, directed and time-varying brain networks.

7.2 Materials and Methods

7.2.1 Dataset

We retrieved preprocessed sensor-level MEG data of 18 healthy participants (22-35 years old, 11 women) from the Human Connectome Project [Van Essen et al., 2013, Larson-Prior et al., 2013]. The preprocessing included the removal of bad channels and noisy epochs, the filtering of time series (bandpass, 1.3-150 Hz) and the removal of power line noise and artefactual components [Larson-Prior et al., 2013]. We used a Linearly Constrained Minimum-Variance (LCMV) beamformer with regularization parameter $\lambda = 15\%$ in order to reconstruct source-level time series [Woolrich et al., 2011], using Fieldtrip release r10442 [Oostenveld et al., 2011]. We spatially averaged the reconstructed sources inside each cortical region defined by Desikan et al. [Desikan et al., 2006] using Connectome Workbench [Marcus et al., 2011]. The final sampling rate of reconstructed signals is 1017.3 Hz.

The participants were instructed to tap their index and thumb fingers or to squeeze their toes following a visual stimulus displayed on a screen. The movements were paced and organized in blocks of 10 trials per limb (right hand, left hand, right foot, left foot). We investigated right-hand trials only. There were two sessions of 8 blocks of right-hand movements, for a total of 160 recorded trials per participant. After exclusion of bad trials during the preprocessing and after source-level reconstruction, we merged the data of all participants and obtained a total of 2725 trials. The task and acquisition protocols are detailed in the HCP reference manual [WU-Minn, 2017].

Muscle activity was recorded in parallel to the MEG data, using an ElectroMyoGraphy (EMG) electrode placed on the first dorsal interosseus muscle between thumb and index fingers of the right hand. EMG signals were bandpass filtered in the same frequency range as the MEG data (1.3-150 Hz). All trials were aligned on the onset of the EMG signal and include 800ms before and 350ms after the EMG onset, for a total of 1171 time steps.

7.2.2 Transfer entropy

We consider a real continuous random variable X with realization $x \in \mathcal{X}$ and associated probability density function p. In information theory, the notion of *information* relates to that of *uncertainty*: observing a highly predictable (or certain) event brings little information, and vice-versa. Formally, the amount of information h gained when observing a realization x is inversely proportional to its probability and has been defined by Shannon [Shannon, 1948] as

$$h(x) = \log \frac{1}{p(x)} \tag{7.1}$$

$$= -\log p(x) \tag{7.2}$$

The differential Shannon entropy of the random variable X is then defined as the expected value of the information over its realizations :

$$h(X) = -\int_{x\in\mathcal{X}} p(x) \log p(x) \mathrm{d}x \tag{7.3}$$

In this text, we adopt the convention that the '$\log$' operator is the natural logarithm, which entails that the entropy $h(X)$ is expressed in *nats*. Considering a second random variable Y with support $\mathcal{Y}$, the conditional entropy of X knowing Y is

$$h(X|Y) = -\int_{x\in\mathcal{X}, y\in\mathcal{Y}} p(x,y) \log p(x|y) \mathrm{d}x\mathrm{d}y \tag{7.4}$$

where $p(x,y)$ and $p(x|y)$ are respectively the joint and conditional probability densities of X and Y. Here, $h(X|Y)$ represents the expected information or uncertainty related to observations of X, knowing everything about Y.

Let $\mathtt{X} = \{X_t\}_{t\geq 0}$ and $\mathtt{Y} = \{Y_t\}_{t\geq 0}$ be stochastic processes indexed by the discrete time variable t. If there is a time-dependence between the random variables X_t of process $\mathtt{X}$, characterized by a dynamical system and a state-space representation, then the vector $\mathbf{X}_{t-1} = [X_{t_1}, X_{t_2}, X_{t_3}, ...]$ with $t_i \leq t-1$ denotes the state variable containing the past variables that are relevant for the prediction of X_t. The transfer entropy TE from $\mathtt{X}$ to $\mathtt{Y}$ at time t is then defined [Schreiber, 2000] as

$$TE_{\mathtt{X}\to\mathtt{Y}}(t) = h(Y_t|\mathbf{Y}_{t-1}) - h(Y_t|\mathbf{X}_{t-1}, \mathbf{Y}_{t-1}), \tag{7.5}$$

Equation 7.5 shows that the transfer entropy from $\mathtt{X}$ to $\mathtt{Y}$ quantifies the uncertainty reduction on $\mathtt{Y}$ when the past of $\mathtt{X}$ is known. Assuming that both processes are stationary, the transfer entropy from $\mathtt{X}$ to $\mathtt{Y}$ can be time-averaged:

$TE_{\mathtt{X}\to\mathtt{Y}} = \langle TE_{\mathtt{X}\to\mathtt{Y}}(t)\rangle_t$.

The procedure to determine the past variables relevant for the prediction of X_t and Y_t, forming $\mathbf{X}_{t-1}$ and $\mathbf{Y}_{t-1}$ respectively, is called a state-space reconstruction. Here we use the delay embedding introduced by Takens [Takens, 1981] in order to reconstruct the state-space. This embedding involves two parameters: the embedding dimension d and the embedding delay τ. The delay embedding of a random variable X_t is a vector of d equally-spaced past variables:

$$\mathbf{X}_t^{d,\tau} = [X_t, X_{t-\tau}, X_{t-2\tau}, ..., X_{t-(d-1)\tau}] \tag{7.6}$$

A standard method to determine the embedding parameters d and τ is Ragwitz's criterion [Ragwitz and Kantz, 2002] based on the principle of optimal self-prediction in the reconstructed state-space. Note that the embedding delay τ is related to the autocorrelation time of the process. The range for the search of this parameter is therefore determined by the nature and the time resolution of the signals investigated (e.g. milliseconds for MEG data and seconds for BOLD signals).

In real-world systems, the information transfer from X to Y necessitates a finite time δ to arrive to the target. Estimating this interaction delay (Figure 7.1A) is important in order to reconstruct the temporality of the interactions. The information arriving at Y at time t was sent from X at time $t-\delta$. In order to estimate δ, we test different interaction delays u and we adapt the conditioning on the past of X accordingly. The transfer entropy from X to Y at time t with interaction delay u is defined [Wibral et al., 2013] as

$$TE_{\mathtt{X}\to\mathtt{Y}}(t,u) = h(Y_t|\mathbf{Y}_{t-1}) - h(Y_t|\mathbf{X}_{t-u}, \mathbf{Y}_{t-1}), \tag{7.7}$$

Wibral et al. have shown that the delay u maximizing Equation 7.7 corresponds to the true interaction delay δ from X to Y in the case of noiseless Markov processes [Wibral et al., 2013].

7.2.3 Numerical estimation

A popular approach to estimate TE from finite data and without assumption on the underlying distributions is based on the idea developed by Kozachenko and Leonenko [Kozachenko and Leonenko, 1987] that, in a reconstructed state-space, the larger the distance from one point to its nearest-neighbors the lower the probability density around that point. The KSG estimator named after Kraskov, Stögbauer and Grassberger [Kraskov et al., 2004] leverages this idea in order to

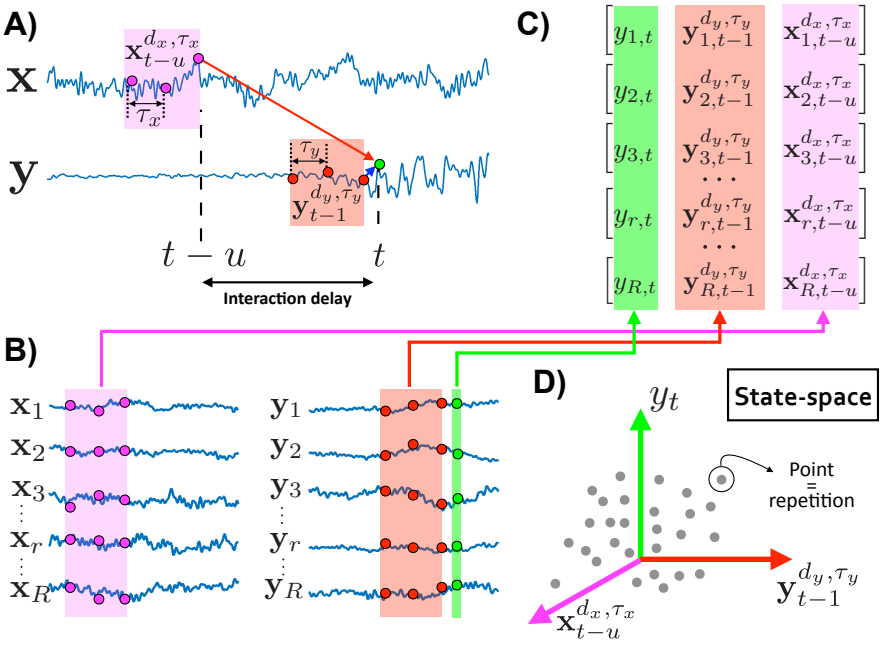

Figure 7.1: **Estimating transfer entropy in non-stationary signals. A)** Transfer entropy estimates the directed transfer of information between two (ensembles of) time series, from a source $\mathbf{x}$ (purple) to a target $\mathbf{y}$ (red). Time series are delay-embedded with optimized parameters d and τ. In real-world systems, the information takes a finite time to arrive to the target, which is refered to as the interaction delay u. **B)** When time series are non-stationary, we can leverage the multi-trials structure of neurophysiological recordings by pooling over trials in order to estimate TE at each time t (green). **C** and **D)** Instead of populating the state-space with time points, we consider each time step separately and populate the state-space with points corresponding to signal repetitions. This procedure enables a modification of the KSG estimator for non-stationary time series and produces time-resolved estimates of directed information transfer. This figure is adapted from [Wollstadt et al., 2014].

evaluate TE more precisely than via binning or kernel approaches [Vicente and Wibral, 2014]. The steps involved in the computation of the KSG estimator for two empirical time series $\mathbf{x} = [x_t]_{0 \leq t \leq T}$ and $\mathbf{y} = [y_t]_{0 \leq t \leq T}$ are:

1. Standardize $\mathbf{x}$ and $\mathbf{y}$ to zero mean and unit variance
2. Determine the embedding parameters d_x, τ_x of $\mathbf{x}$ and d_y, τ_y of $\mathbf{y}$ (here we use Ragwitz's criterion)
3. Reconstruct the state-space spanned by $[y_t \mathbf{y}_{t-1}^{d_y,\tau_y} \mathbf{x}_{t-u}^{d_x,\tau_x}]$ for all possible t
4. For each time point t_i in the reconstructed state-space:
   (a) Compute the distance ϵ_i to its k-th nearest neighbor
   (b) Count the number of points n inside a ball of fixed radius ϵ_i in the subspaces spanned by $[\mathbf{y}_{t-1}^{d_y,\tau_y}]$, $[y_t \mathbf{y}_{t-1}^{d_y,\tau_y}]$ and $[\mathbf{y}_{t-1}^{d_y,\tau_y} \mathbf{x}_{t-u}^{d_x,\tau_x}]$

The KSG estimator writes

$$\widehat{TE}_{\mathtt{X} \to \mathtt{Y}}(u) = \psi(k) + \left\langle \psi\left(n_{\mathbf{y}_{t-1}^{d_y,\tau_y}} + 1\right) - \psi\left(n_{y_t \mathbf{y}_{t-1}^{d_y,\tau_y}} + 1\right) - \psi\left(n_{\mathbf{y}_{t-1}^{d_y,\tau_y} \mathbf{x}_{t-u}^{d_x,\tau_x}} + 1\right) \right\rangle_t \tag{7.8}$$

where $\psi(\cdot)$ denotes the digamma function (monotonic on $\mathbb{R}^+$), $\langle \cdot \rangle_t$ is the average over time points and k is a parameter to fix. We estimate the information transfer delay $\hat{\delta}$ from $\mathbf{x}$ to $\mathbf{y}$ by scanning $\widehat{TE}_{\mathtt{X} \to \mathtt{Y}}(u)$ over u:

$$\hat{\delta} = \arg\max_u \widehat{TE}_{\mathtt{X} \to \mathtt{Y}}(u) \tag{7.9}$$

7.2.4 Dealing with non-stationarity

The KSG estimator (Equation 7.8) assumes that the empirical time series $\mathbf{x}$ and $\mathbf{y}$ come from stationary processes in order to average the nearest-neighbors count over time points. When this assumption is violated but multiple repetitions of the time series are available, it is possible to leverage this multi-trials structure to derive an ensemble estimator of transfer entropy. For instance, in neuroimaging experiments, it is common to monitor the brain activity induced by the execution of a task after the presentation of a stimulus. In that case, signals are expected to be non-stationary and a large number of trials are recorded.

We note $\mathbf{x}_r$, $1 \leq r \leq R$, the r-th repetition recorded from the non-stationary process $\mathtt{X}$. By assuming that the distribution of one time point is stationary over

repetitions, Wollstadt et al. [Wollstadt et al., 2014] and Gómez-Herrero et al. [Gómez-Herrero et al., 2015] proposed to modify the KSG estimator in the following way:

$$\widehat{TE}_{\mathtt{X}\to\mathtt{Y}}(u,t) = \psi(k) + \left\langle \psi\left(n_{\mathbf{y}_{r,t-1}^{d_y,\tau_y}} + 1\right) - \psi\left(n_{y_{r,t}\mathbf{y}_{r,t-1}^{d_y,\tau_y}} + 1\right) - \psi\left(n_{\mathbf{y}_{r,t-1}^{d_y,\tau_y}\mathbf{x}_{r,t-u}^{d_x,\tau_x}} + 1\right)\right\rangle_r \quad (7.10)$$

Here, for each time point, the state-space is populated with points corresponding to repetitions (see Figure 7.1). The averaging over repetitions instead of time not only relaxes the assumption of temporal stationarity but also enables the estimation of time-resolved transfer entropy. This approach requires a large number of repetitions of $\mathbf{x}$ and $\mathbf{y}$ to populate the state-space. For instance, Wollstadt et al. [Wollstadt et al., 2014] tested the modified KSG estimator with a number of repetitions R ranging from 500 to 30,000 and found that larger values produce better TE estimations in simulated data. Gómez-Herrero et al. [Gómez-Herrero et al., 2015] made a similar observation. However, determining the minimum number of repetitions needed to obtain a reliable estimation in experimental data i.e., where the ground truth is unknown, remains an open question.

Numerical estimators of information-theoretic quantities are biased when applied on finite datasets [Panzeri et al., 2007]. In order to test the statistical significance of estimated TE values in empirical data, we must generate surrogate data $\tilde{\mathbf{x}}$ and $\tilde{\mathbf{y}}$ that are assumed independent under the null hypothesis. An approach to generate such surrogate data consists in choosing

$$\tilde{\mathbf{x}}_{s,t} = \mathbf{x}_{r,t} \quad (7.11)$$

$$\tilde{\mathbf{y}}_{s,t} = \mathbf{y}_{\phi(r),t} \text{ , with } \phi(r) \neq r \quad (7.12)$$

where s denotes the repetition index in the surrogate data ($1 \leq s \leq R$), r denotes the repetition index in the original data ($1 \leq r \leq R$), t is the time index and $\phi(\cdot)$ is a random permutation of the integers from 1 to R. In other words, we randomly reassign the repetition indices of target signals. This procedure breaks the information transfer from the source to the target for each repetition while preserving the individual properties of the signals, including their spectrum. Importantly and because we leverage the multi-trials structure of the data, we do *not* shuffle time points inside signals [Wollstadt et al., 2014, Gómez-Herrero et al., 2015]. Repeating TE estimation on multiple surrogate datasets allows us to form a null distribution against which one can compare TE values estimated from the original data.

7.3 Results

We implemented the ensemble KSG estimator (Equation 7.10) using the Julia programming language [Bezanson et al., 2017]. In order to assess that our implementation is able to detect delayed and time-varying information transfer in non-stationary time series, we first test it on a synthetic example derived from empirical data. Then, we turn to the problem of identifying information transfer delays between pairs of Regions of Interest (ROIs) involved in a visually triggered right hand movement.

7.3.1 Validation using synthetic data

We choose the signals reconstructed in the left precentral gyrus (primary motor cortex, M1) during a right-hand movement (see Methods) as the reference data that we denote $\mathbf{x}$. We define $\mathbf{y}$ as the corresponding delayed and transformed signals and we compute the r-th repetition, noted $\mathbf{y}_r$, as

$$\mathbf{y}_r(t) = \mathbf{y}_r(t-1) + \kappa(t)\left(\mathbf{x}_r(t-\delta)\right)^3 + \eta \tag{7.13}$$

$$\kappa(t) = \begin{cases} \sin(\frac{\pi}{100}t) & \text{if } 350 \leq t \leq 850 \\ 0 & \text{otherwise} \end{cases} \tag{7.14}$$

where $t \in [0, 1170]$, κ is the coupling function, δ is the interaction delay and $\eta \sim \mathcal{N}(0, \sigma^2)$ is a normally-distributed noise process with variance σ^2. We apply the ensemble KSG estimator (Equation 7.10) with $k = 15$ on the synthetic example formed by the source process $\mathbf{x}$ and the target process $\mathbf{y}$ (see Figure 7.2A).

Figure 7.2 shows the result of Transfer Entropy (TE) estimation from $\mathbf{x}$ to $\mathbf{y}$ (Equations 7.13 and 7.14) with different noise levels and for different interaction delays $u \in [40, 60]$. In Figure 7.2C, we observe that estimated TE is highest in a band corresponding to the true interaction delay $\delta = 50$, and in a time interval between time steps 350 and 850. When the level of noise increases from $\sigma = 0.5$ (top) to $\sigma = 5.0$ (bottom), we see that identifying the correct interaction delay by visual inspection becomes challenging as estimated TE is high for all tested delays. In Figure 7.2D, we observe that estimated TE at the true interaction delay reproduces the shape of the non-stationary coupling function (Figure 7.2B) in absolute value. The estimated TE curve becomes less smooth when the level of noise introduced in the target process increases from $\sigma = 0.5$ (top) to $\sigma = 5.0$ (bottom).

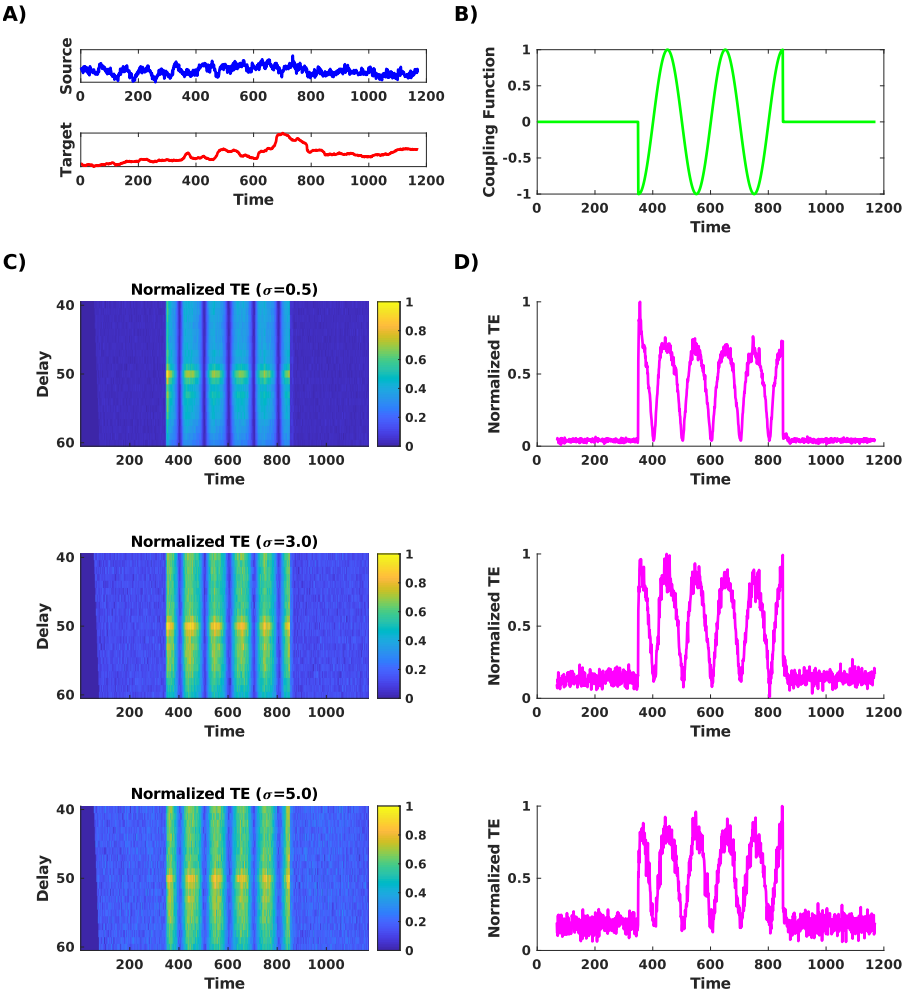

Figure 7.2: **Estimating Transfer Entropy (TE): synthetic example. A)** Example of a realization of the source and target processes defined by Equation 7.13. **B)** Non-stationary coupling function κ used for the synthetic experiment (see Equation 7.14). **C)** Results of the transfer entropy estimation as a function of time and interaction delay, for different noise levels $\sigma \in \{0.5, 3.0, 5.0\}$. The true interaction delay is $\delta = 50$. **D)** Time evolution of estimated transfer entropy, extracted from panel **C** at the true interaction delay. The number of neighbors used for the numerical estimation (Equation 7.10) is $k = 15$.

7.3.2 Estimating interaction delays in empirical MEG data

We turn to the problem of identifying the cortico-muscular delay between the left primary motor cortex (M1, identified as the left precentral gyrus in the parcellation [Desikan et al., 2006]) and the EMG signal recorded from the right hand during a simple motor task (see Methods). The source $\mathbf{x}$ is formed by all trials recorded from M1 during the task (18 participants for a total of 2725 trials; see Methods). The target $\mathbf{y}$ is formed by the corresponding EMG signals. All trials are temporally aligned on the EMG onset time. We apply the ensemble KSG estimator (Equation 7.10) with $k = 15$ and we test delays ranging from $u = 1$ to $u = 100$.

Figure 7.3A shows the result of the TE estimation as a function of time and delay. Before the EMG onset time located at $t = 814$, $\widehat{TE}$ is almost zero for all delays. The bottom left triangle corresponds to time-delay combinations for which TE estimation is undefined because the number of time steps covered by the delay embedding and by the time lag is greater than the time of estimation. At the EMG onset time, we observe a vertical yellow line indicating an increase of $\widehat{TE}$ for all tested delays, which does not allow us to visually determine the optimal interaction delay. After the EMG onset, $\widehat{TE}$ progressively decreases until reaching near-zero values after $t = 1000$. Figure 7.3B shows the column of Figure 7.3A corresponding to $t = 814$ and presents the estimated TE as a function of information transfer delay at the EMG onset time. The curve is irregular with a peak value for the delay $u = 20$ and a monotonically increasing trend for delays larger than $u = 80$.

In order to test the statistical significance of these estimated TE values, we compare them to a null distribution $\widehat{TE}_{surr}$. For that, we perform the TE estimation on surrogate data i.e., from $\tilde{\mathbf{x}}$ to $\tilde{\mathbf{y}}$ where the target signals repetitions have been randomly permuted (see Methods). We perform this procedure 30 times. The distribution of $\widehat{TE} - \widehat{TE}_{surr}$ is referred to as the *excess TE*. Figure 7.3C shows the median of excess TE as a function of time and information transfer delay. The increase of TE locked to the EMG onset time observed in Figure 7.3A is not remarkable when contrasted with the null distribution $\widehat{TE}_{surr}$. Figure 7.3D shows the column of Figure 7.3C corresponding to the EMG onset time ($t = 814$) with the corresponding inter-percentile range (10 and 90 percentiles). A one-sided sign test finds the delays for which the excess TE is significantly greater than 0 ($p < 0.005$, Bonferroni corrected). Isolated significant delays are in the set $u \in \{20, 32, 42, 75\}$. Multiple delays verifying $u \geq 88$ are found significant too. The lowest significant delay of 20 time steps corresponds to a lag of 19.7 ms between evoked activity in M1 and the EMG onset (sampling rate = 1017.3 Hz, see Methods). This lag

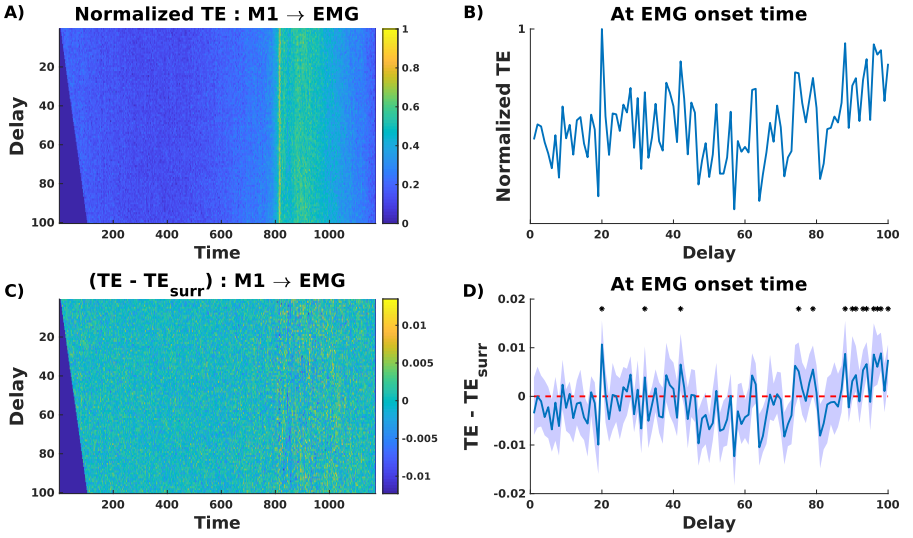

Figure 7.3: **Estimating cortico-muscular conduction delays. A)** Estimated Transfer Entropy ($\widehat{TE}$) from the left primary motor cortex (M1) to the right hand EMG, as a function of time and information transfer delay. **B)** Evolution of $\widehat{TE}$ at the EMG onset time ($t = 814$) with respect to the information transfer delay. **C)** In order to test the significance of estimated TE values, we draw a surrogate distribution $\widehat{TE}_{surr}$ by randomly shuffling the EMG repetitions (see Methods). The difference between actual and surrogate values is called the excess TE. We report the median of excess TE as a function of time and information transfer delay. **D)** The solid line presents the evolution of the TE excess at the EMG onset time with respect to the information transfer delay. The shaded area indicates the inter-percentile range (10 and 90 percentiles). The dashed red line corresponds to the reference level $\widehat{TE} = \widehat{TE}_{surr}$. Black asterisks identify information transfer delays for which estimated TE values are significant (one-sided sign test, $p < 0.005$ Bonferroni corrected).

is close to previously identified cortico-muscular conduction times [Rothwell et al., 1991, Groß et al., 2000].

7.4 Discussion

In this chapter, we examined the application of an information-theoretic measure known as Transfer Entropy (TE) for the estimation of time-resolved effective connectivity. Numerical experiments on a synthetic example showed that TE is able to accurately detect delayed and non-stationary couplings from source to target signals. In empirical data, we observed the importance of using a null distribution in order to identify significant TE values. We found multiple significant information transfer delays from the primary motor cortex to the hand muscle during a simple motor task, at the group-level.

7.4.1 The challenge of exploring interactions in the brain

Mapping functional interactions between brain regions is a fundamental challenge in network neuroscience [Bullmore and Sporns, 2009, Bassett and Sporns, 2017]. Extensions of standard functional connectivity assessment seek to evaluate the time evolution of functional connections [Hutchison et al., 2013, Lurie et al., 2020] and the direction of these interactions [Friston, 2011]. In this context, transfer entropy is an attractive measure expected to provide much insight into the processes supporting brain activity and the consequent behavior [Vicente et al., 2011, Wollstadt et al., 2014].

Still, the detection of significant transfer entropy between two neural processes provides little information about the physiological nature of the interaction [Vicente et al., 2011]. First, we observed in Figure 7.2 that time-resolved TE was sensitive to noise, a problem that some authors proposed to alleviate by smoothing the estimated TE curve [Gómez-Herrero et al., 2015], although the choice of smoothing method and parameters is arbitrary and impacts the shape of the curve. In addition estimated TE values depend monotonically on an arbitrary parameter of the numerical estimator (number of neighbors k in Equation 7.10), which entails that non-zero TE values do not necessarily indicate a non-zero information transfer. Together, these observations suggest that the detection of an interaction is qualitative and does not inform us on the physiological content of the exchange. Second, the analysis presented in this chapter ignored any internal processing or information storage performed individually by the brain regions [Lizier et al., 2012]. The estimated information transfer therefore only reflects part of the

mechanism of a neural interaction [Wibral et al., 2014a]. Third, TE is defined in the strict framework of Shannon's information theory [Shannon, 1948, Schreiber, 2000] and represents a measure of *predictive information transfer* [Wibral et al., 2014b, Lizier et al., 2010]. This interpretation must be differentiated from that of *causality* [Lizier and Prokopenko, 2010] and that of *coupling strength* [Hahs and Pethel, 2013]. As shown by Ay and Polani [Ay and Polani, 2008], causality can take other forms than information transfer, and proving a causal effect ultimately demands an experimental intervention on the studied system. Moreover, the information transfer between two strongly coupled oscillators reaching perfect synchronization is null because the future of each process can be predicted independently from the past of the other [Kaiser and Schreiber, 2002]. Overall, these remarks point out to the importance of the careful interpretation of the results that is necessary in order to further explore interactions among neural processes.

In this chapter we restricted our analysis to bivariate interactions. Estimating TE in order to reconstruct large, multivariate effective brain networks is an NP-hard problem [Lizier and Rubinov, 2012], although heuristic approximate algorithms have been proposed [Lizier and Rubinov, 2012, Runge et al., 2012, Montalto et al., 2014, Novelli et al., 2019, Novelli and Lizier, 2020]. These algorithms require stringent statistical testing and have not been evaluated with the non-stationary TE estimator used in this work [Wollstadt et al., 2014]. In multivariate settings, higher-order phenomena must be accounted for such as synergy when multiple sources collectively transfer information to a target, and redundancy when a source transfers the same information to multiple targets [Chicharro and Panzeri, 2017, Stramaglia et al., 2014]. Moreover, the question of how to determine interaction delays among multiple variables remains open. The presence of multiple feedback loops in the brain (e.g. in motor control [Scott, 2004]), with different lags, origins and destinations adds to this challenge [Dong et al., 2012]. We obtained in Figure 7.3 several significant delays between the activity in M1 and the contralateral EMG signal, which illustrates the difficulty of managing interactions delays even in the bivariate case. Last, the possibility that detected interactions are mediated by unobserved confounders must not be neglected and can hinder the search of *direct* information transfer [Reid et al., 2019]. In sum, estimating multivariate TE in non-stationary signals faces several computational challenges that limit its application to the investigation of whole-brain, time-resolved effective connectivity.

7.4.2 Model-free, but not parameterless

Transfer entropy relies on probability distributions instead of assuming the structure of the dynamical model generating the data. For this reason, estimating transfer entropy in finite datasets where probability densities are unknown is challenging [Vicente and Wibral, 2014]. The numerical estimator proposed by Kraskov, Stögbauer and Grassberger [Kraskov et al., 2004], although data-efficient because it is based on a nearest-neighbors search, involves several parameters.

The number of neighbors k (Equations 7.8 and 7.10) is arbitrary. The default value used in standard implementations is $k = 4$ [Lindner et al., 2011, Wollstadt et al., 2018, Montalto et al., 2014], although some studies showed that higher values up to $k = 45$ produce more accurate estimates [Vicente et al., 2011, Gómez-Herrero et al., 2015]. Moreover, Vicente et al. [Vicente et al., 2011] showed that the embedding parameters τ and d (see Methods) are sensitive and can generate false positives if chosen inadequately. In this chapter we used Ragwitz's criterion as a principled method to determine both parameters together [Ragwitz and Kantz, 2002], but alternative approaches exist such as Cao's criterion [Cao, 1997]. These parameters (k, τ, d) combined with those related to the preprocessing, denoising and beamforming of neurophysiological data [Gross et al., 2013] are potential sources of confounds in TE analyses.

An important assumption underlying the application of the non-stationary KSG estimator (Equation 7.10) is that all repetitions of the signals are temporally perfectly aligned [Wollstadt et al., 2014, Gómez-Herrero et al., 2015]. In our experiment, all trials were aligned on the onset of the EMG signal and we assumed that the cortico-muscular delay investigated was equal across trials and participants, such that the onset of M1 activity was time-locked. The finding of several significant delays (Figure 7.3D) reflects the possibility that this assumption is not verified. When the maximum temporal deviation among trials is limited to l time steps and that stationarity can be assumed locally in a time window of size $2l$, the state-space can be reconstructed with a mix of points corresponding to repetitions and to the time steps included in the time-window. This approach however requires scanning over the additional parameter l [Wollstadt et al., 2014, Gómez-Herrero et al., 2015]. Alignment methods such as dynamic time warping [Berndt and Clifford, 1994] or continuous profile modeling [Listgarten et al., 2004] should be investigated in future work in order to assess whether they are able to improve the time-locking of time series while preserving their physiological information content.

7.4.3 Limitations

Our study has several limitations. First, we relied on external data provided by the HCP [Van Essen et al., 2013] and had no control over the task protocol. The motor task consisted of *paced* finger movements, which allowed participants to anticipate the visual stimulus. It is possible that the cortico-muscular delay between M1 and the EMG signal varies between anticipated and unanticipated trials. Second, we used a custom implementation of the ensemble KSG estimator [Wollstadt et al., 2014, Gómez-Herrero et al., 2015], which requires further validation. The authors of [Wollstadt et al., 2014] showed that the robustness of TE estimation in non-stationary signals increases with the number of repetitions included in the dataset, at the expense of a prohibitive computational cost requiring specialized GPU implementations. On a synthetic example, they showed that the modified KSG estimator identifies the correct interaction delay between two signals when 10,000 repetitions are used, while experiments using 5000 and 2000 repetitions resulted in an error of less than 4ms. The limited number of repetitions used in our analysis (2725, see Methods) promoted a tractable computational cost with our implementation but might also be a source of estimation bias. Third, we analyzed all signals in the time domain although the information content of electrophysiological signals is known to vary across frequency bands [Oostenveld et al., 2011]. Future work should investigate the transfer entropy estimation in specific frequency bands. For instance, it has been shown that μ-waves (7.5-12.5 Hz) over the primary motor cortex are suppressed during the voluntary execution of a movement [Pfurtscheller et al., 2006].

7.4.4 Conclusion

We investigated and discussed the application of transfer entropy in order to derive time-resolved effective connectivity. We showed its potential on a synthetic example and applied it to the estimation of the cortico-muscular delay between the primary motor cortex and the muscles of the hand. We discussed the limitations in the interpretation of the brain interactions detected via transfer entropy. In sum, transfer entropy is an attractive and theoretically grounded measure to explore interactions in the human brain, but it does not replace modeling approaches that are necessary to test hypotheses on the mechanisms driving these interactions.

8

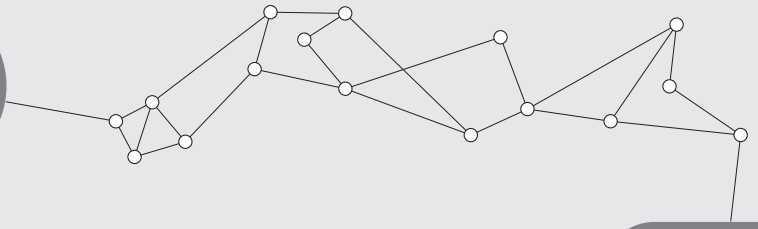

Conclusion

The study of the human brain has known important advances in recent years with the increasing amount of high-quality data derived from novel imaging modalities. Mathematical methods and models are required in order to analyze this data and to advance our knowledge of the mechanisms underlying healthy or disordered brain functioning.

In this thesis, we have studied the human brain as a complex system. This system is characterized by an anatomical network supporting interactions between remote brain regions. We distinguished two types of networks of the brain. Structural networks represent anatomical connections under the form of white matter pathways reconstructed from diffusion-weighted imaging. Functional networks account for the statistical interdependence between the activity of gray matter areas recorded with functional imaging, during the execution of a task or at rest. These two types of networks are distinct and complementary representations of the complex system that is the brain, and understanding their relationship is an important goal of network neuroscience. In addition, functional networks enclose an individual-specific fingerprint and data-driven methods allow us to enhance it in order to focus on the individual-level properties of functional connectivity. Last, while simple correlation-based measures form a useful tool to estimate functional interactions in the brain, more advanced measures are expected to provide much insight into the timing and direction of these interactions.

Summary of the contributions

In Chapter 3, we used structural and functional connectivity as features in a machine learning framework in order to classify schizophrenic patients from healthy controls. Due to the high dimensionality of feature vectors, we applied a multivariate feature selection method in order to identify the most discriminative brain connections. Our analysis allowed us to identify a set brain regions affected in schizophrenia that partially overlaps with previous studies. Moreover, the results

showed that a mix of structural and functional features led to the best trade-off between classification accuracy and feature selection stability. This motivated us to further explore the relationship between structure and function in brain networks.

In Chapter 4, we proposed to model functional connectivity as the state-covariance matrix of a diffusion dynamics unfolding on the anatomical network. This framework requires the definition of control regions (or input nodes) driving the dynamics. We showed that control regions associated with a specific functional state were identifiable. The state-specific sets of control regions that we identified partially overlapped, with the recurring presence of several subcortical regions. We provided a numerical assessment of the identified control regions and suggested that our model, *structure-informed functional connectivity*, can guide future studies investigating control mechanisms in particular brain conditions.

In Chapter 5, we illustrated such an application on two datasets. First, we identified control regions in the same dataset of schizophrenic patients and healthy controls as in Chapter 3. We used these regions as features to classify patients and controls instead of the high-dimensional feature vectors of structural and functional connectivity values used previously. We obtained comparable classification performance and discriminative control regions showed a correspondence with previously reported areas affected in schizophrenia. As a second application, we identified control regions in a dataset of expert meditation practitioners. Because meditation has been linked to several health benefits, active research seeks to understand the mechanisms supporting the meditative state. We used control regions as features to classify meditation from resting-state and obtained a list of discriminative regions potentially involved in the control of sustained meditation. These results provided further numerical evidence that control regions identified via *structure-informed functional connectivity* form a meaningful description of brain states.

In Chapter 6, we focused on the individual-level study of brain connectivity. Enhancing individual-specific properties of brain networks is a necessary step for a refined analysis of the link between brain and behavior, as well as for improved and personalized diagnostic and treatment of brain disorders. Functional connectivity in particular has been shown to contain a fingerprint that one can extract with data-driven methods. We proposed to normalize functional networks by their degree sequence before extracting fingerprints, in order to modulate the excessive influence of common hubs in the networks. The results showed that degree-normalization improves the contrast between individuals and therefore the quality of retrieved fingerprints. This suggests that degree-normalization is beneficial for future research

investigating brain networks at the individual-level.

In Chapter 7, we investigated an alternative approach for measuring functional interactions. Because the exchange of information in the brain is directed and varies with time, we proposed to quantify effective and time-resolved connectivity using an information-theoretic measure called transfer entropy. We showed on a synthetic example that transfer entropy was able to capture non-linear, non-stationary and delayed interactions between two variables. Then we turned to the problem of estimating the information transfer delay between the brain and the hand muscles during the execution of a movement, using MEG data. We identified several significant delays and argued that transfer entropy does not provide information on the physiological nature of the detected interactions, which can restrict our interpretation and its application to the reconstruction of larger networks.

Perspectives

Our contributions open perspectives for investigations that were not covered in this thesis. Future studies should apply the structure-informed functional connectivity model (Chapter 4) to individual-level data where functional networks have been optimally reconstructed in order to enhance their fingerprint (Chapter 6). One could quantify the variations in the identified set of control regions due to the fingerprint extraction, and investigate the link between task-specific control regions and behavior. In turn, future work should investigate to which extent control regions are individual-specific with respect to the brain parcellation that is used. The possibility of deriving brain fingerprints from identified control regions instead of or along with functional connectivity values should also be tested.

Chapter 7 illustrated the challenge of applying model-free measures to explore functional interactions in the brain. At the same time, we showed in Chapters 3, 4 and 5 that structure and function were complementary components in the study of brain connectivity. Future work should evaluate the possibility to include anatomical information in the exploration of functional interactions, without necessarily biasing the search towards brain regions that are strongly anatomically connected. Moreover, estimating the directed information transfer (Chapter 7) from identified *control* regions to the others (Chapter 4) could provide further insights about their involvement in supporting specific functional states.

Future investigations could also leverage biological information that was ignored in the brain networks studied in this thesis. Indeed, we considered structural net-

works where nodes were brain regions and edges were weighted by the number of white matter streamlines reconstructed by tractography (see Section 2.2). First in the abstraction from brain regions to nodes in a network, we lost information such as their geometrical location with respect to each other, their cortical thickness and surface, and we considered them as passive 'relays' rather than units capable of internal processing. Second, alternative weightings of white matter streamlines exist in order to define edges in a brain network. For instance streamline length, average fractional anisotropy and apparent diffusion coefficient all provide complementary information on the anatomical connections of the brain. Recent advances in diffusion-weighted MRI have enabled a more detailed description of microstructural properties of white matter streamlines [Rensonnet et al., 2019]. Advanced network models such as attributed or multilayers networks [Boccaletti et al., 2014] could leverage these pieces of information in order to build more biologically representative brain networks.

Network neuroscience has developed thanks to the progress made in neuroimaging. Various imaging modalities with ever increasing spatial and temporal resolutions continue to provide detailed information on the brain structure and function. However, this variety comes with an heterogeneity in the acquisition parameters and processing steps involved in the construction of a brain network. An example illustrated in Chapter 2 is that of the choice of a brain parcellation to define the nodes of the networks. In this thesis, we used datasets of different origins and obtained with different acquisition parameters, processing pipelines and parcellations. This diversity makes it difficult to reproduce and compare results across studies. This issue could be addressed with the development of standardized pipelines implementing state-of-the-art processing methods and parcellations, and maintained collectively by the community. Such initiatives have recently appeared for the processing of fMRI [Esteban et al., 2019] and dMRI [Cieslak et al., 2020] data. We are thus confident that future network neuroscience studies will gain in reproducibility regarding data processing.

To conclude, we presented in this thesis methods and results combining several research fields in order to study the brain. We focused on the role of controllability in relating structure and function, on the importance of individual variability in brain data and on the challenge of exploring neural interactions. Altogether, we hope that the present work will support future research aiming at improving our understanding of the complex and fascinating organ that is the human brain.

Bibliography

[Abbas et al., 2020a] Abbas, K., Amico, E., Svaldi, D. O., Tipnis, U., Duong-Tran, D. A., Liu, M., Rajapandian, M., Harezlak, J., Ances, B. M., and Goñi, J. (2020a). Geff: Graph embedding for functional fingerprinting. *NeuroImage*, 221:117181.

[Abbas et al., 2020b] Abbas, K., Liu, M., Venkatesh, M., Amico, E., Kaplan, A. D., Ventresca, M., Pessoa, L., Harezlak, J., and Goñi, J. (2020b). Geodesic distance on optimally regularized functional connectomes uncovers individual fingerprints. *arXiv preprint arXiv:2003.05393*.

[Abdelnour et al., 2014] Abdelnour, F., Voss, H. U., and Raj, A. (2014). Network diffusion accurately models the relationship between structural and functional brain connectivity networks. *Neuroimage*, 90:335–347.

[Abeel et al., 2010] Abeel, T., Helleputte, T., Van de Peer, Y., Dupont, P., and Saeys, Y. (2010). Robust biomarker identification for cancer diagnosis with ensemble feature selection methods. *Bioinformatics*, 26(3):392–398.

[Alexander et al., 1986] Alexander, G. E., DeLong, M. R., and Strick, P. L. (1986). Parallel organization of functionally segregated circuits linking basal ganglia and cortex. *Annual review of neuroscience*, 9(1):357–381.

[Alexander et al., 2020] Alexander, R., Aragón, O. R., Bookwala, J., Cherbuin, N., Gatt, J. M., Kahrilas, I. J., Kästner, N., Lawrence, A., Lowe, L., Morrison, R. G., et al. (2020). The neuroscience of positive emotions and affect: Implications for cultivating happiness and wellbeing. *Neuroscience & Biobehavioral Reviews*.

[Amico et al., 2019] Amico, E., Arenas, A., and Goñi, J. (2019). Centralized and distributed cognitive task processing in the human connectome. *Network Neuroscience*, 3(2):455–474.

[Amico et al., 2020] Amico, E., Dzemidzic, M., Oberlin, B. G., Carron, C. R., Harezlak, J., Goñi, J., and Kareken, D. A. (2020). The disengaging brain: Dynamic transitions from cognitive engagement and alcoholism risk. *NeuroImage*, 209:116515.

[Amico and Goñi, 2018] Amico, E. and Goñi, J. (2018). The quest for identifiability in human functional connectomes. *Scientific reports*, 8(1):1–14.

[Andreasen et al., 2010] Andreasen, N. C., Pressler, M., Nopoulos, P., Miller, D., and Ho, B.-C. (2010). Antipsychotic dose equivalents and dose-years: a standardized method for comparing exposure to different drugs. *Biological psychiatry*, 67(3):255–262.

[Aquino et al., 2020] Aquino, K. M., Fulcher, B. D., Parkes, L., Sabaroedin, K., and Fornito, A. (2020). Identifying and removing widespread signal deflections from fmri data: Rethinking the global signal regression problem. *NeuroImage*, 212:116614.

[Attwell and Laughlin, 2001] Attwell, D. and Laughlin, S. B. (2001). An energy budget for signaling in the grey matter of the brain. *Journal of Cerebral Blood Flow & Metabolism*, 21(10):1133–1145.

[Avants et al., 2008] Avants, B. B., Epstein, C. L., Grossman, M., and Gee, J. C. (2008). Symmetric diffeomorphic image registration with cross-correlation: evaluating automated labeling of elderly and neurodegenerative brain. *Medical image analysis*, 12(1):26–41.

[Avena-Koenigsberger et al., 2018] Avena-Koenigsberger, A., Misic, B., and Sporns, O. (2018). Communication dynamics in complex brain networks. *Nature Reviews Neuroscience*, 19(1):17.

[Avena-Koenigsberger et al., 2019] Avena-Koenigsberger, A., Yan, X., Kolchinsky, A., van den Heuvel, M., Hagmann, P., and Sporns, O. (2019). A spectrum of routing strategies for brain networks. *PLoS computational biology*, 15(3):e1006833.

[Ay and Polani, 2008] Ay, N. and Polani, D. (2008). Information flows in causal networks. *Advances in complex systems*, 11(01):17–41.

[Baer, 2003] Baer, R. A. (2003). Mindfulness training as a clinical intervention: A conceptual and empirical review. *Clinical psychology: Science and practice*, 10(2):125–143.

[Bærentsen et al., 2010] Bærentsen, K. B., Stødkilde-Jørgensen, H., Sommerlund, B., Hartmann, T., Damsgaard-Madsen, J., Fosnæs, M., and Green, A. C. (2010). An investigation of brain processes supporting meditation. *Cognitive processing*, 11(1):57–84.

[Balaji et al., 2012] Balaji, P., Varne, S. R., and Ali, S. S. (2012). Physiological effects of yogic practices and transcendental meditation in health and disease. *North American journal of medical sciences*, 4(10):442.

[Bari et al., 2019] Bari, S., Amico, E., Vike, N., Talavage, T. M., and Goñi, J. (2019). Uncovering multi-site identifiability based on resting-state functional connectomes. *NeuroImage*, 202:115967.

[Barnett et al., 2009] Barnett, L., Barrett, A. B., and Seth, A. K. (2009). Granger causality and transfer entropy are equivalent for gaussian variables. *Physical review letters*, 103(23):238701.

[Bassett and Bullmore, 2006] Bassett, D. S. and Bullmore, E. (2006). Small-world brain networks. *The neuroscientist*, 12(6):512–523.

[Bassett et al., 2008] Bassett, D. S., Bullmore, E., Verchinski, B. A., Mattay, V. S., Weinberger, D. R., and Meyer-Lindenberg, A. (2008). Hierarchical organization of human cortical networks in health and schizophrenia. *Journal of Neuroscience*, 28(37):9239–9248.

[Bassett and Bullmore, 2009] Bassett, D. S. and Bullmore, E. T. (2009). Human brain networks in health and disease. *Current opinion in neurology*, 22(4):340.

[Bassett and Bullmore, 2017] Bassett, D. S. and Bullmore, E. T. (2017). Small-world brain networks revisited. *The Neuroscientist*, 23(5):499–516.

[Bassett and Sporns, 2017] Bassett, D. S. and Sporns, O. (2017). Network neuroscience. *Nature neuroscience*, 20(3):353–364.

[Batista-García-Ramó and Fernández-Verdecia, 2018] Batista-García-Ramó, K. and Fernández-Verdecia, C. I. (2018). What we know about the brain structure–function relationship. *Behavioral Sciences*, 8(4):39.

[Baum et al., 2020] Baum, G. L., Cui, Z., Roalf, D. R., Ciric, R., Betzel, R. F., Larsen, B., Cieslak, M., Cook, P. A., Xia, C. H., Moore, T. M., et al. (2020). Development of structure–function coupling in human brain networks during youth. *Proceedings of the National Academy of Sciences*, 117(1):771–778.

[Bell and Shine, 2016] Bell, P. T. and Shine, J. M. (2016). Subcortical contributions to large-scale network communication. *Neuroscience & Biobehavioral Reviews*, 71:313–322.

[Berndt and Clifford, 1994] Berndt, D. J. and Clifford, J. (1994). Using dynamic time warping to find patterns in time series. In *KDD workshop*, volume 16, pages 359–370. Seattle, WA, USA:.

[Bettinardi et al., 2017] Bettinardi, R. G., Deco, G., Karlaftis, V. M., Van Hartevelt, T. J., Fernandes, H. M., Kourtzi, Z., Kringelbach, M. L., and Zamora-López, G. (2017). How structure sculpts function: unveiling the contribution of anatomical connectivity to the brain's spontaneous correlation structure. *Chaos: An Interdisciplinary Journal of Nonlinear Science*, 27(4):047409.

[Betzel et al., 2019] Betzel, R. F., Bertolero, M. A., Gordon, E. M., Gratton, C., Dosenbach, N. U., and Bassett, D. S. (2019). The community structure of functional brain networks exhibits scale-specific patterns of inter-and intra-subject variability. *Neuroimage*, 202:115990.

[Betzel et al., 2016] Betzel, R. F., Fukushima, M., He, Y., Zuo, X.-N., and Sporns, O. (2016). Dynamic fluctuations coincide with periods of high and low modularity in resting-state functional brain networks. *NeuroImage*, 127:287–297.

[Bezanson et al., 2017] Bezanson, J., Edelman, A., Karpinski, S., and Shah, V. B. (2017). Julia: A fresh approach to numerical computing. *SIAM review*, 59(1):65–98.

[Blondel et al., 2005] Blondel, V. D., Hendrickx, J. M., Olshevsky, A., and Tsitsiklis, J. N. (2005). Convergence in multiagent coordination, consensus, and flocking. In *Proceedings of the 44th IEEE Conference on Decision and Control*, pages 2996–3000. IEEE.

[Boccaletti et al., 2014] Boccaletti, S., Bianconi, G., Criado, R., Del Genio, C. I., Gómez-Gardenes, J., Romance, M., Sendina-Nadal, I., Wang, Z., and Zanin, M. (2014). The structure and dynamics of multilayer networks. *Physics reports*, 544(1):1–122.

[Boser et al., 1992] Boser, B. E., Guyon, I. M., and Vapnik, V. N. (1992). A training algorithm for optimal margin classifiers. In *Proceedings of the fifth annual workshop on Computational learning theory*, pages 144–152.

[Breakspear, 2017] Breakspear, M. (2017). Dynamic models of large-scale brain activity. *Nature neuroscience*, 20(3):340–352.

[Brodmann, 1909] Brodmann, K. (1909). *Vergleichende Lokalisationslehre der Grosshirnrinde in ihren Prinzipien dargestellt auf Grund des Zellenbaues*. Barth.

[Buckner et al., 2009] Buckner, R. L., Sepulcre, J., Talukdar, T., Krienen, F. M., Liu, H., Hedden, T., Andrews-Hanna, J. R., Sperling, R. A., and Johnson, K. A. (2009). Cortical hubs revealed by intrinsic functional connectivity: mapping, assessment of stability, and relation to alzheimer's disease. *Journal of neuroscience*, 29(6):1860–1873.

[Bühlmann and Van De Geer, 2011] Bühlmann, P. and Van De Geer, S. (2011). *Statistics for high-dimensional data: methods, theory and applications*. Springer Science & Business Media.

[Bullmore and Sporns, 2009] Bullmore, E. and Sporns, O. (2009). Complex brain networks: graph theoretical analysis of structural and functional systems. *Nature reviews neuroscience*, 10(3):186–198.

[Bullmore and Sporns, 2012] Bullmore, E. and Sporns, O. (2012). The economy of brain network organization. *Nature Reviews Neuroscience*, 13(5):336–349.

[Byrge and Kennedy, 2019] Byrge, L. and Kennedy, D. P. (2019). High-accuracy individual identification using a 'thin slice' of the functional connectome. *Network Neuroscience*, 3(2):363–383.

[Cahn and Polich, 2006] Cahn, B. R. and Polich, J. (2006). Meditation states and traits: Eeg, erp, and neuroimaging studies. *Psychological bulletin*, 132(2):180.

[Cammoun et al., 2012] Cammoun, L., Gigandet, X., Meskaldji, D., Thiran, J. P., Sporns, O., Do, K. Q., Maeder, P., Meuli, R., and Hagmann, P. (2012). Mapping the human connectome at multiple scales with diffusion spectrum mri. *Journal of neuroscience methods*, 203(2):386–397.

[Cao, 1997] Cao, L. (1997). Practical method for determining the minimum embedding dimension of a scalar time series. *Physica D: Nonlinear Phenomena*, 110(1-2):43–50.

[Chicharro and Panzeri, 2017] Chicharro, D. and Panzeri, S. (2017). Synergy and redundancy in dual decompositions of mutual information gain and information loss. *Entropy*, 19(2):71.

[Chiêm et al., 2018] Chiêm, B., Crevecoeur, F., and Delvenne, J.-C. (2018). Supervised classification of structural brain networks reveals gender differences. In *2018 19th IEEE Mediterranean Electrotechnical Conference (MELECON)*, pages 269–274. IEEE.

[Cieslak et al., 2020] Cieslak, M., Cook, P. A., He, X., Yeh, F.-C., Dhollander, T., Adebimpe, A., Aguirre, G. K., Bassett, D. S., Betzel, R. F., Bourque, J., et al. (2020). Qsiprep: An integrative platform for preprocessing and reconstructing diffusion mri. *bioRxiv*.

[Cocchi et al., 2014] Cocchi, L., Harding, I. H., Lord, A., Pantelis, C., Yucel, M., and Zalesky, A. (2014). Disruption of structure–function coupling in the schizophrenia connectome. *NeuroImage: Clinical*, 4:779–787.

[Cole et al., 2014] Cole, M. W., Bassett, D. S., Power, J. D., Braver, T. S., and Petersen, S. E. (2014). Intrinsic and task-evoked network architectures of the human brain. *Neuron*, 83(1):238–251.

[Cole et al., 2013] Cole, M. W., Reynolds, J. R., Power, J. D., Repovs, G., Anticevic, A., and Braver, T. S. (2013). Multi-task connectivity reveals flexible hubs for adaptive task control. *Nature neuroscience*, 16(9):1348.

[Combrisson and Jerbi, 2015] Combrisson, E. and Jerbi, K. (2015). Exceeding chance level by chance: The caveat of theoretical chance levels in brain signal classification and statistical assessment of decoding accuracy. *Journal of neuroscience methods*, 250:126–136.

[Cortes and Vapnik, 1995] Cortes, C. and Vapnik, V. (1995). Support-vector networks. *Machine learning*, 20(3):273–297.

[Crofts and Higham, 2009] Crofts, J. J. and Higham, D. J. (2009). A weighted communicability measure applied to complex brain networks. *Journal of the Royal Society Interface*, 6(33):411–414.

[Daducci et al., 2012] Daducci, A., Gerhard, S., Griffa, A., Lemkaddem, A., Cammoun, L., Gigandet, X., Meuli, R., Hagmann, P., and Thiran, J.-P. (2012). The connectome mapper: an open-source processing pipeline to map connectomes with mri. *PloS one*, 7(12):e48121.

[De Martino et al., 2008] De Martino, F., Valente, G., Staeren, N., Ashburner, J., Goebel, R., and Formisano, E. (2008). Combining multivariate voxel selection and support vector machines for mapping and classification of fmri spatial patterns. *Neuroimage*, 43(1):44–58.

[Deco et al., 2011] Deco, G., Jirsa, V. K., and McIntosh, A. R. (2011). Emerging concepts for the dynamical organization of resting-state activity in the brain. *Nature Reviews Neuroscience*, 12(1):43–56.

[Delgado et al., 2000] Delgado, M. R., Nystrom, L. E., Fissell, C., Noll, D., and Fiez, J. A. (2000). Tracking the hemodynamic responses to reward and punishment in the striatum. *Journal of neurophysiology*, 84(6):3072–3077.

[Desikan et al., 2006] Desikan, R. S., Ségonne, F., Fischl, B., Quinn, B. T., Dickerson, B. C., Blacker, D., Buckner, R. L., Dale, A. M., Maguire, R. P., Hyman, B. T., et al. (2006). An automated labeling system for subdividing the human cerebral cortex on mri scans into gyral based regions of interest. *Neuroimage*, 31(3):968–980.

[Destrieux et al., 2010] Destrieux, C., Fischl, B., Dale, A., and Halgren, E. (2010). Automatic parcellation of human cortical gyri and sulci using standard anatomical nomenclature. *Neuroimage*, 53(1):1–15.

[Dhollander and Connelly, 2016] Dhollander, T. and Connelly, A. (2016). A novel iterative approach to reap the benefits of multi-tissue csd from just single-shell (+ b= 0) diffusion mri data. In *Proc ISMRM*, volume 24, page 3010.

[Dhollander et al., 2016] Dhollander, T., Raffelt, D., and Connelly, A. (2016). Unsupervised 3-tissue response function estimation from single-shell or multi-shell diffusion mr data without a co-registered t1 image. In *ISMRM Workshop on Breaking the Barriers of Diffusion MRI*, volume 5, page 5.

[Diedrichsen et al., 2011] Diedrichsen, J., Maderwald, S., Küper, M., Thürling, M., Rabe, K., Gizewski, E., Ladd, M. E., and Timmann, D. (2011). Imaging the deep cerebellar nuclei: a probabilistic atlas and normalization procedure. *Neuroimage*, 54(3):1786–1794.

[Dong et al., 2012] Dong, C.-Y., Shin, D., Joo, S., Nam, Y., and Cho, K.-H. (2012). Identification of feedback loops in neural networks based on multi-step granger causality. *Bioinformatics*, 28(16):2146–2153.

[Dosenbach et al., 2007] Dosenbach, N. U., Fair, D. A., Miezin, F. M., Cohen, A. L., Wenger, K. K., Dosenbach, R. A., Fox, M. D., Snyder, A. Z., Vincent, J. L., Raichle, M. E., et al. (2007). Distinct brain networks for adaptive and stable task control in humans. *Proceedings of the National Academy of Sciences*, 104(26):11073–11078.

[DSM-IV-TR., 2000] DSM-IV-TR., A. (2000). *Diagnostic and statistical manual of mental disorders*. American Psychiatric Association Washington, DC.

[Eisenreich et al., 2017] Eisenreich, B. R., Akaishi, R., and Hayden, B. Y. (2017). Control without controllers: toward a distributed neuroscience of executive control. *Journal of cognitive neuroscience*, 29(10):1684–1698.

[Esteban et al., 2019] Esteban, O., Markiewicz, C. J., Blair, R. W., Moodie, C. A., Isik, A. I., Erramuzpe, A., Kent, J. D., Goncalves, M., DuPre, E., Snyder, M., et al. (2019). fmriprep: a robust preprocessing pipeline for functional mri. *Nature methods*, 16(1):111–116.

[Estrada et al., 2012] Estrada, E., Hatano, N., and Benzi, M. (2012). The physics of communicability in complex networks. *Physics reports*, 514(3):89–119.

[Fan et al., 2016] Fan, L., Li, H., Zhuo, J., Zhang, Y., Wang, J., Chen, L., Yang, Z., Chu, C., Xie, S., Laird, A. R., et al. (2016). The human brainnetome atlas: a new brain atlas based on connectional architecture. *Cerebral cortex*, 26(8):3508–3526.

[Finn et al., 2015] Finn, E. S., Shen, X., Scheinost, D., Rosenberg, M. D., Huang, J., Chun, M. M., Papademetris, X., and Constable, R. T. (2015). Functional connectome fingerprinting: identifying individuals using patterns of brain connectivity. *Nature neuroscience*, 18(11):1664–1671.

[Fonov et al., 2009] Fonov, V. S., Evans, A. C., McKinstry, R. C., Almli, C., and Collins, D. (2009). Unbiased nonlinear average age-appropriate brain templates from birth to adulthood. *NeuroImage*.

[Fornito et al., 2015] Fornito, A., Zalesky, A., and Breakspear, M. (2015). The connectomics of brain disorders. *Nature Reviews Neuroscience*, 16(3):159–172.

[Fornito et al., 2016] Fornito, A., Zalesky, A., and Bullmore, E. (2016). *Fundamentals of brain network analysis*. Academic Press.

[Fox et al., 2014] Fox, K. C., Nijeboer, S., Dixon, M. L., Floman, J. L., Ellamil, M., Rumak, S. P., Sedlmeier, P., and Christoff, K. (2014). Is meditation associated with altered brain structure? a systematic review and meta-analysis of morphometric neuroimaging in meditation practitioners. *Neuroscience & Biobehavioral Reviews*, 43:48–73.

[Friston, 2011] Friston, K. J. (2011). Functional and effective connectivity: a review. *Brain connectivity*, 1(1):13–36.

[Friston et al., 2014] Friston, K. J., Kahan, J., Biswal, B., and Razi, A. (2014). A dcm for resting state fmri. *Neuroimage*, 94:396–407.

[Galán, 2008] Galán, R. F. (2008). On how network architecture determines the dominant patterns of spontaneous neural activity. *PloS one*, 3(5).

[Galante et al., 2014] Galante, J., Galante, I., Bekkers, M.-J., and Gallacher, J. (2014). Effect of kindness-based meditation on health and well-being: a systematic review and meta-analysis. *Journal of consulting and clinical psychology*, 82(6):1101.

[Gilson et al., 2020] Gilson, M., Zamora-López, G., Pallarés, V., Adhikari, M. H., Senden, M., Campo, A. T., Mantini, D., Corbetta, M., Deco, G., and Insabato, A. (2020). Model-based whole-brain effective connectivity to study distributed cognition in health and disease. *Network Neuroscience*, 4(2):338–373.

[Glasser et al., 2018] Glasser, M. F., Coalson, T. S., Bijsterbosch, J. D., Harrison, S. J., Harms, M. P., Anticevic, A., Van Essen, D. C., and Smith, S. M. (2018). Using temporal ica to selectively remove global noise while preserving global signal in functional mri data. *NeuroImage*, 181:692–717.

[Glasser et al., 2016] Glasser, M. F., Coalson, T. S., Robinson, E. C., Hacker, C. D., Harwell, J., Yacoub, E., Ugurbil, K., Andersson, J., Beckmann, C. F., Jenkinson, M., et al. (2016). A multi-modal parcellation of human cerebral cortex. *Nature*, 536(7615):171–178.

[Glasser et al., 2013] Glasser, M. F., Sotiropoulos, S. N., Wilson, J. A., Coalson, T. S., Fischl, B., Andersson, J. L., Xu, J., Jbabdi, S., Webster, M., Polimeni, J. R., et al. (2013). The minimal preprocessing pipelines for the human connectome project. *Neuroimage*, 80:105–124.

[Glickstein, 2006] Glickstein, M. (2006). Golgi and cajal: The neuron doctrine and the 100th anniversary of the 1906 nobel prize. *Current Biology*, 16(5):R147–R151.

[Goebel, 2012] Goebel, R. (2012). Brainvoyager – past, present, future. *Neuroimage*, 62(2):748–756.

[Gómez-Herrero et al., 2015] Gómez-Herrero, G., Wu, W., Rutanen, K., Soriano, M. C., Pipa, G., and Vicente, R. (2015). Assessing coupling dynamics from an ensemble of time series. *Entropy*, 17(4):1958–1970.

[Goñi et al., 2014] Goñi, J., van den Heuvel, M. P., Avena-Koenigsberger, A., de Mendizabal, N. V., Betzel, R. F., Griffa, A., Hagmann, P., Corominas-Murtra, B., Thiran, J.-P., and Sporns, O. (2014). Resting-brain functional connectivity predicted by analytic measures of network communication. *Proceedings of the National Academy of Sciences*, 111(2):833–838.

[Gorgolewski et al., 2011] Gorgolewski, K., Burns, C. D., Madison, C., Clark, D., Halchenko, Y. O., Waskom, M. L., and Ghosh, S. S. (2011). Nipype: a flexible, lightweight and extensible neuroimaging data processing framework in python. *Frontiers in neuroinformatics*, 5:13.

[Granger, 1969] Granger, C. W. (1969). Investigating causal relations by econometric models and cross-spectral methods. *Econometrica: journal of the Econometric Society*, pages 424–438.

[Gratton et al., 2018] Gratton, C., Laumann, T. O., Nielsen, A. N., Greene, D. J., Gordon, E. M., Gilmore, A. W., Nelson, S. M., Coalson, R. S., Snyder, A. Z., Schlaggar, B. L., et al. (2018). Functional brain networks are dominated by stable group and individual factors, not cognitive or daily variation. *Neuron*, 98(2):439–452.

[Greicius et al., 2003] Greicius, M. D., Krasnow, B., Reiss, A. L., and Menon, V. (2003). Functional connectivity in the resting brain: a network analysis of the default mode hypothesis. *Proceedings of the National Academy of Sciences*, 100(1):253–258.

[Griffa et al., 2015] Griffa, A., Baumann, P. S., Ferrari, C., Do, K. Q., Conus, P., Thiran, J.-P., and Hagmann, P. (2015). Characterizing the connectome in schizophrenia with diffusion spectrum imaging. *Human brain mapping*, 36(1):354–366.

[Griffa et al., 2019] Griffa, A., Baumann, P. S., Klauser, P., Mullier, E., Cleusix, M., Jenni, R., van den Heuvel, M. P., Do, K. Q., Conus, P., and Hagmann, P. (2019). Brain connectivity alterations in early psychosis: from clinical to neuroimaging staging. *Translational psychiatry*, 9(1):1–10.

[Griffa et al., 2013] Griffa, A., Baumann, P. S., Thiran, J.-P., and Hagmann, P. (2013). Structural connectomics in brain diseases. *Neuroimage*, 80:515–526.

[Griffa et al., 2017] Griffa, A., Ricaud, B., Benzi, K., Bresson, X., Daducci, A., Vandergheynst, P., Thiran, J.-P., and Hagmann, P. (2017). Transient networks of spatio-temporal connectivity map communication pathways in brain functional systems. *NeuroImage*, 155:490–502.

[Gross et al., 2013] Gross, J., Baillet, S., Barnes, G. R., Henson, R. N., Hillebrand, A., Jensen, O., Jerbi, K., Litvak, V., Maess, B., Oostenveld, R., et al. (2013). Good practice for conducting and reporting meg research. *Neuroimage*, 65:349–363.

[Groß et al., 2000] Groß, J., Tass, P., Salenius, S., Hari, R., Freund, H.-J., and Schnitzler, A. (2000). Cortico-muscular synchronization during isometric muscle contraction in humans as revealed by magnetoencephalography. *The Journal of Physiology*, 527(3):623–631.

[Grossman et al., 2004] Grossman, P., Niemann, L., Schmidt, S., and Walach, H. (2004). Mindfulness-based stress reduction and health benefits: A meta-analysis. *Journal of psychosomatic research*, 57(1):35–43.

[Gu et al., 2017] Gu, S., Betzel, R. F., Mattar, M. G., Cieslak, M., Delio, P. R., Grafton, S. T., Pasqualetti, F., and Bassett, D. S. (2017). Optimal trajectories of brain state transitions. *Neuroimage*, 148:305–317.

[Gu et al., 2015] Gu, S., Pasqualetti, F., Cieslak, M., Telesford, Q. K., Alfred, B. Y., Kahn, A. E., Medaglia, J. D., Vettel, J. M., Miller, M. B., Grafton, S. T., et al. (2015). Controllability of structural brain networks. *Nature communications*, 6(1):1–10.

[Guimera et al., 2005] Guimera, R., Mossa, S., Turtschi, A., and Amaral, L. N. (2005). The worldwide air transportation network: Anomalous centrality, community structure, and cities' global roles. *Proceedings of the National Academy of Sciences*, 102(22):7794–7799.

[Gutiérrez-Gómez et al., 2020] Gutiérrez-Gómez, L., Vohryzek, J., Chiêm, B., Baumann, P. S., Conus, P., Do Cuenod, K., Hagmann, P., and Delvenne, J.-C. (2020). Stable biomarker identification for predicting schizophrenia in the human connectome. *NeuroImage: Clinical*, 27:102316.

[Guyon et al., 2002] Guyon, I., Weston, J., Barnhill, S., and Vapnik, V. (2002). Gene selection for cancer classification using support vector machines. *Machine learning*, 46(1):389–422.

[Hagmann et al., 2008] Hagmann, P., Cammoun, L., Gigandet, X., Meuli, R., Honey, C. J., Wedeen, V. J., and Sporns, O. (2008). Mapping the structural core of human cerebral cortex. *PLoS Biol*, 6(7):e159.

[Hahs and Pethel, 2013] Hahs, D. W. and Pethel, S. D. (2013). Transfer entropy for coupled autoregressive processes. *Entropy*, 15(3):767–788.

[Hiemstra and Jones, 1994] Hiemstra, C. and Jones, J. D. (1994). Testing for linear and nonlinear granger causality in the stock price-volume relation. *The Journal of Finance*, 49(5):1639–1664.

[Hlinka et al., 2011] Hlinka, J., Paluš, M., Vejmelka, M., Mantini, D., and Corbetta, M. (2011). Functional connectivity in resting-state fmri: is linear correlation sufficient? *Neuroimage*, 54(3):2218–2225.

[Hölzel et al., 2011a] Hölzel, B. K., Carmody, J., Vangel, M., Congleton, C., Yerramsetti, S. M., Gard, T., and Lazar, S. W. (2011a). Mindfulness practice leads to increases in regional brain gray matter density. *Psychiatry research: neuroimaging*, 191(1):36–43.

[Hölzel et al., 2011b] Hölzel, B. K., Lazar, S. W., Gard, T., Schuman-Olivier, Z., Vago, D. R., and Ott, U. (2011b). How does mindfulness meditation work? proposing mechanisms of action from a conceptual and neural perspective. *Perspectives on psychological science*, 6(6):537–559.

[Honey et al., 2009] Honey, C. J., Sporns, O., Cammoun, L., Gigandet, X., Thiran, J.-P., Meuli, R., and Hagmann, P. (2009). Predicting human resting-state functional connectivity from structural connectivity. *Proceedings of the National Academy of Sciences*, 106(6):2035–2040.

[Honey et al., 2010] Honey, C. J., Thivierge, J.-P., and Sporns, O. (2010). Can structure predict function in the human brain? *Neuroimage*, 52(3):766–776.

[Hutchison et al., 2013] Hutchison, R. M., Womelsdorf, T., Allen, E. A., Bandettini, P. A., Calhoun, V. D., Corbetta, M., Della Penna, S., Duyn, J. H., Glover, G. H., Gonzalez-Castillo, J., et al. (2013). Dynamic functional connectivity: promise, issues, and interpretations. *Neuroimage*, 80:360–378.

[Insel et al., 2013] Insel, T. R., Landis, S. C., and Collins, F. S. (2013). The nih brain initiative. *Science*, 340(6133):687–688.

[Ito et al., 2017] Ito, T., Kulkarni, K. R., Schultz, D. H., Mill, R. D., Chen, R. H., Solomyak, L. I., and Cole, M. W. (2017). Cognitive task information is transferred between brain regions via resting-state network topology. *Nature communications*, 8(1):1–14.

[Iturria-Medina et al., 2018] Iturria-Medina, Y., Carbonell, F. M., Evans, A. C., Initiative, A. D. N., et al. (2018). Multimodal imaging-based therapeutic fingerprints for optimizing personalized interventions: Application to neurodegeneration. *Neuroimage*, 179:40–50.

[James et al., 2013] James, G., Witten, D., Hastie, T., and Tibshirani, R. (2013). *An introduction to statistical learning*, volume 112. Springer.

[Jenkinson et al., 2002] Jenkinson, M., Bannister, P., Brady, M., and Smith, S. (2002). Improved optimization for the robust and accurate linear registration and motion correction of brain images. *Neuroimage*, 17(2):825–841.

[Jenkinson et al., 2012] Jenkinson, M., Beckmann, C. F., Behrens, T. E., Woolrich, M. W., and Smith, S. M. (2012). Fsl. *Neuroimage*, 62(2):782–790.

[Jeurissen et al., 2014] Jeurissen, B., Tournier, J.-D., Dhollander, T., Connelly, A., and Sijbers, J. (2014). Multi-tissue constrained spherical deconvolution for improved analysis of multi-shell diffusion mri data. *NeuroImage*, 103:411–426.

[Kaiser and Schreiber, 2002] Kaiser, A. and Schreiber, T. (2002). Information transfer in continuous processes. *Physica D: Nonlinear Phenomena*, 166(1-2):43–62.

[Karrer et al., 2020] Karrer, T. M., Kim, J. Z., Stiso, J., Kahn, A. E., Pasqualetti, F., Habel, U., and Bassett, D. S. (2020). A practical guide to methodological considerations in the controllability of structural brain networks. *Journal of Neural Engineering*, 17(2):026031.

[Ketteler et al., 2008] Ketteler, D., Kastrau, F., Vohn, R., and Huber, W. (2008). The subcortical role of language processing. high level linguistic features such as ambiguity-resolution and the human brain; an fmri study. *NeuroImage*, 39(4):2002–2009.

[Kiebel et al., 2008] Kiebel, S. J., Garrido, M. I., Moran, R. J., and Friston, K. J. (2008). Dynamic causal modelling for eeg and meg. *Cognitive neurodynamics*, 2(2):121.

[Kim et al., 2010] Kim, D. I., Sui, J., Rachakonda, S., White, T., Manoach, D. S., Clark, V. P., Ho, B.-C., Schulz, S. C., and Calhoun, V. D. (2010). Identification of imaging biomarkers in schizophrenia: a coefficient-constrained independent component analysis of the mind multi-site schizophrenia study. *Neuroinformatics*, 8(4):213–229.

[Kim et al., 2018] Kim, J. Z., Soffer, J. M., Kahn, A. E., Vettel, J. M., Pasqualetti, F., and Bassett, D. S. (2018). Role of graph architecture in controlling dynamical networks with applications to neural systems. *Nature physics*, 14(1):91.

[Korhonen et al., 2021] Korhonen, O., Zanin, M., and Papo, D. (2021). Principles and open questions in functional brain network reconstruction. *Human Brain Mapping*.

[Kozachenko and Leonenko, 1987] Kozachenko, L. and Leonenko, N. N. (1987). Sample estimate of the entropy of a random vector. *Problemy Peredachi Informatsii*, 23(2):9–16.

[Koziol and Budding, 2009] Koziol, L. F. and Budding, D. E. (2009). *Subcortical structures and cognition: Implications for neuropsychological assessment*. Springer Science & Business Media.

[Kraskov et al., 2004] Kraskov, A., Stögbauer, H., and Grassberger, P. (2004). Estimating mutual information. *Physical review E*, 69(6):066138.

[Kumar et al., 2017] Kumar, K., Desrosiers, C., Siddiqi, K., Colliot, O., and Toews, M. (2017). Fiberprint: A subject fingerprint based on sparse code pooling for white matter fiber analysis. *NeuroImage*, 158:242–259.

[Kumar et al., 2018] Kumar, K., Toews, M., Chauvin, L., Colliot, O., and Desrosiers, C. (2018). Multi-modal brain fingerprinting: a manifold approximation based framework. *NeuroImage*, 183:212–226.

[Kuncheva, 2007] Kuncheva, L. I. (2007). A stability index for feature selection. In *Artificial intelligence and applications*, pages 421–427.

[Lambiotte et al., 2014] Lambiotte, R., Delvenne, J.-C., and Barahona, M. (2014). Random walks, markov processes and the multiscale modular organization of complex networks. *IEEE Transactions on Network Science and Engineering*, 1(2):76–90.

[Lambiotte et al., 2011] Lambiotte, R., Sinatra, R., Delvenne, J.-C., Evans, T. S., Barahona, M., and Latora, V. (2011). Flow graphs: Interweaving dynamics and structure. *Physical Review E*, 84(1):017102.

[Larson-Prior et al., 2013] Larson-Prior, L. J., Oostenveld, R., Della Penna, S., Michalareas, G., Prior, F., Babajani-Feremi, A., Schoffelen, J.-M., Marzetti, L., De Pasquale, F., Di Pompeo, F., et al. (2013). Adding dynamics to the human connectome project with meg. *Neuroimage*, 80:190–201.

[Lazar et al., 2005] Lazar, S. W., Kerr, C. E., Wasserman, R. H., Gray, J. R., Greve, D. N., Treadway, M. T., McGarvey, M., Quinn, B. T., Dusek, J. A., Benson, H., et al. (2005). Meditation experience is associated with increased cortical thickness. *Neuroreport*, 16(17):1893.

[Liégeois et al., 2020] Liégeois, R., Santos, A., Matta, V., Van De Ville, D., and Sayed, A. H. (2020). Revisiting correlation-based functional connectivity and its relationship with structural connectivity. *Network Neuroscience*, pages 1–17.

[Lindner et al., 2011] Lindner, M., Vicente, R., Priesemann, V., and Wibral, M. (2011). Trentool: A matlab open source toolbox to analyse information flow in time series data with transfer entropy. *BMC neuroscience*, 12(1):1–22.

[Listgarten et al., 2004] Listgarten, J., Neal, R., Roweis, S., and Emili, A. (2004). Multiple alignment of continuous time series. *Advances in neural information processing systems*, 17:817–824.

[Liu et al., 2018] Liu, J., Liao, X., Xia, M., and He, Y. (2018). Chronnectome fingerprinting: identifying individuals and predicting higher cognitive functions using dynamic brain connectivity patterns. *Human brain mapping*, 39(2):902–915.

[Liu et al., 2011] Liu, Y.-Y., Slotine, J.-J., and Barabási, A.-L. (2011). Controllability of complex networks. *nature*, 473(7346):167–173.

[Lizier and Rubinov, 2012] Lizier, J. and Rubinov, M. (2012). Multivariate construction of effective computational networks from observational data. *Preprints of the Max Planck Institute for Mathematics in the Sciences*.

[Lizier and Prokopenko, 2010] Lizier, J. T. and Prokopenko, M. (2010). Differentiating information transfer and causal effect. *The European Physical Journal B*, 73(4):605–615.

[Lizier et al., 2010] Lizier, J. T., Prokopenko, M., and Zomaya, A. Y. (2010). Information modification and particle collisions in distributed computation. *Chaos: An Interdisciplinary Journal of Nonlinear Science*, 20(3):037109.

[Lizier et al., 2012] Lizier, J. T., Prokopenko, M., and Zomaya, A. Y. (2012). Local measures of information storage in complex distributed computation. *Information Sciences*, 208:39–54.

[Luders et al., 2009] Luders, E., Toga, A. W., Lepore, N., and Gaser, C. (2009). The underlying anatomical correlates of long-term meditation: larger hippocampal and frontal volumes of gray matter. *Neuroimage*, 45(3):672–678.

[Lurie et al., 2020] Lurie, D. J., Kessler, D., Bassett, D. S., Betzel, R. F., Breakspear, M., Kheilholz, S., Kucyi, A., Liégeois, R., Lindquist, M. A., McIntosh, A. R., et al. (2020). Questions and controversies in the study of time-varying functional connectivity in resting fmri. *Network Neuroscience*, 4(1):30–69.

[Lynall et al., 2010] Lynall, M.-E., Bassett, D. S., Kerwin, R., McKenna, P. J., Kitzbichler, M., Muller, U., and Bullmore, E. (2010). Functional connectivity and brain networks in schizophrenia. *Journal of Neuroscience*, 30(28):9477–9487.

[Maaten and Hinton, 2008] Maaten, L. v. d. and Hinton, G. (2008). Visualizing data using t-sne. *Journal of machine learning research*, 9(Nov):2579–2605.

[Marcus et al., 2011] Marcus, D., Harwell, J., Olsen, T., Hodge, M., Glasser, M., Prior, F., Jenkinson, M., Laumann, T., Curtiss, S., and Van Essen, D. (2011). Informatics and data mining tools and strategies for the human connectome project. *Frontiers in neuroinformatics*, 5:4.

[Marinazzo et al., 2008] Marinazzo, D., Pellicoro, M., and Stramaglia, S. (2008). Kernel method for nonlinear granger causality. *Physical review letters*, 100(14):144103.

[Marrelec et al., 2006] Marrelec, G., Krainik, A., Duffau, H., Pélégrini-Issac, M., Lehéricy, S., Doyon, J., and Benali, H. (2006). Partial correlation for functional brain interactivity investigation in functional mri. *Neuroimage*, 32(1):228–237.

[Mars et al., 2018] Mars, R. B., Passingham, R. E., and Jbabdi, S. (2018). Connectivity fingerprints: from areal descriptions to abstract spaces. *Trends in cognitive sciences*, 22(11):1026–1037.

[Medaglia, 2019] Medaglia, J. D. (2019). Clarifying cognitive control and the controllable connectome. *Wiley Interdisciplinary Reviews: Cognitive Science*, 10(1):e1471.

[Menon and Krishnamurthy, 2019] Menon, S. S. and Krishnamurthy, K. (2019). A comparison of static and dynamic functional connectivities for identifying subjects and biological sex using intrinsic individual brain connectivity. *Scientific reports*, 9(1):1–11.

[Messé, 2020] Messé, A. (2020). Parcellation influence on the connectivity-based structure–function relationship in the human brain. *Human brain mapping*, 41(5):1167–1180.

[Meunier et al., 2010] Meunier, D., Lambiotte, R., and Bullmore, E. T. (2010). Modular and hierarchically modular organization of brain networks. *Frontiers in neuroscience*, 4:200.

[Micheloyannis et al., 2006] Micheloyannis, S., Pachou, E., Stam, C. J., Breakspear, M., Bitsios, P., Vourkas, M., Erimaki, S., and Zervakis, M. (2006). Small-world networks and disturbed functional connectivity in schizophrenia. *Schizophrenia research*, 87(1-3):60–66.

[Milham et al., 2020] Milham, M. P., Vogelstein, J., and Xu, T. (2020). Removing the reliability bottleneck in functional magnetic resonance imaging research to achieve clinical utility. *JAMA psychiatry*.

[Mišić et al., 2016] Mišić, B., Betzel, R. F., De Reus, M. A., van den Heuvel, M. P., Berman, M. G., McIntosh, A. R., and Sporns, O. (2016). Network-level structure-function relationships in human neocortex. *Cerebral Cortex*, 26(7):3285–3296.

[Mišić et al., 2015] Mišić, B., Betzel, R. F., Nematzadeh, A., Goni, J., Griffa, A., Hagmann, P., Flammini, A., Ahn, Y.-Y., and Sporns, O. (2015). Cooperative and competitive spreading dynamics on the human connectome. *Neuron*, 86(6):1518–1529.

[Mohar et al., 1991] Mohar, B., Alavi, Y., Chartrand, G., and Oellermann, O. (1991). The laplacian spectrum of graphs. *Graph theory, combinatorics, and applications*, 2(871-898):12.

[Montalto et al., 2014] Montalto, A., Faes, L., and Marinazzo, D. (2014). Mute: A new matlab toolbox for estimating the multivariate transfer entropy in physiological variability series. In *2014 8th Conference of the European Study Group on Cardiovascular Oscillations (ESGCO)*, pages 59–60. IEEE.

[Mori and Zhang, 2006] Mori, S. and Zhang, J. (2006). Principles of diffusion tensor imaging and its applications to basic neuroscience research. *Neuron*, 51(5):527–539.

[Murphy et al., 2009] Murphy, K., Birn, R. M., Handwerker, D. A., Jones, T. B., and Bandettini, P. A. (2009). The impact of global signal regression on resting state correlations: are anti-correlated networks introduced? *Neuroimage*, 44(3):893–905.

[Murphy and Fox, 2017] Murphy, K. and Fox, M. D. (2017). Towards a consensus regarding global signal regression for resting state functional connectivity mri. *Neuroimage*, 154:169–173.

[Newman, 2018] Newman, M. (2018). *Networks*. Oxford university press.

[Newman and Park, 2003] Newman, M. E. and Park, J. (2003). Why social networks are different from other types of networks. *Physical review E*, 68(3):036122.

[Novelli and Lizier, 2020] Novelli, L. and Lizier, J. T. (2020). Inferring network properties from time series using transfer entropy and mutual information: validation of multivariate versus bivariate approaches. *Network Neuroscience*, pages 1–52.

[Novelli et al., 2019] Novelli, L., Wollstadt, P., Mediano, P., Wibral, M., and Lizier, J. T. (2019). Large-scale directed network inference with multivariate transfer entropy and hierarchical statistical testing. *Network Neuroscience*, 3(3):827–847.

[Ogawa et al., 1990] Ogawa, S., Lee, T.-M., Kay, A. R., and Tank, D. W. (1990). Brain magnetic resonance imaging with contrast dependent on blood oxygenation. *proceedings of the National Academy of Sciences*, 87(24):9868–9872.

[Oldham et al., 2020] Oldham, S., Arnatkeviciute, A., Smith, R. E., Tiego, J., Bellgrove, M. A., and Fornito, A. (2020). The efficacy of different preprocessing steps in reducing motion-related confounds in diffusion mri connectomics. *NeuroImage*, 222:117252.

[Omrani et al., 2016] Omrani, M., Murnaghan, C. D., Pruszynski, J. A., and Scott, S. H. (2016). Distributed task-specific processing of somatosensory feedback for voluntary motor control. *Elife*, 5:e13141.

[Oostenveld et al., 2011] Oostenveld, R., Fries, P., Maris, E., and Schoffelen, J.-M. (2011). Fieldtrip: open source software for advanced analysis of meg, eeg, and invasive electrophysiological data. *Computational intelligence and neuroscience*, 2011.

[Osmanlıoğlu et al., 2019] Osmanlıoğlu, Y., Tunç, B., Parker, D., Elliott, M. A., Baum, G. L., Ciric, R., Satterthwaite, T. D., Gur, R. E., Gur, R. C., and Verma, R. (2019). System-level matching of structural and functional connectomes in the human brain. *Neuroimage*, 199:93–104.

[Ospina et al., 2007] Ospina, M. B., Bond, K., Karkhaneh, M., Tjosvold, L., Vandermeer, B., Liang, Y., Bialy, L., Hooton, N., Buscemi, N., Dryden, D. M., et al. (2007). Meditation practices for health: state of the research. *Evid Rep Technol Assess (Full Rep)*, 155(155):1–263.

[Pallarés et al., 2018] Pallarés, V., Insabato, A., Sanjuán, A., Kühn, S., Mantini, D., Deco, G., and Gilson, M. (2018). Extracting orthogonal subject-and condition-specific signatures from fmri data using whole-brain effective connectivity. *Neuroimage*, 178:238–254.

[Panzeri et al., 2007] Panzeri, S., Senatore, R., Montemurro, M. A., and Petersen, R. S. (2007). Correcting for the sampling bias problem in spike train information measures. *Journal of neurophysiology*, 98(3):1064–1072.

[Parkes et al., 2018] Parkes, L., Fulcher, B., Yücel, M., and Fornito, A. (2018). An evaluation of the efficacy, reliability, and sensitivity of motion correction strategies for resting-state functional mri. *Neuroimage*, 171:415–436.

[Pasqualetti et al., 2019] Pasqualetti, F., Gu, S., and Bassett, D. S. (2019). Re: Warnings and caveats in brain controllability. *NeuroImage*, 197:586–588.

[Pasqualetti et al., 2014] Pasqualetti, F., Zampieri, S., and Bullo, F. (2014). Controllability metrics, limitations and algorithms for complex networks. *IEEE Transactions on Control of Network Systems*, 1(1):40–52.

[Pedregosa et al., 2011] Pedregosa, F., Varoquaux, G., Gramfort, A., Michel, V., Thirion, B., Grisel, O., Blondel, M., Prettenhofer, P., Weiss, R., Dubourg, V., et al. (2011). Scikit-learn: Machine learning in python. *the Journal of machine Learning research*, 12:2825–2830.

[Pernet et al., 2021] Pernet, C. R., Belov, N., Delorme, A., and Zammit, A. (2021). Mindfulness related changes in grey matter: a systematic review and meta-analysis. *Brain Imaging and Behavior*, pages 1–11.

[Pfurtscheller et al., 2006] Pfurtscheller, G., Brunner, C., Schlögl, A., and Da Silva, F. L. (2006). Mu rhythm (de) synchronization and eeg single-trial classification of different motor imagery tasks. *NeuroImage*, 31(1):153–159.

[Ponten et al., 2009] Ponten, S. C., Douw, L., Bartolomei, F., Reijneveld, J., and Stam, C. (2009). Indications for network regularization during absence seizures: weighted and unweighted graph theoretical analyses. *Experimental neurology*, 217(1):197–204.

[Power et al., 2014] Power, J. D., Mitra, A., Laumann, T. O., Snyder, A. Z., Schlaggar, B. L., and Petersen, S. E. (2014). Methods to detect, characterize, and remove motion artifact in resting state fmri. *Neuroimage*, 84:320–341.

[Power and Petersen, 2013] Power, J. D. and Petersen, S. E. (2013). Control-related systems in the human brain. *Current opinion in neurobiology*, 23(2):223–228.

[Power et al., 2017] Power, J. D., Plitt, M., Laumann, T. O., and Martin, A. (2017). Sources and implications of whole-brain fmri signals in humans. *Neuroimage*, 146:609–625.

[Preisig et al., 1999] Preisig, M., Fenton, B. T., Matthey, M.-L., Berney, A., and Ferrero, F. (1999). Diagnostic interview for genetic studies (digs): inter-rater and test-retest reliability of the french version. *European archives of psychiatry and clinical neuroscience*, 249(4):174–179.

[Preti and Van De Ville, 2019] Preti, M. G. and Van De Ville, D. (2019). Decoupling of brain function from structure reveals regional behavioral specialization in humans. *Nature communications*, 10(1):1–7.

[Puxeddu et al., 2020] Puxeddu, M. G., Faskowitz, J., Betzel, R. F., Petti, M., Astolfi, L., and Sporns, O. (2020). The modular organization of brain cortical connectivity across the human lifespan. *NeuroImage*, 218:116974.

[Ragwitz and Kantz, 2002] Ragwitz, M. and Kantz, H. (2002). Markov models from data by simple nonlinear time series predictors in delay embedding spaces. *Physical Review E*, 65(5):056201.

[Rajapandian et al., 2020] Rajapandian, M., Amico, E., Abbas, K., Ventresca, M., and Goñi, J. (2020). Uncovering differential identifiability in network properties of human brain functional connectomes. *Network Neuroscience*, 4(3):698–713.

[Reid et al., 2019] Reid, A. T., Headley, D. B., Mill, R. D., Sanchez-Romero, R., Uddin, L. Q., Marinazzo, D., Lurie, D. J., Valdés-Sosa, P. A., Hanson, S. J., Biswal, B. B., et al. (2019). Advancing functional connectivity research from association to causation. *Nature neuroscience*, 22(11):1751–1760.

[Rensonnet et al., 2019] Rensonnet, G., Scherrer, B., Girard, G., Jankovski, A., Warfield, S. K., Macq, B., Thiran, J.-P., and Taquet, M. (2019). Towards microstructure fingerprinting: Estimation of tissue properties from a dictionary of monte carlo diffusion mri simulations. *NeuroImage*, 184:964–980.

[Rosenthal et al., 2018] Rosenthal, G., Váša, F., Griffa, A., Hagmann, P., Amico, E., Goñi, J., Avidan, G., and Sporns, O. (2018). Mapping higher-order relations between brain structure and function with embedded vector representations of connectomes. *Nature communications*, 9(1):2178.

[Rothwell et al., 1991] Rothwell, J., Thompson, P., Day, B., Boyd, S., and Marsden, C. (1991). Stimulation of the human motor cortex through the scalp. *Experimental Physiology: Translation and Integration*, 76(2):159–200.

[Rubinov and Sporns, 2010] Rubinov, M. and Sporns, O. (2010). Complex network measures of brain connectivity: uses and interpretations. *Neuroimage*, 52(3):1059–1069.

[Runge et al., 2012] Runge, J., Heitzig, J., Petoukhov, V., and Kurths, J. (2012). Escaping the curse of dimensionality in estimating multivariate transfer entropy. *Physical review letters*, 108(25):258701.

[Satterthwaite et al., 2018] Satterthwaite, T. D., Xia, C. H., and Bassett, D. S. (2018). Personalized neuroscience: Common and individual-specific features in functional brain networks. *Neuron*, 98(2):243–245.

[Sauerbrei et al., 2020] Sauerbrei, B. A., Guo, J.-Z., Cohen, J. D., Mischiati, M., Guo, W., Kabra, M., Verma, N., Mensh, B., Branson, K., and Hantman, A. W. (2020). Cortical pattern generation during dexterous movement is input-driven. *Nature*, 577(7790):386–391.

[Schaefer et al., 2014] Schaefer, A., Margulies, D. S., Lohmann, G., Gorgolewski, K. J., Smallwood, J., Kiebel, S. J., and Villringer, A. (2014). Dynamic network participation of functional connectivity hubs assessed by resting-state fmri. *Frontiers in human neuroscience*, 8:195.

[Schaub et al., 2015] Schaub, M. T., Billeh, Y. N., Anastassiou, C. A., Koch, C., and Barahona, M. (2015). Emergence of slow-switching assemblies in structured neuronal networks. *PLoS computational biology*, 11(7).

[Schreiber, 2000] Schreiber, T. (2000). Measuring information transfer. *Physical review letters*, 85(2):461.

[Scott, 2004] Scott, S. H. (2004). Optimal feedback control and the neural basis of volitional motor control. *Nature Reviews Neuroscience*, 5(7):532–545.

[Sedlmeier et al., 2012] Sedlmeier, P., Eberth, J., Schwarz, M., Zimmermann, D., Haarig, F., Jaeger, S., and Kunze, S. (2012). The psychological effects of meditation: a meta-analysis. *Psychological bulletin*, 138(6):1139.

[Seeley et al., 2009] Seeley, W. W., Crawford, R. K., Zhou, J., Miller, B. L., and Greicius, M. D. (2009). Neurodegenerative diseases target large-scale human brain networks. *Neuron*, 62(1):42–52.

[Seguin et al., 2018] Seguin, C., van den Heuvel, M. P., and Zalesky, A. (2018). Navigation of brain networks. *Proceedings of the National Academy of Sciences*, 115(24):6297–6302.

[Seitzman et al., 2019] Seitzman, B. A., Gratton, C., Laumann, T. O., Gordon, E. M., Adeyemo, B., Dworetsky, A., Kraus, B. T., Gilmore, A. W., Berg, J. J., Ortega, M., et al. (2019). Trait-like variants in human functional brain networks. *Proceedings of the National Academy of Sciences*, 116(45):22851–22861.

[Seth et al., 2015] Seth, A. K., Barrett, A. B., and Barnett, L. (2015). Granger causality analysis in neuroscience and neuroimaging. *Journal of Neuroscience*, 35(8):3293–3297.

[Sexton et al., 2014] Sexton, C. E., Walhovd, K. B., Storsve, A. B., Tamnes, C. K., Westlye, L. T., Johansen-Berg, H., and Fjell, A. M. (2014). Accelerated changes in white matter microstructure during aging: a longitudinal diffusion tensor imaging study. *Journal of Neuroscience*, 34(46):15425–15436.

[Shadmehr and Krakauer, 2008] Shadmehr, R. and Krakauer, J. W. (2008). A computational neuroanatomy for motor control. *Experimental brain research*, 185(3):359–381.

[Shannon, 1948] Shannon, C. E. (1948). A mathematical theory of communication. *The Bell system technical journal*, 27(3):379–423.

[Shine et al., 2018] Shine, J. M., Aburn, M. J., Breakspear, M., and Poldrack, R. A. (2018). The modulation of neural gain facilitates a transition between functional segregation and integration in the brain. *Elife*, 7:e31130.

[Shine et al., 2016] Shine, J. M., Bissett, P. G., Bell, P. T., Koyejo, O., Balsters, J. H., Gorgolewski, K. J., Moodie, C. A., and Poldrack, R. A. (2016). The dynamics of functional brain networks: integrated network states during cognitive task performance. *Neuron*, 92(2):544–554.

[Shine et al., 2019] Shine, J. M., Breakspear, M., Bell, P. T., Martens, K. A. E., Shine, R., Koyejo, O., Sporns, O., and Poldrack, R. A. (2019). Human cognition involves the dynamic integration of neural activity and neuromodulatory systems. *Nature neuroscience*, 22(2):289–296.

[Smith et al., 2012] Smith, R. E., Tournier, J.-D., Calamante, F., and Connelly, A. (2012). Anatomically-constrained tractography: improved diffusion mri streamlines tractography through effective use of anatomical information. *Neuroimage*, 62(3):1924–1938.

[Smith et al., 2015] Smith, R. E., Tournier, J.-D., Calamante, F., and Connelly, A. (2015). Sift2: Enabling dense quantitative assessment of brain white matter connectivity using streamlines tractography. *Neuroimage*, 119:338–351.

[Smith et al., 2013] Smith, S. M., Beckmann, C. F., Andersson, J., Auerbach, E. J., Bijsterbosch, J., Douaud, G., Duff, E., Feinberg, D. A., Griffanti, L., Harms, M. P., et al. (2013). Resting-state fmri in the human connectome project. *Neuroimage*, 80:144–168.

[Smith et al., 2004] Smith, S. M., Jenkinson, M., Woolrich, M. W., Beckmann, C. F., Behrens, T. E., Johansen-Berg, H., Bannister, P. R., De Luca, M., Drobnjak, I., Flitney, D. E., et al. (2004). Advances in functional and structural mr image analysis and implementation as fsl. *Neuroimage*, 23:S208–S219.

[Sporns, 2010] Sporns, O. (2010). *Networks of the Brain*. MIT press.

[Sporns and Betzel, 2016] Sporns, O. and Betzel, R. F. (2016). Modular brain networks. *Annual review of psychology*, 67:613–640.

[Sporns et al., 2005] Sporns, O., Tononi, G., and Kötter, R. (2005). The human connectome: a structural description of the human brain. *PLoS Comput Biol*, 1(4):e42.

[Sripada et al., 2019] Sripada, C., Angstadt, M., Rutherford, S., Kessler, D., Kim, Y., Yee, M., and Levina, E. (2019). Basic units of inter-individual variation in resting state connectomes. *Scientific reports*, 9(1):1–12.

[Stam and Van Straaten, 2012] Stam, C. v. and Van Straaten, E. (2012). The organization of physiological brain networks. *Clinical neurophysiology*, 123(6):1067–1087.

[Stanley et al., 2013] Stanley, M. L., Moussa, M. N., Paolini, B., Lyday, R. G., Burdette, J. H., and Laurienti, P. J. (2013). Defining nodes in complex brain networks. *Frontiers in computational neuroscience*, 7:169.

[Stephan et al., 2010] Stephan, K. E., Penny, W. D., Moran, R. J., den Ouden, H. E., Daunizeau, J., and Friston, K. J. (2010). Ten simple rules for dynamic causal modeling. *Neuroimage*, 49(4):3099–3109.

[Stramaglia et al., 2014] Stramaglia, S., Cortes, J. M., and Marinazzo, D. (2014). Synergy and redundancy in the granger causal analysis of dynamical networks. *New Journal of Physics*, 16(10):105003.

[Suárez et al., 2020] Suárez, L. E., Markello, R. D., Betzel, R. F., and Misic, B. (2020). Linking structure and function in macroscale brain networks. *Trends in Cognitive Sciences*, 24(4):302–315.

[Sun et al., 2004] Sun, F. T., Miller, L. M., and D'Esposito, M. (2004). Measuring interregional functional connectivity using coherence and partial coherence analyses of fmri data. *Neuroimage*, 21(2):647–658.

[Supekar et al., 2008] Supekar, K., Menon, V., Rubin, D., Musen, M., and Greicius, M. D. (2008). Network analysis of intrinsic functional brain connectivity in alzheimer's disease. *PLoS Comput Biol*, 4(6):e1000100.

[Svaldi et al., 2019] Svaldi, D. O., Goñi, J., Abbas, K., Amico, E., Clark, D. G., Muralidharan, C., Dzemidzic, M., West, J. D., Risacher, S. L., Saykin, A. J., et al. (2019). Optimizing differential identifiability improves connectome predictive modeling of cognitive deficits in alzheimer's disease. *arXiv preprint arXiv:1908.06197*.

[Takens, 1981] Takens, F. (1981). Detecting strange attractors in turbulence. In *Dynamical systems and turbulence, Warwick 1980*, pages 366–381. Springer.

[Tang et al., 2017] Tang, E., Giusti, C., Baum, G. L., Gu, S., Pollock, E., Kahn, A. E., Roalf, D. R., Moore, T. M., Ruparel, K., Gur, R. C., et al. (2017). Developmental increases in white matter network controllability support a growing diversity of brain dynamics. *Nature communications*, 8(1):1–16.

[Tang et al., 2015] Tang, Y.-Y., Hölzel, B. K., and Posner, M. I. (2015). The neuroscience of mindfulness meditation. *Nature Reviews Neuroscience*, 16(4):213–225.

[Tang et al., 2012] Tang, Y.-Y., Lu, Q., Fan, M., Yang, Y., and Posner, M. I. (2012). Mechanisms of white matter changes induced by meditation. *Proceedings of the National Academy of Sciences*, 109(26):10570–10574.

[Tewarie et al., 2020] Tewarie, P., Prasse, B., Meier, J. M., Santos, F. A., Douw, L., Schoonheim, M., Stam, C. J., Van Mieghem, P., and Hillebrand, A. (2020). Mapping functional brain networks from the structural connectome: relating the series expansion and eigenmode approaches. *NeuroImage*, page 116805.

[Thomas Yeo et al., 2011] Thomas Yeo, B., Krienen, F. M., Sepulcre, J., Sabuncu, M. R., Lashkari, D., Hollinshead, M., Roffman, J. L., Smoller, J. W., Zöllei, L., Polimeni, J. R., et al. (2011). The organization of the human cerebral cortex estimated by intrinsic functional connectivity. *Journal of neurophysiology*, 106(3):1125–1165.

[Tipnis et al., 2018] Tipnis, U., Amico, E., Ventresca, M., and Goni, J. (2018). Modeling communication processes in the human connectome through cooperative learning. *IEEE Transactions on Network Science and Engineering*.

[Tomasi and Volkow, 2011] Tomasi, D. and Volkow, N. D. (2011). Association between functional connectivity hubs and brain networks. *Cerebral cortex*, 21(9):2003–2013.

[Tournier et al., 2010] Tournier, J. D., Calamante, F., and Connelly, A. (2010). Improved probabilistic streamlines tractography by 2nd order integration over fibre orientation distributions. In *Proceedings of the international society for magnetic resonance in medicine*, volume 1670. Ismrm.

[Tournier et al., 2004] Tournier, J.-D., Calamante, F., Gadian, D. G., and Connelly, A. (2004). Direct estimation of the fiber orientation density function from diffusion-weighted mri data using spherical deconvolution. *Neuroimage*, 23(3):1176–1185.

[Tournier et al., 2019] Tournier, J.-D., Smith, R., Raffelt, D., Tabbara, R., Dhollander, T., Pietsch, M., Christiaens, D., Jeurissen, B., Yeh, C.-H., and Connelly, A. (2019). Mrtrix3: A fast, flexible and open software framework for medical image processing and visualisation. *NeuroImage*, 202:116137.

[Tournier et al., 2008] Tournier, J.-D., Yeh, C.-H., Calamante, F., Cho, K.-H., Connelly, A., and Lin, C.-P. (2008). Resolving crossing fibres using constrained spherical deconvolution: validation using diffusion-weighted imaging phantom data. *Neuroimage*, 42(2):617–625.

[Towlson and Barabási, 2020] Towlson, E. K. and Barabási, A.-L. (2020). Synthetic ablations in the c. elegans nervous system. *Network Neuroscience*, 4(1):200–216.

[Travis and Wallace, 1999] Travis, F. and Wallace, R. K. (1999). Autonomic and eeg patterns during eyes-closed rest and transcendental meditation (tm) practice: the basis for a neural model of tm practice. *Consciousness and cognition*, 8(3):302–318.

[Tu et al., 2018] Tu, C., Rocha, R. P., Corbetta, M., Zampieri, S., Zorzi, M., and Suweis, S. (2018). Warnings and caveats in brain controllability. *NeuroImage*, 176:83–91.

[Tustison et al., 2010] Tustison, N. J., Avants, B. B., Cook, P. A., Zheng, Y., Egan, A., Yushkevich, P. A., and Gee, J. C. (2010). N4itk: improved n3 bias correction. *IEEE transactions on medical imaging*, 29(6):1310–1320.

[Valizadeh et al., 2018] Valizadeh, S. A., Liem, F., Mérillat, S., Hänggi, J., and Jäncke, L. (2018). Identification of individual subjects on the basis of their brain anatomical features. *Scientific reports*, 8(1):1–9.

[van den Heuvel and Fornito, 2014] van den Heuvel, M. P. and Fornito, A. (2014). Brain networks in schizophrenia. *Neuropsychology review*, 24(1):32–48.

[van den Heuvel et al., 2012] van den Heuvel, M. P., Kahn, R. S., Goñi, J., and Sporns, O. (2012). High-cost, high-capacity backbone for global brain communication. *Proceedings of the National Academy of Sciences*, 109(28):11372–11377.

[van den Heuvel and Pol, 2010] van den Heuvel, M. P. and Pol, H. E. H. (2010). Exploring the brain network: a review on resting-state fmri functional connectivity. *European neuropsychopharmacology*, 20(8):519–534.

[van den Heuvel and Sporns, 2011] van den Heuvel, M. P. and Sporns, O. (2011). Rich-club organization of the human connectome. *Journal of Neuroscience*, 31(44):15775–15786.

[van den Heuvel and Sporns, 2013] van den Heuvel, M. P. and Sporns, O. (2013). Network hubs in the human brain. *Trends in cognitive sciences*, 17(12):683–696.

[van der Knaap and van der Ham, 2011] van der Knaap, L. J. and van der Ham, I. J. (2011). How does the corpus callosum mediate interhemispheric transfer? a review. *Behavioural brain research*, 223(1):211–221.

[Van Essen et al., 2013] Van Essen, D. C., Smith, S. M., Barch, D. M., Behrens, T. E., Yacoub, E., Ugurbil, K., Consortium, W.-M. H., et al. (2013). The wu-minn human connectome project: an overview. *Neuroimage*, 80:62–79.

[Van Essen et al., 2012] Van Essen, D. C., Ugurbil, K., Auerbach, E., Barch, D., Behrens, T. E., Bucholz, R., Chang, A., Chen, L., Corbetta, M., Curtiss, S. W., et al. (2012). The human connectome project: a data acquisition perspective. *Neuroimage*, 62(4):2222–2231.

[Van Os et al., 2010] Van Os, J., Kenis, G., and Rutten, B. P. (2010). The environment and schizophrenia. *Nature*, 468(7321):203–212.

[Vázquez-Rodríguez et al., 2019] Vázquez-Rodríguez, B., Suárez, L. E., Markello, R. D., Shafiei, G., Paquola, C., Hagmann, P., van den Heuvel, M. P., Bernhardt, B. C., Spreng, R. N., and Misic, B. (2019). Gradients of structure–function tethering across neocortex. *Proceedings of the National Academy of Sciences*, 116(42):21219–21227.

[Venkatesh et al., 2020] Venkatesh, M., Jaja, J., and Pessoa, L. (2020). Comparing functional connectivity matrices: A geometry-aware approach applied to participant identification. *NeuroImage*, 207:116398.

[Vicente and Wibral, 2014] Vicente, R. and Wibral, M. (2014). Efficient estimation of information transfer. In *Directed Information Measures in Neuroscience*, pages 37–58. Springer.

[Vicente et al., 2011] Vicente, R., Wibral, M., Lindner, M., and Pipa, G. (2011). Transfer entropy – a model-free measure of effective connectivity for the neurosciences. *Journal of computational neuroscience*, 30(1):45–67.

[Vidal et al., 2011] Vidal, M., Cusick, M. E., and Barabási, A.-L. (2011). Interactome networks and human disease. *Cell*, 144(6):986–998.

[Wachinger et al., 2015] Wachinger, C., Golland, P., Kremen, W., Fischl, B., Reuter, M., Initiative, A. D. N., et al. (2015). Brainprint: A discriminative characterization of brain morphology. *NeuroImage*, 109:232–248.

[Watts and Strogatz, 1998] Watts, D. J. and Strogatz, S. H. (1998). Collective dynamics of 'small-world' networks. *nature*, 393(6684):440–442.

[Wedeen et al., 2005] Wedeen, V. J., Hagmann, P., Tseng, W.-Y. I., Reese, T. G., and Weisskoff, R. M. (2005). Mapping complex tissue architecture with diffusion spectrum magnetic resonance imaging. *Magnetic resonance in medicine*, 54(6):1377–1386.

[White et al., 1986] White, J. G., Southgate, E., Thomson, J. N., and Brenner, S. (1986). The structure of the nervous system of the nematode caenorhabditis elegans. *Philos Trans R Soc Lond B Biol Sci*, 314(1165):1–340.

[Wibral et al., 2014a] Wibral, M., Lizier, J., Vögler, S., Priesemann, V., and Galuske, R. (2014a). Local active information storage as a tool to understand distributed neural information processing. *Frontiers in neuroinformatics*, 8:1.

[Wibral et al., 2013] Wibral, M., Pampu, N., Priesemann, V., Siebenhühner, F., Seiwert, H., Lindner, M., Lizier, J. T., and Vicente, R. (2013). Measuring information-transfer delays. *PloS one*, 8(2):e55809.

[Wibral et al., 2014b] Wibral, M., Vicente, R., and Lindner, M. (2014b). Transfer entropy in neuroscience. In *Directed information measures in neuroscience*, pages 3–36. Springer.

[Wollstadt et al., 2018] Wollstadt, P., Lizier, J. T., Vicente, R., Finn, C., Martinez-Zarzuela, M., Mediano, P., Novelli, L., and Wibral, M. (2018). Idtxl: The information dynamics toolkit xl: a python package for the efficient analysis of multivariate information dynamics in networks. *arXiv preprint arXiv:1807.10459*.

[Wollstadt et al., 2014] Wollstadt, P., Martínez-Zarzuela, M., Vicente, R., Díaz-Pernas, F. J., and Wibral, M. (2014). Efficient transfer entropy analysis of non-stationary neural time series. *PloS one*, 9(7):e102833.

[Wolsey and Nemhauser, 1999] Wolsey, L. A. and Nemhauser, G. L. (1999). *Integer and combinatorial optimization*, volume 55. John Wiley & Sons.

[Woolrich et al., 2011] Woolrich, M., Hunt, L., Groves, A., and Barnes, G. (2011). Meg beamforming using bayesian pca for adaptive data covariance matrix regularization. *Neuroimage*, 57(4):1466–1479.

[WU-Minn, 2017] WU-Minn, H. (2017). 1200 subjects data release reference manual. *URL https://www. humanconnectome. org*.

[Yan et al., 2017] Yan, G., Vértes, P. E., Towlson, E. K., Chew, Y. L., Walker, D. S., Schafer, W. R., and Barabási, A.-L. (2017). Network control principles predict neuron function in the caenorhabditis elegans connectome. *Nature*, 550(7677):519–523.

[Yendiki et al., 2014] Yendiki, A., Koldewyn, K., Kakunoori, S., Kanwisher, N., and Fischl, B. (2014). Spurious group differences due to head motion in a diffusion mri study. *Neuroimage*, 88:79–90.

[Yeo et al., 2011] Yeo, B. T., Krienen, F. M., Sepulcre, J., Sabuncu, M. R., Lashkari, D., Hollinshead, M., Roffman, J. L., Smoller, J. W., Zöllei, L., Polimeni, J. R., et al. (2011). The organization of the human cerebral cortex estimated by intrinsic functional connectivity. *Journal of neurophysiology*.

[Zalesky et al., 2010] Zalesky, A., Fornito, A., Harding, I. H., Cocchi, L., Yücel, M., Pantelis, C., and Bullmore, E. T. (2010). Whole-brain anatomical networks: does the choice of nodes matter? *Neuroimage*, 50(3):970–983.

[Zeidan et al., 2011] Zeidan, F., Martucci, K. T., Kraft, R. A., Gordon, N. S., McHaffie, J. G., and Coghill, R. C. (2011). Brain mechanisms supporting the modulation of pain by mindfulness meditation. *Journal of Neuroscience*, 31(14):5540–5548.

[Zhang et al., 2001] Zhang, Y., Brady, M., and Smith, S. (2001). Segmentation of brain mr images through a hidden markov random field model and the expectation-maximization algorithm. *IEEE transactions on medical imaging*, 20(1):45–57.

A

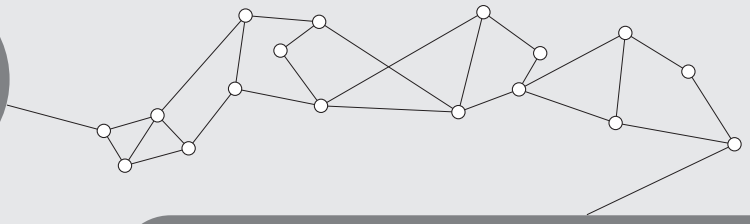

Supplementary Material of Chapter 4

A.1 Supplementary Notes

A.1.1 Linear models to map structure and function in brain networks

We use a linear time-invariant model of the form

$$\mathbf{x}(k+1) = \mathbf{A}\mathbf{x}(k) + \mathbf{B}\mathbf{u}(k) \tag{A.1}$$

where $\mathbf{x}(k)$ describes the level of neurophysiological activity at time k in each node of a brain network. The model parameters are the system matrix $\mathbf{A}$, the input matrix $\mathbf{B}$ and the input signals $\mathbf{u}$.

Roberto Galán proposed such a model based on the linearization and discretization of a general Wilson-Cowan model [Galán, 2008]. The author obtained $\mathbf{A}$ as a linear transformation of the structural connectivity matrix (i.e. the connectome), fixed $\mathbf{B}$ as the identity matrix, modelled $\mathbf{u}$ as white noise signals and derived an analytical expression of the state-covariance matrix of the nodal dynamics. This model was further explored by Honey and colleagues [Honey et al., 2009]. Based on this work, Gu et al. leveraged the established theory of linear systems to investigate the controllability of brain networks [Gu et al., 2015]. By choosing $\mathbf{B}$ as the i-th canonical vector, they derived quantitative control properties of each node i through the computation of the controllability Gramian. Later, Gu et al. focused on optimal trajectories of brain state transitions [Gu et al., 2017] and computed the input signals $\mathbf{u}$ minimizing the energy for the transitions between predefined brain states. For that, they took a hypothesis-driven approach and fixed the input matrix $\mathbf{B}$ based on *a priori* knowledge. The authors pointed out to the theoretical and empirical motivations of considering a *set* of control regions (*multipoint control*) instead of a single input node. However, the question of how to identify the control set associated with a given brain state from empirical data remains challenging.

In parallel, recent studies investigated how information propagates in the white matter wiring in order to generate the observed patterns of functional activity

[Avena-Koenigsberger et al., 2018]. A spectrum of communication strategies have been investigated [Avena-Koenigsberger et al., 2019] among which several models based on information diffusion [Abdelnour et al., 2014, Goñi et al., 2014, Mišić et al., 2015, Bettinardi et al., 2017]. These models account for the autonomous dynamics of System A.1 through modifications of the system matrix $\mathbf{A}$ [Lambiotte et al., 2011] in the absence of external stimulation ($\mathbf{B} = \mathbf{0}$).

Here, we propose a principled method to identify state-specific sets of control regions from empirical data. For that, we use System A.1 in which $\mathbf{A}$ describes a Laplacian diffusion dynamics [Abdelnour et al., 2014] although the general framework is valid for other dynamics. We derive a model of correlation-based functional connectivity that is linked to the controllability Gramian and find the input matrix $\mathbf{B}$ such that the similarity between modelled and empirical functional connectivity is maximized, assuming white driving noise signals $\mathbf{u}$.

A.1.2 Structural connectivity weighting

In our analysis, we weighted the structural connection between two regions of the connectome as the number of streamlines reconstructed by the tractography algorithm between both regions, normalized by the volume of the regions. This process has been proposed by Hagmann and colleagues [Hagmann et al., 2008] in order to mitigate the bias due to the variable size of ROIs, larger ROIs receiving more reconstructed streamlines. In Supplementary Figure A.2.2, we observe that some regions such as the cerebellum are particularly affected by this normalization. Alternative weightings of structural connections exist in the literature, related to the length of reconstructed streamlines, their fractional anisotropy or the apparent diffusion coefficient for instance. Choosing the edges weighting scheme remains an open question in diffusion MRI connectomics [Oldham et al., 2020] and our results should be interpreted with respect to this choice as the nodal strength has been shown to be linked to the chance of a ROI to be selected as an input node.

A.1.3 Impact of Global Signal Regression

Global Signal Regression (GSR) is a highly debated preprocessing operation [Murphy and Fox, 2017, Power et al., 2017, Glasser et al., 2018, Aquino et al., 2020] because the global signal is thought to include components of both neuronal and non-neuronal origin. Here, we can anticipate that GSR will have a negative impact on the correlation score between structure-informed and empirical functional connectivity. On the one hand, the solution $\mathbf{\Sigma}$ of the Lyapunov equation used in our

our model is written

$$\mathbf{\Sigma} = \sum_{i=0}^{\infty} \mathbf{A}^i \mathbf{B}\mathbf{B}^T (\mathbf{A}^T)^i \tag{A.2}$$

and cannot have negative entries with our choice for $\mathbf{A}$ and $\mathbf{B}$. On the other hand, GSR has been shown to introduce negative correlations in empirical FC [Murphy et al., 2009]. Therefore, our model is expected to show lower performance when GSR is applied to the fMRI data, because it cannot predict the negative correlations that are introduced. To illustrate this, we reproduced Figures 2A, 2B, 3A and 3B of the manuscript using fMRI data that underwent GSR. In Supplementary Figure A.2.13A, we observe that correlation scores are indeed lower for all states, with the relational processing task being the most affected. Compared to the results of the main text, less control ROIs are selected for all states except the resting-state (Supplementary Figure A.2.13B). Our previous observation that subcortical areas are consistently selected across states remains valid (Supplementary Figure A.2.13C and D for the motor task and the resting-state respectively ; result not shown for the other tasks).

A.1.4 Structure-function correlation in open and closed subsystems

In order to compute the structure-function correlation score for a subsystem, one can consider two options : (i) comparing the edges with both extremities belonging to the subsystem ('closed' subsystem) or (ii) comparing the edges with *at least one* extremity belonging to the subsystem ('open' subsystem). The first option ignores all edges linking two subsystems while the second includes these edges in the computation of the correlation score for both subsystems. In the manuscript, Figure 3D is obtained with open subsystems and shows a gradient of structure-function coupling in resting-state, from high correlation in primary sensory areas to low correlation in regions associated with higher-order cognitive functions [Vázquez-Rodríguez et al., 2019]. In Supplementary Figure A.2.8, we show the result of the same analysis with closed subsystems. This result is similar to that reported by Tipnis et al. [Tipnis et al., 2018], and the gradient observed in resting-state is different from that of the manuscript. We also observe that the visual subsystem is the most affected by taking into account the edges linking different subsystems, indicating that the connections between visual areas and other systems show a closer structure-function relationship, compared to intrinsic connections of the visual subsystems.

A.1.5 Expected value of Jaccard index

To derive the expected value of the Jaccard index J, we consider a set of N elements from which we draw two subsets $\mathcal{S}_1$ and $\mathcal{S}_2$ having the same cardinality m and whose elements are chosen uniformly at random. We denote the number of common elements between $\mathcal{S}_1$ and $\mathcal{S}_2$ as $|\mathcal{S}_1 \cap \mathcal{S}_2| = k$. The corresponding Jaccard index is

$$J(\mathcal{S}_1, \mathcal{S}_2) = \frac{k}{2m - k}$$

Now, the probability that the number of common elements is exactly k is

$$P(|\mathcal{S}_1 \cap \mathcal{S}_2| = k) = \frac{\binom{m}{k}\binom{N-m}{m-k}}{\binom{N}{m}}$$

since we have $\binom{N}{m}$ choices for the elements of $\mathcal{S}_1$ and $\binom{m}{k}\binom{N-m}{m-k}$ choices left for the elements of $\mathcal{S}_2$. Therefore, the expected value of Jaccard index between two random sets of size m drawn from N elements is

$$\mathbb{E}\{J(\mathcal{S}_1, \mathcal{S}_2)\} = \sum_{k=0}^{m} \frac{\binom{m}{k}\binom{N-m}{m-k}}{\binom{N}{m}} \frac{k}{2m - k}$$

For $N = 164$ and $m = 40$ (see Figure 4.2), we obtain $\mathbb{E}\{J\} \approx 0.1389$.

A.2 Supplementary Figures

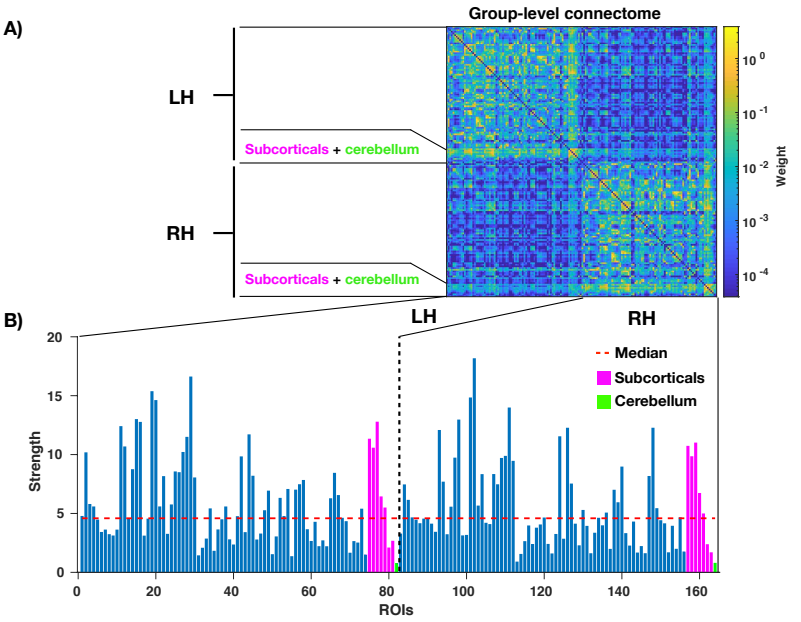

Figure A.2.1: **Group-level connectome. A)** Adjacency matrix (Destrieux parcellation, 164 ROIs including subcorticals and cerebellum, streamline density weighting). LH: Left hemisphere. RH: Right hemisphere. **B)** Bar plot of the corresponding nodal strengths.

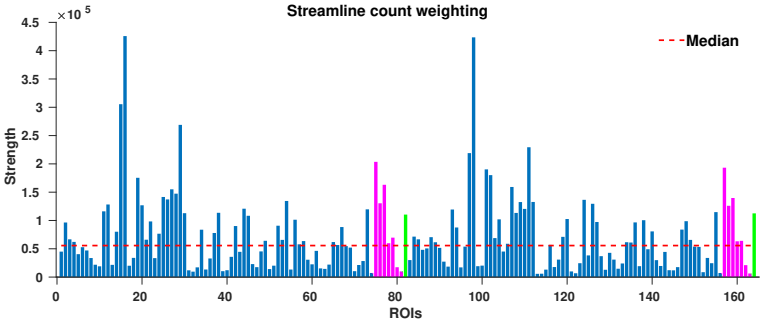

Figure A.2.2: Bar plot of the nodal strengths in the connectome reconstructed using the streamline count weighting. Blue: cortical ROIS. Purple: subcorticals. Green: cerebellum.

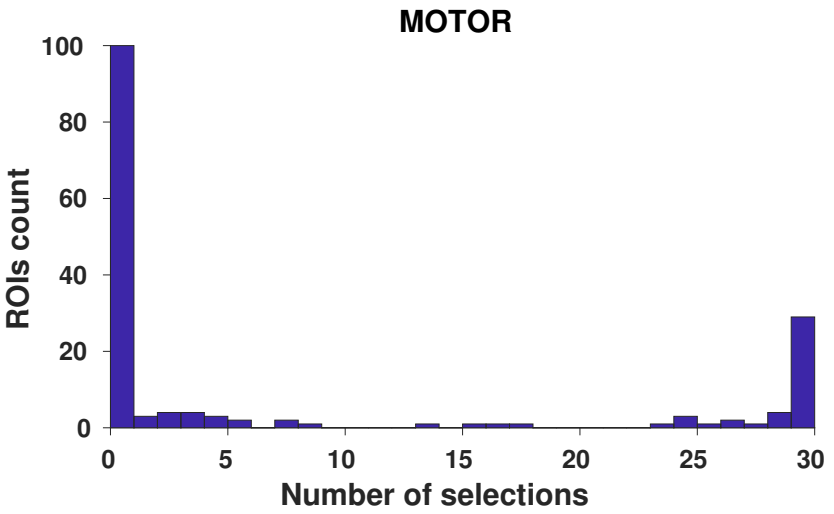

Figure A.2.3: Histogram of ROIs selections (over 30 optimization runs) for the motor task, with no constraint on the number of input nodes allowed ($U = N$).

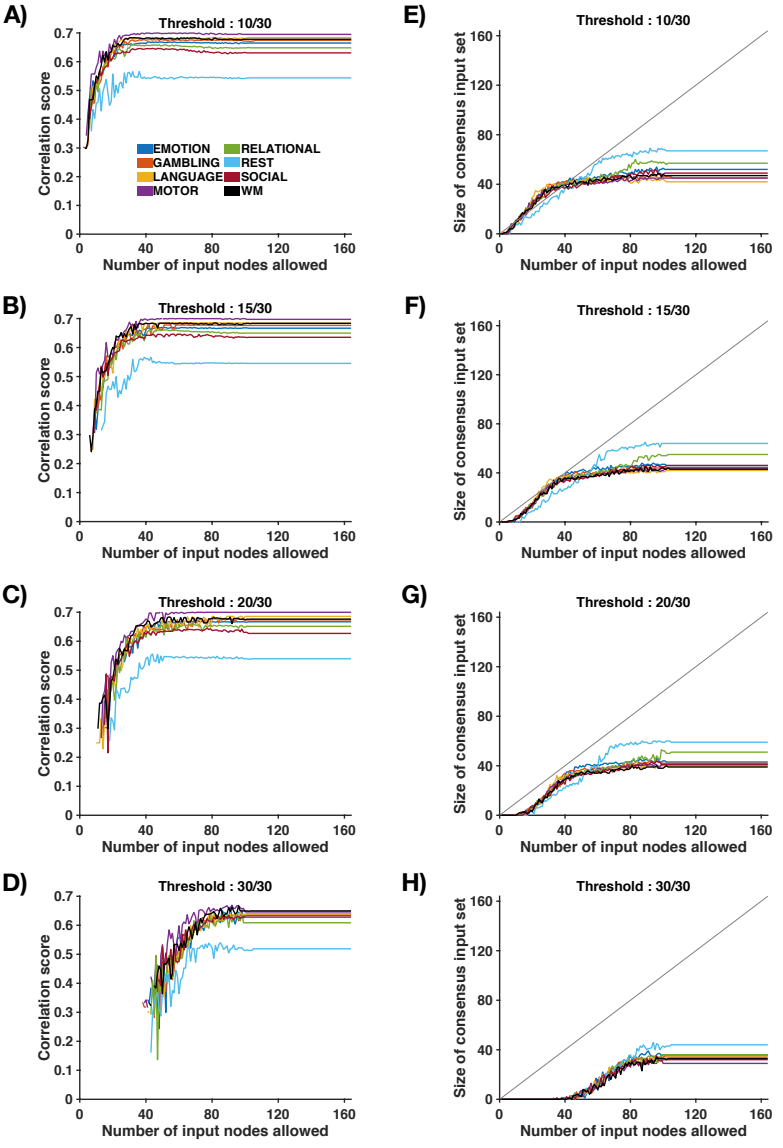

Figure A.2.4: **Robustness with respect to consensus input set thresholds. A)** (resp. **B**, **C**, **D**) Correlation score between structure-informed and empirical functional connectivity with respect to the number of input nodes allowed U (group-level). $\mathbf{F}_{SI}$ is obtained using the consensus input set formed by ROIs selected at least 10 (resp. 15, 20, 30) times over 30 optimization runs. **E)** (resp. **F**, **G**, **H**) Size of the corresponding consensus input set with respect to the number of input nodes allowed U (group-level). The gray line denotes the identity function $y = x$.

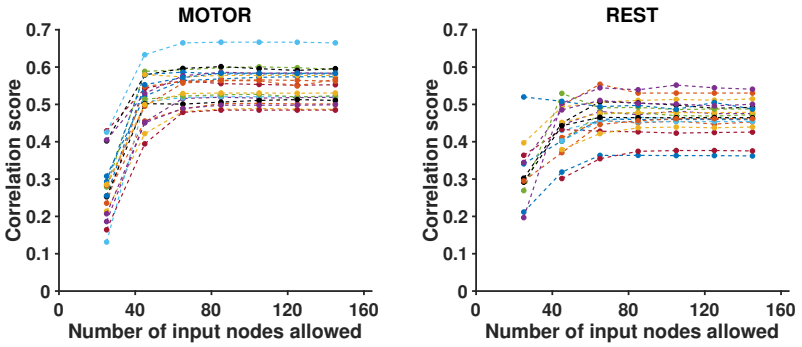

Figure A.2.5: Correlation score between structure-informed and empirical functional connectivity with respect to the number of input nodes allowed $U \in \{5, 25, 45, 65, 85, 105, 125, 145\}$, for 20 randomly selected individuals. Left: motor task. Right: resting-state. The consensus input set is defined as the set of ROIs selected at least 25 times over 30 optimization runs.

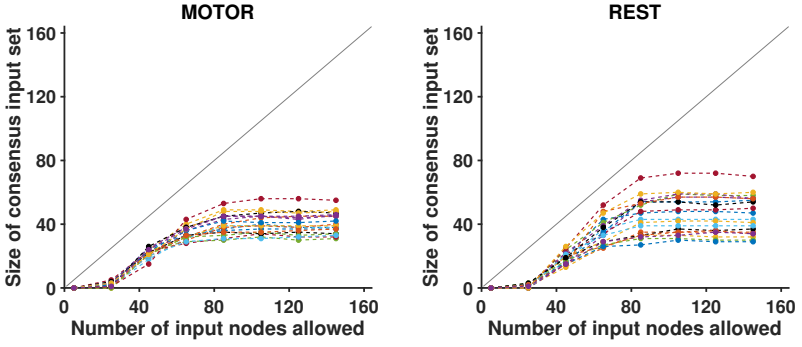

Figure A.2.6: Size of the consensus input set with respect to the number of input nodes allowed $U \in \{5, 25, 45, 65, 85, 105, 125, 145\}$, for 20 randomly selected individuals. Left: motor task. Right: resting-state. The consensus input set is defined as the set of ROIs selected at least 25 times over 30 optimization runs.

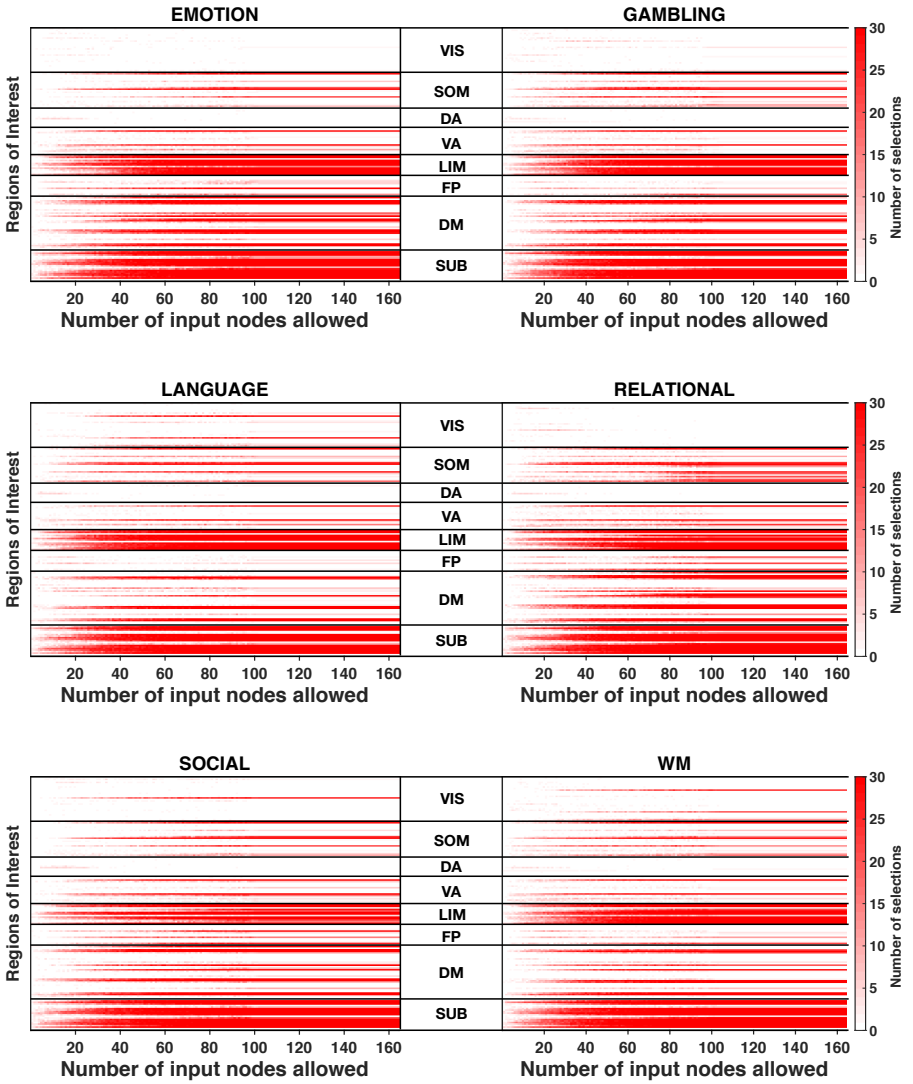

Figure A.2.7: Analysis across functional subsystems (group-level). Evolution of the number of selections (from 0-white, to 30-red) of each Region of Interest (ROI) with respect to the number of input nodes allowed U for different tasks (MOTOR and REST are presented in the main manuscript). ROIs are arranged according to the functional subsystems described by Yeo and colleagues. The cerebellum is included in the "subcorticals" subsystem for visualisation and corresponds to the last two lines (left and right hemispheres)

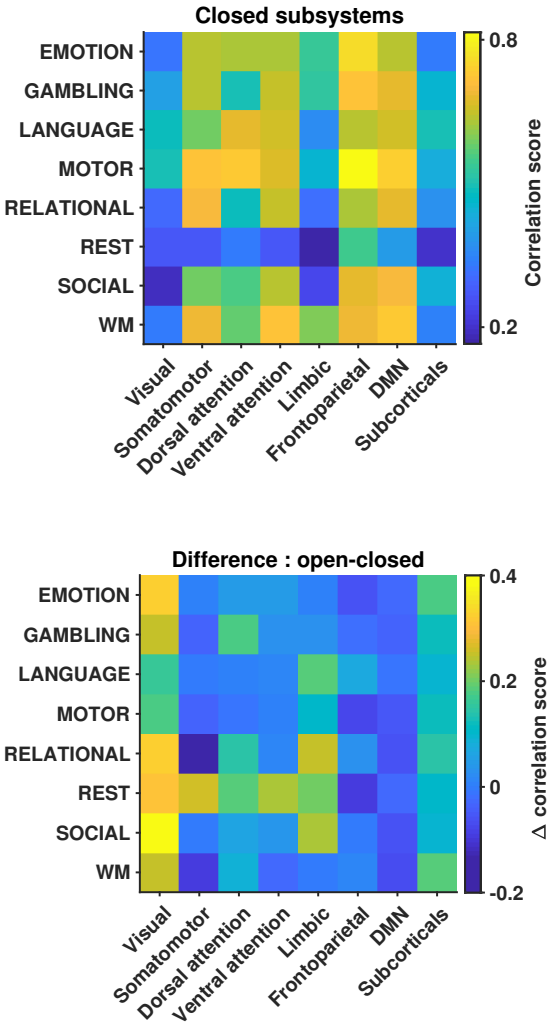

Figure A.2.8: Top : Correlation between structure-informed and empirical functional connectivity with $U = N$, considering closed subsystems. Bottom : Difference of correlation scores across subsystems, when considering open (Figure 3D of the manuscript) or closed subsystems.

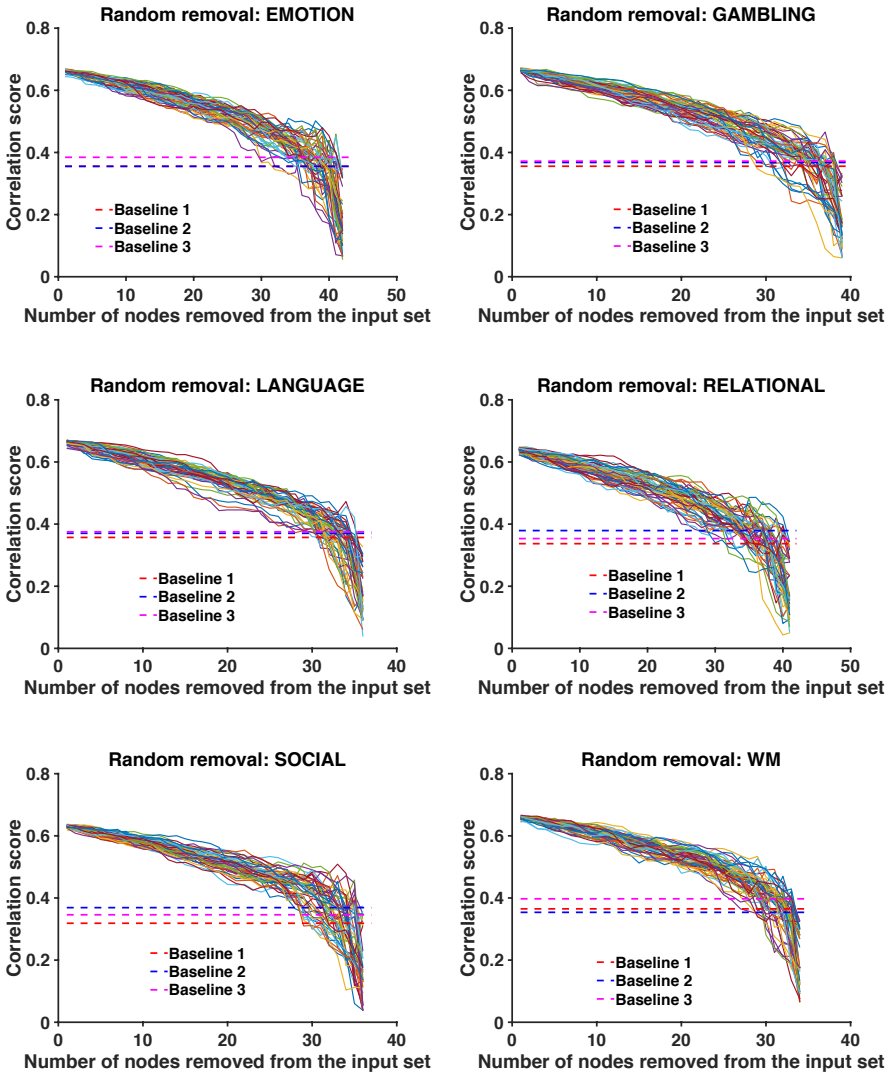

Figure A.2.9: Robustness analysis. Evolution of the correlation between structure-informed $\mathbf{F}_{SI}$ and empirical functional connectivity $\mathbf{F}_{emp}$ as a function of the number of ROIs removed from the consensus input set. Dashed lines represent the three baselines, i.e. the correlation between $\mathbf{F}_{emp}$ and (i) the adjacency matrix of the connectome, (ii) $\mathbf{F}_{SI}$ based on a re-labelled connectome and (iii) $\mathbf{F}_{SI}$ obtained with a random input set. We consider 50 random removal orderings.

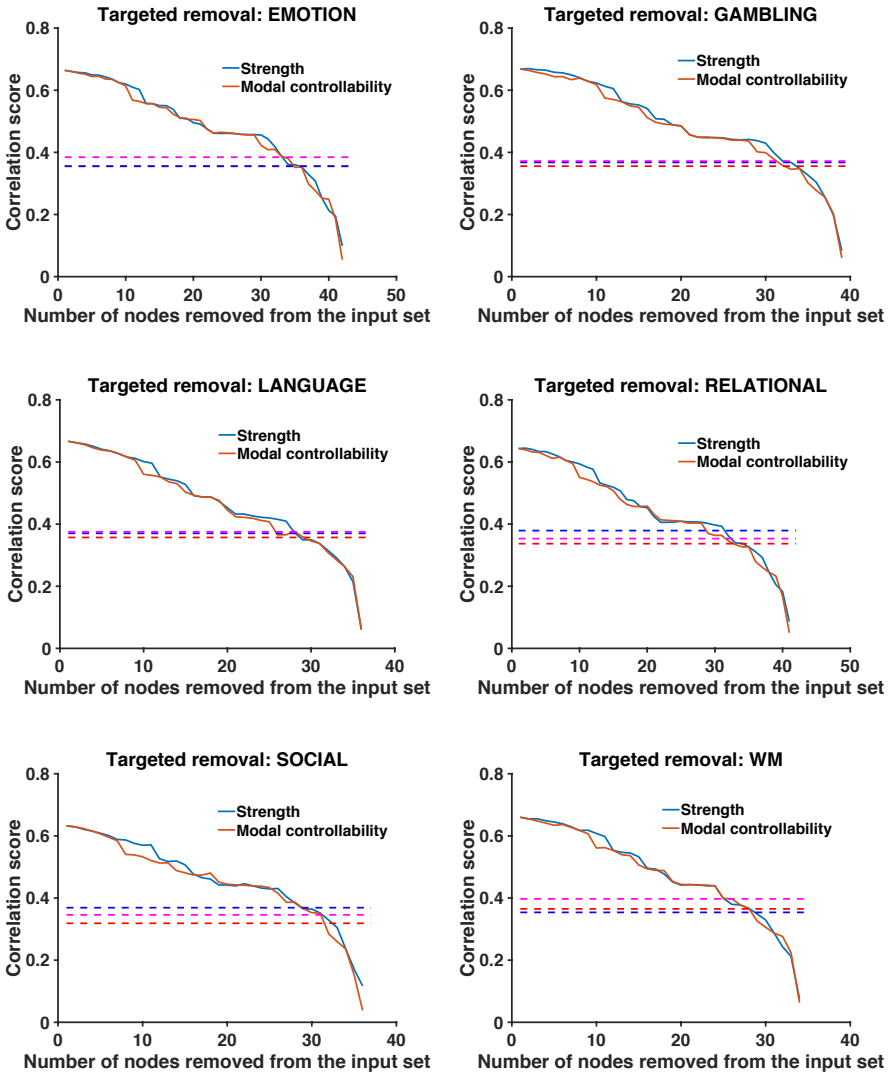

Figure A.2.10: Robustness analysis. Evolution of the correlation between structure-informed $\mathbf{F}_{SI}$ and empirical functional connectivity $\mathbf{F}_{emp}$ as a function of the number of ROIs removed from the consensus input set. Dashed lines represent the three baselines, i.e. the correlation between $\mathbf{F}_{emp}$ and (i) the adjacency matrix of the connectome, (ii) $\mathbf{F}_{SI}$ based on a re-labelled connectome and (iii) $\mathbf{F}_{SI}$ obtained with a random input set. The removal ordering is fixed either by increasing weighted degree or decreasing model controllability.

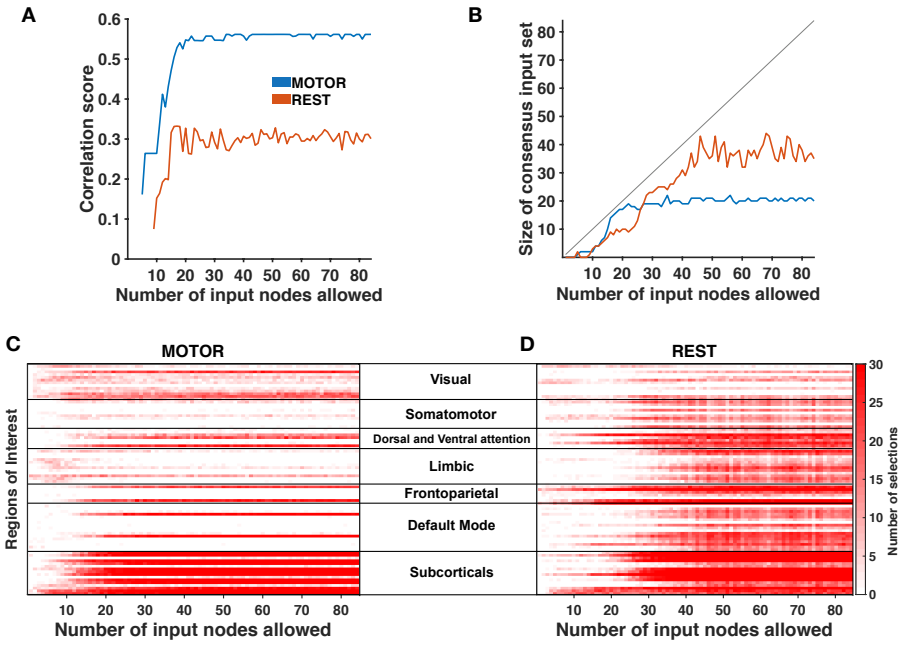

Figure A.2.11: **Effect of brain parcellation. A**, **B**, **C** and **D** respectively reproduce the results presented in Figures 2A, 2B, 3A and 3B of the main text (motor task and resting-state only), when using the Desikan-Killiany atlas (84 ROIs).

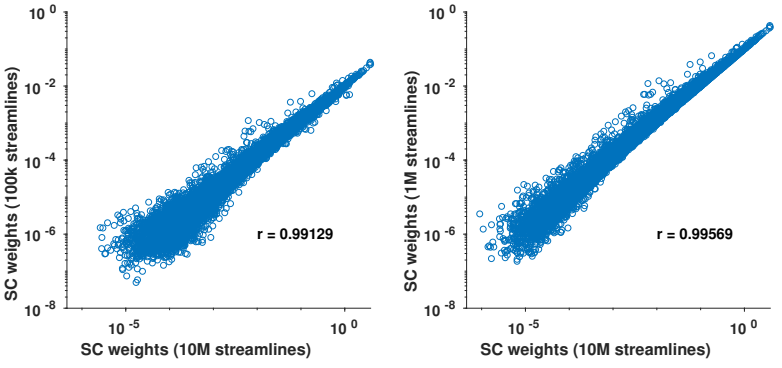

Figure A.2.12: Comparison of structural connectivity (SC) values of the group-level connectomes derived from 10^5- and 10^6-streamlines-tractograms, with respect to that of the connectome used in the main analysis (10^7 streamlines).

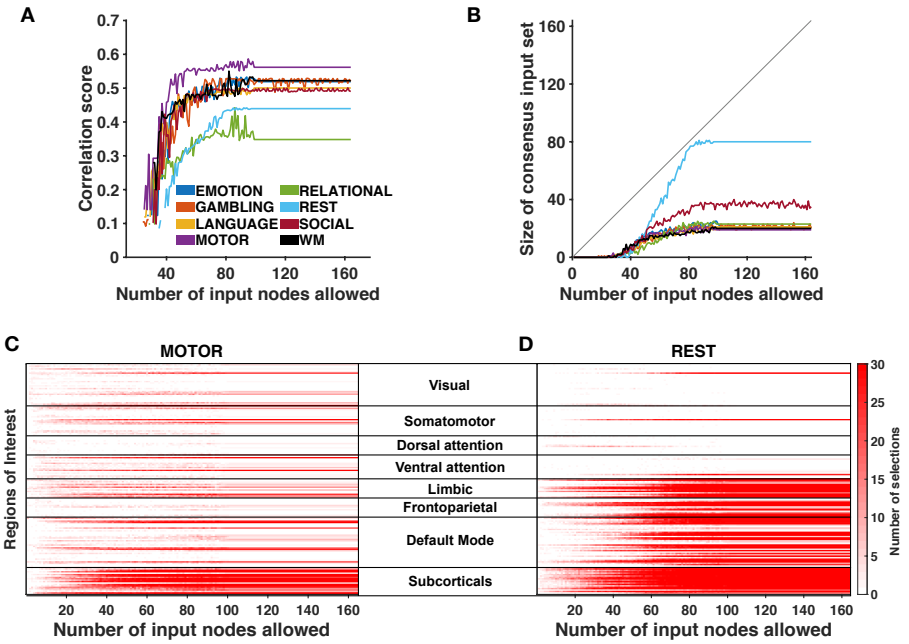

Figure A.2.13: **Effect of Global Signal Regression on the main results. A**, **B**, **C** and **D** respectively reproduce the results presented in Figures 2A, 2B, 3A and 3B of the main text, when regressing out the global signal from the functional data.

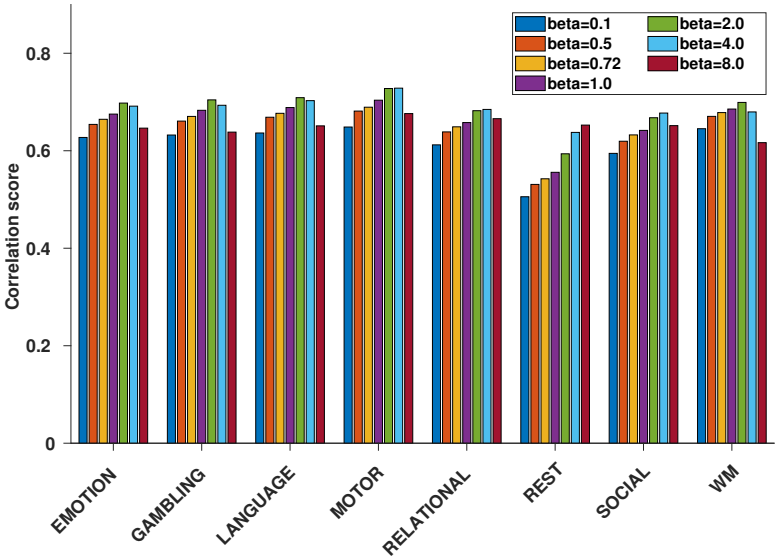

Figure A.2.14: Comparison of optimized correlation scores for different values of β.

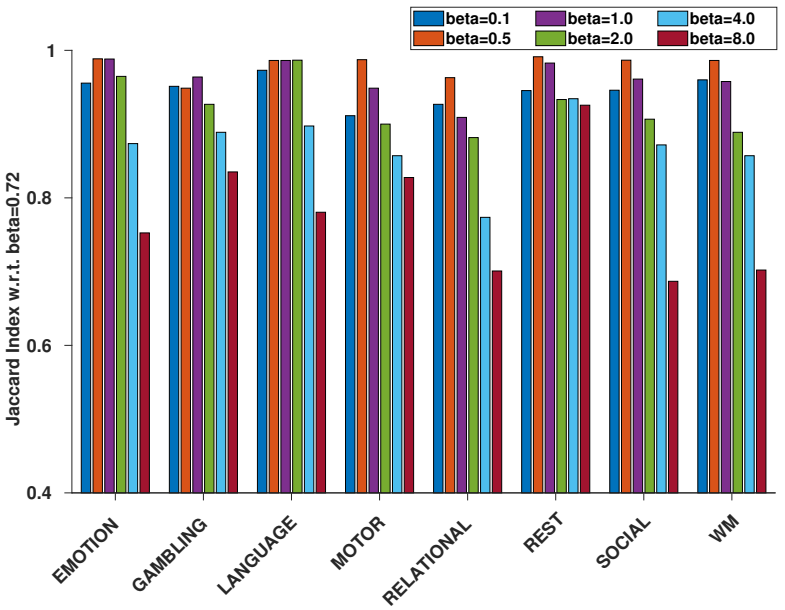

Figure A.2.15: Jaccard index between the consensus input set (threshold: 25 selections over 30 runs) obtained with $\beta = 0.72$ and the consensus input sets obtained when varying β.

A.3 Supplementary Tables

Table A.3.1: Comparison between three linear dynamics : the normalized Laplacian diffusion dynamics used in the main manuscript (DIFF), the dynamics defined by fixing the transition matrix $\mathbf{A}$ to the adjacency matrix of the connectome (ADJ) and the random-walk Laplacian diffusion dynamics (RW). In all cases, we performed 100 runs of the optimization algorithm, with $U = N$. The Jaccard index J is computed between the consensus input sets ($\geq$ 90 selections).

	EMO	GAM	LAN	MOT	REL	REST	SOC	WM
Mean correlation score : DIFF	0.66	0.67	0.68	0.7	0.65	0.54	0.63	0.68
Mean correlation score : ADJ	0.7	0.7	0.69	0.71	0.7	0.62	0.68	0.69
Mean correlation score : RW	0.67	0.68	0.68	0.7	0.66	0.56	0.65	0.68
J(DIFF,ADJ)	0.92	0.88	0.88	0.87	0.92	0.86	0.77	0.93
J(DIFF,RW)	0.96	0.94	0.93	0.91	0.99	0.94	0.96	0.97

Table A.3.2: ROI-by-ROI numerical results coming along with Figures 4 and 5 of the main manuscript.ROIs that are consistently selected at least 90 times over 100 runs for all functional states are highlighted in blue.

			Number of selections by task								
ID	**Hemisphere**	**Region of Interest**	**EMOTION**	**GAMBLING**	**LANGUAGE**	**MOTOR**	**RELATIONAL**	**REST**	**SOCIAL**	**WM**	**Yeo System**
1	Left	Fronto-marginal gyrus and sulcus	5	2	0	0	3	99	5	0	DMN
2	Left	Inferior occipital gyrus and sulcus	0	0	0	0	0	0	0	0	VIS
3	Left	Paracentral lobule and sulcus	92	99	97	97	99	11	90	97	SOM
4	Left	Subcentral gyrus (central operculum) and sulci	0	0	0	0	0	0	1	0	SOM
5	Left	Transverse frontopolar gyri and sulci	97	28	0	53	86	100	100	2	DMN
6	Left	Anterior part of the cingulate gyrus and sulcus (ACC)	1	0	0	2	8	97	2	0	DMN
7	Left	Middle-anterior part of the cingulate gyrus and sulcus (aMCC)	1	1	0	0	0	2	3	0	VA
8	Left	Middle-posterior part of the cingulate gyrus and sulcus (pMCC)	1	3	1	0	5	0	1	0	SOM
9	Left	Posterior-dorsal part of the cingulate gyrus (dPCC)	100	97	10	85	100	97	100	53	DMN
10	Left	Posterior-ventral part of the cingulate gyrus (vPCC)	100	100	100	100	99	96	100	100	DMN
11	Left	Cuneus	0	0	0	0	0	0	4	0	VIS
12	Left	Opercular part of the inferior frontal gyrus	0	0	0	0	0	0	0	0	VA
13	Left	Orbital part of the inferior frontal gyrus	97	86	80	84	75	99	26	54	DMN
14	Left	Triangular part of the inferior frontal gyrus	1	0	0	2	0	17	0	0	DMN
15	Left	Middle frontal gyrus	0	0	0	0	0	0	0	0	FP
16	Left	Superior frontal gyrus	0	0	0	0	0	0	0	0	DMN
17	Left	Long insular gyrus and central sulcus of the insula	100	100	86	98	100	2	100	100	VA
18	Left	Short insular gyri	9	6	1	2	8	5	22	2	VA
19	Left	Middle occipital gyrus	0	0	0	0	0	0	0	0	VIS
20	Left	Superior occipital gyrus	0	0	0	0	0	0	0	0	VIS
21	Left	Lateral occipito-temporal gyrus	0	0	0	1	0	0	0	0	VIS
22	Left	Lingual gyrus, ligual part of the medial occipito-temporal gyrus	0	0	0	0	0	0	0	0	VIS
23	Left	Parahippocampal gyrus, parahippocampal part of the medial occipito-temporal gyrus	100	100	100	99	100	98	100	99	SUB
24	Left	Orbital gyri	11	5	0	9	3	97	2	3	LIM
25	Left	Angular Gyri	0	1	0	0	0	39	0	0	DMN
26	Left	Supramarginal gyrus	0	0	0	0	0	1	0	0	VA
27	Left	Superior parietal lobule	0	0	0	0	0	0	0	0	DA
28	Left	Postcentral gyrus	0	0	0	0	0	0	0	0	SOM
29	Left	Precentral gyrus	0	0	0	0	0	0	0	0	SOM
30	Left	Precuneus	0	0	0	1	0	4	0	0	DMN
31	Left	Straight gyrus	100	100	100	100	100	100	100	100	LIM
32	Left	Subcallosal area	100	100	100	100	100	100	100	100	SUB

ID	Hemisphere	Region of Interest	EMOTION	GAMBLING	LANGUAGE	MOTOR	RELATIONAL	REST	SOCIAL	WM	Yeo System
33	Left	Anterior transverse temporal gyrus	23	18	37	4	32	0	19	19	SOM
34	Left	Lateral aspect of the superior temporal gyrus	1	1	8	1	0	0	0	0	SOM
35	Left	Planum polare of the superior temporal gyrus	99	100	100	100	100	71	100	99	LIM
36	Left	Planum temporale or temporal plane of the superior temporal gyrus	0	1	0	0	2	0	0	0	VA
37	Left	Inferior temporal gyrus	0	0	0	1	0	22	0	0	LIM
38	Left	Middle temporal gyrus	0	0	0	0	0	4	0	0	DMN
39	Left	Horizontal ramus of the anterior segment of the lateral sulcus	64	29	26	21	25	97	10	15	DMN
40	Left	Vertical ramus of the anterior segment of the lateral sulcus	36	15	6	11	9	99	8	3	DMN
41	Left	Posterior ramus of the lateral sulcus	1	1	0	0	3	0	0	1	SOM
42	Left	Occipital pole	0	0	5	7	0	100	0	0	VIS
43	Left	Temporal pole	100	100	100	100	100	99	84	76	LIM
44	Left	Calcarine sulcus	0	0	0	0	0	0	0	0	VIS
45	Left	Central sulcus	0	0	0	0	0	0	0	0	SOM
46	Left	Marginal branch of the cingulate sulcus	1	0	0	1	3	0	0	2	VA
47	Left	Anterior segment of the circular sulcus of the insula	99	94	7	88	89	100	98	77	DMN
48	Left	Inferior segment of the circular sulcus of the insula	3	16	3	1	13	0	14	3	VA
49	Left	Superior segment of the circular sulcus of the insula	1	1	0	0	0	0	1	0	VA
50	Left	Anterior transverse collateral sulcus	100	100	100	100	50	100	50	100	LIM
51	Left	Posterior transverse collateral sulcus	0	3	85	82	0	0	0	68	VIS
52	Left	Inferior frontal sulcus	0	0	0	0	0	0	0	0	FP
53	Left	Middle frontal sulcus	0	0	0	0	0	65	0	0	FP
54	Left	Superior frontal sulcus	0	0	0	0	0	20	0	0	DMN
55	Left	Sulcus intermedius primus	99	84	3	4	95	99	34	0	DMN
56	Left	Intraparietal sulcus and transverse parietal sulci	0	0	0	0	0	0	0	0	DA
57	Left	Middle occipital sulcus and lunatus sulcus	0	0	0	0	0	0	0	0	VIS
58	Left	Superior occipital sulcus and transverse occipital sulcus	0	0	0	0	0	0	0	0	VIS
59	Left	Anterior occipital sulcus and preoccipital notch	0	0	1	1	0	0	0	0	VIS
60	Left	Lateral occipito-temporal sulcus	1	0	1	0	0	0	0	0	DA
61	Left	Medial occipito-temporal sulcus and lingual sulcus	1	2	13	8	0	0	0	1	VIS
62	Left	Lateral orbital sulcus	6	2	0	2	0	100	2	0	FP
63	Left	Medial orbital sulcus	100	100	100	100	100	100	100	100	LIM
64	Left	Orbital sulci	26	3	1	62	67	100	94	9	FP
65	Left	Parieto-occipital sulcus	0	0	0	0	0	0	83	0	VIS
66	Left	Pericallosal sulcus	100	100	95	100	100	100	100	98	DMN

ID	Hemisphere	Region of Interest	EMOTION	GAMBLING	LANGUAGE	MOTOR	RELATIONAL	REST	SOCIAL	WM	Yeo System
67	Left	Postcentral sulcus	0	0	0	0	0	0	0	0	DA
68	Left	Inferior part of the precentral sulcus	0	1	0	0	0	1	0	0	DA
69	Left	Superior part of the precentral sulcus	0	0	0	0	0	0	0	0	DA
70	Left	Suborbital sulcus	100	99	100	100	100	100	100	98	LIM
71	Left	Subparietal sulcus	28	28	6	11	64	18	7	8	DMN
72	Left	Inferior temporal sulcus	0	0	0	0	0	12	0	0	DMN
73	Left	Superior temporal sulcus	0	0	2	0	0	4	0	0	DMN
74	Left	Transverse temporal sulcus	66	81	67	8	79	0	71	44	SOM
75	Left	Cerebellum	0	0	0	0	0	61	0	2	CER
76	Left	Thalamus	100	100	100	95	100	99	99	100	SUB
77	Left	Caudate	36	7	1	53	15	100	12	4	SUB
78	Left	Putamen	49	13	1	19	51	100	30	32	SUB
79	Left	Pallidum	100	100	100	100	100	100	100	100	SUB
80	Left	Hippocampus	100	100	100	100	100	100	100	100	SUB
81	Left	Amygdala	100	100	100	100	100	100	100	100	SUB
82	Left	Accumbens area	100	100	100	100	100	100	100	100	SUB
83	Right	Thalamus	99	100	100	100	99	100	97	100	SUB
84	Right	Caudate	24	6	7	20	11	100	8	12	SUB
85	Right	Putamen	86	61	30	51	92	100	68	83	SUB
86	Right	Pallidum	100	100	100	100	100	100	100	100	SUB
87	Right	Hippocampus	100	100	100	100	100	99	100	100	SUB
88	Right	Amygdala	100	100	100	100	100	100	100	100	SUB
89	Right	Accumbens area	100	100	100	100	100	100	100	100	SUB
90	Right	Fronto-marginal gyrus and sulcus	23	2	1	3	15	100	23	4	FP
91	Right	Inferior occipital gyrus and sulcus	0	0	0	0	0	0	0	1	VIS
92	Right	Paracentral lobule and sulcus	99	98	100	95	100	98	99	98	SOM
93	Right	Subcentral gyrus (central operculum) and sulci	1	6	0	1	59	0	1	3	SOM
94	Right	Transverse frontopolar gyri and sulci	10	1	1	0	4	100	9	0	DMN
95	Right	Anterior part of the cingulate gyrus and sulcus (ACC)	1	0	0	0	3	96	1	0	DMN
96	Right	Middle-anterior part of the cingulate gyrus and sulcus (aMCC)	1	1	0	0	1	1	2	0	VA
97	Right	Middle-posterior part of the cingulate gyrus and sulcus (pMCC)	0	2	0	0	14	0	1	1	SOM
98	Right	Posterior-dorsal part of the cingulate gyrus (dPCC)	100	99	4	31	100	98	100	21	DMN
99	Right	Posterior-ventral part of the cingulate gyrus (vPCC)	100	100	100	100	100	5	100	100	DMN
100	Right	Cuneus	0	0	0	0	0	0	1	0	VIS
101	Right	Opercular part of the inferior frontal gyrus	0	0	0	0	0	0	0	0	VA

ID	Hemisphere	Region of Interest	EMOTION	GAMBLING	LANGUAGE	MOTOR	RELATIONAL	REST	SOCIAL	WM	Yeo System
102	Right	Orbital part of the inferior frontal gyrus	90	80	100	96	97	100	29	95	DMN
103	Right	Triangular part of the inferior frontal gyrus	1	1	5	2	1	8	0	0	FP
104	Right	Middle frontal gyrus	0	0	0	0	0	63	0	0	FP
105	Right	Superior frontal gyrus	0	0	0	0	0	0	0	0	DMN
106	Right	Long insular gyrus and central sulcus of the insula	99	100	100	98	100	1	99	100	VA
107	Right	Short insular gyri	14	9	8	1	42	4	55	12	VA
108	Right	Middle occipital gyrus	0	0	0	0	0	0	0	0	VIS
109	Right	Superior occipital gyrus	0	0	0	0	0	0	0	0	VIS
110	Right	Lateral occipito-temporal gyrus	0	0	1	0	0	0	0	0	VIS
111	Right	Lingual gyrus, ligual part of the medial occipito-temporal gyrus	0	0	0	0	0	0	0	0	VIS
112	Right	Parahippocampal gyrus, parahippocampal part of the medial occipito-temporal gyrus	100	100	100	100	98	57	100	100	SUB
113	Right	Orbital gyri	32	15	4	16	35	97	11	35	LIM
114	Right	Angular Gyri	0	0	0	0	1	88	0	0	DMN
115	Right	Supramarginal gyrus	0	0	0	0	0	0	0	0	VA
116	Right	Superior parietal lobule	0	0	0	0	0	0	0	0	DA
117	Right	Postcentral gyrus	0	1	0	0	1	0	0	0	SOM
118	Right	Precentral gyrus	0	0	0	1	0	0	0	0	SOM
119	Right	Precuneus	0	0	0	1	0	0	0	0	DA
120	Right	Straight gyrus	100	100	99	99	99	100	100	99	LIM
121	Right	Subcallosal area	100	100	100	100	100	100	100	100	SUB
122	Right	Anterior transverse temporal gyrus	57	74	68	13	80	0	65	53	SOM
123	Right	Lateral aspect of the superior temporal gyrus	0	0	21	0	61	0	0	2	SOM
124	Right	Planum polare of the superior temporal gyrus	100	100	100	99	100	52	100	100	LIM
125	Right	Planum temporale or temporal plane of the superior temporal gyrus	0	1	0	0	1	0	0	2	SOM
126	Right	Inferior temporal gyrus	0	0	0	2	0	0	0	0	DA
127	Right	Middle temporal gyrus	0	0	0	1	4	27	0	0	DMN
128	Right	Horizontal ramus of the anterior segment of the lateral sulcus	38	22	42	12	73	95	14	20	VA
129	Right	Vertical ramus of theanterior segment of the lateral sulcus	24	21	19	15	28	99	14	21	DMN
130	Right	Posterior ramus of the lateral sulcus	2	6	2	0	68	0	2	4	SOM
131	Right	Occipital pole	0	0	0	0	0	0	0	0	VIS
132	Right	Temporal pole	99	100	98	100	100	100	68	100	LIM
133	Right	Calcarine sulcus	0	0	0	0	0	0	0	0	VIS
134	Right	Central sulcus	0	0	0	0	11	0	0	0	SOM
135	Right	Marginal branch of the cingulate sulcus	2	6	0	0	13	0	2	4	VA
136	Right	Anterior segment of thecircular sulcus of the insula	96	32	18	71	54	97	55	26	FP

ID	Hemisphere	Region of Interest	EMOTION	GAMBLING	LANGUAGE	MOTOR	RELATIONAL	REST	SOCIAL	WM	Yeo System
137	Right	Inferior segment of thecircular sulcus of the insula	6	19	2	2	66	0	22	16	SOM
138	Right	Superior segment of thecircular sulcus of the insula	1	3	2	1	4	1	8	1	VA
139	Right	Anterior transverse collateral sulcus	100	100	100	100	100	100	47	100	LIM
140	Right	Posterior transverse collateral sulcus	1	0	71	8	0	0	0	39	VIS
141	Right	Inferior frontal sulcus	0	0	0	0	0	0	0	0	FP
142	Right	Middle frontal sulcus	0	0	0	0	0	33	0	0	FP
143	Right	Superior frontal sulcus	0	0	0	0	0	15	0	0	DMN
144	Right	Sulcus intermedius primus	0	0	1	0	1	94	0	0	DMN
145	Right	Intraparietal sulcus and transverse parietal sulci	0	0	0	0	0	0	0	0	DA
146	Right	Middle occipital sulcus and lunatus sulcus	0	0	0	0	0	0	0	0	VIS
147	Right	Superior occipital sulcus and transverse occipital sulcus	0	0	0	0	0	0	0	0	VIS
148	Right	Anterior occipital sulcus and preoccipital notch	0	0	0	0	2	0	0	2	VIS
149	Right	Lateral occipito-temporal sulcus	1	0	7	4	0	0	0	3	VIS
150	Right	Medial occipito-temporal sulcus and lingual sulcus	4	10	27	28	1	0	0	48	VIS
151	Right	Lateral orbital sulcus	1	2	0	1	3	98	2	2	FP
152	Right	Medial orbital sulcus	100	100	100	100	100	100	100	100	LIM
153	Right	Orbital sulci	47	61	2	90	65	100	85	64	FP
154	Right	Parieto-occipital sulcus	0	0	0	0	1	0	73	0	VIS
155	Right	Pericallosal sulcus	100	100	99	99	100	100	100	100	DMN
156	Right	Postcentral sulcus	0	0	0	0	0	0	0	0	DA
157	Right	Inferior part of the precentral sulcus	0	0	0	0	0	0	0	0	DA
158	Right	Superior part of the precentral sulcus	0	0	0	0	0	0	0	0	DA
159	Right	Suborbital sulcus	100	100	100	100	100	100	100	100	DMN
160	Right	Subparietal sulcus	6	3	1	3	14	39	6	0	DMN
161	Right	Inferior temporal sulcus	1	0	0	0	0	89	0	0	DMN
162	Right	Superior temporal sulcus	0	0	0	0	0	1	0	0	DMN
163	Right	Transverse temporal sulcus	32	33	62	14	75	0	36	50	SOM
164	Right	Cerebellum	0	0	0	0	0	39	0	1	CER

B

Supplementary Material of Chapter 5

B.1 Supplementary Figures

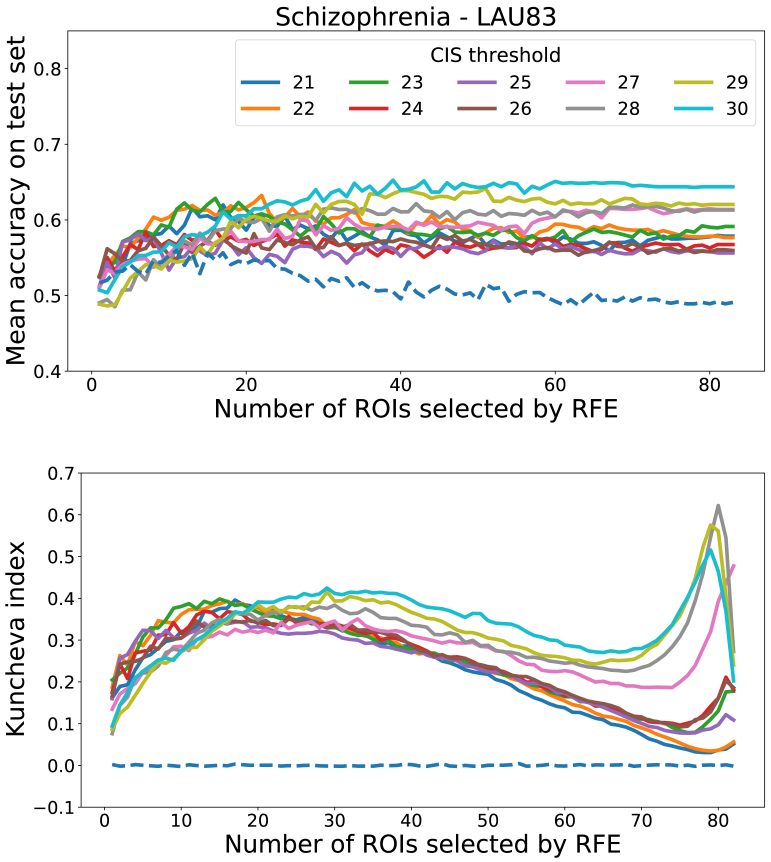

Figure B.1.1: **Schizophrenia : Accuracy and stability.** Analogous results to that of Figure 5.2 with the 83 × 83 Lausanne parcellation.

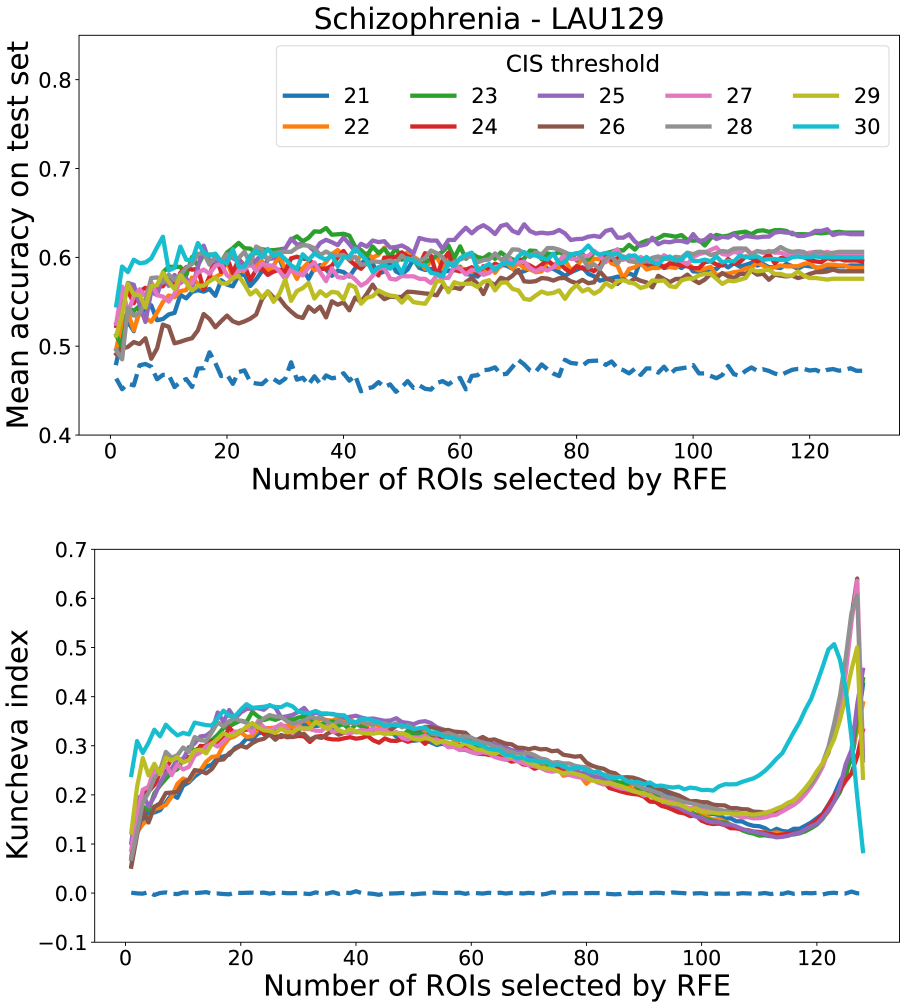

Figure B.1.2: **Schizophrenia : Accuracy and stability.** Analogous results to that of Figure 5.2 with the 129 × 129 Lausanne parcellation.

C

Supplementary Material of Chapter 6

C.1 Supplementary Figures

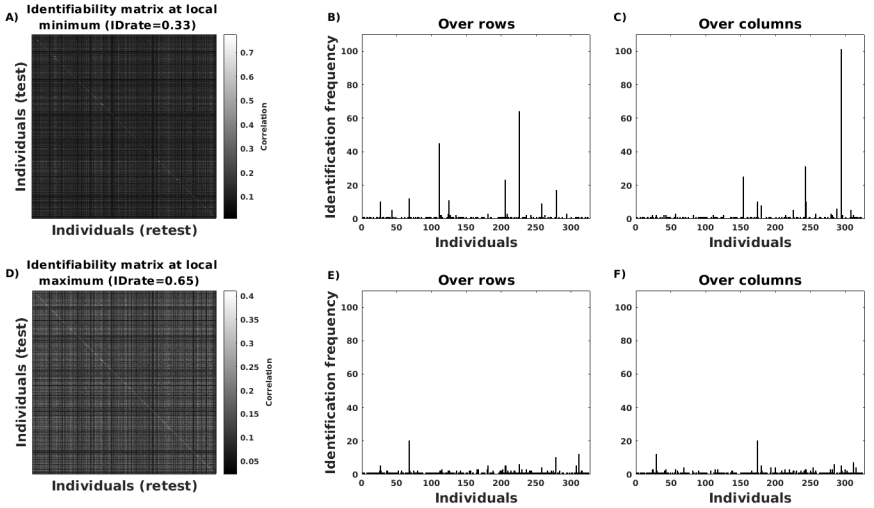

Figure C.1.1: **Identification rate is driven down by a few individuals.** We illustrate the undesired behavior of the identification rate (ID_{rate}), using one typical subsample of the database related to normalized FCs of the relational processing task (see Figure 6C). **A)** Identifiability matrix computed at a local minimum of the ID_{rate} curve (ID_{rate}=0.33, 617 components). **B)** (resp. **C)**) Number of occurences of each individual as the maximum of the rows (resp. columns) of the identifiability matrix. The bottom row shows the same analysis when using all components (ID_{rate}=0.65, 654 components, right end of the ID_{rate} curve in Figure 6C).

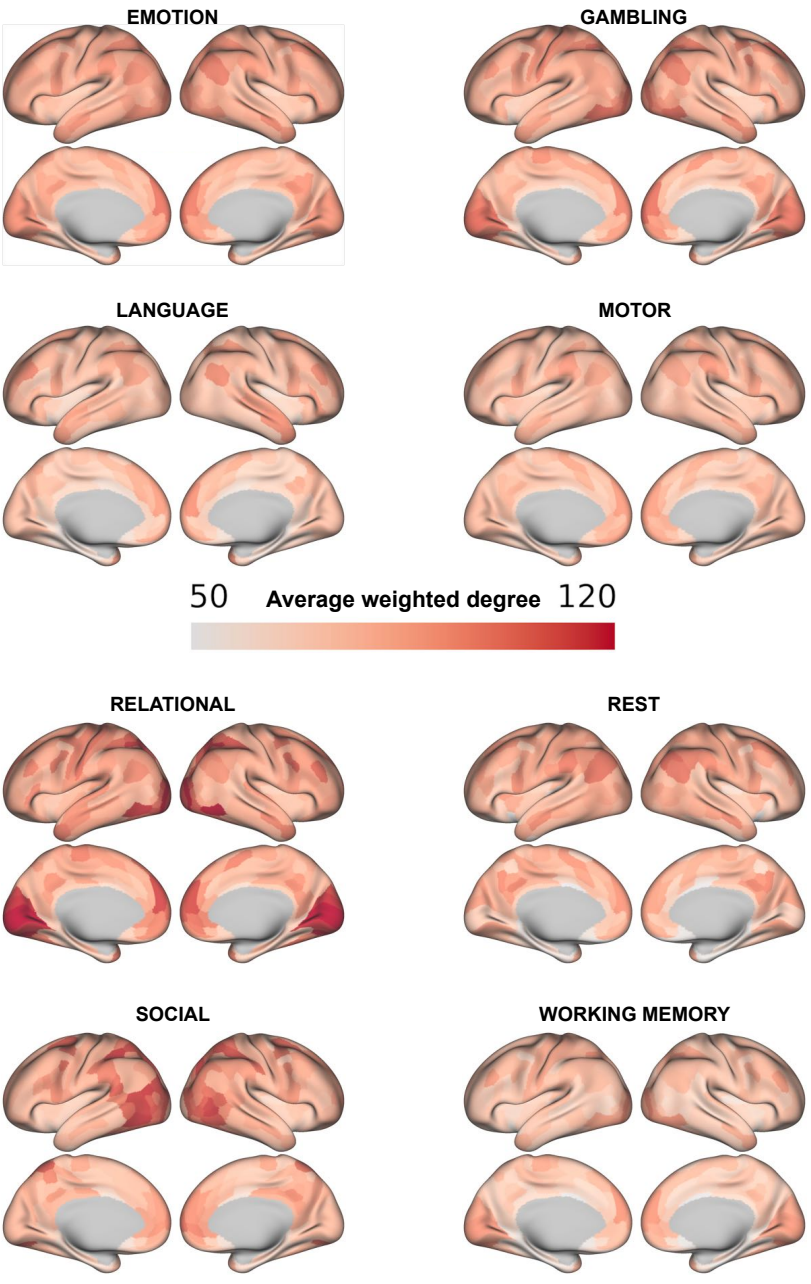

Figure C.1.2: Average weighted degree sequence across individuals (Absolute FC), displayed along the cortical surface for each fMRI condition.

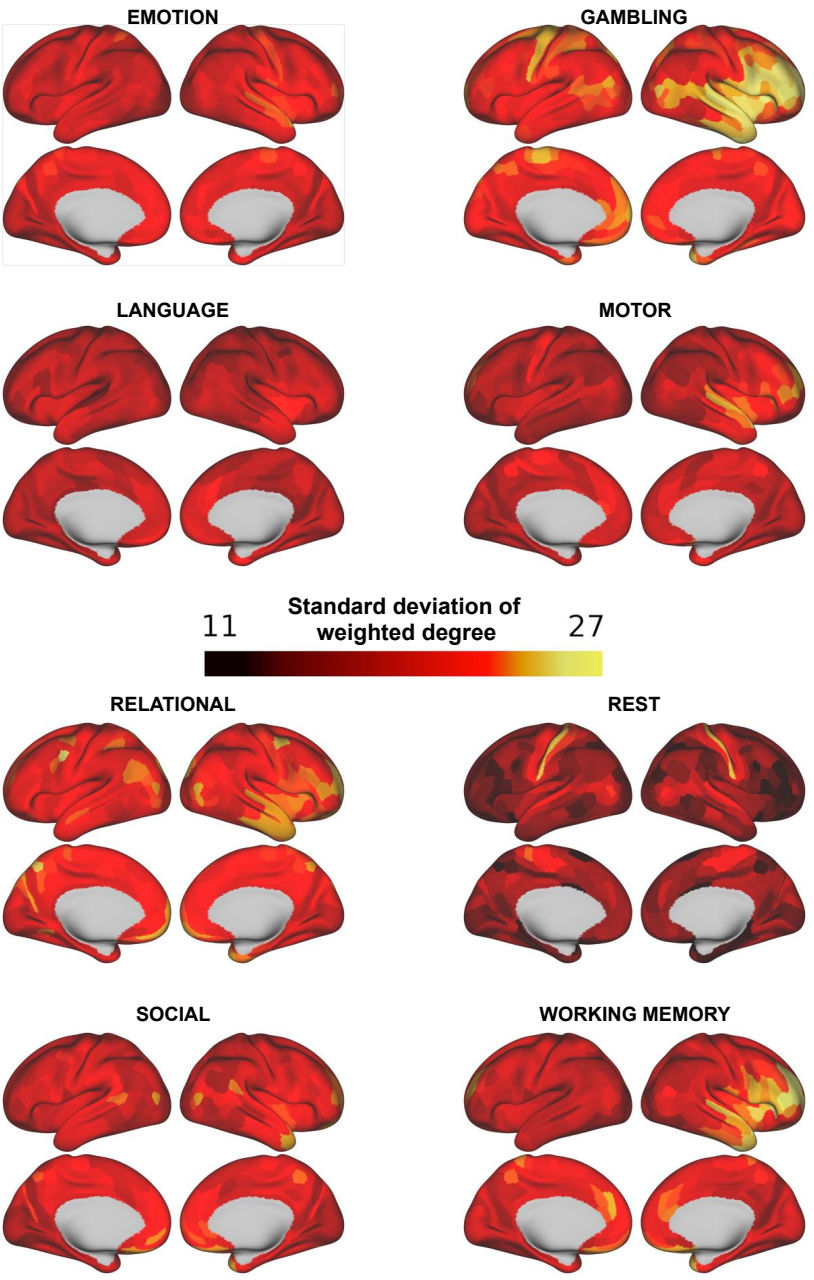

Figure C.1.3: Standard deviation of weighted degree sequence across individuals (Absolute FC), displayed along the cortical surface for each fMRI condition.

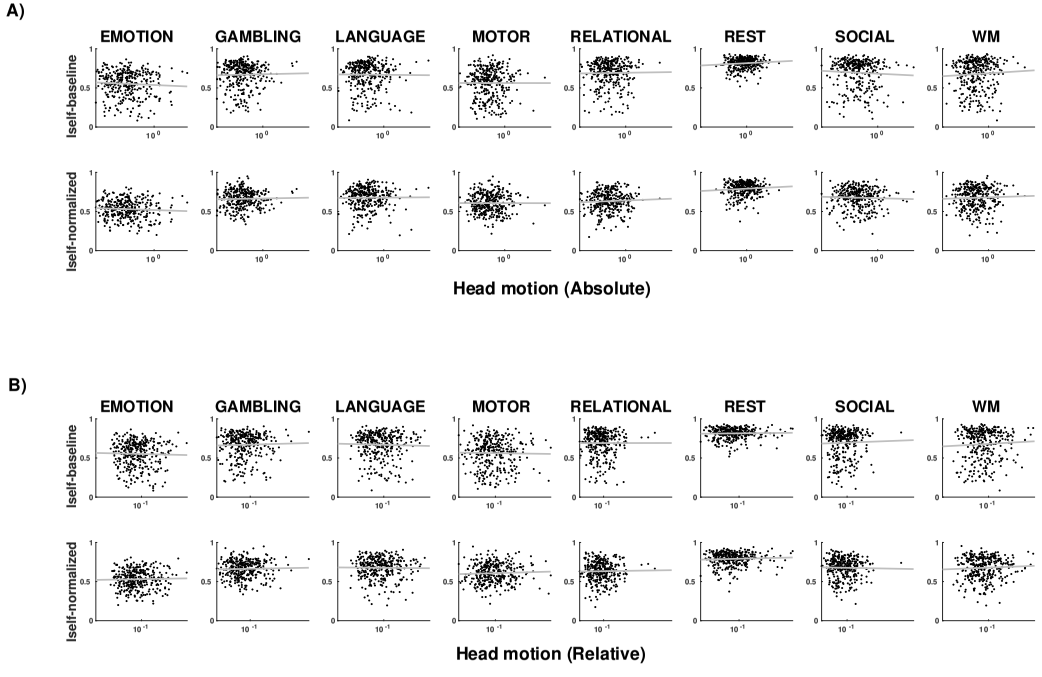

Figure C.1.4: **Effect of head motion on identifiability A)** Scatter plot of average absolute head motion versus I_{self} at optimal I_{diff}, in baseline FCs (top row) and normalized FCs (bottom row), for one random subsample representing 80% (327 subjects) of the entire cohort (409 subjects). The head motion estimates were retrieved from the HCP files 'Movement_AbsoluteRMS_mean.txt' . The highest estimate across left-to-right and right-to-left acquisitions is used as the overall head motion score per subject in the x-Axes (in $\log_{10}$ scale) of the scatter plots. **B)** Analogous results are presented for relative Root Mean Square Frame Displacement as obtained from 'Movement_RelativeRMS_mean.txt'. In all plots for A) and B), the explained variance for linear regression models between $\log_{10}$ of head motion score and I_{self} values was smaller than 1%.

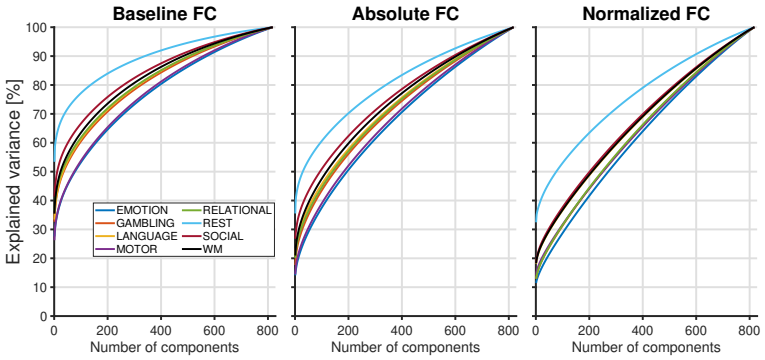

Figure C.1.5: **Cumulative percentage of explained variance.** Components resulting from the PCA decomposition of the database (409 individuals, 2 scans by individual) are added in decreasing order of explained variance, for baseline (left), absolute (middle) and normalized FCs (right).

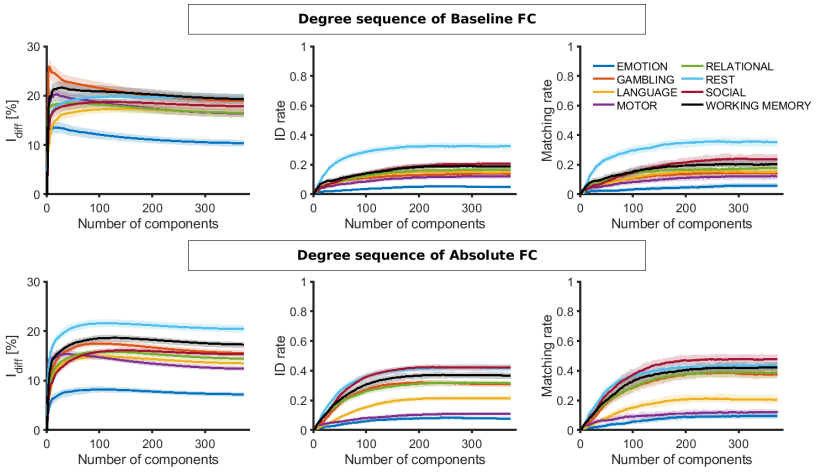

Figure C.1.6: **Fingerprinting the weighted degree sequence.** We applied the PCA decomposition-reconstruction procedure [Amico and Goñi, 2018] to a data matrix whose columns are the weighted degree sequence of both test and retest FCs, instead of using the vectorized upper triangular part of FC matrices as done in the main analysis. Solid lines represent the median value across 100 random subsamples of the database and shaded areas correspond to the inter-percentile range (2.5 and 97.5 percentiles). Top row: the weighted degree sequence is computed from the baseline FC. Bottom row: the weighted degree sequence is computed from the absolute FC. We computed the three metrics used in the main manuscript: differential identifiability (left), identification rate (middle) and matching rate (right).

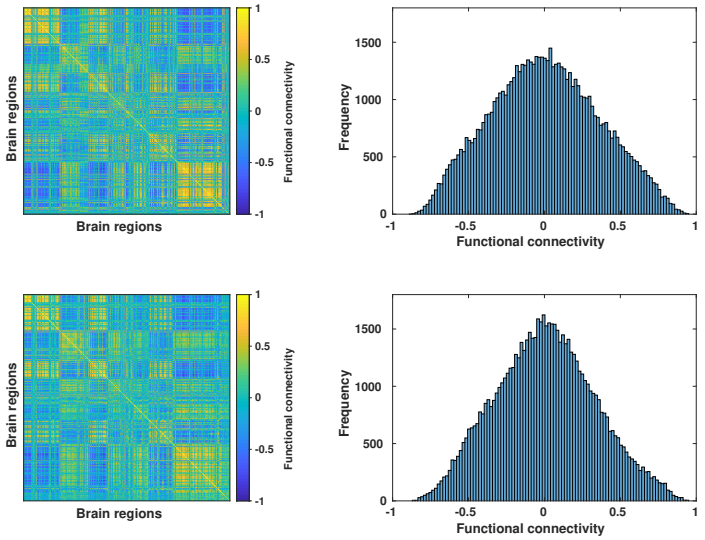

Figure C.1.7: Two examples of FCs producing 'best-matchings' with many FCs of the other session when computing ID_{rate}.

C.2 Supplementary Tables

Table C.2.1: Five highest-strength (weighted degree on absolute FCs) regions for each fMRI condition. In each cell, the brain region identity is provided in bold (R : right hemisphere ; L : left hemisphere) along with its mean (+/- standard deviation) weighted degree across individuals.

Emotion	Gambling	Language	Motor	Relational	Rest	Social	Working memory
R_Area 10d 102.8 +/-20.7	**L_Fourth Visual Area** 107.9+/-19.9	**L_Area IntraParietal 2** 100.1+/-19.1	**R_Area PF Complex** 91.2+/-17.0	**L_Primary Visual Cortex** 123.3+/-18.7	**R_Area PGs** 104.4+/-17.5	**L_Area PH** 115.6+/-17.9	**R_Fourth Visual Area** 98.9+/-15.1
L_Area 9 Middle 101.4+/-20.6	**L_Area Lateral IntraParietal dorsal** 105.9+/-20.4	**R_Area IntraParietal 2** 98.6+/-18.9	**L_Area PF Complex** 90.0+/-17.5	**R_Primary Visual Cortex** 122.6+/-18.7	**L_Area PGs** 100.9+/-16.9	**L_IntraParietal Sulcus Area 1** 115.1+/-17.6	**L_Fourth Visual Area** 98.5+/-15.4
L_Area IntraParietal 0 100.4+/-18.8	**R_Area Lateral IntraParietal dorsal** 105.3+/-20.2	**L_Area posterior 9-46v** 95.9+/-19.6	**R_Area 10d** 90.0+/-18.0	**L_Fourth Visual Area** 121.9+/-17.9	**L_Area PGi** 100.7+/-16.6	**L_Anterior IntraParietal Area** 115.0+/-18.6	**R_Area Lateral IntraParietal dorsal** 95.1+/-17.4
R_Area PGs 100.0+/-18.6	**R_Fourth Visual Area** 105.3+/-19.8	**R_Area STSv anterior** 95.4+/-21.5	**L_ Area 9 Middle** 90.0+/-19.3	**R_Fourth Visual Area** 121.2+/-17.9	**R_Area PGi** 99.5+/-15.5	**R_Area FST** 114.9+/-17.6	**L_Area IntraParietal 0** 94.6+/-17.2
L_Area 10d 100.0+/-21.2	**R_Area 10d** 105.2+/-22.3	**R_Area posterior 9-46v** 94.7+/-19.8	**L_Area 10d** 88.4+/-19.1	**R_Area PH** 119.5+/-19.4	**L_Area PF Complex** 98.2+/-15.1	**R_IntraParietal Sulcus Area 1** 114.9+/-18.2	**R_Area IntraParietal 0** 94.2+/-17.8

Table C.2.2: Five lowest-strength (weighted degree on absolute FCs) regions for each fMRI condition. In each cell, the brain region identity is provided in bold (R : right hemisphere ; L : left hemisphere) along with its mean (+/- standard deviation) weighted degree across individuals.

Emotion	Gambling	Language	Motor	Relational	Rest	Social	Working memory
L_Pallidum 64.3 +/-21.5	**R_Area 33 prime** 57.3+/-19.7	**R_PreSubiculum** 53.8+/-20.6	**L_Area 33 prime** 60.0+/-20.0	**L_Area 33 prime** 61.5+/-20.3	**R_Pirform Cortex** 45.8+/-11.3	**R_Accumbens-area** 56.3+/-19.7	**L_Area 33 prime** 50.1+/-19.4
L_Pirform Cortex 64.2+/-18.6	**L_Area 33 prime** 57.1+/-19.0	**L_PreSubiculum** 53.5+/-18.7	**R_Accumbens-area** 59.2+/-19.6	**L_Pallidum** 61.2+/-22.6	**R_Pallidum** 44.3+/-12.1	**L_Pirform Cortex** 55.9+/-20.4	**R_Area 33 prime** 49.8+/-19.9
R_Pirform Cortex 64.1+/-21.0	**L_Pallidum** 56.8+/-21.9	**L_Pallidum** 52.5+/-20.7	**L_Accumbens-area** 59.2+/-19.2	**L_Accumbens-area** 60.1+/-20.0	**R_Accumbens-area** 43.3+/-10.2	**R_Pallidum** 55.2+/-20.4	**L_Pallidum** 49.3+/-21.2
R_Accumbens-area 63.5+/-19.5	**R_Accumbens-area** 55.8+/-20.2	**R_Accumbens-area** 51.5+/-19.3	**L_Pirform Cortex** 59.0+/-18.5	**R_Area 33 prime** 60.4+/-19.7	**L_Accumbens-area** 42.7+/-10.1	**L_Pallidum** 55.2+/-21.0	**R_Accumbens-area** 48.7+/-20.1
L_Accumbens-area 63.1+/-19.2	**L_Accumbens-area** 53.8+/-17.7	**L_Accumbens-area** 49.9+/-17.3	**R_Area 33 prime** 58.9+/-19.6	**R_Accumbens-area** 60.1+/-19.7	**L_Pallidum** 42.4+/-10.7	**L_Accumbens-area** 55.0+/-19.5	**L_Accumbens-area** 48.1+/-19.7

Table C.2.3: Number of frames for each fMRI condition (HCP datasets).

Condition	Number of frames
EMOTION	176
GAMBLING	253
LANGUAGE	316
MOTOR	284
RELATIONAL	232
RESTING-STATE	1200
SOCIAL	274
WORKING MEMORY	405

D

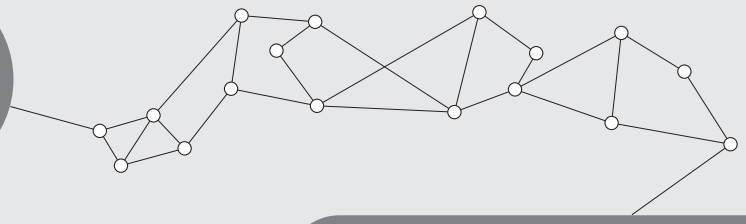

MRI acquisition parameters

D.1 Schizophrenia dataset

All individuals were scanned on a 3T Siemens Trio scanner with a 32-channels head coil. Structural data was acquired using a magnetization-prepared rapid acquisition gradient echo (MPRAGE) sequence with in-plane resolution of 1 mm, slice thickness of 1.2 mm of total voxel number of $240 \times 257 \times 160$ and TR, TE and TI were 2300, 2.98 and 900 ms respectively. Diffusion spectrum imaging (DSI) data was obtained as a sequence of 128 diffusion-weighted images, with a b_0 reference image and a maximum b-value of 8000 s/mm^2. The acquisition length was 13 min and 27s. The number of voxels was $96 \times 96 \times 34$ with a resolution of $2.2 \times 2.2 \times 3.0$ mm, and TR and TE were 6100 and 144 ms respectively. The issue of motion- artifacts linked to signal drop-outs was dealt with by visually inspecting the signal, and no subject had to be excluded as a result of this [Yendiki et al., 2014]. A resting-state functional MRI (fMRI) scan was acquired for 8 minutes ($3.3 \times 3.3 \times 3.3$ mm voxel size, TR = 1920ms, TE = 30ms, 32 slices, flip angle $85°$). During the fMRI acquisition, participants were asked not to fall asleep and let their mind wander while fixating their vision to the cross on the screen.

D.2 Meditation dataset

All participants were scanned on a 3T Philips Achieva scanner with a 32-channel phased array head coil. For each participant, the Magnetic Resonance Imaging (MRI) session included 4 acquisitions: one anatomical sequence (T1-weighted image), one eyes-closed resting-state functional MRI (fMRI) scan, one Diffusion Tensor Imaging (DTI) sequence and one fMRI scan before which participants were instructed to enter a meditation state. Due to technical problems, the DTI sequence was acquired on a different scanner (3T Siemens Skyra) for 9 participants.

The T1-weighted anatomical image was obtained with of a gradient-echo sequence with an inversion prepulse (Turbo Field Echo, TFE) acquired in the sagittal

plane with parameters TR = 9.1 ms, TE = 4.6 ms, flip angle = 8°, number of slices = 150, slice thickness = 1 mm, in-plane resolution reconstructed in 0.75 × 0.75 mm^2. DTI images were acquired on the Philips Achieva scanner using a spin-echo planar sequence with parameters TE = 83 ms, TR = 6422 ms, bandwidth = 2790 Hz/pixel, number of slices = 70, slice thickness = 2 mm, in-plane resolution = 2 × 2 mm^2, matrix size = 112 × 112, FOV = 224×224 mm^2, 55 directions. A reference b_0 image and one b = 800 s/mm^2 image were acquired. The DTI images from the Siemens Skyra scanner (9 participants) were obtained with a spin-echo planar sequence with parameters TE = 74 ms, TR = 9000 ms, bandwidth = 1776 Hz/pixel, number of slices = 64, slice thickness = 2mm, in-plane resolution = 1.953 × 1.953 mm^2, matrix size = 128 × 128, FOV = 250 × 250 mm^2, 64 directions. A reference b_0 image and one b = 1000 s/mm^2 image were acquired. Resting-state (eyes closed) and meditation fMRI images were acquired using repeated single-shot echo-planar imaging. The following parameters were used: TE = 30ms, FA = 90°, in plane resolution = 3.44 × 3.44mm^2, 35 slices acquired in an ascending order, slice thickness = 3.44mm, TR = 2000ms and number of TR = 200 (acquisition length = 6min 40s).